Hippocampal Interneuron Dynamics Supporting Memory Encoding and Consolidation

Bert Vancura

Submitted in partial fulfillment of the
requirements for the degree of
Doctor of Philosophy
under the Executive Committee
of the Graduate School of Arts and Sciences

COLUMBIA UNIVERSITY

2022

Abstract

Hippocampal Interneuron Dynamics Supporting Memory Encoding and Consolidation

Bert Vancura

Neural circuits within the hippocampus, a mammalian brain structure critical for both the encoding and consolidation of episodic memories, are composed of intimately connected excitatory pyramidal cells and inhibitory interneurons. While decades of research have focused on how the *in vivo* physiological properties of pyramidal cells may support these cognitive processes, and the anatomical and physiological properties of interneurons have been extensively studied *in vitro,* relatively little is known about how the *in vivo* activity patterns of interneurons support memory encoding and consolidation. Here, I have utilized Acousto-Optic Deflection (AOD)-based two-photon calcium imaging and *post-hoc* immunohistochemistry to perform large-scale recordings of molecularly-defined interneuron subtypes, within both CA1 and CA3, during various behavioral tasks and states. I conclude that the subtype-specific dynamics of inhibitory circuits within the hippocampus are critical in supporting its role in memory encoding and consolidation.

Table of Contents

Acknowledgments

I would like to thank Dr. Attila Losonczy, my thesis committee, and my close friends and family, for all of their support during the work described in this thesis.

Chapter 1: Introduction

1.1 Role of the Hippocampus in Declarative Memory and Spatial Navigation

The modern study of the hippocampus and its role in memory began in 1953, when neurosurgeon William Beecher Scoville resected patient H.M.'s medial temporal lobe structures, including the hippocampus, to treat intractable epilepsy. Although the experimental surgery was largely successful in mitigating H.M.'s seizures, he immediately showed a severe anterograde amnesia, or inability to form new memories (Scoville and Milner, 1957). From this point forward, brain scientists realized that the hippocampus is the likely site of memory formation in the mammalian brain, launching decades of investigation into its anatomy, physiology, and precise role in the formation of different types of memories (Squire, 2009). This discovery represented a true breakthrough in brain science, as it suggested that complex cognitive functions, such as memory, could have a precise anatomical location within discrete structures of the brain (Squire, 2009).

The first clues regarding the role of the hippocampus in memory came from studying H.M.'s deficits (Scoville and Milner, 1957; Squire, 2009; Suzanne Corkin, 2002). These studies found that his amnesia was global: His memory was impaired regardless of the kind of memory test used (cued recall, multiple-choice recognition), regardless of the kind of stimulus material (words, digits, faces), and regardless of the sensory modality through which information was presented (vision, olfaction, somatosensory) (Squire, 2009; Suzanne Corkin, 2002). However, H.M.'s very short-term (immediate) memory was intact, as well as his language capacities and his ability to learn certain visuomotor skills (Squire, 2009; Suzanne Corkin, 2002). For example, H.M. was able to learn to read mirror-reversed words over the course of several days as well as control subjects were, although he could not remember the learning experience itself (Squire,

2009). These seminal studies provided critical insights into the subdivisions of memory and for which types of memory the hippocampus is indispensable.

H.M.'s capacity for short-term memory despite an overall severe anterograde amnesia suggests different mechanisms supporting short-term memory and long-term memory. Amnesic patients, including H.M., can, for example, keep short lists of numbers in mind for several minutes if they repeat them and maintain attention to the task (Squire, 1986). However, their deficit becomes apparent once the amount of material to be remembered exceeds what can be held in immediate memory or when an intervening period of distraction is introduced (Squire, 1986). These findings support a distinction between short-term or immediate memory, which is capacity-limited and intact in patients with hippocampal lesions, and long-term memory, the formation of which is impaired in patients with hippocampal lesions and is thus hippocampal-dependent.

Similarly, H.M.'s ability to learn and retain certain visuomotor skills over many days and longer, but his inability to remember the events of his daily life, suggest a distinction within the domain of long-term memory (Squire, 1986). These findings have led to a distinction between hippocampal-dependent declarative memory and hippocampal-independent procedural memory. Declarative memory includes the facts and experiences of everyday life, and it is accessible to conscious awareness. It can be brought to mind verbally or nonverbally as an image (Squire, 1986). In contrast, the knowledge stored within procedural memory is implicit, as it is accessible only by engaging in the skills in which the knowledge is embedded (Squire, 1986). It is likely that procedural learning and memory are phylogenetically old, depending on subcortical brain structures that are already well developed in invertebrates. On the other hand, declarative knowledge and memory are phylogenetically more recent, reaching their full potential in

mammals with fully developed medial temporal lobes structures, including the hippocampus and related cortical areas (Squire, 1986). This full development of the hippocampus and surrounding structures in higher mammals could allow for more sophisticated forms of learning, by allowing animals to record and assess experiences that led to either positive or negative outcomes, leading to future behavioral changes (Squire, 1986).

Declarative memory itself can be subdivided into episodic and semantic memory. Episodic memory includes memory for events in one's life that have a specific spatial and temporal context (i.e., I saw a cat on the way to the subway this morning), while semantic memory refers to facts and general information about the world that are not tied to specific individual experience (i.e., Barack Obama was elected US president in 2008) (Squire, 1986).

In addition to anterograde amnesia, many patients with hippocampal lesions, including H.M., exhibit a temporally-graded retrograde amnesia (Scoville and Milner, 1957; Squire, 1986). That is, the retrograde amnesia only affects events that occurred during the years immediately preceding the onset of the amnesia. For example, H.M. exhibited amnesia extending from a few years to approximately ~10 years before his surgery in 1953 (Squire, 1986). On the other hand, he could recall detailed biographical episodes and information about public events that occurred in his childhood, well before his surgery (Squire, 1986). Similar observations have been made in rodents. For example, rats or mice given an electroconvulsive shock after training in a behavioral task later exhibit impaired memory for the training experience (Squire, 1986). However, as the time between the training experience and the shock increases, the extent of the retrograde amnesia decreases (Squire, 1986). These observations suggest that the hippocampus is required for the formation of declarative memories, but is not the site of their ultimate storage, as it becomes dispensable for recall of the memory after enough time has elapsed. In addition, the

hippocampus is required for some time after the encoding of the declarative memory, during which time the memory consolidates after initial encoding and is still susceptible to hippocampal lesion. During this period of memory consolidation, it is hypothesized that the representations of the memory in the brain are reorganized, causing some aspects of the initial representation to be forgotten and other parts to become more stable and coherent (Squire, 1986). In addition, during this period of memory consolidation, the hippocampus is thought to communicate with the ultimate sites of declarative memory storage in the brain, facilitating the gradual transfer of memories to them. Interestingly, although the process of memory consolidation can last from weeks to months in rodents, it can last many years in humans (Squire, 1986). In summary, the hippocampus is required for the formation and consolidation of long-term declarative memories.

In parallel to this line of work over the past few decades that has focused on the role of the hippocampus in declarative memory in humans, a complementary line of work has focused on the role of the hippocampus in spatial navigation in rodents. In early studies on animal learning, many psychologists and neuroscientists believed that relatively involved behaviors, such as learning how to navigate through a maze, were performed by animals learning the many associations between specific sensory stimuli and rewarded behavioral responses ('stimulus-response' theory) (Eichenbaum, 2017). However, in 1948, Edward Tolman convincingly showed that rats can learn to navigate from one location to another in a maze via short-cuts or roundabouts instead of always following learned routs, suggesting that the rats must be generating a cognitive map that guides behavior (Tolman, 1948). More generally, Tolman argued that these experiments show that rodents can learn more generally by understanding the relationships between objects, locations, and experiences, rather than learning just by memorizing various stimulus-outcome associations (Eichenbaum, 2017; Tolman, 1948). Several

decades later, in 1971, O'Keefe and Dostrovsky described neurons in the hippocampus of rats that increased their firing rates selectively in specific parts of an environment ("place cells", see below for more details on the physiology of hippocampal pyramidal cells) (O'Keefe and Dostrovsky, 1971). At the population level, different neurons encoded different locations within the environment, such that the whole environment was represented by the hippocampal neural population. Thus, these place cells could be the neural substrate of a cognitive map capable of guiding behavior. Later lesion experiments provided the first evidence for a causal role for the hippocampus in spatial navigation, as rats with hippocampal, but not cortical, lesions were impaired in the Morris Water Maze (Morris et al., 1982).

While the roles of the hippocampus in declarative memory and in spatial navigation have been studied largely in parallel over the past several decades, many recent theories of hippocampal function suggest that the neural mechanisms supporting these two cognitive functions may be fundamentally very similar. For example, both the memory and spatial navigation functions of the hippocampus are thought to involve the formation of mental maps that can be organized along spatial, temporal, and conceptual dimensions (Milivojevic and Doeller, 2013). Other investigators have proposed that the hippocampus is fundamentally a relational processing system, specializing in, for example, the relational mapping of objects and actions within spatial contexts and the representation of spatial routes as episodes defined by sequences of places traversed (Eichenbaum, 2017; Eichenbaum and Cohen, 2014). Thus, the relational processing ability of the hippocampus makes is particularly well suited for spatial navigation, although navigation may not be the explicit function of the hippocampus *per se*. Although the declarative memory and spatial navigation accounts of hippocampal function remain incompletely reconciled, it is likely that the neural circuit mechanisms supporting these

cognitive functions share many similarities. In this thesis, I will consider hippocampal function primarily through its role in supporting spatial navigation in mice. In the next section, I will provide a brief overview of the neural circuits and cell types of the hippocampus and related brain structures.

1.2 Overview of Neural Circuits of the Hippocampus and Entorhinal Cortex: Anatomical Organization, Major Cell Types, and Connectivity

The hippocampus can be divided into several subregions, including the dentate gyrus (DG), and the CA3, CA2, and CA1 regions of the hippocampus proper. The hippocampus is often considered a simplified cortical structure, as information largely flow unidirectionally through this laminar structure. In addition, the excitatory inputs to principal cells throughout the hippocampus are spatially organized along their dendritic trees. Below, I will review the basic anatomical characteristics of the hippocampal circuitry, including the cell types within each subregion, the connectivity within and between subregions, and the proposed roles of each subregion in supporting episodic memory and spatial navigation.

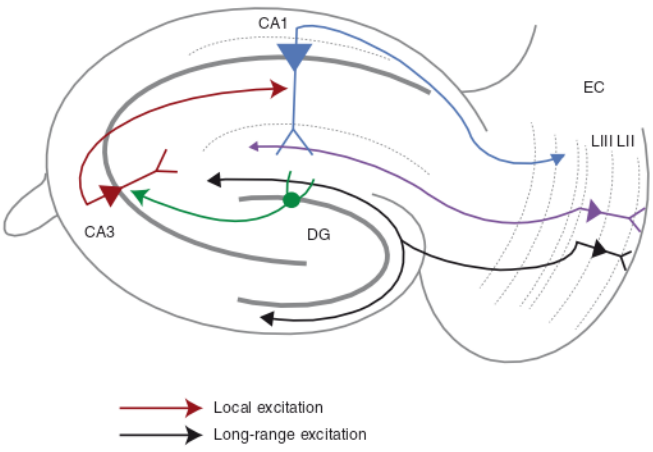

Figure 1: Excitatory connections within the hippocampal-entorhinal circuit. Neural information flows largely unidirectionally from the entorhinal cortex to the DG, CA3, and finally to CA1 (Source: Basu and Siegelbaum, 2015).

Information processing within the hippocampus begins as input from the medial entorhinal cortex (MEC) and the lateral entorhinal cortex (LEC) arrives at the DG (Basu and Siegelbaum, 2015). Layer II stellate cells from both the MEC and the LEC

send excitatory, glutamatergic projections to the DG via the perforant path, and these terminals form synapses on the dendrites of DG granule cells (Basu and Siegelbaum, 2015). The MEC and LEC in turn receive inputs from both primary sensory cortices and higher sensory areas, thus serving as the interface between the cortex and the hippocampus and providing the real-time sensory input required for episodic memory formation. While the MEC is thought to primarily convey spatial information to the hippocampus, the LEC is thought to carry information related to objects, specific sensory modalities (i.e., odors), and time (Mallory and Giocomo, 2018). The entorhinal cortex input to the hippocampus is thus often conceptualized as consisting of a "where" stream, corresponding to the MEC input, and a "what" stream, corresponding to the LEC input. Once the axons of MEC and LEC neurons arrive in the DG, their terminals form synapses on the dendrites of granule cells within the *stratum moleculare*. Specifically, LEC inputs form synapses on DG granule cells within the outer third of the *stratum moleculare*, while MEC inputs form synapses within the middle third of the molecular layer (Fernández-Ruiz et al., 2021). The cell bodies of granule cells are densely packed within the *stratum granulosum* sublayer (approximately ~1,000,000 granule cells in the adult rat brain), which consists of both an upper blade and a lower blade (Basu and Siegelbaum, 2015). Between the *stratum granulosum* upper and lower blades is the hilus of the dentate gyrus. Within the hilus is found the other class of excitatory neurons within the dentate gyrus, the mossy cells (Scharfman, 2016). The DG is thus unique from the other hippocampal subregions in that it contains two glutamatergic cell types (Hainmueller and Bartos, 2020; Scharfman, 2016). Mossy cells project to hilar interneurons and granule cells, both in the ipsilateral and the contralateral DG (Hainmueller and Bartos, 2020; Scharfman, 2016). They receive inputs from granule cells, other mossy cells, CA3 pyramidal cells, and hilar interneurons, embedding them in a complex circuitry

(Hainmueller and Bartos, 2020). While the functional roles of mossy cells in the DG circuitry remain incompletely understood, recent work has shown that mossy cells are selectively vulnerable to neurotoxic insults, including ischemia and epilepsy, potentially implicating them in the pathophysiology of these disorders (Scharfman, 2016). The DG circuitry is also unique because the DG is one of the few regions in the mammalian brain where neurogenesis continues throughout adulthood (Zhao et al., 2008). Adult neural stem/progenitor cells proliferate in the subgranular zone of the DG and undergo differentiation into adult-born granule cells, which are then functionally incorporated into the existing DG neural circuitry (Zhao et al., 2008). While the mechanisms regulating this neurogenesis and incorporation remain incompletely understood, both positive (exercise, environmental stimulation) and negative factors (ageing, stress) of neurogenesis have been identified (Zhao et al., 2008). In addition, the ablation of neurogenesis/adult-born neurons has resulted in behavioral deficits in hippocampal-dependent tasks (Zhao et al., 2008), highlighting its importance in the hippocampal circuitry. The production of new neurons and its regulation within the DG could indeed have important implications for the memory-storing capacity of the hippocampus as a whole. Overall, the DG is thought to be critical for several cognition functions, including pattern separation, novelty detection, the binding of information to spatial contexts, and working memory (Hainmueller and Bartos, 2020).

Information processing continues within the hippocampus as DG granule cells send their axons to area CA3. These granule cell axons, also called mossy fibers, form synapses on the proximal apical dendrites of CA3 pyramidal cells within the *stratum lucidum* (SL). CA3 pyramidal cells also receive input from layer II LEC and MEC neurons, which form synapses at the distal apical tuft dendrites of CA3 pyramidal cells within *stratum lacunosum-moleculare*

(SLM) (Basu and Siegelbaum, 2015; Rebola et al., 2017). CA3 pyramidal cells are recurrently connected with each other, forming one of the largest recurrent networks in the mammalian brain (Buzsáki, 2015). These excitatory connections between CA3 pyramidal cells are found both ipsilaterally and contralaterally; the ipsilateral projections are known as the commissural fibers, while the contralateral projections are known as the associational fibers (Rebola et al., 2017). These recurrent synapses form on the apical dendrites in *stratum radiatum* (SR) and the basal dendrites in *stratum oriens* (SO). The soma of CA3 pyramidal cells are located within *stratum pyramidale* (SP); the rat brain contains approximately 300,000 CA3 pyramidal cells (Basu and Siegelbaum, 2015). The CA3 subregion is thought to be critical for the rapid encoding of novel memories, memory consolidation, and pattern completion (Rebola et al., 2017).

CA3 pyramidal cells subsequently send their axons to CA1, both ipsilaterally and contralaterally, via the Schaffer collateral pathway. The terminals of these axons form synapses on the basal and proximal apical dendrites of CA1 pyramidal cells within SO and SR, respectively (Basu and Siegelbaum, 2015). CA1 pyramidal cells also receive input from Layer III MEC and LEC neurons, which form synapses on the distal apical dendrites of CA1 pyramidal cells within SLM. Thus, CA1 pyramidal cells receive indirect input from Layer II EC neurons, which is processed through the DG and CA3 before reaching CA1, and direct, monosynaptic input from Layer III EC neurons (Basu and Siegelbaum, 2015). The indirect pathway, from Layer II EC to the DG, CA3, and ultimately CA1, is referred to as the trisynaptic pathway, while the direct pathway from Layer III EC to CA1 is commonly referred to as the temporoammonic pathway (Basu and Siegelbaum, 2015). It is hypothesized that CA1 may form comparison between internally stored representations held within CA3 and real-time sensory information coming in from MEC/LEC. As CA1 serves as the output node of the hippocampus, the axons of

CA1 pyramidal cells send the hippocampus' output to several downstream brain structures: the subiculum, entorhinal cortex, lateral septum, and prefrontal cortex. Notably, CA1 pyramidal cells target the deep layers of both MEC and LEC (Layers V/VI), completing the loop between the hippocampus and the entorhinal cortex (Basu and Siegelbaum, 2015).

While area CA2, the comparatively small subregion between CA3 and CA1, has been traditionally understudied, recent investigations have begun to shed light on the unique circuitry of the CA2 subregion. CA2 pyramidal cells are unique from their counterparts in CA1 and CA3 with respect to their gene expression profiles, intrinsic physiological properties, and unique inputs (Dudek et al., 2016). Similar to CA3 pyramidal cells, CA2 pyramidal cells receive feedforward excitatory input from dentate granule cell mossy fibers, recurrent input from other CA2 pyramidal cells, and input from neighboring CA3 pyramidal cells (Dudek et al., 2016). In addition, CA2 receives unique subcortical inputs from the supramammillary nucleus and the paraventricular nucleus of the hypothalamus (Basu and Siegelbaum, 2015; Dudek et al., 2016). CA2 pyramidal cells send excitatory outputs both to CA1 and back to CA3. Within CA1, afferent CA2 fibers preferentially target the basal dendrites of CA1 pyramidal cells in SO over the apical dendrites in SR (Dudek et al., 2016). Thus, in addition to the classical excitatory hippocampal trisynaptic pathway, from DG to CA3 and ending in CA1, a complementary pathway exists through CA2: from the entorhinal cortex to CA2 and ending in CA1 (Basu and Siegelbaum, 2015). Functionally, CA2 pyramidal cells display unique activity dynamics from their hippocampal counterparts in that they specifically store social representations, and are thought to play a critical role in supporting social memories (Donegan et al., 2020; Hitti and Siegelbaum, 2014).

Although the majority of cells in each hippocampal subregion are excitatory neurons, each subregion also contains a wide diversity of GABAergic interneurons, which make up approximately ~10-20% of the total neuronal population (Pelkey et al., 2017). In contrast to the excitatory pyramidal cell population, hippocampal interneurons are scattered across all sublayers, from SO to SLM. These cells comprise many different subtypes, each with their own anatomical, molecular, and physiological properties (Pelkey et al., 2017). This neuronal population is the main subject of this thesis and is described in detail below.

The hippocampus also receives neuromodulatory inputs from several subcortical nuclei. Cholinergic neurons in the medial septum and diagonal band of Broca in the basal forebrain send dense projections to the hippocampus, where they ramify across all sublayers and release acetylcholine (Teles-Grilo Ruivo and Mellor, 2013). Serotonergic input arrives from both the dorsal and the median raphe in the midbrain (Freund et al., 1990). While projections from the dorsal raphe are diffuse and release serotonin nonsynaptically, fibers from the median raphe selectively target specific subtypes of inhibitory interneurons, onto which they can corelease serotonin and glutamate (Freund et al., 1990; Varga et al., 2009). Although dopamine release throughout the brain is primarily associated with neurons in the ventral tegmental area (VTA) of the midbrain, this nucleus projects sparsely to the hippocampus (Palacios-Filardo and Mellor, 2019). Instead, both

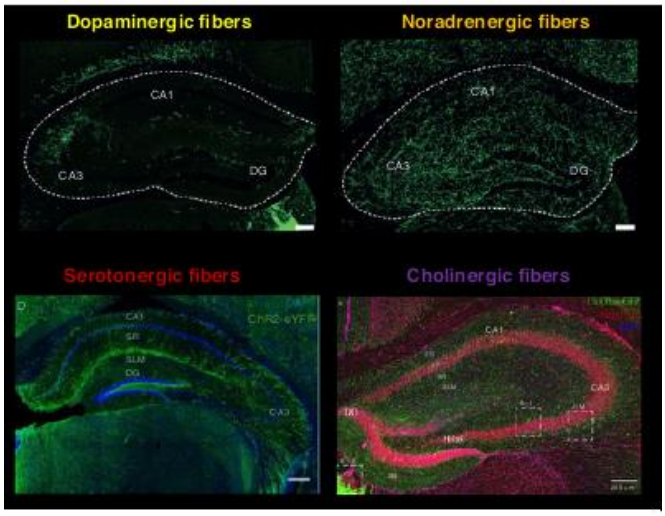

Figure 2: Neuromodulatory inputs to the hippocampus. Dopaminergic, noradrenergic, serotonergic, and cholinergic fibers all ramify extensively within all hippocampal subfields (Source: Palacios-Filardo and Mellor, 2019).

dopaminergic and noradrenergic fibers to the hippocampus originate in the locus coeruleus of the pons (Palacios-Filardo and Mellor, 2019). Each of these neuromodulatory inputs has complex effects on the hippocampal circuit, as these molecules act on a wide range of ionotropic and metabotropic receptors, located on both pyramidal cells and interneurons (Palacios-Filardo and Mellor, 2019). While most of these receptors are GPCRs and thus have slower and more complex effects on circuit function via changes in gene expression, direct, depolarizing action of neuromodulators has also been shown (Varga et al., 2009). Although we are only beginning to understand the effects of neuromodulators on hippocampal function, they have already been shown to be critical for network activity and learning (Kaufman et al., 2020).

1.3 Hippocampal Development: Early Patterning Events, Neurogenesis and Migration of Pyramidal Cells and Interneurons, and Circuit Assembly

The organized, laminar structure of the hippocampus, including its subfield organization, connectivity, and rich diversity of principal cells and GABAergic interneurons, forms during embryonic development during a precisely timed and coordinated series of events. In this section, I will review provide a brief overview of the key events in hippocampal development, with an emphasis on the principles governing the neurogenesis, migration, and circuit integration of pyramidal cells, and especially interneurons, into hippocampal CA1.

The hippocampus forms from the dorso-medial region of the telencephalon, which invaginates around E8.5 to form the medial wall (Khalaf-Nazzal and Francis, 2013). The cortical hem, a critical embryonic signaling structure that instructs and organizes the formation of the hippocampus via its robust expression and secretion of morphogens including Wnts and Bmps, forms within the medial wall (Khalaf-Nazzal and Francis, 2013). Accordingly, the hippocampus was largely missing in mice in which the cortical hem was deleted, or when the hem-specific

expression of Wnt3a molecules was disrupted (Khalaf-Nazzal and Francis, 2013; Lee et al., 2000).

Hippocampal CA1 pyramidal cells are generated from radial glial cells, progenitor cells located in the proliferative ventricular zone (VZ), between E12 and E18 in mice (Khalaf-Nazzal and Francis, 2013). Once post-mitotic, these cells undergo radial migration along the fibers of radial glial cells to reach the hippocampal plate, the precursor of the *stratum pyramidale*. The hippocampal plate splits the preplate into the subplate and marginal zone – the subplate corresponds to the prospective SO, while the marginal zone corresponds to the prospective SR and SLM (Khalaf-Nazzal and Francis, 2013). Migrating hippocampal pyramidal cells pause for several days during their journey from the ventricular zone (place of birth) to the hippocampal plate (final destination); although the reasons for this pause are not fully understood, it is likely to be necessary to allow hippocampal pyramidal cells to coordinate with other cell types, including DG granule cells and local interneurons (Khalaf-Nazzal and Francis, 2013). A similar pattern of neurogenesis and radial migration is seen between hippocampal pyramidal cells and neocortical pyramidal cells. Hippocampal pyramidal cells thus occupy positions relatively close to where they are born, in contrast to interneurons (see below). Hippocampal pyramidal cells ultimately occupy the pyramidal cell layer in an "inside out" pattern, as early born cells take deeper positions (closer to SO), while late born cells take more superficial positions (closer to SR) (Slomianka et al., 2011).

Contrary to hippocampal pyramidal cells, interneurons are generated from progenitor cells in the embryonic subpallium (ventral telencephalon) and migrate to the pallium (dorsal telencephalon), where they insert in the hippocampus from E14 onward (Lim et al., 2018). This long-distance migration, occurring shortly after they become post-mitotic, is known as tangential

migration, in contrast to the radial migration that pyramidal cells undergo (Lim et al., 2018). The subpallium can be divided into several distinct progenitor domains, each characterized by the expression of a specific combination of transcription factors: the lateral ganglionic eminence (LGE), medial ganglionic eminence (MGE), caudal ganglionic eminence (CGE), the preoptic region, and the septum. Cortical and hippocampal interneurons are derived from the MGE, CGE, and the preoptic region, and the vast majority are derived from either the MGE or CGE (Lim et al., 2018).

The MGE gives rise to ~60% of all hippocampal and neocortical interneurons (Pelkey et al., 2017). In the hippocampus, this includes all of the parvalbumin (PV)-expressing subtypes (including PV basket cells, axo-axonic cells, and bistratified cells), most somatostatin (SOM)-expressing subtypes (~60% of oriens lacunosum moleculare cells), ivy cells, and a subset of neurogliaform cells (Pelkey et al., 2017). The regional identity of the MGE is specified by the homeobox transcription factor Nkx2.1, which is critical for the production and specification of interneuron subtypes derived from MGE progenitors (Pelkey et al., 2017). Although Nkx2.1 is downregulated during development, the downstream transcription factor Lhx6 is upregulated in MGE progenitors upon exiting the ventricular zone and persists throughout adulthood in most MGE-derived interneurons (Du et al., 2008; Fogarty et al., 2007). Downstream of Lhx6, the transcription factors Sox6 and SATB1 continue to direct the survival and specification of MGE-derived interneurons (Azim et al., 2009; Batista-Brito et al., 2009). Thus, Nkx2.1 is the master regulator for MGE-derived interneurons, as its expression drives signaling cascades that ensure maturation of MGE-derived subtypes. As the spatial location of progenitors within the embryonic subpallium (ie. whether MGE or CGE) is an important determinant of the resulting interneuron subtype, it is natural to ask whether smaller subdivisions can be found within the

MGE progenitor pool, so that certain subregions of the MGE would produce PV+ interneurons and others would produce SOM+ interneurons, for example. However, recent studies have revealed that individual MGE progenitors can give rise to both PV+ and SOM+ interneurons, suggesting that these progenitors are not restricted to producing one interneuron subtype (Brown et al., 2011; Harwell et al., 2015). Nevertheless, a spatial bias can be observed within the MGE progenitor pool, such that the dorsal MGE tends to produce more SOM+ interneurons, while the ventral MGE tends to produce more PV+ interneurons (Flames et al., 2007; Pelkey et al., 2017). In addition to this spatial gradient in interneuron production within the MGE, a temporal gradient is also observed. For example, SOM-expressing and neocortex-bound interneurons exhibit a peak in neurogenesis around E11.5, while PV-expressing interneurons and neocortex-bound interneurons exhibit a peak in neurogenesis around E13.5 (Inan et al., 2012). Notably, the neurogenesis of hippocampal axo-axonic cells occurs preferentially after E15.5, significantly later than that of the other interneuron subtypes (Taniguchi et al., 2013). In summary, although both spatial and temporal patterns exist with respect to the final interneuron subtype of progenitors within the ganglionic eminences, neither factor is completely deterministic.

The CGE gives rise to ~30% of all hippocampal and neocortical interneurons (Pelkey et al., 2017). In this hippocampus, this includes all cholecystokinin (CCK)-expressing interneurons, all vasoactive intestinal polypeptide (VIP)-expressing interneurons, all calretinin (CR)-expressing interneurons, a subset of neurogliaform cells, and ~40% of SOM-expressing interneurons (Pelkey et al., 2017). Although a master regulator transcription factor analogous to Nkx2.1 has yet to be discovered for the CGE, a number of transcription factors are known to play important roles in the neurogenesis, migration, and maturation of CGE-derived interneurons, including COUP-TFI, COUP-TFII, and SP8 (Pelkey et al., 2017). Neurogenesis within the CGE generally

takes place several days later than neurogenesis within the MGE, and some temporal gradients of subtype production have also been described, such as the relatively early production of CCK-expressing interneurons and the relatively late production of CR-expressing interneurons (Tricoire et al., 2011). CGE-derived interneurons can be conveniently studied in the adult using 5-HT3AR-Cre or 5-HT3AR-GFP reporter mice.

After neurogenesis within the MGE or the CGE, interneurons undergo long-distance, tangential migration to arrive and disperse in the hippocampus or the neocortex. MGE- and CGE-derived interneurons follow stereotyped migratory routes to the dorsal telencephalon: MGE-derived interneurons migrate via dorsolateral routes, while CGE-derived interneurons travel laterally, medially, and caudally (Lim et al., 2018; Pelkey et al., 2017). The available evidence suggests that the choice of migratory stream is genetically determined. MGE-derived interneurons transplanted into the CGE do not follow typical CGE migratory streams, but rather those of other MGE-derived interneurons (Yozu et al., 2005). However, they can be persuaded to follow a typical CGE migratory stream when forced to overexpress the transcription factor COUP-TFII (Kanatani et al., 2008). Interestingly, downregulation of the master transcription factor Nkx2.1 at this point in the development of MGE-derived interneurons is necessary to ensure that they reach the neocortex or hippocampus instead of the striatum, as the downregulation of Nkx2.1 induces the expression of neuropilin-2, a receptor needed for repulsion by semaphorin 3F, which is expressed in the striatum (Marín et al., 2001; Nóbrega-Pereira et al., 2008).

Once interneurons complete their tangential migration and reach either the neocortex or hippocampus, they must subsequently undergo radial migration to the appropriate sublayer (ie. SO, SP, SR, or SLM) and properly integrate into local circuits of pyramidal cells and other

interneurons. Within both the neocortex and hippocampus, the final radial location of interneurons strongly correlates with their embryonic origin: MGE-derived interneurons tend to reside in deeper sublayers (SO and SP in the hippocampus), while CGE-derived interneurons tend to reside in more superficial sublayers (SR and SLM in the hippocampus) (Lim et al., 2018; Pelkey et al., 2017). Interestingly, at birth, all interneurons are initially evenly distributed throughout the cortical and hippocampal sublayers; they only take up their final positions by the end of the first postnatal week (Miyoshi and Fishell, 2011). This observation suggests that the genetic profile of a given interneuron and the local environment interact to jointly guide the interneuron to its proper final location. In support of this idea, several studies have suggested that pyramidal cells guide interneurons to their final radial position within the circuit. For example, knockout of the *doublecortin* gene prevents radial migration of neocortical pyramidal cells out of the ventricular zone, leading to an ectopic cluster of pyramidal cells below layer VI to which interneurons are subsequently attracted (Ramos et al., 2006). In addition, knockout of Fezf2, a transcription factor necessary for the development of subcortical projection pyramidal cells within the deep cortical layers, results in loss of these projection neurons and a corresponding ectopic location of PV- and SOM-expressing interneurons in superficial cortical layers (Lodato et al., 2011). On the other hand, overexpression of Fezf2 *in utero* resulted in ectopic subcortical-projecting pyramidal cells below the white matter that preferentially attracted PV- and SOM-expressing interneurons (Lodato et al., 2011). Together, these studies suggest that local cues from pyramidal cells guide interneurons to proper radial positions within local circuits in a subtype-specific manner.

Once pyramidal cells and interneurons have assumed proper positions within local circuits and have selected the correct synaptic partners, neural circuit formation and maturation depends

critically on early activity patterns to induce plasticity (Lim et al., 2018; Pelkey et al., 2017). Notably, interneurons play an important role in this early circuit activity via the depolarizing action of GABA on postsynaptic pyramidal cell targets early in development (Pelkey et al., 2017). This depolarizing action of GABA early in development, but hyperpolarizing action in adulthood, depends on differential expression of the chloride cotransporters KCC2 and NKCC1 and the resulting chloride gradient that is established (Pelkey et al., 2017; Rivera et al., 1999).

1.4 Hippocampal Network Activity Supporting Spatial Navigation and Episodic Memory: Feature Selectivity of Pyramidal Cells within the Hippocampal-Entorhinal System

In 1971, O'Keefe and Dostrovsky observed spatially modulated spiking in extracellular electrophysiological recordings from hippocampal CA1 neurons as rats navigated in an environment ("place cells") (O'Keefe and Dostrovsky, 1971). While individual cells were selective for a given area of the environment, different neurons were selective for different areas, such that the whole neural population could represent the entire environment (O'Keefe and Dostrovsky, 1971). This finding provided the neural correlate of Tolman's cognitive map hypothesis, as these spatially modulated neurons together could support spatial navigation by representing the entire spatial environment. The discovery of place cells in hippocampal CA1 represented a landmark achievement for neuroscience, as it provided a critical link between neural activity and physical variables in the external world, which at that point had only been observed in primary sensory or motor areas of the brain. In the decades since the original discovery of place cells, many different labs have furthered our understanding of both spatial and nonspatial coding in the hippocampal formation as well as the neural mechanisms supporting

these representations. Below, I will review several aspects of these representations, including the nature of CA1 spatial coding, CA1 nonspatial coding, spatial and nonspatial representations within the entorhinal cortex, responses of CA1 place cells to various experimental manipulations, hypothesized mechanisms of place cell formation, and how the observed heterogeneity in CA1 pyramidal cell physiology may relate to known differences along the various anatomical axes of the hippocampus.

Physiologically, CA1 place cells are characterized by a robust increase in firing rate when an animal enters the place field of that cell. These spatial responses can be dissociated from behavior, although rewarded locations or other environmental manipulations can modify place cell responses (see below). Spatial responses of CA1 pyramidal cells are not driven by any one sensory stimulus, but rather reflect the overall presence and arrangement of multiple environmental cues. Unlike neural responses in many sensory cortical areas, place cells are not topographically organized within CA1 (Moser et al., 2008). That is, neighboring CA1 pyramidal cells could show spatial tuning for locations that are far apart in the actual environment, while pyramidal cells that are far apart within the CA1 pyramidal cell layer could code for adjacent spatial locations. As approximately 10-40% of the CA1 neuronal population shows place cell responses during spatial navigation in a given environment, the remainder of the pyramidal cells are either silent or display firing patterns that are not spatially modulated. While some silent neurons may become active on subsequent days or in a different environment, other silent neurons remain silent over time and different experimental conditions. Place cells show variability on a trial-to-trial basis; a given place cell does not discharge on every pass through the place field, and different place cells vary in their trial-to-trial stability. Place cells also vary in their spatial stability over longer timescales. For several decades, place cell dynamics were

studies using extracellular recordings with electrodes (tetrodes or silicon probes), which do not allow longitudinal tracking of the same cells over many days or weeks because of slow drift of the probe relative to any given cell. However, recent advances in one- and two-photon calcium imaging have allowed unambiguous tracking of the same cells for many days or weeks (Grosmark et al., 2021; Ziv et al., 2013). These experiments have revealed that some CA1 place cells consistently code for the same location across several weeks, while others change their firing fields or stop firing in a given location between days. Currently, both the neural mechanisms supporting these differences in spatial stability, and the utility of stable or unstable place cells for memory-guided behaviors, remain incompletely understood. However, some insights from recent experiments have emerged. For example, place cells that are recruited to memory replay events (sharp-wave ripples (SWRs), see below) in post-task epochs or sleep are generally more stable over days than place cells that are not recruited to these events (Grosmark et al., 2021). Qualitatively, these cells with differential levels of stability could subserve both memory recall, which would require stable representations over time, and learning, which would require plastic representations. Spatially selective neurons have been observed in several mammalian and non-mammalian species to date, suggesting that their evolutionary conservation is of critical importance. For example, at one end of the spectrum, spatially localized firing fields were recently observed in the hippocampus of the tufted titmouse, a food-caching bird species capable of remembering many concealed food locations (Payne et al., 2021). At the other end of the spectrum, place cells have been observed in the hippocampus of human patients navigating virtual environments who have been implanted with intracranial electrodes are part of the diagnosis and treatment of their medication-resistant epilepsy (Ekstrom et al., 2003; Jacobs, 2014; Miller et al., 2013). While the relationship between the spatial coding of place cells and

spatial navigation behaviors has remained correlational for many decades, very recent experimental advances have permitted causal testing of the role of place cells in guiding spatial navigation behaviors. Robinson et al. (2020) utilized an 'all-optical' combination of two-photon calcium imaging and targeted optogenetics to first identify and then selectively activate place cells that encoded rewarded locations in a virtual reality environment (Robinson et al., 2020). The authors found that the selective activation of a small number of place cells encoding the reward location was sufficient to bias the behavior of the animal, leading to increased licking in the stimulation zone (Robinson et al., 2020). These findings suggest that hippocampal spatial representations actively support spatial navigation and memory, providing a causal link between decades of physiological and behavioral observations made in the hippocampus.

While decades of investigations have focused on the responses of CA1 pyramidal cells in behavioral tasks with significant spatial elements, it has become increasingly appreciated that these pyramidal cells do not simply code for space. For example, CA1 pyramidal cells have been demonstrated to encode many variables beyond current position, including past and future spatial trajectories, goal locations and distance to goal, the position of other objects, odors, tactile cues, and the temporal ordering of items or events (Mallory and Giocomo, 2018). In one recent notable study, hippocampal neurons were recorded from rats trained to use a joystick to manipulate sound along a continuous frequency axis (Aronov et al., 2017). The authors observed hippocampal representations of the entire frequency space, including individual neurons that had selective firing fields at particular sound frequencies (Aronov et al., 2017). These results demonstrate that hippocampal neurons can represent task variables in diverse behavioral tasks beyond those involving spatial navigation. Thus, hippocampal spatial representations may simply be a prominent example of a more general representational framework, possibly linking the role

of the hippocampus in supporting spatial navigation to its role in episodic memory more generally.

Several decades after the discovery of place cells in hippocampal CA1, spatially modulated neurons were also discovered in a primary input structure to the hippocampus, the MEC (Hafting et al., 2005). These projection neurons located in layers II and III of the MEC, now know as grid cells, did not display single firing fields as did hippocampal place cells, but rather multiple fields that formed a periodic, hexagonally arranged array, or grid, that tiled the whole environment (Hafting et al., 2005; Moser et al., 2008). Each of these grids can be described by its spacing (the distance between fields), its orientation (the tilt relative to an external reference axis), and the phase (its *xy* displacement relative to an external reference point) (Moser et al., 2008). While adjacent cells within the same region of the MEC have similar grid spacing and orientations, they do not have the same phase, resulting in the firing vertices of neighboring grid cells to be randomly shifted relative to one another (Moser et al., 2008). Thus, the grid phase within the MEC is nontopographic, just like the place fields of neighboring place cells in hippocampal CA1 (Moser et al., 2008). The spatially selective firing of grid cells persists after removal or replacement of major sensory cues or landmarks within an environment, suggesting that self-motion information is the major determinant of grid cell representations (Moser et al.,

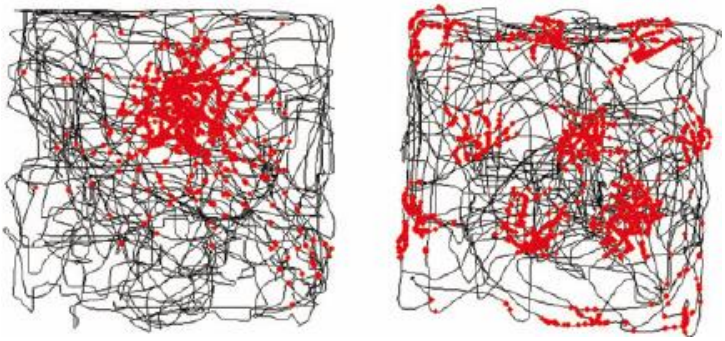

Figure 3: Firing patterns of a place cell within hippocampal CA1 (left) and a grid cell within the MEC (right). Note the single firing field of the place cell and the multiple, hexagonally arranged firing fields of the grid cell. The black lines represent the animal's position, while the red dots represent spikes from a single neuron (Source: Moser et al., 2008).

2008). In addition to grid cells, the MEC also contains a number of additional spatially tuned functional cell types. These include both border cells that increase their firing rate near environmental boundaries and head direction cells that fire when an animal faces in a particular direction (Mallory and Giocomo, 2018). To complement the diversity of functional cell types encoding spatial variables in the MEC, a number of functional cell types encoding non-spatial variables have also been found in the LEC. These include layer II/III projection neurons that respond to odors (Leitner et al., 2016; Xu and Wilson, 2012), the presence or absence of objects (Deshmukh and Knierim, 2011; Tsao et al., 2013), and time (Tsao et al., 2018). Thus, the MEC and the LEC contain primarily spatial and non-spatial cell types, respectively, that could support the spatial and non-spatial representations found in the hippocampus.

Shortly after the discovery of grid cells in the MEC, many researchers hypothesized that grid cell tuning may give rise to place cell tuning in hippocampal CA1, as inputs from many grid cells could be summed by a single hippocampal neuron to generate a place cell. In support of this idea, it was observed that remapping in CA1 occurs together with rotations or translations of grid cells firing fields (Fyhn et al., 2007), and that the increase in CA1 place field size along the dorsal-ventral axis corresponds to the increase in the spatial scale grid cells along the same axis (Hafting et al., 2005; Jung et al., 1994). Although several computational models have also explored the relationship between MEC grid cells and CA1 place cells (Cheng and Frank, 2011; Monaco and Abbott, 2011; Solstad et al., 2006), experimental support for the idea that grid cells sum to form hippocampal place fields remains weak. Early experiments either electrolytically lesioned or pharmacologically silenced the MEC and measured the impact on CA1 neural activity (Brun et al., 2008; Van Cauter et al., 2008). These experiments largely resulted in increased CA1 place field size, although place cells were still present (Mallory and Giocomo,

2018). More recent experiments have instead utilized transient optogenetic silencing of the MEC and observed significant place cell remapping in CA1 (Rueckemann et al., 2016). Place cell remapping was also observed in response to chemogenetic depolarization of the MEC (Kanter et al., 2017). Taken together, these studies suggest that MEC activity biases the active ensemble of CA1 place cells and controls certain aspects of place cell responses, but MEC activity alone is unlikely to be responsible for spatial tuning within hippocampal CA1.

Since the original observation of place cells by O'Keefe and Dostrovsky, many different groups have sought to determine how the firing patterns of hippocampal place cells respond to various experimental manipulations. In one prominent line of work, experimenters have sought to determine how place cell firing patterns are modified in response to changes in the sensory stimuli comprising the environment. In one of the first such studies, simply changing the shape of the recording enclosure from circular to rectangular resulted in some place cells to have unrelated fields in the two enclosure shapes, while other cells had place fields in one shape but not the other (Muller and Kubie, 1987). These representational changes in response to small changes in stimuli comprising the environment, known as remapping, were later confirmed and expanded on in subsequent studies. For example, remapping was observed in hippocampal place cells when animals were recorded from in the light versus the darkness (Quirk et al., 1990), or when a white intramaze cue card was replaced with a black one (Bostock et al., 1991). Overall, the extent of remapping in hippocampal place cells seems to depend on the extent of differences between environments, as well as on the animal's training history (Colgin et al., 2008). In addition, remapping was later shown to occur not only in response to manipulations of the recording environment, but also in response to changes in motivational state or behavioral context (Colgin et al., 2008). For example, many cells remapped when two different tasks,

random foraging and moving between goal locations, were performed in the same recording apparatus located in the same place (Colgin et al., 2008; Markus et al., 1995). Remapping can be expressed primarily as rate remapping, in which cells keep their same firing fields but their discharge rate within the field can change significantly, or as global remapping, in which both firing rates and place fields change significantly (Colgin et al., 2008). While rate remapping between experimental environments is more likely when the differences in environments are minor, global remapping is more likely to occur when the environmental changes are more substantial (Colgin et al., 2008). Finally, while these traditional studies of place cell remapping were conducted with extracellular recordings, more recent remapping experiments have been conducted using two-photon imaging and virtual reality setups, enabling recordings of hundreds of CA1 pyramidal cells and instantaneous switching between different, well-controlled contexts (Priestley et al., 2021). These studies have demonstrated that CA1 pyramidal cells undergo burst firing within the first few laps of novel environment exposure, likely reflecting a period of increased synaptic plasticity during which novel place fields can form (Priestley et al., 2021).

In addition to these experiments involving environmental manipulations and remapping, another important line of work has examined how CA1 pyramidal cell dynamics respond in response to a particularly salient location within an environment, such as a rewarded location. These studies, employing both extracellular recordings and two-photon imaging, have found that place fields tend to be enriched at rewarded locations, suggesting that hippocampal spatial maps overrepresent locations of increased behavioral significance (Hollup et al., 2001; Kaufman et al., 2020; Zaremba et al., 2017). However, as with remapping, the neural circuit mechanisms supporting this behavior-dependent plasticity of hippocampal codes remain unknown.

The presence of pyramidal cells encoding both spatial and nonspatial variables within CA1, as well as the presence of spatial and nonspatial functional cell types within the MEC and LEC, respectively, suggests that the functional differences between pyramidal cells observed within CA1 may result from biased afferent connectivity from either MEC or LEC. Indeed, gradients of entorhinal cortex afferent connectivity have been observed along both the transverse (proximal-distal) and the radial (deep-superficial) axes of the hippocampus (Masurkar et al., 2017). MEC neurons preferentially provide spatial information to proximal (towards CA2) CA1 pyramidal neurons, while LEC neurons preferentially provide nonspatial information to distal (towards the subiculum) CA1 pyramidal neurons (Masurkar et al., 2017). More specifically, MEC inputs preferentially excite deep (closer to SO) pyramidal cells in proximal CA1, and LEC inputs preferentially excite superficial (closer to SR) pyramidal cells in distal CA1 (Masurkar et al., 2017). More generally, heterogeneity between hippocampal pyramidal cells is becoming increasingly appreciated across all three anatomical axes of the hippocampus with respect to their inputs, gene expression profiles, intrinsic biophysical properties, and functional properties during behavior (Mallory and Giocomo, 2018; Soltesz and Losonczy, 2018). Thus although hippocampal pyramidal cells are traditionally thought of as a relatively homogenous population within each hippocampal subregion, their diversity may support spatial and nonspatial information processing in distinct channels, ultimately enabling the hippocampus to support both spatial and nonspatial behaviors (Soltesz and Losonczy, 2018).

In addition to providing rich information about the spiking patterns of individual hippocampal neurons during behavior, early electrophysiological investigations in the hippocampus have also revealed an intimate relationship between hippocampal spiking and the local field potential (LFP), as well as important relationships between hippocampal LFP and the

animal's behavior. As the LFP is a readily measured extracellular signal that largely reflects the summed synaptic input to a given tissue volume, it provides a robust, large-scale readout of the overall activity patterns within the hippocampus at any given time. Below, I will review the major oscillatory patterns found in the hippocampal LFP, especially as it pertains to their relationship with behavior, the mechanisms of their generation, their relationship with neuronal spiking, and their proposed functions.

1.5 Behavior-State Dependence of Hippocampal Network Activity: Theta Oscillations during Active Behavior and Memory Encoding

Theta oscillations are one of the largest and most regular rhythms in the mammalian brain (Colgin, 2013). These large amplitude, 4-12 Hz sinusoidal oscillations are most prominent during active behaviors and REM sleep. Accordingly, they are most readily observed in rodents during locomotion, but they are also present during behaviors associated with the active intake of environmental stimuli, such as whisking and sniffing (Colgin, 2013).

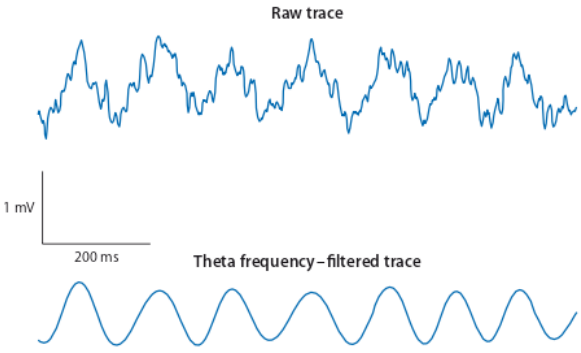

Figure 4: LFP example of theta oscillations. The top trace denotes the raw LFP signal, while the bottom trace is filtered in the theta frequency band (Source: Colgin, 2013).

Early studies have suggested that the medial septum (MS) of the basal forebrain generates theta, as lesions or inactivation of the MS disrupts hippocampal theta (Mitchell et al., 1982; Mizumori et al., 1990; Petsche et al., 1962). Specifically, the theta pacemaker cells are believed to be a subset of GABAergic cells within the MS, as they have been shown to fire rhythmically

at theta frequencies and are phase-locked to hippocampal theta (Hangya et al., 2009). Further supporting this idea, the MS theta state begins ~500 ms before theta appears in the hippocampus, and spikes of these interneurons are maximally phase-locked to hippocampal theta that occurs ~80 ms later (Bland et al., 1999; Hangya et al., 2009). These MS GABAergic cells express hyperpolarization-activated and cyclic nucleotide-gated nonselective cation channels (HCN channels); activation of these channels in response to hyperpolarization leads to slow depolarizing currents that bring the membrane potential back to action potential threshold (Varga et al., 2008). Thus, in neurons that express HCN channels, a repeating sequence of action potential, afterhyperpolarization, depolarization via HCN channels, and another action potential can function to have the cell fire at theta frequency (Colgin, 2013), these channels thus provide a potential molecular mechanism for theta generation. However, theta rhythms *in vivo* are not decreased in HCN1 knockout mice, suggesting that the mechanisms underlying theta generation appear to be more complicated (Giocomo et al., 2011; Nolan et al., 2004). Accordingly, more recent work has challenged the long-held view that the MS generates theta, as the intact hippocampus *in vitro* generates theta spontaneously (without any connections to the MS) (Goutagny et al., 2009). In addition, multiple theta oscillators seem to coexist. The amplitude of theta is largest in SLM, and the surgical removal of the entorhinal cortex leaves theta sensitive to the cholinergic antagonist atropine, while theta rhythms that occur in vivo are atropine-resistant (Kramis et al., 1975). Backprojections from hippocampal interneurons to MS GABAergic neurons may also synchronize theta rhythms between the two regions (Colgin, 2013; Jinno, 2009; Jinno et al., 2007). While a unifying mechanism for theta oscillations remains elusive, evidence points to roles for the medial septum, entorhinal cortex, and the intrinsic hippocampal

circuitry; seems likely that some combination of intrinsic neuronal conductances and network mechanism support hippocampal theta.

As theta oscillations are most readily observed in the hippocampal LFP during locomotion, the spiking of individual place cells occurs on a background of theta oscillations during spatial navigation. Thus, the timing of an individual place cell's spikes relative to the phase of the extracellular theta oscillation can constitute a temporal code, complementary to the rate code provided by the cell's firing rate within its place field (Ahmed and Mehta, 2009; Colgin, 2013; Losonczy et al., 2010). This framework of joint rate and temporal coding, exemplified by CA1 place cell firing relative to theta, expands the repertoire of information coding by neuronal networks and greatly increases the amount of information that can be extracted by downstream cells (Ahmed and Mehta, 2009; Colgin, 2016, 2013). Indeed, early electrophysiological investigations in the hippocampus have revealed important relationships between pyramidal cell spiking and the theta phase, most notably the phenomenon of theta phase precession (O'Keefe and Recce, 1993; Skaggs et al., 1996). In this phenomenon, spikes from a CA1 place cell initially occur at late phases of theta as the animal enters the cell's place field and then occur at progressively earlier phase on following theta cycles. As the spikes from multiple place cells with sequentially occurring place fields are often contained within a single theta cycle, a given theta cycle contains a compressed representation of space (Colgin, 2013; Skaggs et al., 1996). The precession of spikes from each cell relative to the theta phase ensures that the representation of the current location is preceded by representations of recently visited locations on earlier theta phases and followed by representations of future locations on later theta phases (Dragoi and Buzsáki, 2006).

In addition to the role of theta oscillations in providing a timing signal for pyramidal cell firing, several other functions have been proposed for theta rhythms in supporting cognition. First, each theta cycle may serve as a fundamental processing unit during spatial navigation (Kepecs et al., 2006) by discretizing incoming sensory information and packaging it into related "chunks" (Colgin, 2013). Support for this idea comes from a recent study which "teleported" rats between two different environments by rapidly changing the environment's light cues (Jezek et al., 2011). When this was done quickly, the hippocampal representation would sometimes flicker back and forth between the separate representations of the two environments. However, during this flickering, each theta cycle contained information from only one of the two representations, suggesting that theta cycles may function to group together related aspects of sensory experience (Jezek et al., 2011). Second, theta oscillations may function to aid communication between separate brain regions. Accordingly, several experiments have connected interregional theta coherence or spike-theta coupling with behavioral performance on various spatial memory tasks. For example, during a spatial working memory task, spikes from medial prefrontal cortex neurons were more strongly phase-locked to CA1 theta during correct-choice trials compared to error trials (Jones and Wilson, 2005). During a tone-cued T-maze task, theta coherence between the hippocampus and striatum increased before the selected turn, but only in animals that successfully learned the task (DeCoteau et al., 2007). Together, these experiments suggest that the interregional communication needed for good performance on various behavioral tasks may rely on theta-related synchronization. Although the mechanisms mediating these effects are not understood, one can speculate that increased theta coupling between brain regions may lead to a more effective activation of downstream neurons via increased synchronization of synaptic inputs.

1.6 Behavior-State Dependence of Hippocampal Network Activity: Sharp-Wave Ripples during Awake Immobility and Slow-Wave Sleep

While theta oscillations dominate the hippocampal LFP during active behaviors, such as spatial navigation, and rapid eye movement (REM) sleep, large irregular activity dominates the hippocampal LFP during awake immobility and slow-wave sleep. Dispersed within these bouts of large-amplitude irregular activity are sharp-wave ripples (SWRs), transient fast oscillatory events measured in and around the CA1 pyramidal cell layer. SWRs are composed of two spectral components: 1) the sharp-wave, a large-amplitude, slow, negative polarity deflection in the LFP, and 2) the ripple, the fast 125-275 Hz oscillation (Buzsáki, 2015). SWRs are generated by the synchronous activation of a subset of CA3 pyramidal cells, which impinge upon and depolarize the apical dendrites of CA1 pyramidal cells, generating the sharp-wave component of the SWR (Csicsvari et al., 2000). This initial depolarization is quickly followed by the activation of local interneurons, which in turn interact rapidly with pyramidal cells to generate the ripple component of the SWR oscillation in the pyramidal cell layer. While SWRs last approximately 50-100ms and occur, on average, once every few seconds during awake immobility and NREM sleep, there is considerable variability in their duration, frequency, and the strength of the oscillation (Buzsáki, 2015). This variability is thought to primarily reflect differences in the size of the CA3 pyramidal cell burst that generates the oscillation, as larger fractions of activated CA3 pyramidal cells are associated with both a larger sharp-wave component and a higher power ripple component measured in the CA1

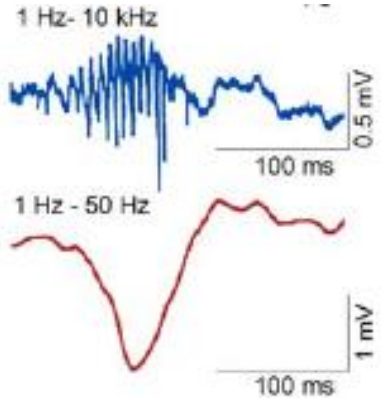

Figure 5: LFP example of a SWR. The top trace represents the fast ripple component, while the bottom trace represents the slow sharp wave component (Source: Buzsaki, 2015).

pyramidal cell layer (Buzsáki, 2015; Csicsvari et al., 2000). Although generated locally within the recurrent CA3 network of the hippocampus, SWRs are brain-wide events: while dispersed cortical regions are activated around these events, many subcortical structures are inhibited around SWRs (Logothetis et al., 2012). Additionally, SWRs appear to be an evolutionarily conserved LFP event, as they have been observed in the hippocampus of many different species, including mice, rats, rabbits, bats, cats, monkeys, and humans (Buzsáki, 2015).

The spiking of hippocampal pyramidal cells during SWRs, both in CA1 and CA3, appears to be under tight temporal control (Buzsáki, 2015). SWRs represent one of the most synchronous population events in the mammalian brain, as large fractions of hippocampal neurons are activated within a small time window around these events (Buzsáki, 2015). However, at closer inspection, it can be appreciated that the spikes from individual neurons during SWRs are not completely synchronous, but are rather structured to reflect a time-compressed reactivation of the sequential spiking patterns observed during active behaviors, such as spatial navigation (Buzsáki, 2015). This phenomenon, known as replay, has been demonstrated during many different behavioral tasks and under many different experimental conditions, and is thus thought to represent a critical mechanism supporting critical cognitive functions, including memory consolidation (Buzsáki, 2015; Klinzing et al., 2019). Recently, replay has also been observed in humans, highlighting its potential importance and generality (Liu et al., 2019).

In this framework, sensory and spatial aspects of experience during active behavior are first encoded in the hippocampus via rapid synaptic plasticity between pyramidal cells during theta

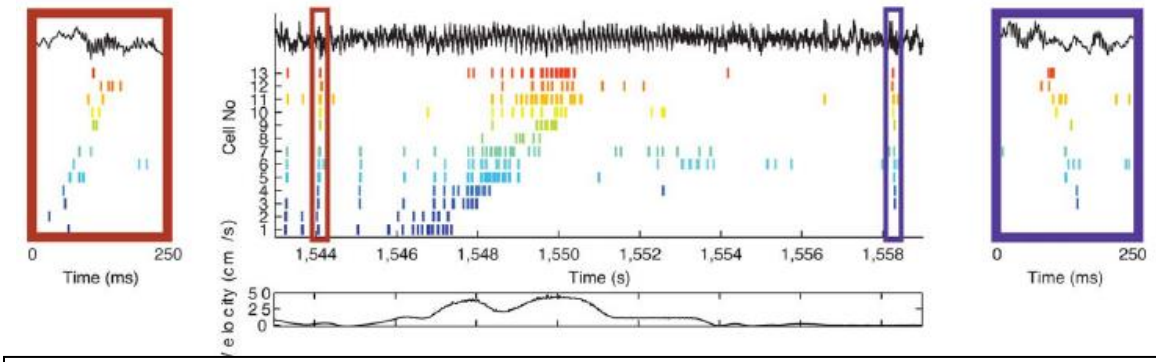

Figure 6: Example of hippocampal replay during SWRs. During locomotion epochs, place cells are sequentially activated during theta oscillations (center). During immobility epochs, these place cell sequences are replayed in time-compressed, forward or reverse trajectories during SWRs (left and right sides) (Source: Buzsaki, 2015).

oscillations. Subsequently, these nascent representations are reactivated during the SWRs of awake immobility and NREM sleep, promoting their transfer to the neocortex and consolidation into long-term memory (Buzsáki, 1986). The hypothesis that SWRs subserve memory consolidation is supported by several lines of evidence, in addition to the observation of neural replay. First, the rate of SWR incidence is significantly increased following novel experience, learning, and in the sleep epochs following these events as well (Buzsáki, 2015). Second, selective suppression of SWRs during post-learning sleep impairs behavioral performance in spatial memory tasks (Girardeau et al., 2009). Relatedly, selective optogenetic silencing of hippocampal CA1 pyramidal cell activity during sleep SWRs after the exploration of novel environments impairs the reinstatement of those representations upon re-exposure to the same environment (van de Ven et al., 2016). By taking advantage of recent technological advances that allow for closed-loop manipulation of neural circuits triggered by SWRs, these experiments suggest that SWRs are critical for stabilizing newly formed hippocampal representations, and that this stabilization is critical for behavior. Third, hippocampal SWRs are associated with neocortical activity and oscillations known to support memory consolidation, including slow

oscillations and sleep spindles (Klinzing et al., 2019). For example, SWRs often co-occur with spindles recorded in the medial prefrontal cortex (Siapas and Wilson, 1998), and enhancing the temporal correlation between hippocampal SWRs and neocortical down state-spindle complexes has been shown to improve behavioral performance on memory tasks (Maingret et al., 2016). Taken together, this body of work supports the idea that hippocampal replay during SWRs is critical for stabilizing nascent representations and supporting memory consolidation via hippocampal-neocortical communication.

As the importance of replay during SWRs in memory consolidation has become more established, a critical question has emerged: How does the hippocampus determine which representations should be replayed, and which should not? In other words, which cells should be recruited to SWRs, and which should be suppressed from these events? While our understanding of the regulation of replay and the selective recruitment of subsets of pyramidal cells to SWRs remains far from complete, recent studies have shown that neurons encoding behaviorally relevant stimuli are preferentially recruited to SWRs over those encoding less important stimuli (Grosmark et al., 2021; Terada et al., 2022). How this plasticity is implemented at the neural circuit level remains a major open question.

1.7 Major Hippocampal Inhibitory Subtypes: Anatomical, Molecular, and Physiological Properties

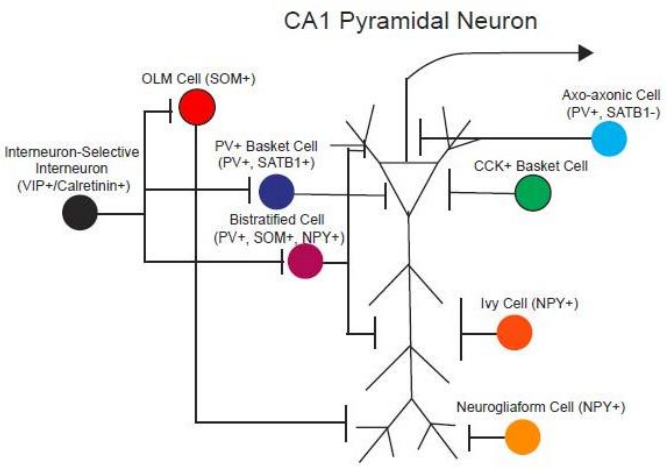

Figure 7: Schematic of the key subtypes of CA1 inhibitory interneurons, their axonal termination locations along the somatodendritic axis of a CA1 pyramidal cell, and their molecular compositions.

While pyramidal cells make up the large majority of neurons in the CA3-CA1 regions of the hippocampus, inhibitory, GABAergic interneurons regulate many aspects of circuit function and are significantly more diverse with respect to their anatomical, morphological, molecular, and physiological properties. Hippocampal CA1 has served as a prototype region for the study of cortical interneurons for the past several decades; below I will review what is known about the anatomical, molecular, and physiological properties of the basic CA1 interneuron cell types. Although the precise number of interneuron subtypes that exists in hippocampal CA1 can be debated and depends on the precise definitions used, I will review the most abundant subtypes below.

PV basket cells (PVBCs) make up approximately 14% of all inhibitory interneurons in CA1 (Bezaire and Soltesz, 2013). These cells target the soma and very proximal dendrites of CA1PCs, providing perisomatic inhibition. PVBCs derive their name from the large, dense boutons they form on their postsynaptic pyramidal cell targets, resembling "baskets". They are located most densely in and around the pyramidal cell layer; they are found rarely in SR and never or almost never in SLM. PVBCs have dendrites in all CA1 sublayers, from SO to SLM, and these dendrites can have either vertical or horizontal morphologies; these differences in dendritic morphology are likely to correlate with very different input sources. PVBCs are embryonically derived from the medial ganglionic eminence (MGE), with their specification driven by the transcription factor Nkx2.1. *In vitro* studies of PVBC physiological properties have revealed a fast-spiking phenotype without frequency adaptation (no change in the interspike interval from the beginning to the end of a depolarizing current pulse). Individual action potentials from PVBCs have short half-widths and are followed by large and fast afterhyperpolarizations (Pelkey et al., 2017). These physiological properties position PVBCs to coordinate high-frequency network activity via precisely timed release of GABA onto postsynaptic pyramidal cells. Molecularly, PVBCs are defined by the expression of the calcium-binding protein parvalbumin (PV), as well as the expression of the transcription factor SATB1 (Viney et al., 2013). However, PV expression levels in PVBCs have been reported to be plastic and modifiable by behavioral experience (Donato et al., 2015, 2013). PVBCs are negative for the calcium-binding proteins calbindin (CB) and CR, and they are

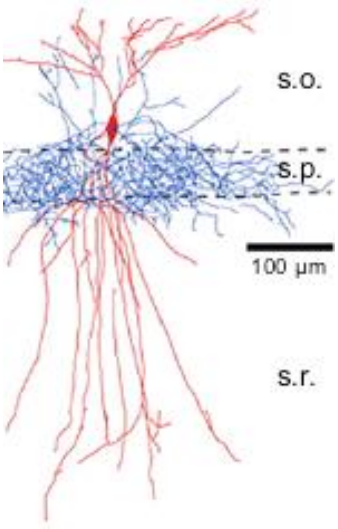

Figure 8: Morphology of a PVBC. Red denotes the soma and dendrites, while blue represents the axonal arborization (Source: Pelkey et al., 2017).

negative for the neuropeptides SOM, Neuropeptide Y (NPY), CCK, and VIP (Pelkey et al., 2017). Although a single PVBC targets many CA1 pyramidal cells throughout the CA1 pyramidal cell layer, some target specificity has been demonstrated: PVBC boutons preferentially target deep CA1PCs over superficial CA1PCs (Lee et al., 2014), providing evidence for specialized excitatory-inhibitory microcircuits within CA1. PVBCs can be genetically labeled in PV-Cre transgenic mice, although not specifically; these mice also label axo-axonic cells and bistratified cells (see below). Overall, PVBCs constitute one of the best studied interneuron subtypes, as their relative abundance, fast-spiking phenotype, strong expression of PV, and characteristic baskets on postsynaptic pyramidal cell somas have all facilitated anatomical and physiological studies.

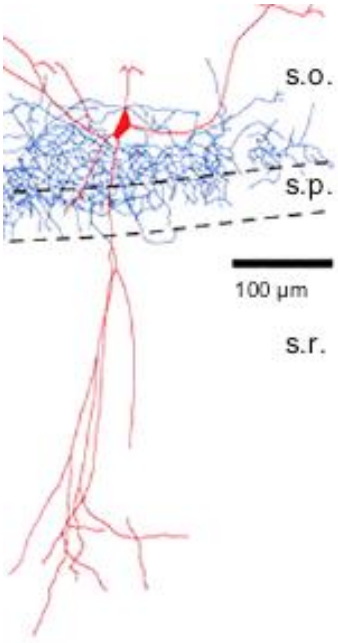

Figure 9: Morphology of a AAC. Red denotes the soma and dendrites, while blue represents the axonal arborization (Source: Pelkey et al., 2017).

Axo-axonic cells (AACs) make up approximately 4% of all inhibitory interneurons in CA1 (Bezaire and Soltesz, 2013). These cells exhibit the most specific postsynaptic targeting of all interneuron subtypes, as they form synapses exclusively on the axon-initial segment (AIS) of pyramidal cells. The main axonal branches of AACs run along the SO-SP border and send collaterals into the CA1 pyramidal cell layer, where their terminals are arranged in rows of boutons, each innervating the AIS of pyramidal cells. These characteristic axonal cartridges of AACs are the distinguishing anatomical feature responsible for the alternative name given to AACs, “chandelier cells”. The pyramidal cell axon initial segment, rich in voltage-gated Na+ channels, is the site of action potential initiation;

AACs are thus positioned to exert great control over pyramidal cell output and what information is transmitted to downstream cells. AACs are located most densely in and around the pyramidal cell layer; they are never or almost never found in SR and SLM (Bezaire and Soltesz, 2013). Although most AACs have vertical dendrites that span from SO to SLM, positioning them to receive excitatory inputs from all afferent regions to the hippocampus, a subset of AACs are located in SO and have primarily horizontal dendrites (Ganter et al., 2004). These AACs with horizonal dendrites may received primarily feedback input from CA1PCs, potentially differentiating them functionally from those with vertical dendrites. All AACs are MGE-derived, although they are derived later in gestation than the other MGE-derived interneuron subtypes (Pelkey et al., 2017). *In vitro* recordings of AACs have revealed a fast-spiking, non-accommodating phenotype, similar to that of PVBCs. Additionally, AAC action potentials have short half-widths and large, fast afterhyperpolarizations, allowing them to generate rapid sequences of action potentials. Immunohistochemically, AACs are characterized by their expression of PV and their lack of detectable SATB1 expression, distinguishing them molecularly from PVBCs (Viney et al., 2013). In fact, AACs represent the only MGE-derived interneurons that lack SATB1 expression, perhaps due to their later specification during development. However, recent studies of genetically labeled neocortical AACs have found that only some of these cells express PV (Taniguchi et al., 2013). Nevertheless, all histologically-confirmed hippocampal AACs to date have expressed PV. In addition, immunohistochemical identification of AACs can be confirmed by examining bouton alignment against ankyrin G-expressing AISs of pyramidal cells. Similar to PVBCs, AACs do not express CR, CB, SOM, NPY, CCK, or VIP. AACs can be genetically labeled in PV-Cre mice, although not selectively.

However, recent work has enabled more selective labeling of hippocampal AACs with a Unc5b-Cre mouse line (Dudok et al., 2021b), paving the way for more selective interrogation of AACs.

Bistratified cells (BiCs) make up approximately 6% of all inhibitory interneurons in CA1 (Bezaire and Soltesz, 2013). These cells target the proximal dendrites of CA1 pyramidal cells in SO and SR; their axons thus overlap with CA3 inputs onto CA1 pyramidal cells. BiCs are located most densely in SO and SP, although some are found in SR as well (Bezaire and Soltesz, 2013). Substantial portions of BiCs have both primarily vertical and horizonal dendrites; interestingly, BiCs with these different dendritic morphologies have been shown to have distinct firing patters *in vivo* (Varga et al., 2014). BiCs also express the calcium-binding protein PV; however, they are distinct from the other two PV-expressing subtypes (PVBCs and AACs) in that they also consistently express SOM and NPY. In addition, BiCs express SATB1, consistent with their origin from the MGE (Viney et al., 2013). Vertical BiCs are unique from the other PV-expressing subtypes in that their dendritic trees do not extend to SLM. Presumably, vertical BiCs thus do not receive functional input from the entorhinal cortex, but rather only feedforward input from CA3 and feedback input from CA1 pyramidal cells. Physiologically, BiCs have a fast-spiking, non-accommodating phenotype, similar to the other PV-expressing subtypes. Although BiCs are labeled in PV-Cre mice, the labeling is not selective; this genetic strategy also labels PVBCs and AACs. Currently, no method exists to genetically label hippocampal BiCs selectively.

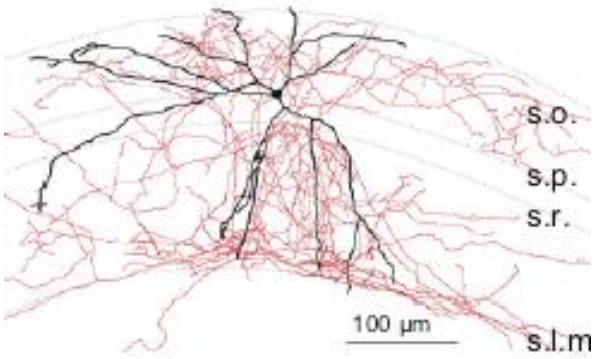

Figure 10: Morphology of a BiC. Black denotes the soma and dendrites, while red represents the axonal arborization (Source: Pelkey et al., 2017).

Oriens-lacunosum moleculare (OLM) cells make up approximately 4% of all inhibitory interneurons in CA1 (Bezaire and Soltesz, 2013). OLM cells have a distinct morphology; they are located exclusively in SO but send their axon down to SLM, where it ramifies and targets the distal apical tuft dendrites of CA1 pyramidal cells. As OLM cells are located in SO with horizontal morphologies and dendrites confined to SO, they are strategically positioned to receive strong excitatory input from CA1 pyramidal cells and provide feedback inhibition to their distal dendrites. OLM cells are immunohistochemically defined by their expression of SOM. Although they lack strong PV expression, some studies have reported weak PV expression in OLM cells (Pelkey et al., 2017). Nevertheless, PV expression in OLM cells is significantly weaker than in the PV-expressing subtypes (PVBCs, AACs, BiCs), and is likely often not detectable with antibody labeling. Although classic studies of OLM cells in rats have reported that OLM cells lack NPY expression, more recent studies in mice have found that some OLM cells express NPY (Winterer et al., 2019); NPY expression in OLM cells may thus vary between rats and mice. In addition, Reelin is frequently coexpressed with SOM in OLM cells, and OLM cells express high levels of the metabotropic glutamate receptor 1 alpha along their horizontal dendrites. OLM cells consistently lack expression of CCK, VIP, and CR. Physiologically, OLM cells display a regular spiking

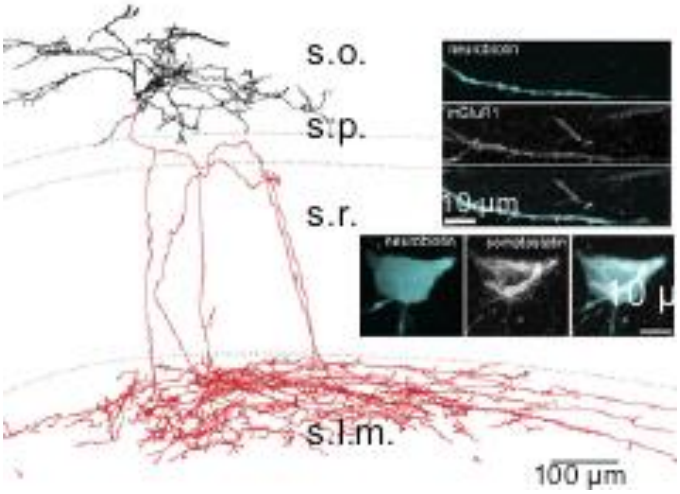

Figure 11: Morphology of an OLM cell. Black denotes the soma and dendrites, while red represents the axonal arborization (Source: Pelkey et al., 2017).

firing pattern with adaptation (increasing interspike intervals with depolarizing current injection). This accommodation thus limits the maximum firing frequency of OLM cells to lower values than what is observed in the fast-spiking, PV-expressing interneurons (PVBCs, AACs, and BiCs). Individual action potentials from OLM cells display longer half-widths (wider spikes) than those observed in the PV-expressing subtypes. Interestingly, OLM cells have been shown to comprise both MGE- and CGE-derived subpopulations, and these subpopulations differ both in their molecular expression profiles and in their activity patterns *in vitro* (Chittajallu et al., 2013). OLM cells can be genetically labeled in SOM-Cre mice, although not selectively. However, a transgenic mouse line, Chrna2-Cre, has been recently developed that allows selective targeting of CA1 OLM cells (Leão et al., 2012).

CCK-expressing basket cells (CCKBCs) make up approximately 9% of all inhibitory interneurons in CA1 (Bezaire and Soltesz, 2013). Like PVBCs, CCKBCs selectively target the soma and proximal dendrites of CA1 pyramidal cells, providing perisomatic inhibition. Their cell bodies are located in all CA1 sublayers, from SO to SL, and they can have either vertical or horizontal dendritic morphologies. All CCKBCs are CGE-derived, contrasting them with MGE-derived PVBCs. Molecularly, all CCKBCs express the neuropeptide CCK and lack PV and SOM expression. Additionally, CCKCBs can coexpress VIP or VGLUT3, and they express the endocannabinoid receptor CB1 at their terminals. However, recent single-cell transcriptomic data has revealed a molecular diversity within CCK-expressing interneurons that has not been

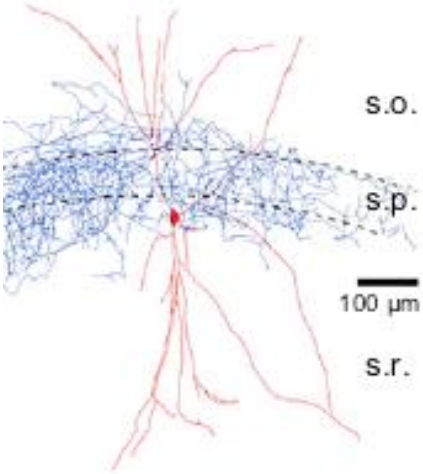

Figure 12: Morphology of a CCKBC. Red denotes the soma and dendrites, while blue represents the axonal arborization (Source: Pelkey et al., 2017).

previously appreciated with traditional immunohistochemistry (Harris et al., 2018). Physiologically, CCKBCs display a regular-spiking, adapting firing pattern in response to current injection. Critically, the release of GABA from the terminals of CCKBCs has been shown to be asynchronous, or not tightly coupled to action potential invading the presynaptic terminal (Daw et al., 2009). In addition, the CB1 receptor at the terminals of CCKBCs has been shown to mediate the phenomenon of depolarization-induced suppression of inhibition (DSI). In DSI, the depolarization of a postsynaptic cell releases a retrograde lipid messenger that acts on presynaptic CB1 receptors to silence output from these CB1-expressing terminals (Pelkey et al., 2017). DSI thus represents a unique mechanism in synaptic physiology in which the postsynaptic cell can modulate the activity of its presynaptic partners. Although this phenomenon has been convincingly demonstrated *in vitro*, the existence or utility of such a retrograde synaptic mechanism has yet to be determined *in vivo*. Nevertheless, the expression of the CB1 receptor at the terminals of CCKBCs endows these cells with unique synaptic properties. Although our understanding of the inputs to different classes of interneurons is far from complete, CCKBCs have been shown to receive unique afferents compared to other interneuron classes. For example, CCKBCs receive relatively large proportions of inhibitory synapses on their cell body compared to other subtypes (Matyas et al., 2004). In addition, serotonergic afferents from the median raphe have been show to selectively target CCK- and CB-expressing interneurons in CA1, positioning CCKBCs to be under a distinct neuromodulatory control from the other subtypes (Freund, 2003; Freund et al., 1990). CCKBCs can be targeted with CCK-Cre transgenic lines; however, this line is nonspecific, as it also labels large proportions of pyramidal cells (Pelkey et al., 2017). Recently, the development of the Sncg-Flp mouse line has allowed selective access to CCKBCs, opening the door to increased interrogation of this cell type (Dudok et al., 2021a). Taken

together, we now know that although CCKBCs overlap with PVBCs with respect to their postsynaptic targeting, they are endowed with unique physiological and synaptic properties and receive unique afferents. Thus, it is very likely that PVBCs and CCKCs exert different forms of perisomatic inhibitory control over their CA1 pyramidal cells targets, thus differentially influencing hippocampal network activity.

Dendrite-targeting, CCK-expressing interneurons make up approximately 5% of all inhibitory interneurons in CA1 (Bezaire and Soltesz, 2013). Although all cells within this inhibitory population target the dendrites of pyramidal cells, this subtype is morphologically diverse, and individual cells each target more specific dendritic compartments. The axonal projections of Schaffer collateral-associated cells (SCAs) target the basal and apical oblique dendrites of pyramidal cells, overlapping with the termination zone of the Schaffer collateral CA3 input. Apical dendrite targeting interneurons (ADIs) target the main apical shaft of pyramidal cells, avoiding smaller dendritic compartments. Finally, the axons of perforant path-associated cells (PPAs) target the distal apical tuft dendrites of pyramidal cells within SLM, overlapping with the termination zone of excitatory inputs from the entorhinal cortex. Thus, all major dendritic compartments of pyramidal cells receive GABAergic inputs from CCK-expressing interneurons. Although dendrite-targeting, CCK-expressing interneurons are found within all CA1 sublayers, they have a tendency to concentrate within SR and the SR-SLM border. They have mostly vertical dendritic

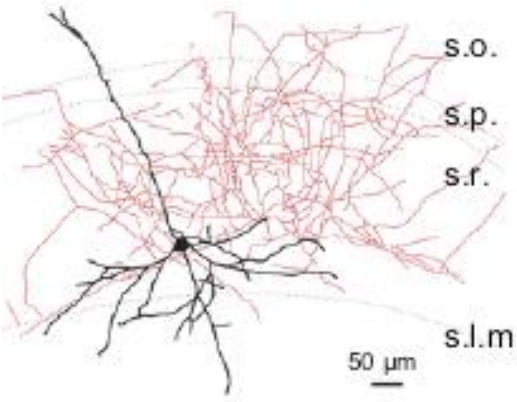

Figure 13: Morphology of a dendrite-targeting, CCK+ cell. Black denotes the soma and dendrites, while red represents the axonal arborization (Source: Pelkey et al., 2017).

morphologies that span all sublayers, although horizonal morphologies, especially with dendrites confined to SR, have also been observed. Molecularly, these cells all express CCK, and some additionally express Calbindin. However, no known marker currently exists to reliably separate dendrite-targeting CCK cells from their somatic-targeting counterparts. These cells are derived from the CGE and they are physiologically similar to CCK basket cells, as they display a regular-spiking and adapting firing pattern in response to depolarizing current injection. There is currently no reliable method to genetically target dendrite-targeting CCK-expressing interneurons, and they remain one of the least studied subtypes.

Ivy cells make up approximately 23% of all inhibitory interneurons in CA1 (Bezaire and Soltesz, 2013), making them the largest inhibitory population. Ivy cells are named for the ivy-like appearance of their axons, which branch extensively close to the soma and form a dense cloud of collaterals. These axons target the basal and proximal apical dendrites of CA1 pyramidal cells in SO and SR, providing dendritic inhibition. The soma of Ivy cells are found largely in and around the pyramidal cell layer, although some are located in SO and SR as well. Ivy cells are MGE-derived and express NPY, nNOS, and COUP-TFII, and they do not express PV, SOM, CCK, and VIP. Physiologically, Ivy cells display a "late-spiking" phenotype, characterized by a considerable delay between depolarization onset and action potential discharge in response to depolarizing current injection. These cells are also characterized by modest frequency accommodation, broad spikes, and they achieve considerably lower firing frequencies than the fast-spiking cells

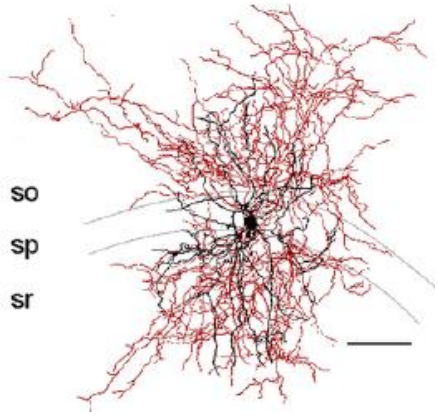

Figure 14: Morphology of an ivy cell. Black denotes the soma and dendrites, while red represents the axonal arborization (Source: Krook-Magnuson et al., 2011).

(PVBCs, AAC, and BiCs). Ivy cells are characterized by a unique mode of synaptic transmission, as most of their terminals do not form classical synaptic contacts with clear postsynaptic targets. This feature of Ivy cells, combined with their dense, local axonal plexus, is thought to support their ability to mediate volume GABAergic transmission. This diffuse spread of GABA is thought to act via both GABA-A and GABA-B receptors on pyramidal cells, leading to a slower and less temporally precise inhibition (Krook-Magnuson et al., 2011; Pelkey et al., 2017). Although Ivy cells can be genetically targeted with NPY-Cre transgenic lines, this strategy is not specific for Ivy cells. No reliable genetic method currently exists to label them.

Neurogliaform cells are similar in many respects to Ivy cells. They make up approximately 9% of all inhibitory interneurons in CA1 (Bezaire and Soltesz, 2013). Neurogliaform cells provide inhibition to the distal apical tuft dendrites of pyramidal cells, separating them from Ivy cells with respect to their postsynaptic targeting. Additionally, the soma and dendrites of neurogliaform cells reside almost exclusively within SLM, while the soma of Ivy cells populate the other CA1 sublayers (SO, SP, and SR). This positions neurogliaform cells to receive feedforward excitatory input from the entorhinal cortex, while Ivy cells should presumably receive their feedforward excitatory input mostly from CA3. Molecularly, neurogliaform cells are similar to Ivy cells, as they also express NPY, nNOS, and COUP-TFII. Additionally, many neurogliaform cells express Reelin, which Ivy cells do not.

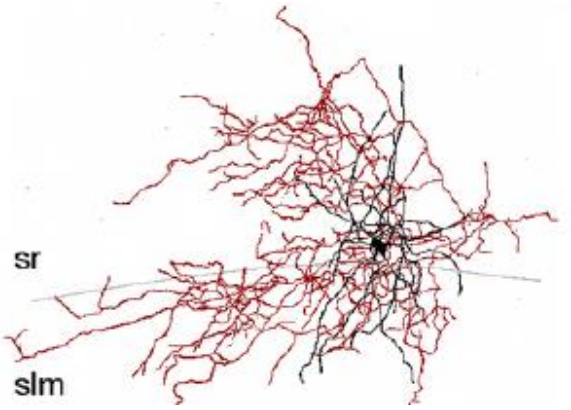

Figure 15: Morphology of a neurogliaform cell. Black denotes the soma and dendrites, while red represents the axonal arborization (Source: Krook-Magnuson et al., 2011).

Neurogliaform cells do not express PV, SOM, CCK, or VIP. However, neurogliaform cells are still molecularly heterogeneous, such that no combination of markers can be used to identify all of the with certainty (Pelkey et al., 2017). Neurogliaform cells display the same basic physiologic characteristics as Ivy cells, as they are late-spiking, with broad spikes and an accommodating firing pattern. Additionally, neurogliaform cells do not form classical synapses on clear postsynaptic targets and rather release GABA via volume transmission, similarly to Ivy cells. Like OLM cells, neurogliaform cells can be either MGE- or CGE-derived, and nNOS expressing can be used to generally differentiate between these two embryonic origins: MGE-derived neurogliaform cells generally express nNOS, while CGE-derived neurogliaform cells do not. As with Ivy cells, no genetic strategy is currently available to selectivity target neurogliaform cells, although they can be labeled with NPY-Cre transgenic lines.

Interneuron-selective interneurons (ISIs) comprise an anatomically unique set of hippocampal interneurons that preferentially target other interneurons instead of pyramidal cells. ISIs are thus positioned to provide network disinhibition via the inhibition of other inhibitory circuit motifs. All ISIs are CGE-derived. However, ISIs can be divided into three primary subclasses based on their unique morphological and neurochemical profiles: Type I ISIs, Type II ISIs, and Type III ISIs.

Type I ISIs are defined by their expression of Calretinin (CR) and lack of VIP expression (CR+/VIP-). The soma of these cells are located throughout the SO, SP, and SR sublayers, and the dendrites of different Type I ISIs often intermingle within SR, likely functioning to synchronize their activity via electrical connections (Gulyás et al., 1996). These cells preferentially target CB-expressing, CCK-expressing, and other CR-expressing interneurons located throughout the CA1 sublayers (Gulyás et al., 1996).

Type II ISIs are defined by their expression of VIP and lack of CR expression (VIP+/CR-). The soma of these cells are typically located near the SR-SLM border and their dendrites are largely restricted to SLM, positioning these cells to be recruited by excitatory input from the entorhinal cortex. Like Type I ISIs, these cells preferentially target CB-expressing, CCK-expressing, and other ISIs throughout the CA1 sublayers (Acsády et al., 1996b).

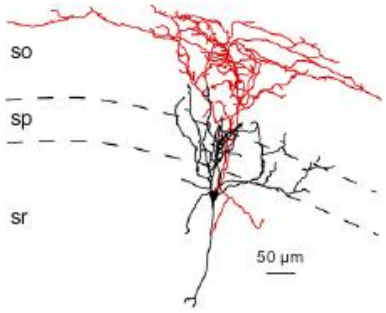

Figure 16: Morphology of an ISI Type III cell. Black denotes the soma and dendrites, while red represents the axonal arborization (Source: Pelkey et al., 2017).

Type III ISIs are defined by their coexpression of VIP and CR (VIP+/CR+). These cells have fusiform cell bodies and reside in and around SP. While their vertical dendrites typically span all CA1 sublayers, their axons characteristically target the horizonal dendrites of OLM cells in SO. Additionally, these axons can also target BiCs and PVBCs, although to a lesser extend (Acsády et al., 1996b). These anatomical characteristics position Type III ISIs to provide disinhibition to the distal tuft dendrites of CA1 pyramidal cells via robust inhibition of OLM interneurons.

In addition to the CA1 pyramidal cell- and interneuron-targeting interneuron subtypes detailed above, a small, yet significant, population of CA1 interneurons is primarily long-range projecting. This includes populations that target other hippocampal subregions (Szabo et al., 2017), as well as distant brain regions, including the medial septum, entorhinal cortex, subiculum, and retrosplenial cortex (Jinno, 2009; Jinno et al., 2007).

1.8 Role of Interneuron Subtypes in Controlling Hippocampal Network Activity

While a major line of interneuron research has utilized *in vitro* recordings and cell fillings to detail the unique anatomical, molecular, and physiological properties of the various interneuron

subtypes (especially within CA1), a complementary line of work has employed manipulations of the CA1 microcircuit in combination with recordings to discover how interneuron subtypes differentially regulate network activity, both *in vitro* and *in vivo*. These studies first utilized sublayer-specific electrical stimulations, and subsequently genetically-targeted optogenetic or pharmacogenetic manipulations, to discover the role of various subtypes in mediating feedforward inhibition, feedback inhibition, somatic inhibition, dendritic inhibition, and disinhibition. Here, I will briefly review several of these key studies, and what they reveal about the structure and function of inhibition within hippocampal circuits.

Early functional studies examining the role of inhibition in regulating CA1 network dynamics utilized *in vitro* electrical stimulation of CA1 afferents or efferents, in combination with intracellular recordings from pyramidal cells, to compare the properties of feedforward and feedback inhibition. Electrical stimulation within the SR, mimicking the excitatory drive CA1 pyramidal cells receive from CA3 afferents, reliably elicits an EPSC-IPSC sequence in pyramidal cells (Pouille and Scanziani, 2001). The inhibition is significantly stronger at the soma than in the dendrites, suggesting a predominant role for perisomatic-targeting interneurons in mediating feedforward inhibition (Pouille and Scanziani, 2001). Normally, several of these stimulations needed to occur within a tight temporal window to elicit spiking from the CA1 pyramidal cells. However, blockade of GABAA receptors significantly expanded this temporal window, suggesting that the perisomatic-targeting interneurons recruited by feedforward excitation from CA3 play an important role in regulating the spike timing of pyramidal cells. On the other hand, electrical stimulation within the alveus, predominantly exciting the axons of CA1 pyramidal cells and recruiting feedback inhibition, reliably recruits two distinct subtypes of local interneurons with different physiological properties and axonal arborizations (Pouille and

Scanziani, 2004). One of these two interneuron subtypes reliably fired action potentials at the beginning of the stimulus train, while the other subtype fired later in the stimulus train, and its firing rate increased in proportion to the stimulus strength (Pouille and Scanziani, 2004). While the axons of the interneurons activated at the onset of the stimulus predominantly terminated in the perisomatic region of pyramidal cells, the axons of those activated later in the stimulus terminated at the distal apical dendrites (Pouille and Scanziani, 2004). Taken together, these studies show that feedforward and feedback inhibitory circuits engage different interneuron subtypes, each regulating pyramidal cell activity in different ways.

With the development of optogenetics and pharmacogenetics, starting in the mid-2000s, researchers could subsequently perform conceptually similar experiments, but now targeting manipulations to specific interneuron subtypes and measuring the effects on surrounding pyramidal cells. Silencing SOM-expressing interneurons *in vitro* revealed that dendritic inhibition is the primary regulator of burst spiking in CA1 pyramidal cells via regulation of dendritic electrogenesis (Lovett-Barron et al., 2012). Similar results were also found when silencing SOM-expressing interneurons *in vivo*, and additionally silencing PV-expressing interneurons was shown to primarily affect the spike time of pyramidal cells relative to theta oscillations (Royer et al., 2012). Subsequent *in vivo* studies have revealed roles for dendritic inhibition in shunting aversive sensory excitation from the entorhinal cortex during contextual fear conditioning (Lovett-Barron et al., 2014), as well as for VIP-expressing, disinhibitory interneurons in regulating place cell representations during spatial learning (Turi et al., 2019). Recent studies utilizing pan-interneuron silencing have also revealed roles for local inhibition in suppressing out-of-field excitation in place cells (Grienberger et al., 2017), and in limiting the recruitment of place cells to ensemble representations (Rolotti et al., 2021). In summary, these

studies, employing different methods to manipulate various CA1 microcircuit elements, have revealed several subtype-specific roles for interneurons in controlling network activity.

1.9 Structural, Molecular, and *in vitro* Physiological Plasticity of Hippocampal Inhibitory Circuits in Response to Experience

Although learning is typically associated with activity-induced changes in synaptic strength at excitatory synapses, hippocampal inhibitory circuits have been shown to also undergo structural, molecular, and physiological changes in response to learning or experience. For example, contextual fear conditioning and Morris water maze learning induce increased numbers of mossy fiber synapses onto fast-spiking interneurons within hippocampal CA3, and this increase in feedforward connectivity has an important role in learning (Ruediger et al., 2011). Relatedly, contextual fear conditioning was also found to promote the emergence of large fractions of local PVBCs with high levels of PV immunoreactivity and high levels of excitatory synaptic inputs, while environmental enrichment conversely promotes the emergence of large fractions of CA3 PVBCs with low levels of PV immunoreactivity and high levels of inhibitory synaptic inputs (Donato et al., 2015, 2013). Exploration of a novel spatial environment was found to induce enhanced perisomatic inhibition onto activated, c-fos positive CA1 pyramidal neurons from PVBCs, while weakening perisomatic inhibition originating from CCKBCs onto these same neurons (Yap et al., 2021). Together, these studies demonstrate robust hippocampal inhibitory plasticity induced by novel experience and learning.

Despite these documented structural, molecular, and *in vitro* physiological changes in inhibitory circuits during experience or explicit learning, very little is known about how inhibitory activity patterns change in response to these behavioral events. In fact, many *in vivo*

functional properties of interneuron activity are thought to depend largely on the interneuron subtype, with little attention paid to possible changes in activity induced by experience. For example, as detailed above, the various interneuron subtypes are thought to exhibit subtype-specific dynamics during SWRs which do not significantly change over time or as a function of experience, although the properties of SWRs themselves are readily modulated by behavior. However, this idea remains largely a conjecture, as very little data exists regarding the dynamics of interneuron subtypes during behavior and how these dynamics can be modulated with experience.

1.10 Methods for Recording the *in vivo* Dynamics of Defined Interneuron Subtypes

While *in vitro* studies of hippocampal interneurons have provided a wealth of information regarding the anatomy, molecular characteristics, and *in vitro* physiology of defined interneuron subtypes, comparatively little is known about the *in vivo* activity patterns of specific subtypes during behavior. To date, the vast majority of *in vivo* interrogations of hippocampal networks have focused on excitatory pyramidal cells, detailing their firing properties, feature selectivity, and responses to various behavioral manipulations, such as context change or association of environmental locations with reward (Colgin et al., 2008; Danielson et al., 2016; Moser et al., 2008; Sosa and Giocomo, 2021; Zaremba et al., 2017). Defined hippocampal interneuron subtypes have remained much more difficult to sample at large-scale during behavior because of technical limitations associated with various methods of recording the *in vivo* activity dynamics of interneurons. Below I will detail the current methodologies for recording interneuron dynamics *in vivo*, as well as the strengths and limitations of each method.

Extracellular electrophysiologic recordings with metal electrodes (i.e. tetrodes, silicon probes) have been the workhorse of *in vivo* hippocampal physiology for many decades (Csicsvari et al., 2000; Dupret et al., 2010; English et al., 2017; Grosmark and Buzsáki, 2016). These recordings enable the measurement of interneuron activity from many individual cells with single spike resolution, and allow simultaneous recordings of pyramidal cell spiking and the extracellular oscillatory network patterns (LFP) with which interneurons are intimately linked. In addition, extracellular electrophysiology can be used to record from deep brain areas, such as hippocampal CA3, and it can be flexibly combined with a wide range of behaviors in awake, freely moving rodents. However, the sampling ability of interneurons is typically limited to a handful of cells, and the same neurons generally cannot be tracked across days due to movement of the electrode relative to individual neurons. Critically, these recordings cannot target particular interneuron subtypes, and the subtype of the recorded interneurons cannot be known, although they can be broadly distinguished based on their electrophysiological properties (fast-spiking vs. regular spiking). Lastly, these recordings are biased to record from fast-spiking subtypes, such as PVBCs, as regular spiking subtypes do not emit nearly as many action potentials that could be detected by the electrode. Thus, subtypes such as CCKBCs are likely not recorded from with this method.

A complementary electrophysiological approach to record form interneurons *in vivo* is juxtacellular recordings with glass electrodes, combined with *post hoc* identification of the recorded cells (Katona et al., 2014; Klausberger et al., 2005, 2003; Viney et al., 2013). These recordings enable measurement of neuronal activity from individual neurons with single spike resolution, as well as simultaneous recording of the LFP. As the recorded cells can be recovered *post hoc* and tested for expression of various molecular markers with immunohistochemistry, the

subtype of the recorded cell can be known unambiguously. Thus, to date, juxtacellular recordings with *post hoc* identification provide the most detailed information from single interneurons, combining detailed physiological data with rigorous anatomical identification. However, these recordings are very laborious, and only one cell can be recorded from at a time. Studies employing juxtacellular recordings typically only report data from a handful of interneurons, leaving it unclear how broadly the findings apply at the population level. In addition, recordings are short and often conducted under anesthesia because it is difficult to hold the recording for extended periods of time. Thus, it is very difficult to combine these juxtacellular recordings with sophisticated learning behaviors, or to track the same cell over long time scales. Finally, in most instantiations, these recordings cannot target specific subtypes *a priori*, making them biased to more frequent subtypes and making it difficult to systematically study certain interneuronal populations.

More recently, both one- and two-photon functional calcium imaging approaches have been used to interrogate interneurons (Arriaga and Han, 2019, 2017; Sheffield et al., 2017; Turi et al., 2019). These methods can provide better sampling of interneurons than electrophysiological methods, as dozens of neurons can typically be imaged at once. However, calcium imaging does not have single spike resolution of interneuron activity, and it is thus unclear how the observed activity patterns relate to individual action potentials. In addition, most applications of these imaging approaches are restricted to a single, or at most several, imaging planes, and hippocampal interneurons are dispersed within three dimensions, making large-scale imaging difficult. Specific interneuron subtypes can be targeted with Cre-driver lines, enabling subtype-specific recordings. However, this typically only enables broad subsets of interneurons to be recorded from, such as PV- or SOM-expressing cells, as most *bona fide* subtypes are defined by

the expression of multiple molecular makers. Additionally, these approaches in Cre lines allow the experimenter to only record from one cell type at a time. Finally, these imaging approaches are compatible with more complex behavioral tasks, and longitudinal tracking of the same cells over many days or weeks is possible.

Recent experimental approaches to recording *in vivo* interneuron activity have combined these three basic strategies in creative ways to overcome some of the limitations of each method. For example, tetrode or silicon probe recordings can be combined with optogenetic tagging of specific subtypes in Cre-drive lines to extracellularly record from specific cell types (‘optotagging’) (Dudok et al., 2021b). In addition, juxtacellular recordings can be conducted under visual guidance and in specific Cre-driver lines to systematically target defined cell types.

Overall, although great progress has been made in characterizing CA1 pyramidal cell dynamics during various behavioral tasks, relatively little remains known about the activity patterns of molecularly-defined CA1 interneurons during behavior. The ideal approach to record interneuron activity *in vivo* would allow for large-scale, unbiased recordings of many defined cell types simultaneously during various behavioral tasks. In this thesis, I employ large-scale AOD-based two-photon calcium imaging *in vivo* combined with *post-hoc*, multiplexed immunohistochemistry, both within hippocampal CA1 and CA3, to survey the activity and plasticity of defined interneuron subtypes during various behavioral tasks and states.

Chapter 2: Large-Scale 3D Two-Photon Imaging of Molecularly-Identified CA1 Interneuron Dynamics in Behaving Mice [1]

Tristan Geiller[1,2,*], Bert Vancura[1,2,*], Satoshi Terada[1,2], Eirini Troullinou[3,4], Spyridon Chavlis[5], Grigorios Tsagkatakis[4], Panagiotis Tsakalides[3,4], Katalin Ócsai[6], Panayiota Poirazi[5], Balázs J Rózsa[6,7], and Attila Losonczy[1,2,8]

1) Department of Neuroscience, Columbia University, New York, NY, USA.
2) Mortimer B. Zuckerman Mind Brain Behavior Institute, Columbia University, New York, NY, USA.
3) Institute of Computer Science, Foundation for Research and Technology Hellas, Heraklion, 70013, Greece
4) Department of Computer Science, University of Crete, Heraklion, 70013, Greece
5) Institute of Molecular Biology and Biotechnology (IMBB), Foundation for Research and Technology-Hellas (FORTH), Heraklion, Crete, 700 13, Greece
6) Faculty of Information Technology, Pázmány Péter University, Budapest
7) Laboratory of 3D Functional Network and Dendritic Imaging, Institute of Experimental Medicine, Hungarian Academy of Sciences, Eötvös Loránd Research Network, Budapest, Hungary
8) The Kavli Institute for Brain Science, Columbia University, New York, NY, USA.

** These authors contributed equally to this work.*[2]

Lead contact: Attila Losonczy – al2856@columbia.edu

[1] This study was published in *Neuron* in December 2020.
[2] I performed experiments and analysis together with TG, and I wrote the manuscript together with TG and AL.

2.1 Introduction

Local circuits throughout the mammalian brain are composed of relatively homogenous populations of glutamatergic principal cells and numerically fewer but highly diverse gamma-aminobutyric acid (GABA)-releasing interneurons (INs). While cortical functions are thought to be primarily carried out by excitatory cells, GABAergic inhibition provided by INs has been shown to be indispensable for a range of elementary cortical computations (Isaacson and Scanziani, 2011; Tremblay, Lee and Rudy, 2016; Fishell and Kepecs, 2020).

Much of our current knowledge about cortical INs comes from decades of investigations in the mammalian hippocampus. Pioneering studies have uncovered an astounding anatomical, physiological, developmental and molecular diversity of hippocampal INs and parsed them into distinct cell-types in each hippocampal region (Freund and Buzsaki, 1996; Klausberger and Somogyi, 2008; Pelkey *et al.*, 2017; Booker and Vida, 2018). To date, there has been an unprecedented characterization of the IN populations that comprise hippocampal region CA1, revealing several organizational principles of local circuit inhibition. First, excitatory input-output transformation in CA1 pyramidal cells (CA1PCs) is under strong inhibitory control by feedforward and feedback inhibitory circuits (Pouille and Scanziani, 2001, 2004; Lovett-Barron *et al.*, 2012). Second, subpopulations of CA1 INs inhibit specific subcellular compartments of CA1PCs, such as the axon initial segment, soma, and different dendritic domains (Buhl, Halasy and Somogyi, 1994; Freund and Buzsaki, 1996; Klausberger and Somogyi, 2008; Bloss *et al.*, 2016). Third, these IN subtypes are differentially modulated during hippocampal network oscillations, thus organizing the release of GABA onto PCs in both space and time (Klausberger et al., 2004, 2003; Somogyi et al., 2014). Finally, subpopulations of INs preferentially innervate other INs (Acsády et al., 1996b; Chamberland and Topolnik, 2012; Gulyás et al., 1996), as well as distant brain regions via long-

range projections (Caputi et al., 2013; Francavilla et al., 2018; Jinno et al., 2007; Katona et al., 2017; Wick et al., 2019).

While these features of inhibitory circuit organization collectively point to specialized behavioral functions for IN subtypes in the hippocampus, this long-standing hypothesis remains largely open as little is known about the *in vivo* activity dynamics of identified INs in behaving animals. This knowledge gap partly stems from the limited ability of traditional electrophysiological techniques to study the *in vivo* population-level activity dynamics of identified INs, as they are either too low-throughput or unable to molecularly or morphologically identify the recorded cells (Dupret, O'Neill and Csicsvari, 2013; English *et al.*, 2017, Klausberger *et al.*, 2003; Varga, Golshani and Soltesz, 2012). Similarly, more recent one- or two-photon (2p) imaging approaches in Cre-driver lines are typically limited to one or several imaging planes and broad classes of INs (Arriaga and Han, 2019, 2017; Sheffield et al., 2017; Turi et al., 2019). An optimal strategy would offer monitoring of the collective activity dynamics of all INs in large tissue volumes *in vivo* in combination with *post hoc* multiplexed characterization of the recorded cells, as has been implemented in the neocortex (Langer and Helmchen, 2012; Kerlin *et al.*, 2010; Khan *et al.*, 2018). As a step towards a comprehensive characterization of inhibitory circuit dynamics in the behaving mouse hippocampus, here we combine acousto-optic deflection (AOD) microscopy-based 3D calcium imaging (Katona et al., 2012; Szalay et al., 2016) with *post hoc*, multiplexed fluorescence immunohistochemistry to record simultaneously from populations of molecularly-defined INs throughout all CA1 strata during spatial navigation, learning, and sharp-wave ripple (SWR) events during quiet wakefulness. Our results demonstrate the validity and utility of this approach, as they largely confirm previous findings in cases where similar data is available, extend previous findings in cases where existing data is hampered by small sample sizes

or a lack of subtype-specific information, and provide several novel insights about IN subtype dynamics during behavior.

2.2 Results

Fast, targeted *in vivo* calcium imaging in 3D and *post hoc* molecular identification of CA1 INs

To obtain large-scale functional recordings of CA1 INs, we performed 3-dimensional (3D) AOD-2p calcium imaging following virus injection in dorsal CA1 of *VGAT-Cre* mice to express the genetically encoded calcium sensor GCaMP6f in all INs. Then, we implanted a cannula window over dorsal CA1 and trained mice to run head-fixed on a treadmill. We used AOD-2p microscopy to rapidly target small frames in 3D surrounding INs located within an 800x800x500 μm volume (total of 3626 INs in 16 mice, 226.6 ± 27.3 INs per mouse, mean ± std) from the CA1 *stratum oriens/alveus* border to the *stratum lacunosum moleculare*, and imaged them simultaneously at a rate of 4-5 Hz during behavior (Figure 1A, 1B, 1D, 1E, 1F, S1). *Post hoc* immunohistochemistry was then performed in fixed brain slices and the molecular identity of imaged INs was retrospectively determined by registering confocal images to *in vivo* 2p stacks (Figure 1B, 1C, S1). In the first set of experiments we focused on CA1PC-targeting INs by using a combination of 5 molecular markers (Methods, Figure 1C, S1) to identify 6 subsets of INs that account for ~80% of the total IN population in CA1 (Bezaire and Soltesz, 2013). These included three types of parvalbumin (PV)-immunopositive INs: basket cells (PVBC), axo-axonic cells (AAC) and bistratified cells (BiC). In addition, three broader groups included somatostatin (SOM)-expressing cells (SomC), which comprises oriens lacunosum moleculare (OLM) INs and long-range projecting cells; cholecystokinin (CCK)-expressing cells (CCKC), which contain basket and

dendrite-targeting INs; and neuropeptide Y (NPY)-immunopositive and SOM-immunonegative ivy/neurogliaform cells (IvC/NGFC) (Freund and Buzsaki, 1996; Klausberger and Somogyi, 2008; Pelkey *et al.*, 2017). A total of 3129 INs were found *post hoc* in the slices (195.6 ± 42.6 per mouse, mean ± std), and 1936 were assigned to a putative IN subtype identity (121.0 ± 28.4 per mouse, mean ± std). The overall proportion (Figure S1) and layer distribution of each of these subtypes was consistent with previous studies (Figure 1F), which used detailed morphological reconstructions for cell-type identification, demonstrating the utility of our method for high-throughput recordings of distinct IN subpopulations.

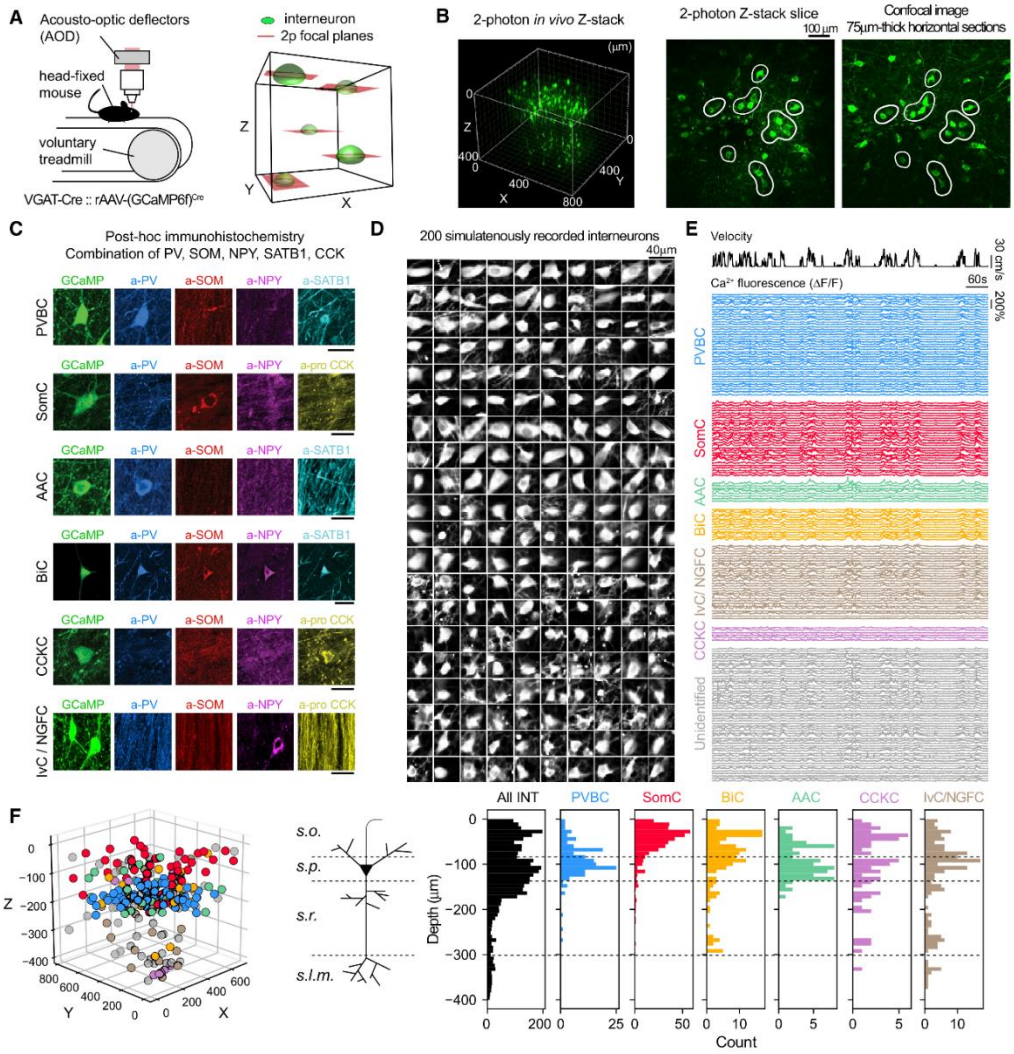

Figure 1 - AOD-based two-photon imaging in 3D and interneuron subtype identification

A. *Left:* Experimental setup. *VGAT-Cre* mice injected in CA1 with a rAAV to express GCaMP6f in all interneuron run voluntarily on a treadmill. *Right:* Schematic of 3D chessboard scanning, based on fast AOD imaging.

B. *Left:* 3D rendering of an *in vivo* CA1 Z-stack, 800x800x450µm FOV. Green cells are GCaMP6f-expressing interneurons. *Middle*: XY-orthoslice of the Z-stack. *Right:* Confocal image of a 75µm-thick horizontal slice from the same brain after fixation. Cells in slices can be found in the *in vivo* Z-stack (white contours).

C. *Post hoc* immunohistochemistry is performed on horizontal slices using a combination of markers and cells are assigned a subtype among parvalbumin basket cells (PVBCs), somatostatin-expressing cells (SomC), bistratified cells (BiC), axo-axonic cells (AAC), cholecystokinin-expressing cells (CCKCs), Ivy/Neurogliaform cells (IvC/NGFC) or unidentified cells.

D. Example time-averaged images of 200 simultaneously recorded interneurons.

E. Relative GCaMP fluorescence ($\Delta F/F$) traces from molecularly-identified interneurons from *D*.

F. *Left:* X-Y-Z positions of molecularly-identified interneurons from *E*. *Right:* Depth distribution for all interneurons (black, all INT) and molecularly-identified subtypes (n = 16 mice). Depth 0 corresponds to the position of the most dorsal interneuron in each mouse, located at the top of *stratum oriens* (see CA1 pyramidal cell schematic). *s.o.: stratum oriens, s.p.: stratum pyramidale, s.r.:stratum radiatum, s.l.m.: stratum lacunosum-moleculare*.

A

Mouse ID	Immunostaining strategy	in vivo ROI	found in confocal	subtype assigned	PVBC	SomC	BiC	AAC	CCKC	IvC NGFC	PVBC AAC
TG14	**1**: PV, SOM, NPY, SATB1, **2**: CCK	247	206	158	40	49	31	20	5	13	0
TG16	**1**: CCK, SOM, NPY, **2**: PV, SATB1	245	165	86	1	19	11	6	8	17	24
TG17	**1**: CCK, SOM, NPY, **2**: PV, SATB1	248	121	66	10	4	7	4	0	17	24
TG18	**1**: CCK, SOM, NPY, **2**: PV, SATB1	223	199	135	45	30	13	8	6	33	0
TG19	**1**: CCK, SOM, NPY, **2**: PV, SATB1	231	84	75	25	10	3	9	15	13	0
BV90	**1**: CCK, SOM, NPY, **2**: PV, SATB1	267	213	138	9	35	25	8	5	8	48
TG300	**1**: CCK, SOM, NPY, **2**: PV, SATB1	245	226	145	15	53	11	9	1	12	44
TG302	**1**: CCK, SOM, NPY, **2**: PV, SATB1	231	211	126	2	46	8	4	9	12	45
TG310	**1**: CCK, SOM, NPY, **2**: PV, SATB1	297	254	130	10	39	5	3	13	21	39
TG325	**1**: PV, SOM, SATB1, **2**: CCK, NPY	240	227	132	23	34	20	30	4	20	1
TG326	**1**: PV, SOM, SATB1, **2**: CCK, NPY	240	172	101	33	22	15	15	1	13	2
TG327	**1**: PV, SOM, SATB1, **2**: CCK, NPY	240	216	113	32	37	14	22	3	2	3

	a-CCK	a-SOM	a-NPY	a-PV	a-SATB1
CCKC	+	-	+/-	-	+/-
SomC	-	+	+/-	-	+/-
PVBC	-	-	-	+	+
AAC	-	-	-	+	-
BiC	-	+	+	+	+
IvC/NGFC	-	-	+	-	+/-

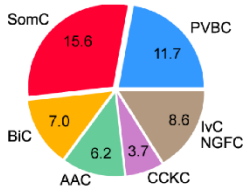

B

Mouse ID	Immunostaining strategy	in vivo ROI	found in confocal	subtype assigned	PV+	SomC	BiC	IvC NGFC	ISI1	VIP+/CR-	ISI3
TG276	**1**: PV, SOM, VIP, **2**: NPY, CR	240	188	96	48	6	18	8	2	6	8
BV106	**1**: PV, SOM, VIP, **2**: NPY, CR	244	221	138	74	26	12	7	6	6	7
BV107	**1**: PV, SOM, VIP, **2**: NPY, CR	234	213	118	70	30	2	3	2	7	4
BV109	**1**: PV, SOM, VIP, **2**: NPY, CR	246	213	148	59	67	11	9	0	2	0

	a-PV	a-SOM	a-NPY	a-VIP	a-CR
PV+	+	-	+	-	-
SomC	-	+	+/-	-	-
BiC	+	+	-	-	-
IvC/NGFC	-	-	+	-	-
ISI1	-	-	-	-	+
VIP+/CR-	-	-	-	+	-
ISI3	-	-	-	+	+

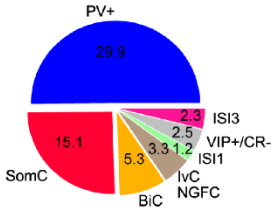

C

VIP-Cre mice

Mouse ID	Immuno.strategy	in vivo ROI	found in confocal	subtype assigned	ISI3	VIP+/CCK+	VIP+/M2R+	ISI2
TG338	**1**: CCK, CR, M2R	110	100	31	11	6	1	13
TG339	**1**: CCK, CR, M2R	126	114	38	21	5	1	11
TG340	**1**: CCK, CR, M2R	150	123	44	27	7	2	8

	a-CR	a-M2R	a-CCK
ISI2	-	-	-
ISI3	+	-	-
VIP+/M2R+	-	+	-
VIP+/CCK+	-	-	+

Figure S1 - Molecular characteristics of interneuron subtypes and breakdown of imaged cells by sub- type (related to all Figures)

A. Top: Overview of the data analyzed in Figures 1-6. Each row includes the antigens stained for in that mouse, the number of imaged cells, the number of cells registered in the confocal images, the number of cells assigned an interneuron subtype, and the

breakdown by subtype. In cases where SATB1 immunostaining was unclear, cells were assigned a general (PVBC/AAC) subtype and excluded from analysis. Bottom left: Overview of the rules used to assign interneurons to a subtype based on immunohistochemistry (see Methods). Bottom right: Percentage of registered cells belonging to each subtype. The most quantitative anatomical characterization of rodent CA1 inhibitory circuits performed to date has produced the following estimates for the numbers of each interneuron subtype (as a percentage of the total CA1 interneuron population): PVBC: 14.4%, SomC: 9.3%, BiC: 5.7%, AAC: 3.8%,CCKC: 13.9%, lvC/NGFC: 32.2% (Bezaire and Soltesz, 2013). The ratio of subtypes we identify is close to these numbers, with the largest differences in the CCKC and lvC/NGFC subtypes. These cells tend to have smaller soma diameter (Capogna, 2011; Armstrong, Krock-Magnuson and Soltesz, 2012; Overstreet-Wadiche and McBain, 2015) and exist in large numbers in the more superficial layers of CA1, making them more difficult to sample during *in vivo* imaging.

B. Top: Overview of the data analyzed in VGAT-Cre mice in Figure 7. Each row of the table includes the same information as above. Bottom left: Overview of the rules used to assign interneurons to a subtype. Bottom Right: Percentage of registered cells belonging to each subtype.

C. Bottom left: Overview of the data analyzed in VIP-Cre mice in Figure 7. Bottom right: Overview of the rules used to assign interneurons to a subtype.

Locomotion-state-dependent activity of molecularly identified IN subpopulations during spatial navigation

To characterize the relationship between the ambulatory state of the animal and each IN's activity, we imaged mice that were water-restricted and trained to run on a 2m-long belt rich in tactile cues during a random foraging task (Figure 2A). We first computed the Pearson's correlation between the animal's velocity and each cell's activity (Figure 2B) and found that the majority of INs were positively correlated with velocity (Varga, Golshani and Soltesz, 2012; Lapray *et al.*, 2012; Varga *et al.*, 2014; Katona *et al.*, 2014; Lee *et al.*, 2014; Somogyi *et al.*, 2014; Fuhrmann *et al.*, 2015; Arriaga and Han, 2017, 2019; Francavilla *et al.*, 2018; Turi *et al.*, 2019) (Figure 2C). However, we also observed that ~10% of cells exhibited negative correlations, present across all subtypes (Figure 2C). Negatively correlated cells were significantly enriched in CCKC, where nearly half of cells showed increased activity during immobility (Figure 2B, 2C). We also found that IvC/NGFC were less modulated by locomotion, consistent with previous results (Fuentealba et al., 2008; Lapray et al., 2012). To examine whether the activity-velocity modulations are reflected in ambulatory state transitions, we calculated the average run-start and run-stop responses for each cell (Figure S2), which further detailed the unicity of immobility-triggered activation of CCKC. Regardless of molecular identity, negatively correlated cells were significantly enriched in *stratum oriens*, while positively correlated cells were predominantly in *stratum pyramidale* (Figure 2D), with small but noticeable differences in multiple subtypes (Figure S2). In addition, while the activity of positively correlated cells generally followed changes in velocity by up to several seconds, the activity of negatively correlated cells was more tightly linked in time to changes in velocity (Figure S2). Together, these results demonstrate that locomotion positively modulates the activity of most INs across molecularly defined subtypes, while identifying CCKC as comprising a significant population of negatively modulated cells.

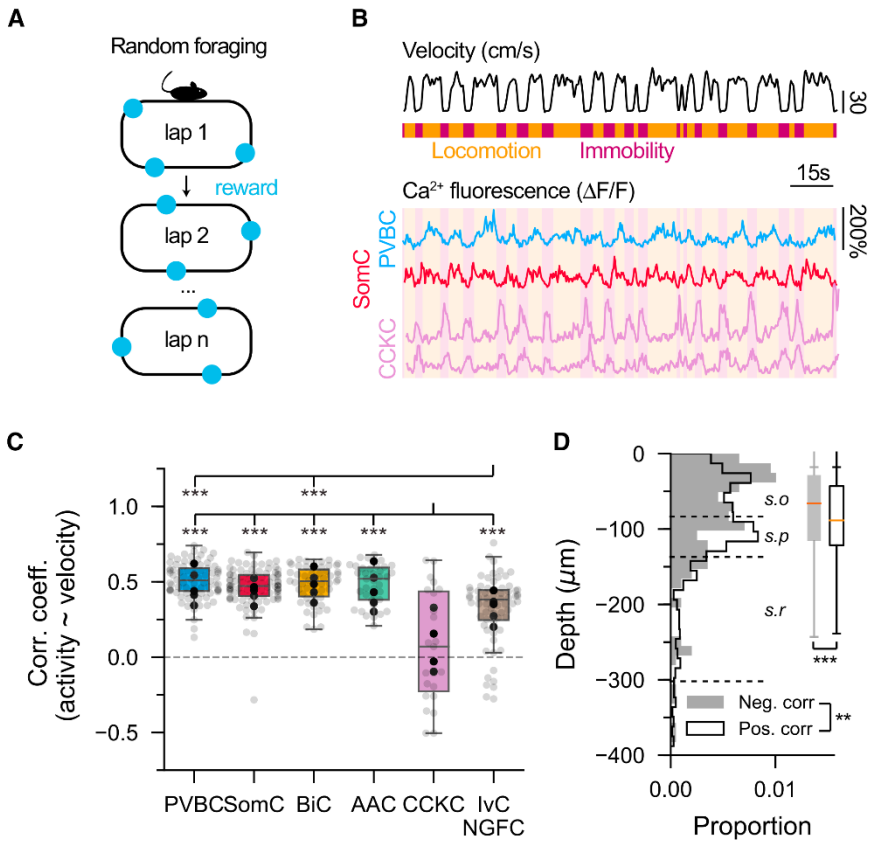

Figure 2 - Locomotion-state-dependent activity of IN subtypes

A. Schematic of the random foraging task.

B. Representative $\Delta F/F$ traces from PVBC, SomC and CCKC. Locomotion and immobility epochs are overlaid in orange and purple, respectively.

C. Pearson's correlation coefficients of $\Delta F/F$ traces and velocity (n = 134 PVBC, 180 SomC, 75 BiC, 56 AAC, 44 CCKC, 119 IvC/NGFC from n = 7 mice). One-way ANOVA ($p < 10^{-10}$) with *post hoc* Tukey's range test corrected for multiple testing. Mouse averages are indicated by the black dots.

D. Depth distribution of all negatively (filled gray, n = 156) and positively (empty black, n = 1429) correlated cells with velocity, regardless of subtype (n = 7 mice). Negatively correlated cells are more dorsal in *stratum oriens* than positively correlated cells, which are closer to

stratum pyramidale. Two-sample Kolmogorov-Smirnov test on distributions (p = 0.02) and Mann-Whitney U test on populations (p < 0.001).

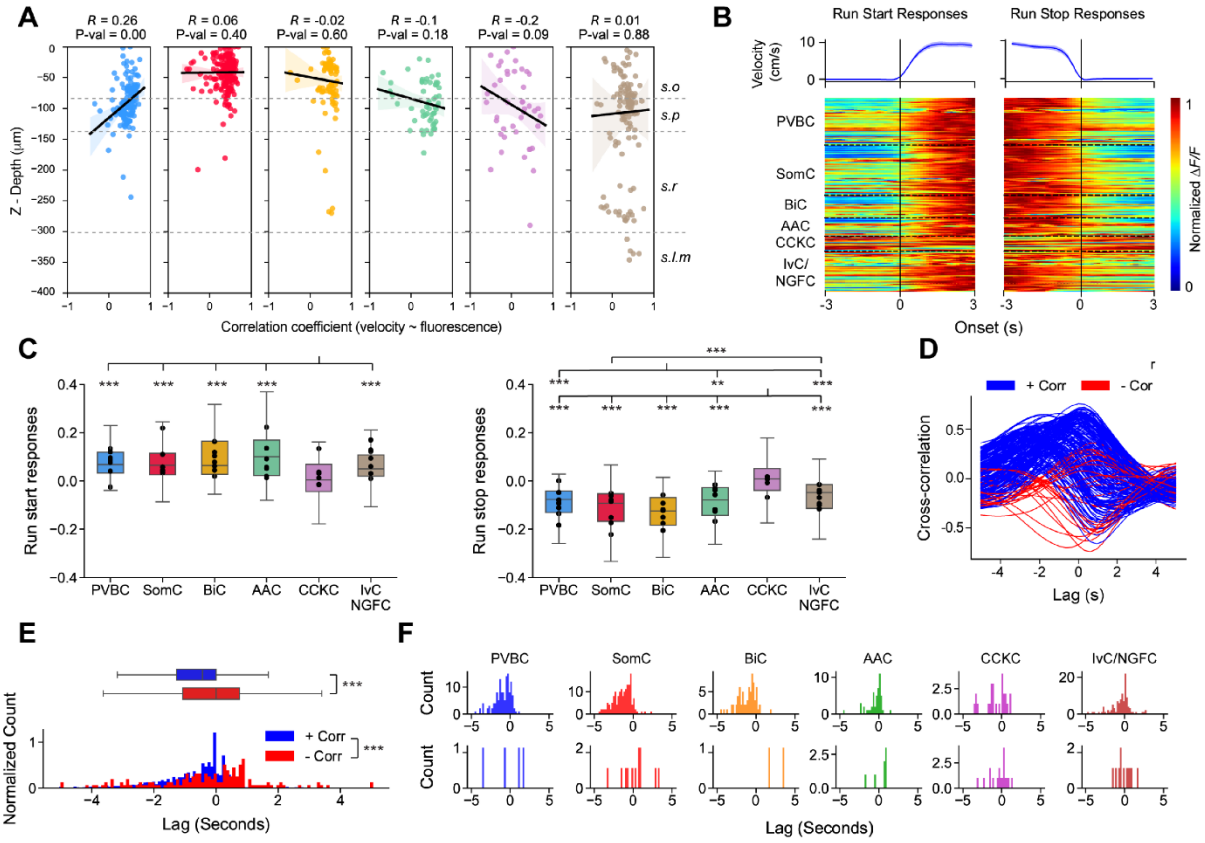

Figure S2 - Locomotion-related activity and depth profiles (related to Figure 2)

A. Depth distribution as a function of correlation with velocity for each subtype. Correlation coefficient (R values) and P-values are reported for the two variables. Shaded area represents bootstrapped confidence intervals.

B. Top: Average velocity profile centered around run initiation (run start) and stop (run stop) events. Bottom: heatmap of activityprofiles for each subtype during run start and run stop events. Each row represents the normalized activity of one neuron.

C. Left: Quantification of run start events. One-way ANOVA (p < 10-5) with post hoc Tukey's range test corrected for multiple testing(PVBC: 0.08 ± 0.08, SomC: 0.08 ± 0.11, BiC: 0.09

± 0.15, AAC: 0.12 ± 0.13, CCKC: -0.005 ± 0.13, lvC/NGFC: 0.062 ± 0.11, median ± IQR). Right: quantification of run stop events. One-way ANOVA ($p < 10\text{-}10$) with post hoc Tukey's range test corrected for multiple testing (PVBC: -0.09 ± 0.11, SomC: -0.12 ± 0.15, BiC: -0.164 ± 0.19, AAC: -0.111± 0.14, CCKC: 0.03 ± 0.16, lvC/NGFC: 0.06 ± 0.09, median ± IQR). Mouse averages are indicated by the black dots.

D. Representative cross-correlation traces between fluorescence signals and animal's velocity. Each line represents one cell, color-codedby its positive (blue) or negative (red) correlation with velocity.

E. Distribution of lags for all positively (n = 1429; median± IQR: -0.44 ± 1.27) and negatively (n = 156; median± IQR: 0 ± 1.8) correlated INs, regardless of subtype (n = 7 mice). Two-sample Kolmogorov-Smirnov test on distributions ($p < 10\text{-}5$). Mann-Whitney U test on populations ($p < 10\text{-}5$).

F. Distribution of lags per subtype for (top row) positively and (bottom row) negatively correlated cells (n = 134 PVBC, 180 SomC, 75 BiC, 56 AAC, 44 CCKC, 119 lvC/NGFC from 7 mice).

*p<0.05, **p<0.01, ***p<0.001.

Decoding of IN molecular identity with a machine-learning approach

The ability to infer the subtype of an imaged interneuron from its fluorescence trace and other easily measured behavioral or anatomical variables, without the need for genetic targeting or *post hoc* identification, would represent a significant advance in the ability to study interneuron subtypes at high throughput during behavior. As a first step towards this goal, we developed a machine learning-based classification tool to ask how well the molecular identity of a given IN

can be predicted from its relative fluorescence calcium signal ($\Delta F/F$), the animal's velocity, and the depth of the cell (Figure S3) (Troullinou et al., 2019). While prediction accuracy was well above chance for all 6 molecularly defined IN subtypes, it remained suboptimal as an automated classification approach. We found that many decoding errors resulted from misclassification between PV-expressing INs (PVBC and AAC) and between SOM-expressing INs (SomC and BiC). Given these findings, we next asked whether discrimination would improve by merging the similar categories to create a 4-class problem consisting of, PV-expressing INs, SOM-expressing INs, CCKC, and IvC/NGFC. The classification showed higher accuracy (64%, 71% 60% and 59%, respectively) (Figure S3). Overall, our findings suggest that the broader groups of molecularly defined INs have general signatures in their dynamics that can be recognized at above chance-level accuracy by a machine learning algorithm, although the error rates still remain too high for general use as an automatic classification approach.

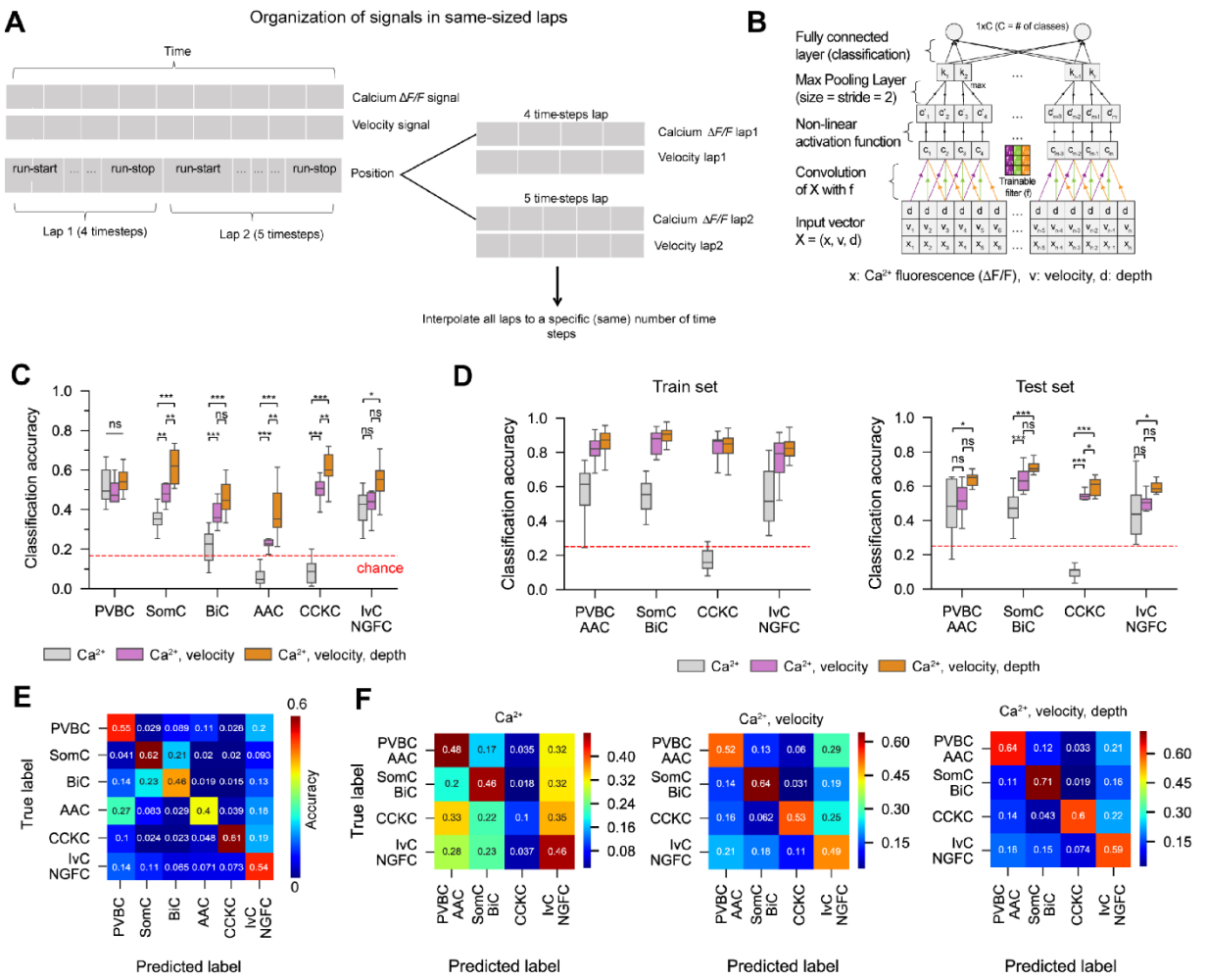

Figure S3 - Machine Learning-based decoding of major IN subtypes (related to Figure 2)

A. Preprocessing flowchart for signal alignment and organization into laps. Both calcium fluorescence and velocity signals are first broken down into laps, based on the run-start and run-stop information for each session. As signals often differ in length for the various laps/sessions, they are interpolated to a common number of data points (length).

B. Proposed deep learning architecture (2D-CNN) for IN subtype decoding: The input vector Xis convolved (stride=1) with a trainable filter f resulting in a vector c, to which a non-linear activation function is applied, resulting in another vector c' with the same size.

A max pooling layer of size 2 is also applied to c' in order to down-sample the input representation, reducing its dimensionality. The number of the output neurons C equals to the number of classes (6 in this case).

C. Classification accuracy achieved by the 1D-CNN (calcium only: grey) and 2D-CNNs (calcium, velocity: purple) or (calcium, velocity, depth: orange) architectures. Prediction accuracy is measured as the percentage of correctly predicted examples for each of the cell classes, using a blind test set. Each boxplot depicts the performance obtained over 10 random splits of the data between Training and Test sets. The sizes of the Training and Test sets were the following: n = 2128 PVBC, 2128 SomC, 1928 BiC, 1248 AAC, 1128 CCKC, 2628 lvC/NGFC in the Training set and n= 75 cells for each type in the Test set. Performance in each type was compared using repeated measures ANOVA (PVBC : $p = 0.16$, SomC : $p < 0.001$, BiC: $p < 0.001$, AAC: $p < 0.001$, CCKC: $p < 0.001$, lvC/NGFC: $p = 0.037$) with post hoc Tukey's range test corrected for multiple testing.

D. Left: Decoding performance measured as prediction accuracy for the Training set, by the 1D-CNN (calcium only: grey) and 2D-CNNs (calcium, velocity: purple) or (calcium, velocity, depth: orange) architectures. Each boxplot depicts the performance obtained over 10 random splits of the data. The Training set consisted of n= 2052 PVBC/AAC, 2052 SomC/BiC, 1053 CCKC, 2552lvC/NGFC training examples. Right: Same, with decoding performance measured on the Test set, consisting of 150 examples for each of the 4 classes (75 examples from each cell type of the mixed categories). Median values are reported in (D).

E. Confusion matrix for the 2D-CNN that was trained and tested using the calcium, velocity and depth information, as shown in panel C (orange). Rows represent the true subtypes

and columns the subtypes predicted by the 2D-CNN. Many decoding errors resulted from misclassification between PV-expressing INs (PVBCs and AACs) and between SOM-expressing INs (SomCs and BiCs). For example, 27% of the AAC were misclassified as PVBC. The opposite was less pronounced as just 11% of PVBC were predicted to be AAC), possibly because the number of training examples was higher for PVBC compared to AAC, thus enabling better learning for this class.

F. Confusion matrices for the CNN classifiers when implementing different features: calcium only; calcium and velocity; or calcium, velocity and depth.

*p<0.05, **p<0.01, ***p<0.001.

Subtype-specific modulation of CA1 INs during sharp-wave ripple oscillations

CA1 INs have been shown to have highly stereotyped, subtype-specific activity patterns during SWRs, fast oscillatory events associated with memory consolidation (Buzsáki, 2015). However, only small numbers of identified INs have been recorded during SWRs in awake mice (Varga *et al.*, 2014), making it unclear how generally these conclusions apply at the population level. To monitor hippocampal network oscillations during imaging, mice were chronically implanted with an extracellular electrode placed in the CA1 region on the contralateral side to record the local field potential (LFP) while simultaneously performing large-scale AOD-2p imaging at an imaging rate of 40Hz (Figure 3A, 3B, 3C, S4). To quantify the SWR-triggered activation in different subtypes, we developed a measure of modulation to assess the percentage of SWRs during which an IN increased its activity above baseline levels during immobility (Figure 3D). We observed subtype-specific modulation patterns that are largely consistent with previous reports. PVBC were generally strongly modulated (Klausberger *et al.*, 2003; Lapray *et al.*, 2012; Varga *et al.*, 2014), while most SomC were not (Katona et al., 2017, 2014) (Figure 3D). AAC and

BiC showed prominent bimodal profiles (Figure S4), with some cells strongly modulated during SWRs but others remaining silent (Katona et al., 2014; Varga et al., 2014; Viney et al., 2013) (Figure 3D), with no correlation with the anatomical depth of each cell (Figure S4). To investigate the differences between modulated and non-modulated INs within each subtype, we used a clustering method to infer the number of functionally distinct groups from the data**.** All subtypes but CCKC and NGFC separated into 2 distinct groups, suggesting within-subtype dissociations in SWR modulation (Figure 3E). Across subtypes, modulation probability values of modulated INs were similar, with slightly lower values for AAC (Figure 3E). The fraction of modulated INs in each group indicate a large proportion of previously unsuspected SWR-modulated AAC and non-SWR-modulated BiC (Figure 3F). Finally, we found differences in the axial location of modulated and non-modulated cells for SomC and BiC, as modulated cells were generally closer to *stratum pyramidale* (Figure 3G). These results reveal that although general trends do exist for the responses of molecularly defined IN subtypes during awake SWRs, there is also a previously underestimated within-subtype heterogeneity at the population level.

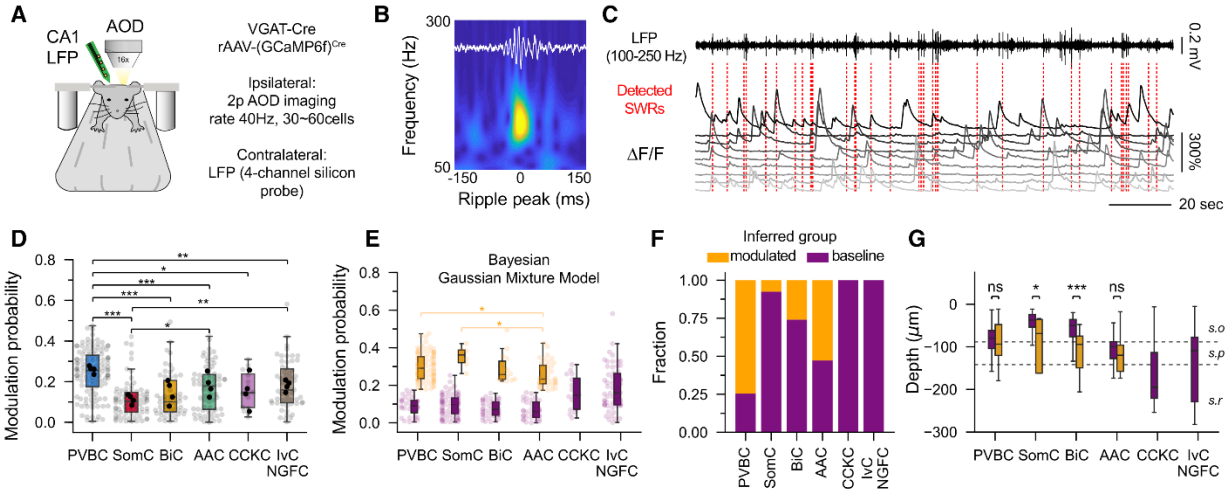

Figure 3: Between- and within-subtype functional heterogeneity during sharp wave ripples

A. Mice are implanted with a 4-channel silicon probe on the contralateral side to record LFP. 3D scanning is performed at higher imaging rates (40Hz) by decreasing the number of simultaneously recorded neurons (~30 cells simultaneously).

B. Representative averaged sharp-wave ripple (SWR)-triggered spectrogram for one session.

C. Representative LFP and $\Delta F/F$ traces. Red dashed lines represent the onset of a detected SWR.

D. SWR modulation probability for each subtype (n = 122 PVBC, 79 SomC, 54 BiC, 72 AAC, 16 CCKC, 58 IvC/NGFC from n = 4 mice, one-way ANOVA, $p < 0.001$).

E. Bayesian Gaussian Mixture Models, in which clusters are inferred from the data, show bimodal distributions for ripple modulation (modulated and non-modulated groups) in PVBC, SomC, BiC and AAC subtypes. Small but significant quantitative differences are seen among the modulated groups (one-way ANOVA, $p = 0.004$).

F. Fraction of cells in each inferred group (orange: modulated, purple: baseline) for the different subtypes.

G. Comparison of the depth profiles between the modulated and baseline groups for the different subtypes (unpaired t-tests).

ANOVA tests are corrected for multiple testing using *post hoc* Tukey's range test. Mouse averages are indicated by the black dots.

*p<0.05, **p<0.01, ***p<0.001.

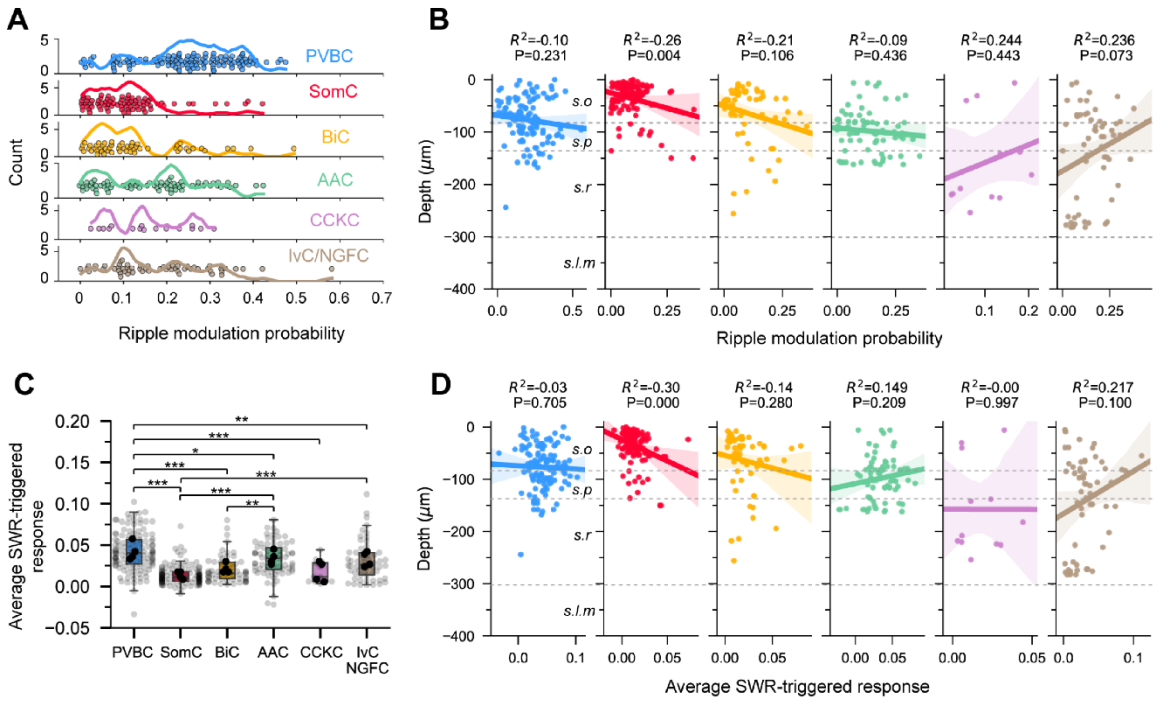

Figure S4 - Sharp-wave ripple modulation and depth profiles (related to Figure 3)

A. Histogram of ripple modulation for each subtype with overlaid density kernel (same data and n as Figure 3).

B. Depth distribution as a function of ripple modulation for each subtype. Correlation coefficient (R values) and P-values are reported for the two variables. Shaded area represents bootstrapped confidence intervals.

C. Distribution of average response (n = 122 PVBC, 79 SomC, 54 BiC, 72 AAC, 16 CCKC, 58 lvC/NGFC from n = 4 mice) also showing bimodal distributions for BiC and AAC (PVBC: 0.04 ± 0.03, SomC: 0.011 ± 0.01, BiC: 0.016 ± 0.02, AAC: 0.034 ± 0.026, CCKC: 0.012 ± 0.023, lvC/NGFC: 0.026 ± 0.027, median ± IQR). One-way ANOVA ($p < 0.001$) with post hoc Tukey's range test corrected for multiple testing. Mouse averages are indicated by the black dots.

D. Depth distribution as a function of average response for each subtype. Correlation coefficient (R values) and P-values are reported for the two variables. Shaded area represents bootstrapped confidence intervals.

*p<0.05, **p<0.01, ***p<0.001.

Spatially selective activity dynamics of CA1 INs during head-fixed spatial navigation

While place cells have been traditionally considered to be principal cells (O'Keefe and Dostrovsky, 1971), spatial modulation has also been sparingly reported for INs, although without rigorous subtype identification (Ego-Stengel and Wilson, 2007; Grienberger et al., 2017; Hangya et al., 2010; Marshall et al., 2002; Wilent and Nitz, 2007). Therefore, we sought to examine spatial information content in a large sample of INs during navigation (Figure 4A). We used standard shuffling procedures for the detection of significant peaks in activity at particular regions on the belt (Figure 4A). We found a wide spectrum of spatially tuned INs, with some exhibiting high and stable selectivity across laps (Figure 4B, 4H). To show that our detection method managed to identify spatially modulated cells, we trained a linear classifier to decode the position of the animal based on IN calcium activity dynamics (Figure 4C). While the errors of the decoded position were largely greater than those reported when decoding position from CA1PC activity (Figure S5), inferring the animal's position from the activity of the small subset of spatially-selective INs (blind of subtype, 17.5 ± 6.4% in total passed the threshold, mean ± sem, n = 6 mice, 3 sessions per mouse) was approximately as effective as doing so from the entire IN population (Figure 4D). Conversely, the decoding error was significantly greater from a subset of randomly chosen INs (matching the number of spatially modulated INs), as well as when the position and activity were randomly shuffled relative to one another (Figure 4D). While spatially selective INs were found in virtually all subtypes, BiC tended to have a significantly higher recurrence probability (Figure

4E). The majority of INs had broad tuning, as measured by the selectivity index, but a subset of SomC and BiC, and to some extent PVBC, displayed sharper fields (Figure 4F). Place field centroids of INs were generally uniformly distributed along the treadmill, with some observable preference in PVBC for the seam of the belt, a location likely providing a very salient sensory cue (Geiller et al., 2017) (Figure 4G). In addition, spatially-selective PVBC displayed a significantly more stable within-session recruitment than spatially-selective SomC (Figure 4H). Previous studies have also reported that some INs selectively decrease their activity in particular regions of an environment ("negative place fields") (Ego-Stengel and Wilson, 2007; Hangya et al., 2010; Marshall et al., 2002; Wilent and Nitz, 2007). Therefore, we also examined negative spatial selectivity but did not find that it was enriched among a specific subtype. The fraction of negative spatially modulated cells was also slightly lower (blind of subtype, 12.7 ± 8.3%, mean ± sem, n = 6 mice, 3 sessions per mouse) than the fraction of positive spatially modulated cells, as was the recurrence probability across all subtypes (Figure S5), although these reduced numbers may originate from difficulties in observing decreased activity with calcium sensors. These results demonstrate that hippocampal INs can represent spatial information at the population level and that a subset of INs exhibit spatial tuning similar to CA1PCs.

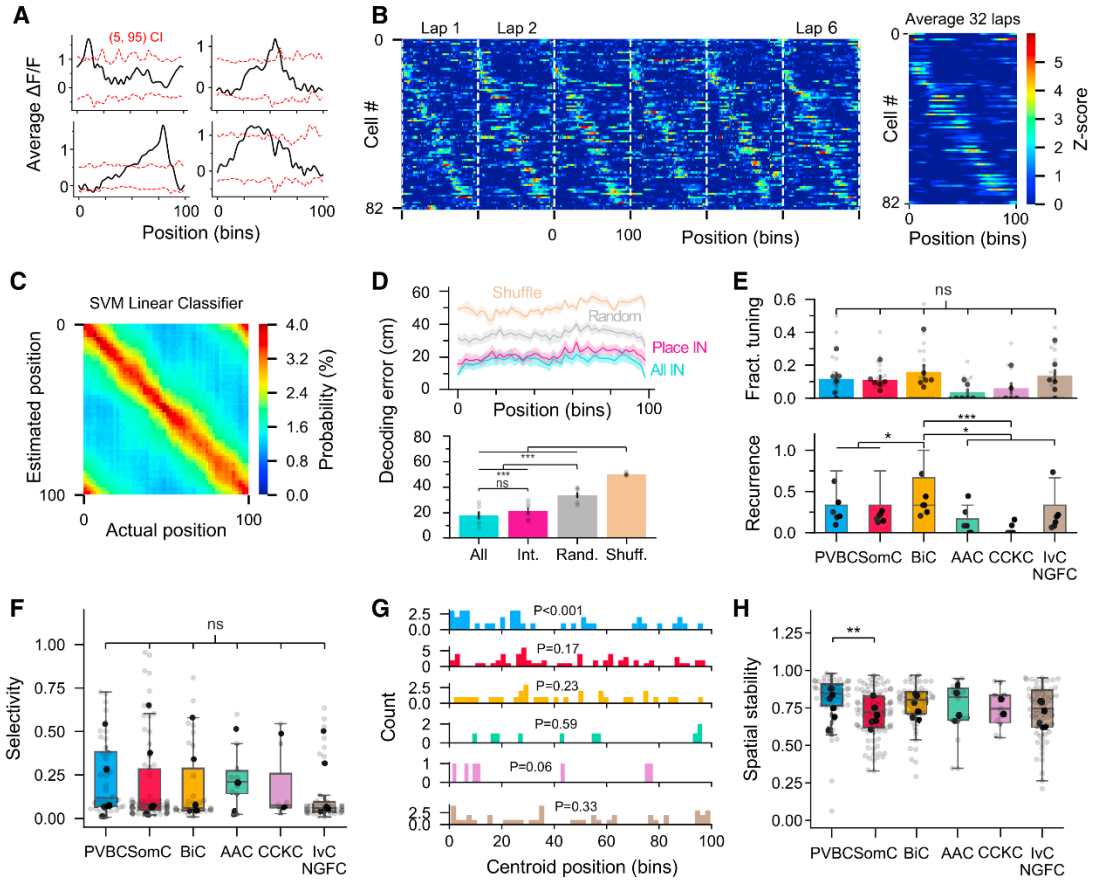

Figure 4: A subset of cells show significant spatial selectivity and drive spatial information content among interneurons at the population level

A. Representative examples of spatially modulated interneurons. Red dashed lines represent the 5% and 95% confidence intervals of the shuffled data.

B. Activity of 82 spatially modulated interneurons recorded simultaneously. Each row is a heatmap of one interneuron's Z-scored $\Delta F/F$ trace. *Left:* Successive laps are concatenated (only the first 6 laps are shown). *Right:* Average of the entire session (32 laps).

C. Representative example of the posterior probabilities obtained from a Support Vector Machine (SVM) classifier used to decode mouse position from interneuron activity.

D. *Top:* Decoding error as a function of position for 4 different groups. Cyan, activity from all interneurons in a given session was used for decoding. Magenta, only interneurons detected as spatially modulated were used. Gray, activity from randomly picked interneurons but matching the number of spatially modulated interneurons in the session. Brown, only spatially modulated interneurons but the position of the animal was randomly shuffled (n = 18 sessions from n = 6 mice).

Bottom: Average decoding error for each group above. Decoding accuracy originates mainly from spatially modulated cells, although they represent only a small fraction of all recorded interneurons (one-way ANOVA, $p < 10^{-8}$).

E. *Top:* Fraction of spatially modulated neurons for each subtype. Light gray dots represent sessions (n = 18 sessions from 6 mice) and black dots represent mouse averages. BiC have higher fractions but the difference is not significant from other subtypes (one-way ANOVA, p = 0.06).

Bottom: Recurrence probability of spatial modulation. BiC have a higher probability to stay spatially modulated on different sessions (one-way ANOVA, $p < 0.001$; n = 105 PVBC, 145 SomC, 50 BiC, 39 AAC, 41 CCKC, 111 IvC/NGFC from n = 6 mice).

F. Selectivity index, quantifying the sharpness of the tuning curve, for the different subtypes. SomC have a subset of cells with sharp fields but the mean is not different from that of the other subtypes (one-way ANOVA, p = 0.35). Each dot represents one neuron's selectivity index or its average over multiple sessions if imaged multiple times (n = 40 PVBC, 66 SomC, 32 BiC, 10 AAC, 7 CCKC, 43 IvC/NGFC from n = 6 mice).

G. Distribution of interneuron activity centroids along the belt. P-values are derived from a Kolmogorov-Smirnov uniformity test (same n as in *F*).

H. Tuning curve correlation coefficients between odd and even laps within the same session for spatially modulated interneurons, depicting the stability of the place field. Mouse averages are indicated by the black dots. ANOVA tests are corrected for multiple testing using *post hoc* Tukey's range test. Data are represented as mean ± sem.

*p<0.05, **p<0.01, ***p<0.001.

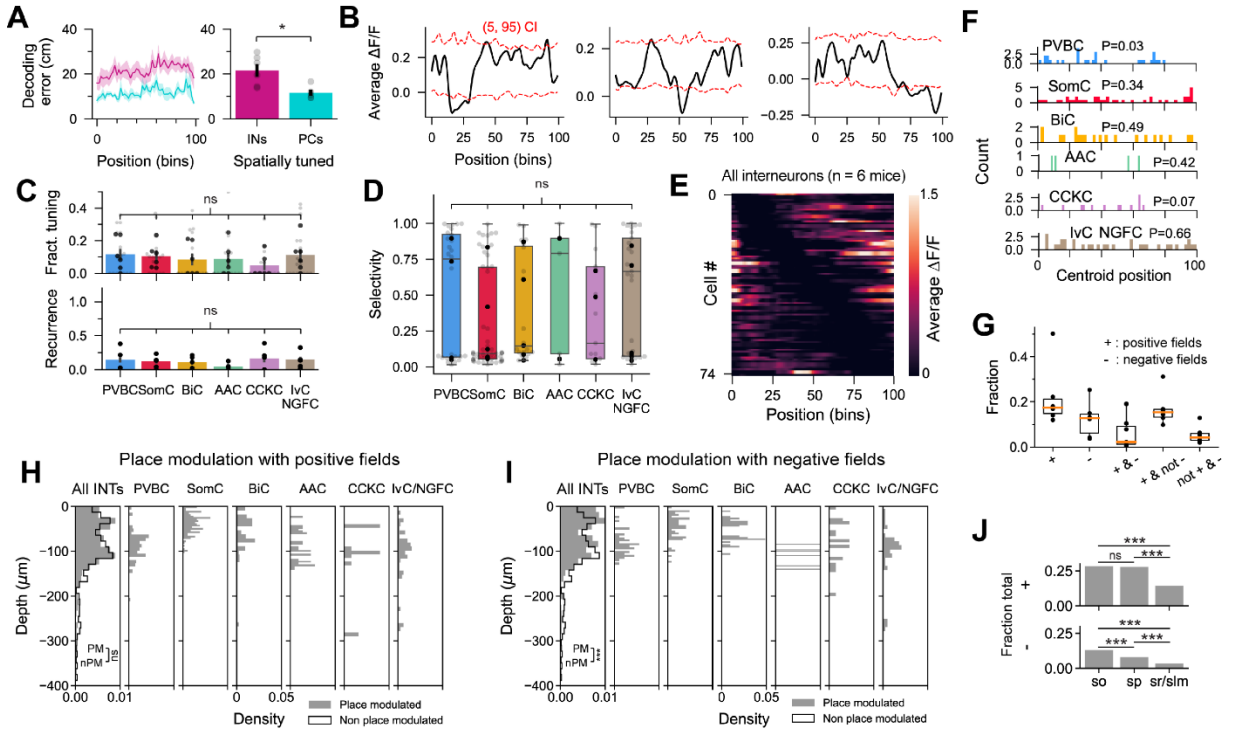

Figure S5 - Spatially modulated interneurons with negative field (related to Figure 4)

A. Left: Decoding error as a function of position for spatially modulated interneurons (n = 6 mice, 21.6 ± 2.76 cm, mean± SEM) and pyramidal place cells (n = 5 mice, 11.6 ± 0.01cm, mean ± SEM). Right: average decoding error for each group, unpaired t-test (p = 0.012). Data are represented as mean± SEM.

B. Representative examples of spatially modulated interneurons with a negative field (trough). Red dashed lines represent the 5% and 95% confidence intervals of the shuffled data.

C. Top: Fraction of spatially modulated neurons for each subtype. Light gray dots represent sessions (n = 18 sessions from 6 mice,PVBC: 12 ± 3%, SomC: 11 ± 3%, BiC: 8 ± 3%, AAC: 9 ± 3%, CCKC: 5 ± 2%, lvC/NGFC: 11 ± 3%, mean± SEM) and black dots represent mouse averages (one-way ANOVA, p = 0.16). Bottom: Recurrence probability (PVBC: 14 ± 2%, SomC: 12 ± 1%, BiC: 11 ± 2%,AAC: 4 ± 2%, CCKC: 16 ± 4%, lvC/NGFC: 15 ± 2%, mean ± SEM) of spatial modulation (one-way ANOVA, p = 0.64). n = 37 PVBC, 43 SomC, 20 BiC, 5 AAC, 15 CCKC, 41 lvC/NGFC from n = 6 mice. Top, bottom, data are represented as mean± SEM.

D. Selectivity index (PVBC: 0.74 ± 0.85, SomC: 0.09 ± 0.64, BiC: 0.14 ± 0.74, AAC: 0.79 ± 0.8, CCKC: 0.17 ± 0.64, lvC/NGFC: 0.66 ± 0.8, median ± IQR) depicting sharpness of the tuning curve (one-way ANOVA, p = 0.35). Each dot represents one neuron's selectivity index or its average over multiple sessions if detected multiple times (n = 29 PVBC, 41 SomC, 20 BiC, 4 AAC, 13 CCKC, 32 lvC/NGFC from n = 6 mice).

E. Activity of 74 spatially modulated interneurons with negative field recorded in 6 mice. Each row is color coded to represent one interneuron's average fluorescence.

F. Distribution of the inverse activity's centroid along the belt. P-values correspond to a Kolmogorov-Smirnov uniformity test (same n as in D).

G. Fraction of spatially modulated interneurons, regardless of subtype identity. "+" represents the neurons with a positive place field, "-" represents those with a negative place field. Overall, 17.4 ± 6.4% had positive fields, 12.7 ± 8.3% had negative fields, 2.1 ± 7.8% had both a positive and negative field, 15.3 ± 3.4% had strictly a positive field and no negative field, 4.2 ± 3.2% had strictly a negative field and no positive field (median± IQR, n = 6 mice). Mouse averages are indicated by the black dots.

H. Depth distribution of place modulated with a positive field (filled gray, n = 1135 cells), and non-place modulated (black step, n = 3224) for all interneurons and different subtypes. Two-sample Kolmogorov-Smirnov test on distributions (p = 0.32).

I. Same analysis as in (H) for negative place fields. Place modulated interneurons (n = 430, non-modulated n = 3929) tended to be in deeper CA1, around s.o (place modulated: -67 ± 70µm, non-place modulated: -97 ± 77µm, median± IQR). Two-sample Kolmogorov-Smirnov test on distributions (p p < 10-5), Mann-Whitney U-test on populations (p < 10-5).

J. Fraction of detected place interneuron with positive (+) and negative (-) peaks, blind of subtype and pooled by layer (positive in so: 28.4%, sp: 27.6%, sr: 14.2%, negative in so: 12.9%, sp: 7.9%, sr: 3.5%, same n as in Hand I). Chi-squared proportion tests. *p<0.05, **p<0.01, ***p<0.001.

We next sought to assess the stability of IN spatial representations by comparing the tuning curves of the same recorded neurons at three different time points, regardless of their spatial modulation: after virtually no delay (within-session), after 1 hour, and finally after 24 hours (Figure S6). While there were differences in within session stability across molecularly defined IN subtypes, with PVBC and CCKC showing the highest and lowest within-session correlations, respectively (Figure S6A, S6B), all subtypes had similar tuning curves correlations after 1 hour and 24 hours (Figure S6I). Interestingly, INs located more superficially within CA1, particularly superficially located PVBC and IvC/NGFC, were more stable within sessions, but the same trend did not hold for 1h correlations (Figure S6C, S6F). Tuning curve correlations after both 1 hour and 24 hours were significantly lower than the within-session correlations across all IN subtypes,

indicating a general reorganization of IN spatial representations with time. This general decorrelation is likely to reflect small fluctuations in the relatively uniform spatial responses of INs, as only a small subset of cells display significant place tuning. However, correlations at later time points (1h and 24h) were still significantly higher than chance levels (a distribution in which IN subtype identity was shuffled), indicating that INs retain a certain degree of spatial information over time (Figure S6I). The general decorrelation of tuning curves is two-fold lower in INs than in CA1PC, as reported previously under similar experimental conditions (Danielson et al., 2016). While it is not surprising that INs are a highly plastic element of the hippocampal network, further experiments can help dissect the causality of these representational drifts.

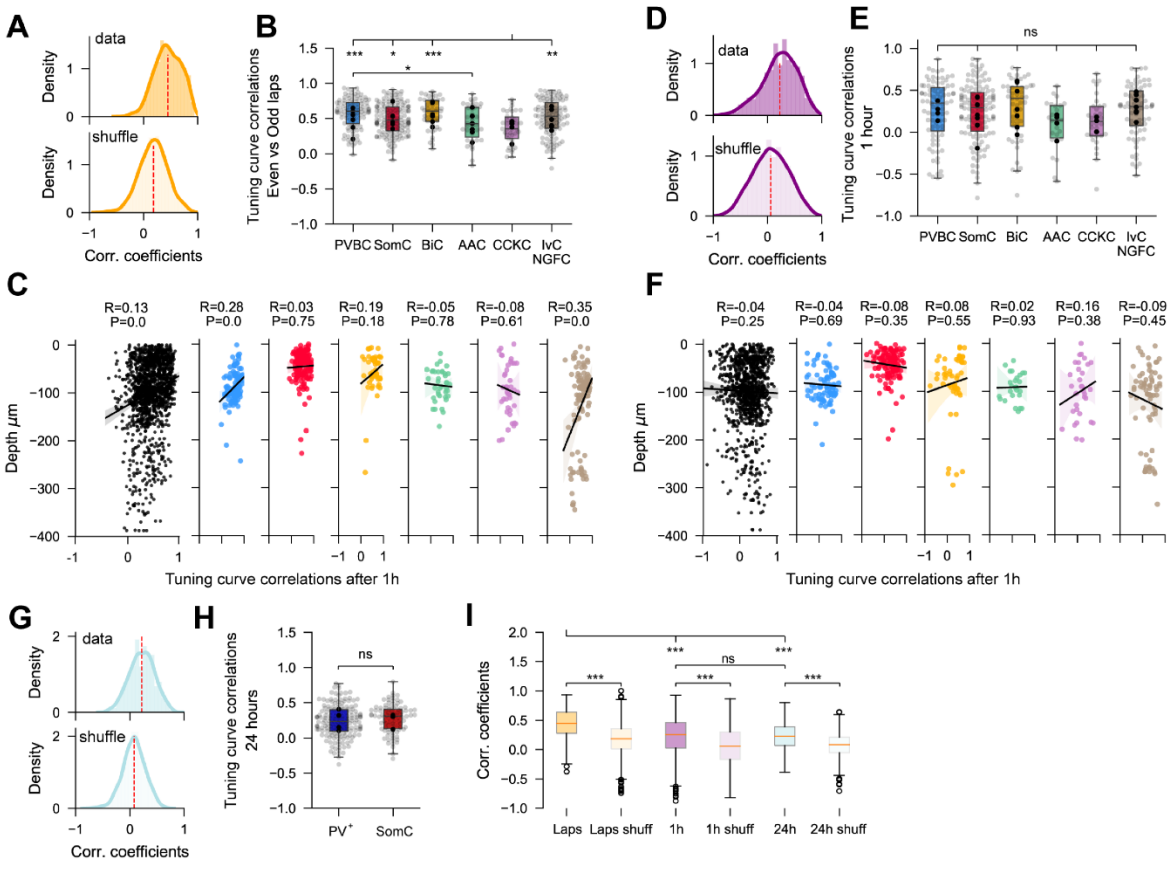

Figure S6 - Context representation drifts rapidly within one day (related to Figure 4 and 5)

A. Distribution of tuning curve correlation coefficients between odd and even laps within the same session for all interneurons and shuffled data (top, bottom, n = 1430 from 6 mice).

B. Correlation coefficients between odd and even laps for molecularly-identified subtypes. One-way ANOVA ($p < 0.001$) with post hoc Tukey's range test corrected for multiple testing (n = 105 PVBC, 145 SomC, 50 BiC, 39 AAC, 41 CCKC, 111 lvC/NGFC from n = 6 mice).

C. Depth distribution for all interneurons (black) and different subtypes as a function of the correlation coefficient between the tuning curve in odd and even laps.

D. Distribution of tuning curve correlation coefficients between 2 sessions separated by 1 hour for all interneurons and shuffle data(top, bottom, n = 1160 from 6 mice).

E. Correlation coefficients between 1-hour apart sessions by molecularly-identified subtypes. One-way ANOVA ($p = 0.10$) with posthoc Tukey's range test corrected for multiple testing (n = 93 PVBC, 125 SomC, 53 BiC, 27 AAC, 34 CCKC, 82 lvC/NGFC from n = 6 mice).

F. Depth distribution for all interneurons (black) and different subtypes as a function of the correlation coefficient between the tuningcurve between sessions separated by 1 hour.

G. Distribution of tuning curve correlation coefficients between 2 sessions separated by 24 hours for all interneurons and shuffle data (top, bottom, n = 643 from 4 mice).

H. Correlation coefficients between 24-hour apart sessions for PV+ (n = 163) and SomC (n = 93) neurons (unpaired t-test, $p = 0.17$). Data from n = 4 mice. Due to the low number of interneurons that were tracked for 24h, data for PV+ cells were pooled with mice without SATB1 staining (see Assignment of subtype identity section in Methods).

I. Summary statistics for (A), (C) and (E). All distributions are compared to their corresponding shuffled distribution (unpaired t-tests). Spatial tuning after 1 hour is as correlated as after 24 hours, and both are significantly lower than within session correlations. One-way ANOVA ($p < 10\text{-}^{10}$) with post hoc Tukey's range test corrected for multiple testing.

CA1 IN activity dynamics rapidly reconfigure in novel contexts

As CA1PC representations have been shown to undergo remapping in response to changes in the environment (Colgin, Moser and Moser, 2008; Kubie, Levy and Fenton, 2019), we next sought to assess the degree to which IN subtypes remap upon exposure to a novel context. To do so, mice performed the random foraging task twice on a familiar belt (context A_1 then A_2) and were finally exposed to a novel belt, decorated with a distinct set of tactile cues (context B) (Figure 5A). At the population level, INs displayed a significant decorrelation in their spatial tuning upon exposure to belt B (Figure 5B). This remapping could not be explained simply by the passage of time, as A_1-A_2 correlations were significantly higher than both A_1-B and A_2-B values, and no difference between A_1-B and A_2-B was observed (Figure 5B). All subtypes, with the exception of CCKC, displayed a significant decrease in tuning curve correlation after exposure to the novel context (Figure 5D), with no subtype-specific differences in the amplitude of this decrease (Figure 5E). A linear classifier trained on a subset of the IN activity could decode the context in which the held-out test data was imaged at near-perfect levels, further suggesting that IN activity carries strong contextual information at the population level (Figure 5C).

Several recent studies have leveraged calcium imaging from genetically-defined CA1 INs in virtual reality systems to assess changes in IN dynamics upon rapid exposure to a novel environment (Arriaga and Han, 2019; Hainmueller and Bartos, 2018; Sheffield et al., 2017). These

experiments revealed that SOM-expressing INs decrease their activity in novel contexts, while conflicting results have been reported for PV-expressing INs. With our treadmill apparatus, we observed a significant decrease in IN activity for the first several laps in context B for PVBC, SomC, BiC, and AAC subtypes (Figure 5F, H). CCKC were not modulated by the context change, while IvC/NGFC displayed a small but statistically nonsignificant increase in activity during the first 2 laps in the novel context (Figure 5F, H). In PVBC and SomC, activity returned to near-baseline levels later in the session, while this appeared more gradual for AAC and BiC (Figure 5F). These results could not be simply explained by differences in locomotion, as the velocity remained nearly identical across laps and between contexts (Figure 5G). To assess whether the decrease in activity was related to the anatomical location of each cell, we correlated the novel context activity modulation with cell depth for each subtype (Figure 5I). Although no statistically significant correlation was found between modulation and depth for a given subtype (Figure 5I), interneurons located deeper in CA1 were generally less modulated by the context change (Figure 5J), consistent with the enrichment of CCKC and IvC/NGFC in deeper sublayers. Taken together, these results indicate that IN activity is modulated by context and can rapidly reconfigure upon exposure to a novel environment. The majority of INs, including both perisomatic-targeting and dendrite-targeting subtypes, modulate their activity in novel contexts *via* both an overall decrease in activity levels and a general reorganization of their tuning properties. Both mechanisms could facilitate remapping in downstream pyramidal cell targets by influencing the rate and place reallocation of the fields.

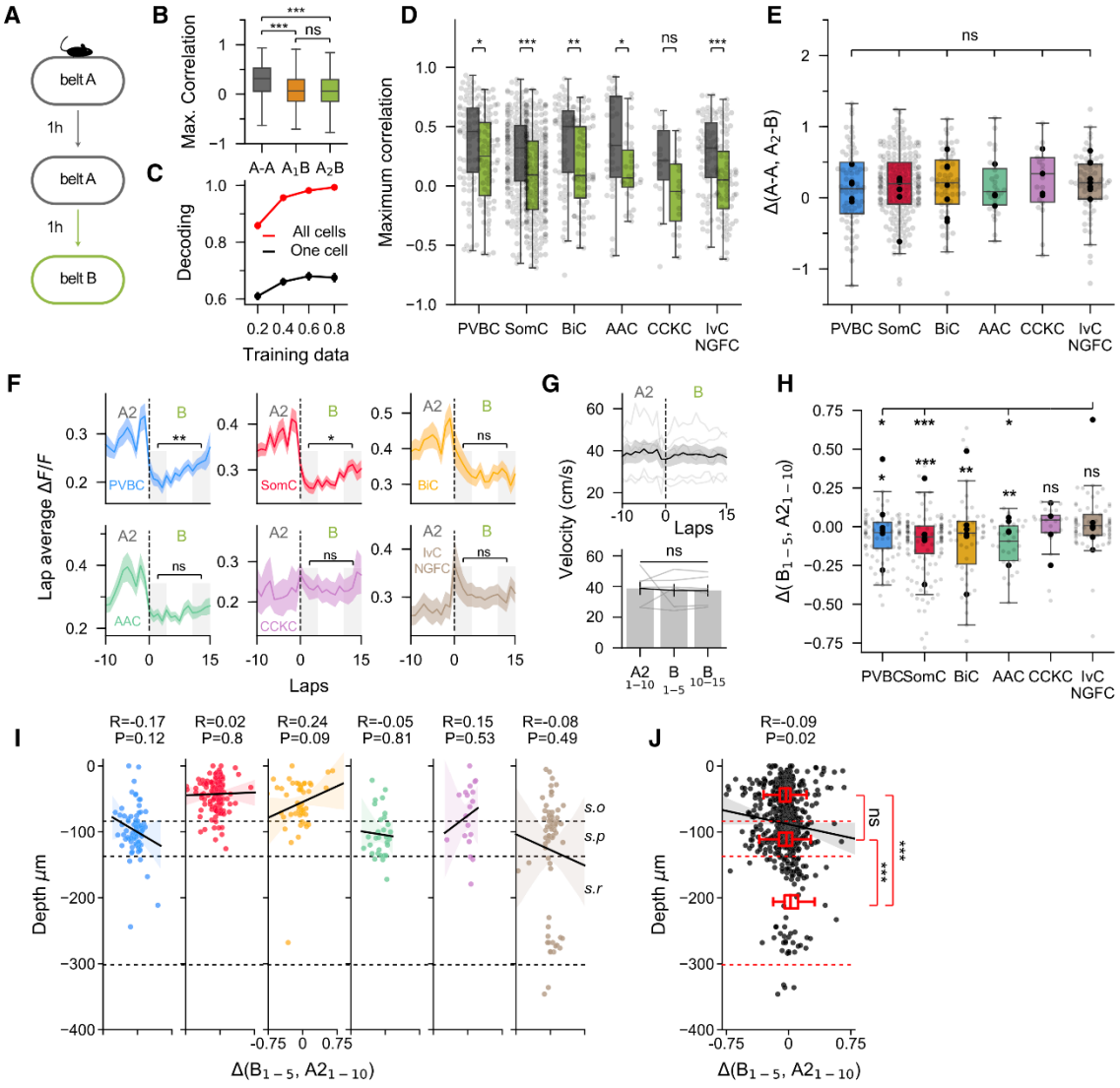

Figure 5: Interneurons encode contextual information at the population level and rapidly modulate their activity in novel contexts

A. Mice ran in a familiar context (belt 'A') twice and were then exposed to a new context (belt 'B').

B. Tuning curve correlation coefficients between contexts 'A' and 'B' (n = 1080 cells from 6 mice, one-way ANOVA, $p < 10^{-10}$).

C. Context identity can be reliably decoded using a SVM classifier (n = 6 mice).

D. Correlations between A_1-A_2 (gray) and between A_2-B (green) for the different subtypes (n = 74 PVBC, 216 SomC, 64 BiC, 29 AAC, 19 CCKC, 73 IvC/NGFC from n = 6 mice, paired t-tests).

E. Difference (delta) between A_1-A_2 and A_2-B correlation coefficients (same n as *K*, one-way ANOVA, p = 0.96).

F. Average Δ*F/F* during running on each lap during the last 10 laps of A_2 and the first 15 laps of B. In belt B, paired t-tests between the first 5 and last 5 laps (same n as *K*).

G. *Top*: Velocity profiles during change of belt for n = 6 mice. *Bottom:* Average velocity quantification in last 10 laps of A_2, first 5 laps in B and last 5 laps in B (one-way ANOVA, p = 0.96).

H. Difference (delta) in Δ*F/F* between the last 10 laps in A_2 and the first 5 laps in B (one-way ANOVA, p < 0.001 between groups). The decrease seen in belt B was also assessed by testing delta to a mean of 0 (one-sample t-test, P-value above each bar).

I. Depth distribution as a function of the change in activity (delta) for each subtype. Shaded areas represent bootstrapped confidence intervals.

J. Depth distribution as a function of delta for all interneurons (n = 660 cells), regardless of subtype identity. Interneurons in *s.r*. are less affected by the change of context (unpaired t-tests).

ANOVA tests are corrected for multiple testing using *post hoc* Tukey's range test. Mouse averages are indicated by the black dots. Data are represented as mean ± sem. *p<0.05, **p<0.01, ***p<0.001.

Reward modulation of IN activity during goal-oriented spatial learning

CA1 place cell maps undergo prominent reorganization toward rewarded locations in goal-directed learning tasks (Hollup *et al.,* 2001; Dupret, O'Neill and Csicsvari, 2013; Zaremba *et al.,* 2017; Kaufman, Geiller and Losonczy, 2020). To investigate if CA1 IN activity is modulated over the course of spatial reward learning, we trained mice in a goal-oriented spatial learning task, in which water-restricted mice run on a cue-rich treadmill belt for a water reward delivered at a fixed location on each lap (Figure 6A). When mice learned the task, they displayed selective, anticipatory licking preceding the reward zone, and their velocity decreased within the same location (Figure 6B). We thus compared the average activity profiles for the various subtypes at different locations along the treadmill (Figure 6C). We observed a selective increase in SomC and BiC activity in the area immediately preceding the reward zone, while the activity of the other subtypes decreased in this region, as did the animal's velocity (Figure 6C). We quantified this increased activity by defining a reward modulation index (RMI), a measure of the activity in the area immediately preceding the reward zone compared to the activity throughout the rest of the treadmill (Figure 6D). On average, SomC and BiC had significantly higher RMI values than the other subtypes, reflecting a preferential reward-related modulation (Figure 6D). More specifically, most subtypes displayed negative RMI values, representing decreased activity in the pre-reward area compared to the rest of the treadmill, consistent with the animal's lower velocity in the pre-reward area (Figure 6D). However, SomC and BiC displayed RMI values near 0, suggesting the contribution of a specific reward-related modulation to their activity. To more formally disambiguate the effects of velocity and position on interneuron activity during the GOL task, we created a multivariate regression model (Figure S7). This analysis revealed positive weights for the position variable immediately preceding the reward zone for SomC and BiC subtypes, but not

other subtypes, confirming their preferential recruitment. To analyze how IN dynamics are reconfigured when the reward location is changed, we then focused on the sessions after translocation of the reward zone. Within these sessions, mice learned to lick in the new reward location, but often also displayed residual licking around the old reward zone (Figure 6E). This residual licking in the old reward zone was accompanied by increased SomC and BiC activity in this area (Figure 6F). To quantify this effect, we directly compared the activity change around the old reward zone and observed a significant increase from chance level only in SomC and BiC (Figure 6G, S7). To show that this increase was the remnant representation of the old reward zone, we split the recording session in half and observed that SomC and BiC activity levels gradually decreased and increased in the old and current reward zones, respectively (Figure 6H). Other IN subtypes did not show such reorganization (Figure S7). Taken together these results demonstrate prominent reward modulation of SOM-immunopositive IN activity during goal-directed spatial learning.

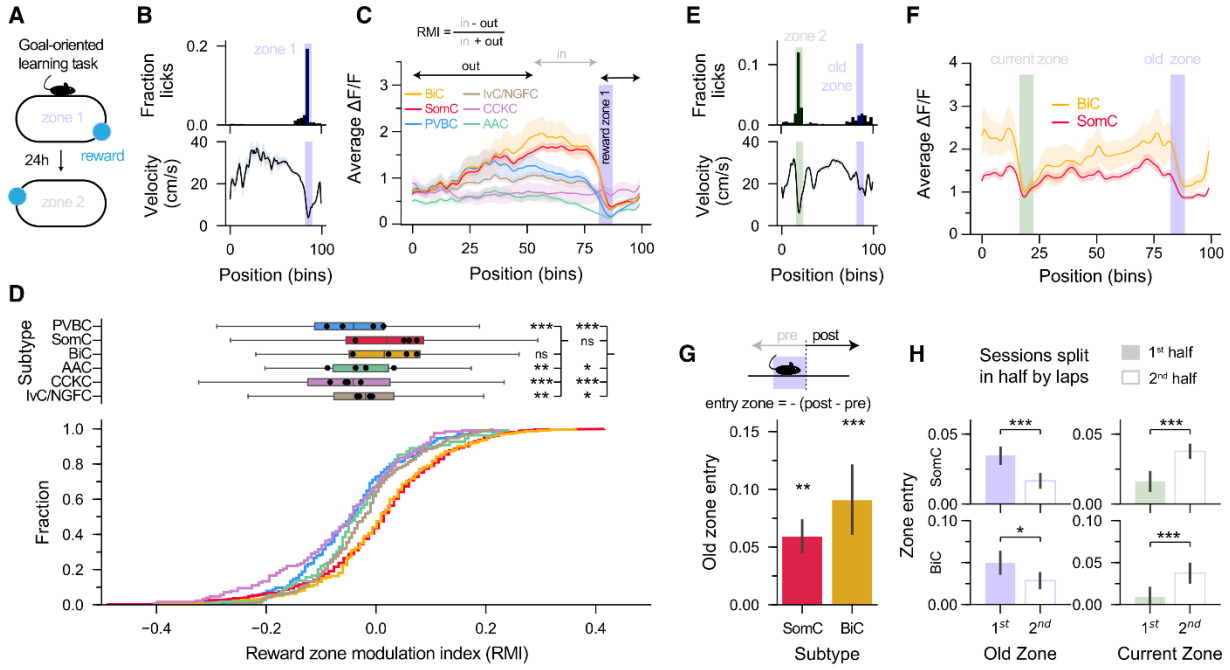

Figure 6: SomC and BiC subtypes are preferentially modulated by reward during goal-oriented learning

A. Mice ran to find a 'hidden' water reward, kept in a fixed location throughout the session, but changed each day (*zone1* to *zone 2*).

B. *Top:* Representative histogram of licks in each position bin from one session. Blue shaded area represents the rewarded zone. *Bottom:* Corresponding velocity profile.

C. Representative average $\Delta F/F$ in each position bin for each subtype. BiC and SomC show increased activity preceding the reward zone.

D. Reward zone modulation index cumulative fraction (*bottom*) and box plots (*top*). BiC and SomC have higher modulations than other subtypes (n = 165 PVBC, 830 SomC, 220 BiC, 109 AAC, 127 CCKC, 228 IvC/NGFC from n = 4 mice, one-way ANOVA, $p < 10^{-10}$).

E. *Top:* Representative histogram of licks and (*bottom*) velocity profile after translocation of the reward zone.

F. Representative BiC and SomC average activity by position bin from one session, showing traces of the old zone location.

G. Quantification of the old zone entry shows significantly higher modulation than expected by chance (n = 314 SomC, 103 BiC from n = 4 mice, one-sample t-test).

H. Quantification of old zone modulation and comparison between the first half and second half of the session. The modulation in the old zone for both BiC and SomC decreases with time while the modulation in the current reward zone increases, showing that BiC and SomC have remnants of the old reward representation (Same n as in *G*, paired t-tests).

ANOVA tests are corrected for multiple testing using *post hoc* Tukey's range test. Mouse averages are indicated by the black dots. Data are represented as mean ± sem. *p<0.05, **p<0.01, ***p<0.001.

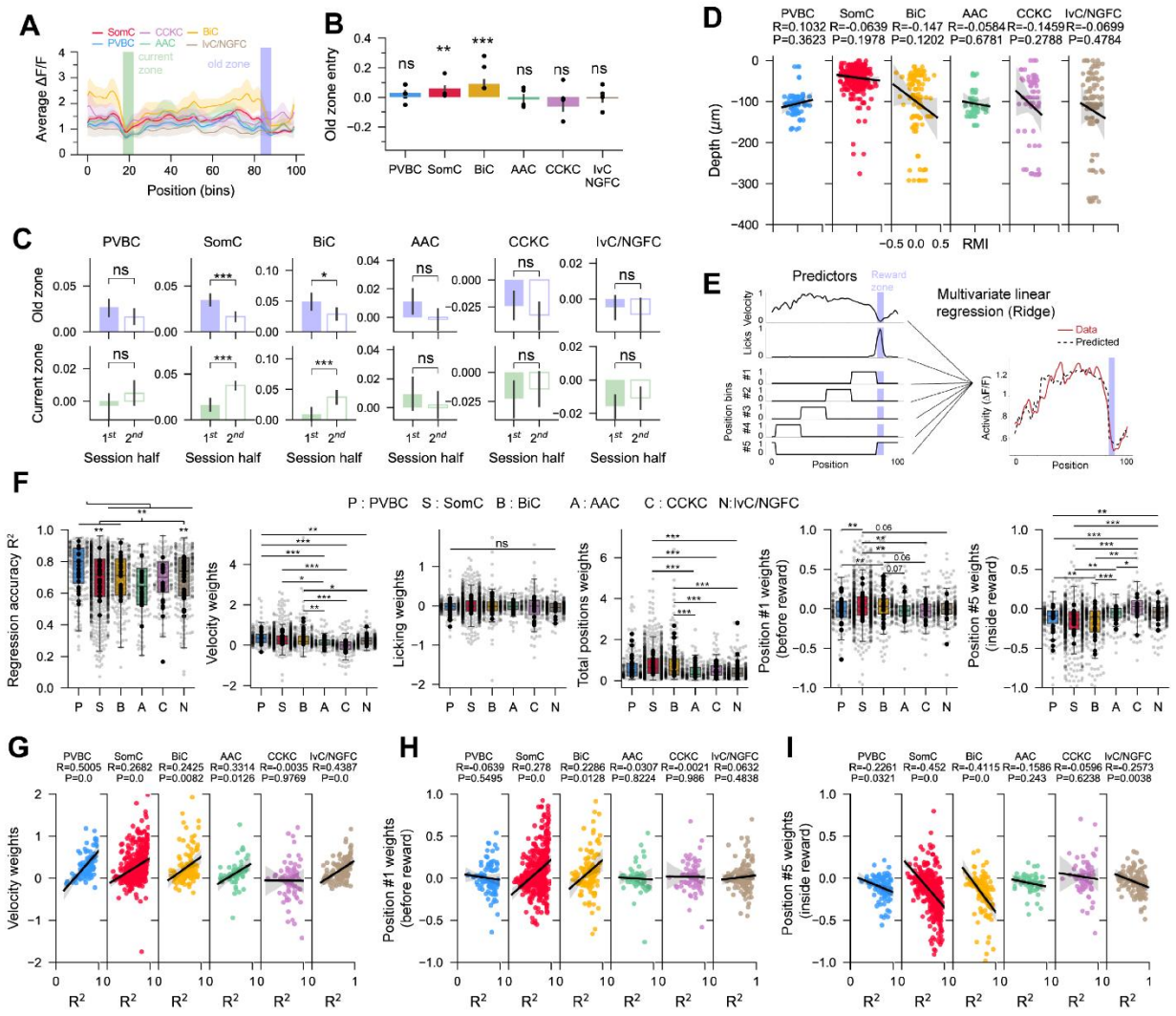

Figure S7 - Traces of old reward zone representation in the goal-oriented learning task and multivariate regression model (related to Figure 6)

A. Representative average tuning curve for each subtype. BiCs and SomCs show increased activity preceding the old reward zone (blue shaded area).

B. Quantification of the old zone (PVBC: 0.03 ± 0.02, SomC: 0.05 ± 0.01, BiC: 0.09 ± 0.03, AAC: -0.02 ± 0.03, CCKC: -0.06 ± 0.03, lvC/NGFC: -0.01 ± 0.02, mean ± SEM) entry shows significantly higher modulation than expected by chance (one-sample t-test). N = 60 PVBC , 314 SomC , 103 BiC, 42 AAC, 38 CCKC, 78 lvC/NGFC from 4 mice.

C. Quantification of old zone modulation and comparison between the first half and second half of the session. The modulation in the old zone for both BiC and Some decreases with time while the modulation in the current reward zone increases, showing that BiC and Some have remnants of the old reward representation. Values for Old zone (average first zone and second zone± SEM, p-value for paired t-test); PVBC: 0.027 and 0.016 ± 0.009, p = 0.14; SomC: 0.035 and 0.017 ± 0.006, p = O; BiC: 0.05 and 0.028 ± 0.013, p = 0.041 ; AAC: 0.011 and -0.001 ± 0.009, p = 0.08 , CCKC: -0.024 and -0.033 ± 0.013, p = 0.52; lvC /NGFC: -0.005 and -0.009 ± 0.007, p = 0.63). Values for Current zone (average first zone and second zone± SEM, p-value for paired t-test); PVBC: -0.003 and 0.005 ± 0.007, p = 0.13; SomC: 0.016 and 0.038 ± 0.007, p = O; BiC : 0.009 and 0.037 ± 0.01, p = O; AAC: 0.009 and 0.002 ± 0.011, p = 0.98 ; CCKC: -0.022 and -0.014 ± 0.015, p = 0.46; lvC/NGFC: -0.016 and 0.011 ± 0.007, p = 0.35).

D. Depth distribution as a function of the Reward Modulation Index (see Figure 6) for the different subtypes.

E. Schematic of the multivariate linear Ridge regression to disentangle the effects of various behavioral variables on interneuron activity. We used 7 variables: the velocity, licking, and positions (binned into 5 segments) to fit to the calcium signal.

F. Results of the regression. PVBC and AAC were respectively the best and the least well fitted subtypes (highest and lowest R^2). The coefficient (weight) for velocity predictor was higher for PVBC, SomC and BiC, meaning that velocity has a higher impact on the regression of the calcium signal, consistent with results in Figure 2. Licking had a low contribution, consistent across all subtypes. The total position weights (sum of all 5 segments) was higher for SomC and BiC. As expected, the segment before the reward zone has a stronger weight for SomC and BiC, while the segment inside the reward zone was increased in CCKC, lvC and decreased in PVBC, Some and BiC (strong negative weights in those 3 subtypes).

G. Correlation between the velocity weights and R^2, confirming that neurons more modulated by speed were more accurately fitted. CCKC did not show such trend, confirming that velocity has no impact on the calcium signal of these cells.

H. Correlation between the weights of position segment #1 and R^2. For SomC and BiC, the increased calcium activity before the reward zone was captured by this segment, which explains that the fit was more accurate in a subset of these neurons. Such correlation is absent in all other subtypes because they do not present such increase (see Figure 6).

I. Inversely, for the position segment inside the reward zone, strong negative weights meant better fit for most subtypes.

*p<0.05, **p<0.01, ***p<0.001.

Disinhibitory circuit dynamics and interactions in CA1

The experiments described above focus on INs directly targeting CA1PCs. These INs are themselves under inhibitory control from distinct types of interneuron-specific INs (ISIs) which

can further be divided into 3 subtypes (Type I, II and III ISI) (Acsády, Arabadzisz and Freund, 1996; Acsády, Görcs and Freund, 1996; Gulyás, Hájos and Freund, 1996; Freund and Buzsaki, 1996; Pelkey *et al.*, 2017). However, little is known regarding the *in vivo* functional properties of ISIs and how their dynamics relate to those of CA1PC-targeting INs. Given that the molecular diversity of ISIs and their postsynaptic IN targets together exceeds the multiplexing capacity of *post hoc* immunohistochemistry, in a next series of experiments we sought to use a two-step strategy to address these outstanding questions. In a first cohort of *VGAT-Cre* mice, we performed *post hoc* immunostaining for vasoactive intestinal polypeptide (VIP) and calretinin (CR) to identify ISI subtypes in addition to PV, SOM and NPY to identify the major postulated targets of ISIs (Chamberland and Topolnik, 2012; Donato et al., 2013; Luo et al., 2020; Pi et al., 2013; Tyan et al., 2014) (Figure S1, 7A, 7B). To characterize ISIs and VIP-expressing populations with greater molecular resolution and at a larger scale, in a second cohort we performed 3D chessboard scanning in *VIP-Cre* mice (Turi et al., 2019) which allowed us to identify additional VIP-expressing classes: VIP+/CCK+ basket cells and a previously described IN subtype with long-range projection targets, expressing VIP and muscarinic acetylcholine receptor 2 (M2R) (Francavilla et al., 2018) (Figure 7A, 7B). We observed that all ISI subtypes were positively correlated with velocity, with the strongest and most uniform modulation from Type II ISIs (Figure 7C). Interestingly, VIP+/CCK+ INs all exhibited negative velocity correlations and were more active during immobility. These results strongly suggest that the functional dichotomy we observe within CCKC (Figure 2C, S1) reflects differences between perisomatic-targeting CCK+ basket cells and dendrite-targeting CCK+ IN subtypes (Cope *et al.*, 2002; Booker and Vida, 2018). We also found that all VIP+/M2R+ cells were activated during immobility (Figure 7C), in accordance with previous work (Francavilla et al., 2018). Interestingly, we observed further major differences

between these two immobility-active VIP+ subpopulations (Figure 7D): VIP+/CCK+ cells transiently responded to run-stop events but their activity subsequently decreased rapidly, while VIP+/M2R+ cell activity remained elevated throughout the duration of the immobility epoch without decay (Figure 7D). This distinction could represent differences in immobility-related inputs between the two subtypes. Finally, Type III ISIs exhibited different response profiles than all other INs, with pyramidal cell-like, phasic bursts of calcium transients (Figure 7E). We next investigated potential interactions between ISI subtypes and other INs in *VGAT-Cre* mice, where we could additionally image and identify PV+ cells, SomC and BiC. We found that the activity dynamics of VIP+/CR- cells and Type III ISIs, but not Type I ISIs, were significantly less correlated with SomC and BiC than with perisomatic-targeting PV+ INs (PVBCs and AACs) (Figure 7H, 7I), suggesting preferential functional connectivity between IN subtypes in CA1 disinhibitory circuits. Together these results demonstrate major differences in the functional dynamics of ISI and VIP-expressing subtypes and in their interactions with downstream IN targets.

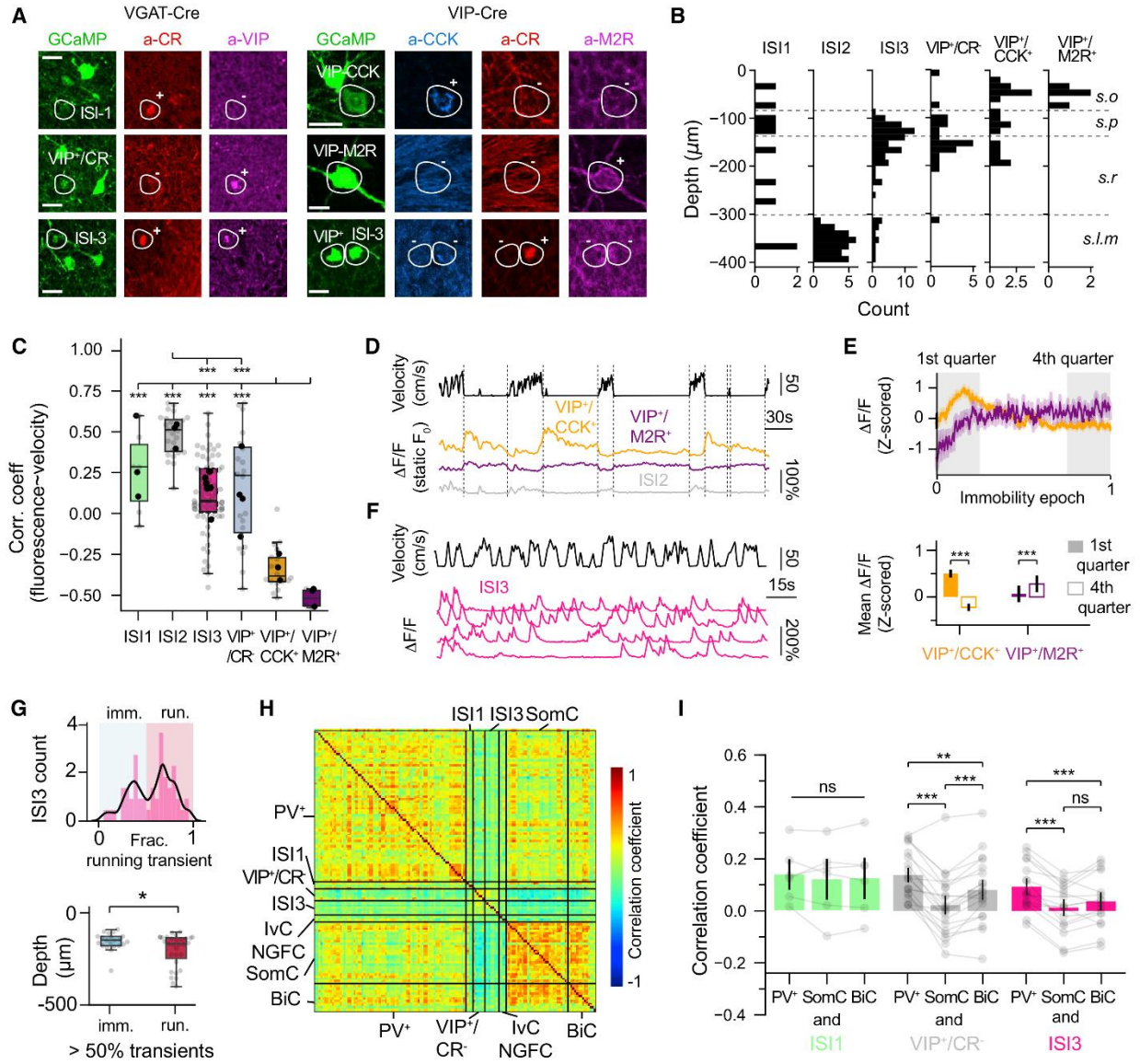

Figure 7: ISIs and VIP+ subpopulations display heterogeneous functional properties and preferential functional connectivity with subtypes of pyramidal cell-targeting interneurons

A. Immunohistochemistry in *VGAT-Cre* and *VIP-Cre* mice. Slices from *VGAT-Cre* animals (n = 4 mice) were immunostained for PV, SOM, NPY, VIP and CR. Slices from *VIP-Cre* animals (n = 3 mice) were immunostained for CCK, CR, M2R. Scale bars: 15 µm.

B. Depth distributions of all ISI subtypes, VIP^+/CR^-, VIP^+/CCK^+ and $VIP^+/M2R^+$ neurons detected in all mice (n = 7, *VGAT-Cre* and *VIP-Cre* pooled).

C. Correlation coefficients between activity and velocity (one-way ANOVA, $p < 0.001$ with n = 6 ISI1, 27 ISI2, 69 ISI3, 20 VIP^+/CR^-, 18 VIP^+/CCK^+ and 4 $VIP^+/M2R^+$ from 4 *VGAT-Cre* and 3 *VIP-Cre* mice).

D. Representative mouse velocity and $\Delta F/F$ traces for 3 simultaneously recorded VIP^+/CCK^+, $VIP^+/M2R^+$ and ISI2 cells. The activity was corrected using a static baseline to show the sustained or decreased activity during immobility.

E. *Top:* Average VIP^+/CCK^+ and $VIP^+/M2R^+$ response profiles (orange and purple, respectively) for all time-normalized immobility epochs across all cells. *Bottom:* Quantification of the difference in activity between the first and last quarter of each time-normalized immobility epoch. VIP^+/CCK^+ slowly decrease their activity while $VIP^+/M2R^+$ have a ramping and sustained activity during immobility (n = 18 VIP^+/CCK^+ cells, n = 4 $VIP^+/M2R^+$ cells from 3 mice, paired t-tests).

F. Representative $\Delta F/F$ traces for 4 simultaneously recorded ISI3 cells. Unlike other interneuron fluorescence traces, ISI3 cells show calcium transients underlying a potential phasic firing mode such as bursts of action potentials.

G. *Top:* Distribution of the ISI3 cells as a function of their number of detected transients occurring during locomotion. The distribution is bimodal with cells firing the majority of their transients either during immobility (blue, *imm.*) or locomotion (red, *loc.*). *Bottom:* Comparison of depth profiles for immobility and locomotion-specific groups (unpaired t-test).

H. Representative correlation matrix between all simultaneously recorded interneurons in one imaging session. The PV^+ group includes both PVBC and AAC subtypes as we did not perform SATB1 immunostaining in these mice.

I. Average correlation coefficients for all ISI subtypes with PV^+, SomC, or BiC neurons (n = 6 ISI1, 20 VIP^+/CR^- and 16 ISI3 from 4 mice, paired t-tests).

ANOVA tests are corrected for multiple testing using *post hoc* Tukey's range test. Mouse averages are indicated by the black dots. Data are represented as mean ± sem. *p<0.05, **p<0.01, ***p<0.001.

2.3 Discussion

In this work, we combine cellular-resolution, fast, targeted 3D calcium imaging and *post hoc* immunolabeling to record simultaneously from populations of molecularly defined subtypes of INs in hippocampal area CA1 during spatial navigation, goal-oriented learning, contextual manipulations, and SWR events during quiet wakefulness. Our results support the fidelity of this approach, as they are largely in agreement with previous findings on CA1 interneuron recruitment in cases where similar data is available. Our results also extend previous studies by separating broad molecular class of PV-expressing and SOM-expressing INs and by providing subtype-specific information or sufficient sample sizes in cases where similar data is available but lacks this information. Finally, our results provide the first population-level description of *in vivo* response profiles and feature selectivity of some major IN subpopulations implicated in regulating CA1PC input-output transformation, such as CCK-expressing or NPY-expressing cells (Fuentealba et al., 2008; Katona and Freund, 2012; Klausberger, 2009; Milstein et al., 2015; Tricoire et al., 2010). Overall, while our results provide some examples of preferential subtype recruitment during behavior, they also suggest significant similarities in the activation patterns of many subtypes, which argues in favor of a previously underestimated functional homogeneity of INs.

In summary, the group of SOM-expressing, dendrite-targeting INs, which includes OLM (McBain et al., 1994; Sik et al., 1995) and bistratified cells (Buhl et al., 1996, 1994), are strongly modulated by locomotion, spatial learning, and are themselves under strong disinhibitory control. These results suggest a close, bi-directional interaction of these INs with active CA1PC ensembles during exploration and a major role for these INs in regulating experience and learning-related reorganization of CA1PC dynamics through flexible regulation of synaptic integration and plasticity in CA1PC dendrites (Lovett-Barron et al., 2014, 2012; Royer et al., 2012). The second group of NPY-expressing and SOM-immunonegative, dendrite-targeting INs, which includes Ivy and neurogliaform cells (Fuentealba et al., 2008; Lapray et al., 2012; Milstein et al., 2015; Overstreet-Wadiche and McBain, 2015; Tricoire et al., 2010), shows overall weaker modulation by locomotion and spatial signals as well as less novelty-induced decrease in their activity following a change of context. The third group of perisomatic targeting PV+ INs, which comprises basket and axo-axonic cells (Buhl et al., 1994; Klausberger et al., 2003; Sik et al., 1995), is strongly modulated by locomotion signals, but exhibits less dynamic reward-related modulation and disinhibitory control, suggesting that these INs predominantly regulate behavioral state and network oscillation-related activity dynamics of the overall CA1PC population (Bartos et al., 2007; Cobb et al., 1995; Hu et al., 2014). Finally, vis-à-vis these exploration- and locomotion-coupled inhibitory subcircuits, perisomatic targeting CCK-expressing INs seem to primarily regulate immobility-related activity of CA1PCs without carrying significant spatial or contextual information. While immobility-related activity is present across all IN subtypes, CCK-VIP basket cells appear to be a major component of an inhibitory subnetwork within CA1 that controls PC excitability primarily during immobility. This unique behavioral function of perisomatic-targeting CCK-expressing INs could be further aided by long-lasting, asynchronous, and retrograde

endocannabinoid signaling-regulated GABA release from their axon terminals (Daw et al., 2009; Hefft and Jonas, 2005; Lee et al., 2010). It remains to be determined how subtype-specific differences in excitatory and inhibitory input convergence and integration onto IN types (Chiovini et al., 2014; Gulyás et al., 1999; Lovett-Barron et al., 2012; Luo et al., 2020; Martina et al., 2000; Matyas et al., 2004; Milstein et al., 2015) as well as cell type-specific differences in neuromodulatory regulation (Freund and Katona, 2007; Varga et al., 2009; Wester and McBain, 2014) specifically contribute to the emergence of distinct *in vivo* response profiles and tuning specificity.

Our results provide a population-level landscape of SWR-related modulation across IN subtypes, by large consistent with previous *in vivo* electrophysiological studies (Katona et al., 2014; Klausberger et al., 2005, 2004, 2003; Lapray et al., 2012; Varga et al., 2012). Our large-scale imaging approach also reveals considerable within-subtype heterogeneity during SWRs, as suggested by a growing body of studies. For instance, AAC have traditionally been considered to be silenced during SWRs (Klausberger et al., 2003; Viney et al., 2013), although very few cells have been recorded in awake rodents. Our observations are in agreement with a recent study reporting heterogeneous dynamics of AAC during SWRs (Varga et al., 2014). However, this study reported a segregation of AAC activity during SWRs based on axial location that we did not observe in our data: within the AAC subtype, modulated and unmodulated INs were present in both *stratum oriens* and *stratum pyramidale*. Finally, while BiC have been previously described as an IN subtype activated during SWRs (Katona et al., 2014; Klausberger et al., 2004), we report here a bimodal distribution of responses. It is possible that further heterogeneity might exist even within canonical inhibitory cell-types, such as axo-axonic cells, related to differential postsynaptic targets (Taniguchi et al., 2013).

Our findings also provide further insights into *in vivo* activity dynamics of disinhibitory circuits. They are consistent with an interpretation that VIP+ ISIs, and in particular Type III ISIs, exert disinhibitory influence on CA1PCs preferentially through SOM-expressing dendrite targeting INs and less so *via* PV-expressing perisomatic-targeting INs. This confirms previous anatomical and *in vitro* electrophysiological results showing that Type III ISIs preferentially innervate and inhibit SOM-expressing OLM cells (Chamberland and Topolnik, 2012; Tyan et al., 2014), similar to neocortical disinhibitory local circuit motifs (Lee et al., 2013; Pfeffer et al., 2013; Pi et al., 2013). We also observe prominent differences in locomotion modulation in CCK-VIP INs and Type II ISIs. While the origin of locomotion and immobility signals remain unclear, the presence of strong and specific anatomical contacts from ISI2s onto CCK-VIP INs suggest that the striking immobility-related activation we observe in CCK-VIP basket cells could result from this inhibitory interaction (Acsády et al., 1996a, 1996b).

The strategy employed here represents a major advance in our ability to record the activity of multiple molecularly-defined populations during behavior, but there are challenges and limitations associated with both calcium imaging in GABAergic cells and *post hoc* cell-type identification. While AOD-based 2p calcium imaging allows for recording of neural dynamics and longitudinal tracking of the same cells in 3D with high signal-to-noise and speed, calcium imaging is not ideal for measuring neural activity from fast-spiking populations, as modulations in constantly high firing rates lead to relatively small changes in collected fluorescence. Conversely, it is not known whether single spikes from low firing-rate GABAergic interneurons would be visible in calcium fluorescence traces *in vivo*, as no simultaneous recordings have been performed in such subtypes, to the best of our knowledge. Thus, heterogeneities in IN recruitment observed with calcium imaging may be due to inherent heterogeneities in the spike-to-calcium relationship

for the different subtypes. In addition, as with all imaging approaches in scattering tissues, the ability to collect dynamic signals at cellular resolution degrades with imaging depth, introducing a potential bias for IN subtypes located more superficially in the hippocampus. For this reason, populations of CCKC and IvC/NGFC located below the pyramidal cell layer may have been less sampled than the other subtypes. In the future, the development of photostable, genetically-encoded voltage indicators compatible with 2p population imaging might enable more detailed measurements of IN activity (Lee et al., 2017; Lin and Schnitzer, 2016). Similarly, retrospective, multiplexed immunohistochemistry is a robust approach for identifying proteins within cells while preserving their relative spatial arrangement, allowing for the *post hoc* registration that we performed here. However, antibody-based probes are inherently constrained in their multiplexing capability and cannot be routinely removed from tissue sections. The development of *in situ* hybridization and high throughput transcriptomics (Cembrowski et al., 2016; Harris et al., 2018; Yao et al., 2020), preserving spatial information in thick tissue sections (Chen et al., 2015; Wang et al., 2018), could circumvent these issues and enable quantitative molecular profiling of imaged cells. Finally, the improvement of automated classification approaches based on machine learning algorithms that incorporate various behavioral and neural response features could achieve high decoding accuracy scores and enable immunolabeling-free identification of various subtypes. These comprehensive characterization efforts should be coupled with cell-type-specific manipulations to directly test for general organizational principles related to segregated behavioral functions of inhibitory circuits.

2.4 Author Contributions

T.G., B.V. and A.L. conceived the study and wrote the manuscript. T.G. and B.V. performed experiments with help from S.T and analyzed the data. P.P. and P.T. conceived the machine-learning analysis, E.T., S.C. and G.T. developed and implemented the machine-learning algorithms for subtype classification. B.R. and K.O. conceived the fast 3D AOD microscope and the corresponding software modules.

2.5 Acknowledgements

A.L. is supported by NIMH-1R01MH100631, NINDS-1U19NS104590, NINDS-1R01NS094668, and the Kavli Foundation. P.P. is supported by the European Commission, FET Open Grant (NEUREKA, 863245), the Fondation Santé, and the Alexander von Humboldt Foundation. B.V. is supported by grant T32 GM007367. E.T. is supported by the program 'Strengthening Human Resources Research Potential via Doctorate Research' (MIS-5000432), implemented by the State Scholarships Foundation (IKY). B.R. is supported by ERC 682426, KFI-2018-00097, VKE-2018-00032, NUMBER 871277 — AMPLITUDE.

2.6 Declaration of Interests

The authors declare no competing interests.

2.7 Methods:

Resource availability

Lead Contact:

Further information and requests for resources and reagents should be directed to and will be fulfilled by the Lead Contact, Attila Losonczy (al2856@columbia.edu).

Materials Availability

This study did not generate new unique reagents.

Data and Code Availability

The machine-learning approach and the dataset are available on GitHub at https://github.com/losonczylab/Geiller_Vancura_Neuron2020. All other codes generated during this study are available upon request.

Experimental model and subject details:

All experiments were conducted in accordance with NIH guidelines and with the approval of the Columbia University Institutional Animal Care and Use Committee. Experiments were performed with healthy, 3-5 month old, heterozygous adult male and female *VGAT-IRES-Cre* mice (Jackson Laboratory, Stock No: 016962, referred to as *VGAT-Cre* mice) and *VIP-IRES-Cre* mice (Jackson Laboratory, Stock No: 010908, referred to as *VIP-Cre* mice). Both strains were kept on a C57BL/6J background. Mice were kept in the vivarium on a 12-hour light/dark cycle and housed 3-5 mice in each cage. Experiments were performed during the light portion of the cycle.

Viruses:

Cre-dependent recombinant adeno-associated virus (rAAV) expressing GCaMP6f under the control of the *Synapsin* promoter (rAAV1-Syn-FLEX-GCaMP6f-WPRE-Sv40, Addgene #100833, titer: $1x10^{13}$ vg/mL, referred to as rAAV2/1:Syn(GCaMP6f)^{Cre}) was used to express GCaMP6f either in VGAT+ interneurons (*VGAT-Cre* mice) or in VIP+ interneurons (*VIP-Cre* mice). Because of the high specificity of the *VIP-Cre* mouse line for labeling VIP-immunopositive cells in CA1 (see *Figure 1* in Turi et al., 2019), interneurons labeled in *VIP-Cre* mice with Cre-dependent AAV were considered VIP-immunopositive in the present study.

Virus injections and hippocampal window/headpost implant:

For viral injections, 2 to 4-month-old *VGAT-Cre* mice were anesthetized with isoflurane and placed into a stereotaxic apparatus. Meloxicam and bupivacaine were administered subcutaneously to minimize discomfort. After the skin was cut in the midline to expose the skull, the skull was leveled, and a craniotomy was made over the right hippocampus using a drill. A sterile glass capillary loaded with rAAV2/1:Syn(GCaMP6f)^{Cre} was attached to a Nanoject syringe (Drummond Scientific) and slowly lowered into the right hippocampus. Dorsal CA1 was targeted at coordinates AP -2.2, ML -1.75, DV -1.8, -1.6, -1,4, -1.2, -1.0, -0.8 relative to Bregma, with 50-64 nL of virus injected at each DV location. After injection, the pipette was left in place for 5-10 minutes and slowly retracted from the brain. The skin was closed with several sutures and the mice were allowed to recover for 4 days before the window/headpost implant.

The surgical procedure for CA1 window/headpost implant has been described previously (Lovett-Barron et al., 2014). Briefly, the injected mice were anesthetized with isoflurane and placed into the stereotaxic apparatus. After subcutaneous administration of meloxicam and bupivacaine, the skull was exposed, leveled, and a 3 mm craniotomy was made over the right hippocampus, centered on coordinates AP -2.2, ML -1.75 relative to Bregma. The dura overlying the cortex was removed, and the cortex overlying the hippocampus was slowly removed with negative pressure while ice-cold cortex buffer was simultaneously applied. This process was performed until the white, horizontal fibers overlying CA1 became visible and any bleeding subsided. A stainless steel, 3 mm circular cannula fitted with a glass window was inserted into the craniotomy and secured in place with Vetbond applied on the skull. Subsequently, dental cement was applied to the entire skull, and a headpost was affixed to the posterior skull with dental cement.

The mice received a 1.0 mL subcutaneous injection of PBS and recovered in their home cage while heat was applied. The mice were monitored for 3 days post-operatively until behavioral training began.

Behavioral training and paradigms:

After recovery from surgery, mice were handled for several days and habituated to head-fixation. Mice were subsequently water-restricted to 85-90% of their original weight and trained to run on a single-fabric, cue-free belt. Mice were trained to operantly lick and receive water rewards (water was delivered in response to tongue contact with a capacitive sensor) at random locations along the belt. As performance improved, the number of rewards delivered on each lap decreased. After several days of training on this cue-free belt, the mice were trained for ~1 week on a 2m long, cue-rich belt for randomly delivered water rewards. The belt consisted of three joined fabric ribbons and included some combination of the following tactile cues: colored pom poms, velcro, glue gun spikes, pink foam strips, and silver glitter masking tape (Danielson et al., 2016; Zaremba et al., 2017). For Random Foraging experiments, imaging was started after mice could run approximately 10 laps in 10 minutes (usually after 10-14 days of total training). For context remapping experiments, mice were subsequently imaged for one or two sessions on a novel belt decorated with a distinct set of tactile cues (Danielson et al., 2016; Zaremba et al., 2017). As the familiar belt, this novel belt was composed of three joined fabric ribbons and some combination of additional tactile cues. However, to maximize the novelty of the new belt, both the fabric ribbons and the tactile cues were different, and they were arranged in a unique order along the belt. For Goal-Oriented Learning (GOL) experiments, the mice were then trained for several days in the GOL paradigm, in which a single water reward was delivered at a fixed location each lap. Imaging

was started for GOL experiments after several days of training in this paradigm; the location of the reward was switched between each training session. For combined imaging and LFP experiments, data acquisition was started once GCaMP6f expression was optimal, hippocampal windows were clear, and the mice were habituated to head-fixation; these mice did not undergo additional behavioral training.

AOD-based two-photon calcium imaging:

Once behavioral training was complete, and 24 hours before functional imaging, mice underwent a single imaging session consisting of a high-resolution structural scan. This step was necessary to obtain a reference Z-stack and derive the X-Y-Z positions of GCaMP-expressing neurons. The mice were head-fixed under a custom-modified AOD microscope (Femto3D-ATLAS, Femtonics Ltd) and anesthetized with ketamine/xylazine to reduce motion artifacts during the stack. To provide stable transmission parameters during chronic imaging in the entire 3D scanning volume, the AOD microscope was extended with a high speed and precision beam stabilization unit which was directly attached to the AOD scan head, sensitive to input beam misalignment. The beam stabilization unit consisted of two quadrant detectors (PDQ80A and TPA101, Thorlabs) and two broadband dielectric mirrors (Thorlabs) mounted on motorized mirror mounts (Femtonics). The beam alignment was performed by the LaserControl software (Femtonics). A water-immersion objective (16x Nikon CFI75) was placed above the glass window and lowered until the CA1 pyramidal cell layer was in focus. At this stage, the objective was fixed in position and focus was subsequently adjusted using AO crystals (Szalay et al., 2016). The laser (Coherent Ultra II) was tuned to λ=920 nm, and the reference Z-stack was taken from the most dorsal position in *stratum oriens/alveus* (150-200 µm above the pyramidal cell layer) to the *stratum*

lacunosum-moleculare layer (~300 µm below the pyramidal cell layer) with 800x800 pixel images (X-Y resolution of 1.25 µm/pixel) every 4 µm. Laser power and photomultiplier (PMT) detectors (GaAsP, H10770PA-40 Hamamatsu) were compensated appropriately in Z throughout the stack (power at 20-40 mW and detector gain at 80% in *stratum oriens/alveus,* power at 120-150 mW and detector gain at 90% in *stratum lacunosum-moleculare*). After completion, the mice were returned to their home cage and allowed to recover for 24h until the start of functional imaging.

To determine X-Y-Z positions of GCaMP-expressing neurons, the Z-stack was scrolled through, and each visible interneuron was manually selected using the integrated software (MES, Femtonics Ltd) to generate a list of 200-300 X-Y-Z coordinates defined as the center of each cell. These points constituted the center of region of interests (ROI) used on subsequent days for functional imaging. Each ROI was defined as a square of 40 to 50 μm^2 (chessboard scan) (Szalay et al., 2016) with a resolution of 1 to 1.5 µm/px. The advantage of the chessboard scanning method is that only neurons and small areas around the pre-selected cells are recorded. Therefore, a high ratio of the total recording time (~20-50%) is spent reading out information from the selected neurons. In contrast, volumetric imaging with the same 2P excitation provides an orders-of-magnitude worse ratio for measurement time utilization as the somata of INs occupy a relatively small ratio of the total scanning volume.

On each day of functional imaging, the same field of view was found using the reference Z-stack and X-Y-Z coordinates were loaded into the software to perform 3D imaging. Once all cells were in focus, 10-15-minute functional imaging sessions were conducted at a frame rate of 3-5 Hz for most experiments (frame rate was dependent on ROI size and resolution). For experiments involving contralateral LFP recordings, imaging was conducted at a higher rate (40

Hz), which restricted imaging to only 30 cells simultaneously. During functional imaging, the laser power and detector gain were compensated based on the reference Z-stack parameters.

Silicon probe implantation, LFP recordings, and sharp-wave ripple identification:

For experiments requiring simultaneous two-photon calcium imaging and LFP recordings, mice were implanted with a glass window over the hippocampus as above, and additionally a chronic, 4-channel silicon probe (Qtrode, Neuronexus) was inserted into the contralateral CA1 at a 45-degree angle. The probe was secured in place with dental acrylic and the mouse was allowed to recover for several days, as above. LFP signals were recorded with a multichannel recording system (Intan Technologies) synchronized with the AOD imaging system. The correct position of the silicon probe was confirmed by the presence of sharp-waves ripples in the data. LFP signals were recorded at 20kHz. To identify putative sharp-wave ripple events, the raw LFP signal was band-pass filtered from 100-250 Hz and thresholded at 3 standard deviations above the mean value with a minimum duration of 50ms. All putative sharp-wave ripple events were then manually inspected to obtain the final set of sharp-wave ripple events used for analysis.

Perfusion and tissue processing:

After the completion of imaging experiments, mice were transcardially perfused with 40 mL of ice-cold Phosphate-Buffered Saline (PBS, Thermo Fisher), followed by 40 mL of ice-cold 4% paraformaldehyde (PFA, Electron Microscopy Sciences). Brains were stored overnight in 4% PFA at 4°C. The next day, the 4% PFA was removed and the brains were rinsed 3x5 min in PBS. 75 µm horizontal sections of the imaged hippocampus were cut on a vibrating microtome (Leica VT1200S) and washed 3x15 minutes in PBS. Subsequently, sections were permeabilized for 2x20 minutes in PBS with 0.3% Triton X-100 (Sigma-Aldrich). Blocking was then performed with 10%

Normal Donkey Serum (Jackson ImmunoResearch, Catalog #017-000-121) in PBST (PBS with 0.3% Triton X-100) for 45 minutes. The sections were then incubated in a PBS solution containing 3 primary antibodies (see below for antibody information and dilutions) for one hour at room temperature, followed by 2 days at 4°C. After 2 days, the primary antibody solution was removed from the slices and the slices were washed 3x15 minutes in PBS to remove unbound primary antibodies. The slices were subsequently incubated in a PBS solution containing a mixture of appropriate secondary antibodies conjugated to fluorescent labels (see below for antibody information and dilutions) for 2 hours at room temperature. The sections were then washed 5x15 minutes in PBS at room temperature. Finally, sections were mounted on glass slides in Fluoromount-G aqueous mounting medium (ThermoFisher Scientific) and coverslipped. The slides were allowed to dry at 4°C for at least one hour before confocal imaging (see below). After confocal imaging, the slides were submerged in PBS to remove the coverslip, and the sections were removed from the slides with gentle rocking. After washing 3x15 min in PBS and blocking with 10% Normal Donkey Serum in PBST for 45 minutes, the sections were incubated in an additional 2-3 primary antibodies. The sections were subsequently washed, incubated in secondary antibodies, washed again, and mounted and imaged, as in the first round of staining. We considered antibody combinations to be compatible for sequential imaging in the same fluorescence channel if they were against antigens known to be present only in non-overlapping interneuron populations in CA1 (see below for detailed strategies).

Immunohistochemistry (see **Key Resources Table** for catalog number)**:**

In V*GAT-Cre* mice, three strategies were used for staining.

Strategy 1. Mice ID: TG16, TG17, TG18, TG19, BV90, TG300, TG302, TG310 (see **Supplementary Figure S1A**)

First round primary antibodies: rabbit anti-proCCK (1:500), rat anti-somatostatin (1:500), and sheep anti-NPY (1:500)

First round secondary antibodies: donkey anti-rabbit DyLight 405 (1:300), donkey anti-rat Alexa 568 (1:300), and donkey anti-sheep $F(ab)_2$ Alexa 647 (1:300)

Second round primary antibodies: chicken anti-PV (1:5,000) and rabbit anti-SATB1 (1:1,000).

Second round secondary antibodies: donkey anti-chicken DyLight 405 (1:300) and donkey anti-rabbit Alexa 647 (1:300)

Strategy 2. Mice ID: TG325, TG326, TG327 (see **Supplementary Figure S1A**)

First round primary antibodies: chicken anti-PV (1:5,000), rat anti-somatostatin (1:500), and rabbit anti-SATB1 (1:1,000)

First round secondary antibodies: donkey anti-chicken DyLight 405 (1:300), donkey anti-rat Alexa 568 (1:300), and donkey anti-rabbit Alexa 647 (1:300)

Second round primary antibodies: rabbit anti-proCCK (1:500) and sheep anti-NPY (1:500)

Second round secondary antibodies: donkey anti-rabbit DyLight 405 (1:300) and donkey anti-sheep $F(ab)_2$ Alexa 647 (1:300)

Strategy 3. Mice ID: TG276, BV106, BV107, BV109 (see **Supplementary Figure S1B**).

First round primary antibodies: chicken anti-PV (1:5,000), rat anti-somatostatin (1:500), and rabbit anti-VIP (1:5,000)

First round secondary antibodies: donkey anti-chicken DyLight 405 (1:300), donkey anti-rat Alexa 568 (1:300), and donkey anti-rabbit Alexa 647 (1:300)

Second round primary antibodies: guinea pig anti-calretinin (1:1,000) and sheep anti-NPY (1:500)

Second round secondary antibodies: donkey anti-guinea pig Rhodamine Red X (1:200) and donkey anti-sheep $F(ab)_2$ Alexa 647 (1:300)

In *VIP-Cre* mice, immunohistochemistry labeling consisted of only one round.

Mice ID: TG338, TG339, TG340 (see **Supplementary Figure S1C**).

Primary antibodies: rabbit anti-proCCK (1:500), guinea pig anti-calretinin (1:1,000), and rat anti-M2R (1: 2,000)

Secondary antibodies: donkey anti-rabbit DyLight 405 (1:300), donkey anti-guinea pig Rhodamine Red X (1:200), and donkey anti-rat Alexa 647 (1:300)

Assignment of subtype identity based on immunostaining:

Axo-axonic cells (AAC):

AAC were immunopositive for PV, and immunonegative for SATB1, SOM, NPY, and CCK (Klausberger et al., 2003; Varga et al., 2014; Viney et al., 2013); they were thus differentiated from parvalbumin-expressing basket cells on the basis of SATB1 transcription factor immunonegativity. Although only 2 anatomically-verified AAC have been shown to be SATB1-immunonegative in CA1 (Varga et al., 2014; Viney et al., 2013), a larger number of identified AAC have been shown to have these molecular characteristics in CA3 (Viney et al., 2013). In addition, recent single-cell RNA sequencing studies have demonstrated the presence of a

significant cluster of PV-immunopositive SATB1-immunonegative cells within mouse CA1, suggesting that the molecular characteristics of CA3 AAC generalize to CA1 (Harris et al., 2018; Qian et al., 2020). To confirm undetectable SATB1 expression, every cell we considered to be an AAC was re-imaged under the confocal microscope at Nyquist resolution and inspected for any evidence of nuclear immunolabeling.

Parvalbumin-expressing basket cells (PVBC):

PVBC were immunopositive for PV and immunonegative for SOM, NPY, and CCK (Sik *et al.*, 1995; Freund and Buzsaki, 1996; Klausberger *et al.*, 2003; Lapray *et al.*, 2012; Viney *et al.*, 2013; Hu, Gan and Jonas, 2014; Pelkey *et al.*, 2017). These cells were also immunopositive for transcription factor SATB1 (Harris et al., 2018; Viney et al., 2013).

Bistratified cells (BiC):

The BiC category included all cells that were immunopositive for PV, SOM, and NPY (Katona et al., 2014; Klausberger et al., 2004; Losonczy et al., 2002; Maccaferri et al., 2000; Pawelzik et al., 2002). Although not used as a criteria, all PV, SOM, and NPY triple immunopositive cells with conclusive SATB1 immunoreactivity were also SATB1-immunopositive, in accordance with a previous study (Viney et al., 2013).

Somatostatin-expressing cells (SomC):

Cells in the SomC category were immunopositive for SOM and immunonegative for CCK and PV. Cells within this category include both OLM interneurons (Forro et al., 2015; Katona et al., 2014; Losonczy et al., 2002; Maccaferri and McBain, 1996) and long-range projecting SOM-

immunopositive cells (Jinno, 2009; Jinno et al., 2007; Katona et al., 2017). Although previous studies have shown that OLM cells can be weakly PV-immunopositive (Katona et al., 2014; Losonczy et al., 2002; Varga et al., 2012), PV levels are universally significantly lower in OLM cells than in PVBC, AAC, or BiC (Pelkey et al., 2017; Winterer et al., 2019). Thus, cells with barely detectable levels of PV immunoreactivity were considered PV-immunonegative. Although studies in rats have shown OLM cells to be immunonegative for NPY (Katona et al., 2014), a more recent study of anatomically identified OLM cells in mice has shown a significant fraction of them to be NPY-immunopositive (Winterer et al., 2019). In addition, some long-range projecting SOM-immunopositive cells have been shown to be NPY-immunopositive (Jinno et al., 2007). Thus, the presence or absence of NPY immunopositivity was not used as a criterion for this category, and this category includes both NPY-immunopositive and NPY-immunonegative cells. Although more than half of cells within this category were SATB1-immunopositive, SATB1 immunoreactivity was not used as a criteria for this category and it includes some SATB1-immunonegative cells.

Cholecystokinin-expressing cells (CCKC):

Cells in the CCKC category were immunopositive for pro-CCK, immunonegative for SOM, PV, and SATB1, and either positive or negative for NPY (Harris et al., 2018; Klausberger et al., 2005; Somogyi et al., 2004). This category includes both CCK-expressing basket cells and CCK-expressing dendrite-targeting cells (Bezaire and Soltesz, 2013; Cope et al., 2002; Klausberger et al., 2005; Pawelzik et al., 2002; Pelkey et al., 2017; Vida et al., 1998).

Ivy cells (IvC) and Neurogliaform cells (NGFC):

Cells in the IvC/NGFC category include both Ivy cells and neurogliaform cells (Armstrong et al., 2012; Capogna, 2011; Fuentealba et al., 2008; Harris et al., 2018; Lapray et al., 2012; Maccaferri, 2011; Overstreet-Wadiche and McBain, 2015; Pelkey et al., 2017; Price et al., 2008, 2005; Tricoire et al., 2010; Vida et al., 1998; Zsiros and Maccaferri, 2005), and these cells were always NPY-immunopositive and immunonegative for CCK, SOM, and PV, while they could be either immunopositive or immunonegative for SATB1. Although long-range projecting interneurons have recently been identified that share these molecular characteristics (Wick et al., 2019), the number of these cells is low compared to estimated numbers of Ivy cells and neurogliaform cells (Bezaire and Soltesz, 2013; Fuentealba et al., 2008). For this reason, we refer to this category as IvC/NGFC.

Type I interneuron-specific interneurons (ISI1):

ISI1 cells were identified as CR-immunopositive and VIP-immunonegative (Bezaire and Soltesz, 2013; Gulyás et al., 1996; Pelkey et al., 2017). These cells were identified in *VGAT-Cre* mice.

Type II interneuron-specific interneurons (ISI2):

ISI2 were always VIP-immunopositive and immunonegative for CCK, CR, M2R (Acsády et al., 1996a, 1996b). We also restricted our definition of ISI2 cells to those located in SR or the SR-SLM border (Acsády et al., 1996a, 1996b). Because we did not stain for CCK, VIP, and M2R simultaneously in *VGAT-Cre* mice (see **Immunohistochemistry** section above), cells matching those criteria could only be identified in *VIP-Cre* mice and are analyzed in **Figure 7**.

Type III interneuron-specific interneurons (ISI3):

ISI3 cells were classified on the basis of the co-expression of VIP and CR (Acsády et al., 1996a, 1996b; Luo et al., 2020; Pelkey et al., 2017; Tyan et al., 2014). All such cells were immunonegative for PV, SOM, and NPY. Cells matching these criteria could be identified in both *VGAT-Cre* and *VIP-Cre* mice.

VIP-immunopositive, CR-immunonegative cells (VIP+/CR-):

Cells within the VIP+/CR- category were immunopositive for VIP and immunonegative for CR, PV, SOM, and NPY. This category potentially includes ISI2 cells (Acsády et al., 1996a, 1996b), VIP+ basket cells (Acsády et al., 1996a, 1996b), or long-range projecting VIP+ interneurons (Francavilla et al., 2018). In *VGAT-Cre* mice, our staining strategies (see **Immunohistochemistry** section above) did not allow us to further separate these subpopulations, so we left them classified by their immunolabel, VIP+/CR-.

VIP-immunopositive, CCK-immunopositive cells (VIP+/CCK+):

VIP/CCK cells were CCK+, CR-, and M2R-. This population represents perisomatic-targeting basket cells (Acsády et al., 1996a, 1996b).

VIP-immunopositive, M2R-immunopositive cells (VIP+/M2R+):

VIP/M2R cells were immunonegative for CCK and CR, and immunopositive for M2R. These cells represent a long-range projecting VIP-expressing subtype (Francavilla et al., 2018).

Parvalbumin-immunopositive cells (PV+): in **Supplementary Figure 6** and **Figure 7H, 7I**.

In mice where staining strategy 3 was used (see **Immunohistochemistry** section above), cells that were PV-immunopositive, SOM-immunonegative, NPY-immunonegative, VIP-immunonegative, and CR-immunonegative were classified as PV+ cells. This category includes both PVBC and AAC, but we could not distinguish between these two populations as we did not stain for SATB1 (see **Supplementary Figure 1**).

Unidentified cells

All cells not assigned to one of the subtypes described above were classified as unidentified.

Confocal imaging: A Nikon A1 confocal microscope was used to acquire multi-channel fluorescence images of the immunolabeled tissue sections. 405 nm, 488 nm, 561 nm, and 640 nm laser lines were used for excitation. Each channel was acquired sequentially with a 10x Plan Apo NA 0.45 objective (Nikon) at 1.2-1.3x Zoom. 2048x 2048 pixel images were acquired every ~3 microns through the entire depth of the tissue sections, with the pinhole size set to ~1 Airy unit. Fluorescence was collected with 2 GaAsP PMTs (488 nm and 561 nm channels) and 2 multi-alkali PMTs (405 nm and 640 nm channels). The resulting 4-channel Z-stacks were viewed in FIJI.

Registration of confocal images to *in vivo* Z-stacks and identification of immunopositivity/negativity: The following steps were performed by an experimenter without the use of any automated methods: First, the confocal stacks were rotated and translated until the cells in the green channel (GCaMP-labeled) matched the cells seen in the in vivo Z stack. Second, each imaged cell was found in the confocal stacks, and it was evaluated for immunopositivity or immunonegativity for the tested molecule. For a cell to be considered positive, the fluorescence

intensity inside the cell had to be significantly greater than the background intensity level. A cell was considered positive for a given marker only if clear examples of immunonegative cells could be found on the same tissue section. Similarly, a cell was considered negative for a given marker only if clear examples of immunopositive cells could be found on the same tissue section. In the case of ambiguous immunolabeling, cells were discarded and not grouped into a subtype for further analysis. In experiments in which PV and SATB1 immunoreactivity were assessed together, all cells that were initially identified as axo-axonic cells (PV+, SATB1-) were imaged again under the confocal microscope at Nyquist resolution to confirm the absence of detectable SATB1 immunoreactivity. Overall, all efforts were made to use the most stringent criteria for cell classification prior to analysis.

Pre-processing of Ca^{2+} imaging data: The raw movies containing each cell were motion corrected independently using a whole-frame cross-correlation algorithm, as implemented in the SIMA software (Kaifosh et al., 2014). The time-average of each imaged cell was manually inspected and a ROI was hand-drawn over each cell. Fluorescence was extracted from each ROI using the FISSA software (Keemink et al., 2018) package to correct for neuropil contamination. For each resulting raw fluorescence trace, a baseline F was calculated by taking the 1st percentile in a rolling window of 30s and a $\Delta F/F$ trace was calculated. The $\Delta F/F$ trace for each cell was smoothed using an exponential filter and all further analysis was performed on the resulting $\Delta F/F$ traces. In **Figure 7D** and **7E**, a static baseline calculated as the 1st percentile of the whole trace was used instead of an adaptive baseline. This way, we could examine small fluctuations during immobility epochs that would otherwise be suppressed by an adaptive baseline. All further analysis was implemented in Python 2.7 and is detailed below.

Cross-correlation between each cell's GCaMP Ca^{2+} activity and velocity:

To calculate the correlation between each cell's activity and the animal's velocity, the Pearson's correlation coefficient was calculated between each cell's $\Delta F/F$ trace and the smoothed velocity trace by shifting each cell's fluorescence trace one frame at a time within a -5s (activity lagging velocity) to +5s (activity leading velocity) interval. The maximum of the absolute value of all correlation coefficients within this interval was taken as the correlation coefficient for the cell, and the shift at which it occurred was taken as the lag. As most cells were cross-registered across many imaging experiments, the correlation coefficients and lags for each cell were averaged across all sessions in which the cell was imaged.

Responses to run-start and run-stop events: Run-start and run-stop events were identified in the imaging data as frames during which the animal's velocity increased above 0.2 cm/s (run-start event) or decreased below 0.2 cm/s (run-stop event). In addition, each run-start/run-stop event had to be separated from the previous run-start/run-stop event by at least several seconds to be considered as a separate event. For each event, the mean of the pre-event $\Delta F/F$ was subtracted from the mean of the post-event $\Delta F/F$ in a -3s to +3s window to calculate a response magnitude. For each cell, the run-start and run-stop responses were averaged over all run-start and run-stop events in the given imaging experiment. If a cell was imaged across more than one imaging experiment, the average run-start and run-stop responses from each experiment were averaged over all experiments.

Spatial tuning curve: To calculate a spatial tuning curve for each imaged cell in a given experiment, the 2m treadmill was divided into 100 2cm-long bins. For each bin, we calculated

the average Δ*F/F* from frames where the animal was in locomotion (velocity > 5cm/s) and smoothed the resulting trace with a Gaussian kernel (σ = 3 bins) to obtain the spatial tuning curve

Spatial tuning analysis: To determine whether a cell was spatially tuned during an imaging session, we generated 1000 shuffled tuning curves by circularly rotating position in relation to Δ*F/F* tuning curves (restricted to frames during locomotion). A cell was detected spatially selective if it had 10 consecutive bins (20cm) exceeding the 95th percentile of the shuffle distribution (or lower than the 5th percentile for negative fields) and a peak firing in the field exceeding 100% Δ*F/F* (no threshold for negative fields). Recurrence probability was calculated as the number of times a cell was detected spatially modulated over the number of times it was imaged. Selectivity index was calculated as previously described (Acharya et al., 2016) by computing the spatial sparsity of the rate map given N bins with r_n the rate in the n^{th} bin as :

$$S = 1 - \frac{1}{N}\frac{(\Sigma r_n)^2}{\Sigma(r_n^2)}$$

Position decoding: We used a linear classifier (support vector machine, SVM) to decode the animal's position from interneuron / pyramidal cell population activity using the spatial tuning curves. For cross-validation, a spatial tuning curve was generated for each lap and we trained the classifier on (*n-1*) laps and then tested on the held-out lap. The testing lap was then rotated to cover all the *n* laps of the session.

Stability analysis: Stability analysis was performed by correlating (Pearson's R) the spatial tuning curves of the same cells at different time points. For the within-session comparison, each session

was first divided between odd and even laps, and stability was calculated as the correlation between the average tuning curve for each split.

Context remapping analysis: In the context remapping analysis, we correlated the tuning curves in two different belts (A_1, A_2 and B). To avoid aligning arbitrarily the two belts, we iteratively rotated the tuning curves in B to maximize the population's average correlation coefficient for each mouse independently, which resulted in reporting the highest possible values.

To analyze the change in activity upon exposure to a new belt, we averaged the $\Delta F/F$ values (restricted to frames during locomotion) in each lap and compared values from the 10 last laps of A_2 (just preceding the change of belt) to the 15 first laps of B.

Context decoding: We used a linear classifier (support vector machine, SVM) to decode the context identity based on interneuron population activity. For cross-validation, a spatial tuning curve was generated for each lap and we trained the classifier on blocks of *n* randomly-chosen laps in the session (20%, 40%, 60% and 80% of the laps used for training and the rest for testing). This training/testing procedure was repeated 100 times.

GOL analysis: We quantified the change in activity for each cell near the reward zone by defining a reward modulation index (RMI) to normalize activity amplitudes across different IN subtypes. RMI is defined as the difference of the average activity preceding the reward zone (10cm) and the average activity in the rest of the belt, divided by the sum of the two. To quantify the representation of the old reward zone by different subtypes without being affected by the activity in the current

zone, we calculated a reward zone entry value as the difference in activity between 10cm after the start of the old zone and 10cm before it (based on the spatial tuning curves).

Multivariate ridge regression: To more explicitly dissociate the effects of the various behavioral variables on each cell's activity during the GOL task, we developed a multivariate linear regression model to predict each cell's spatial tuning curve (the average ΔF/F value in each position bin) from the following behavioral variables: 1) the animal's velocity, 2) licking, and 3) position. The position variable was itself divided into 5 predictors, corresponding to 5 zones of the treadmill. The model utilized Ridge regression to minimize the effects of potential relationships between the independent variables. The fit values are reported in Supplementary Figure S7, as well as the coefficients for the predictors for each subtype, and the relationship between predictors and fit quality.

Ripple modulation probability: We used two measures of activity during sharp-wave ripple (SWR) events. The average response was defined as the averaged difference in activity in a 400ms window centered around each SWR onset. The first 200ms (left side of the window) serves as the baseline and the baseline is subtracted from the average value in the 200ms on the right side of the window. Here, the baseline is subtracted in case multiple ripples occur successively and that the GCaMP signal is on the descending phase, which could have potential confounds on the fluorescence values. Therefore, only 200ms is used to compute a modulation value and not the full 400ms. This analysis is similar to a PSTH, but it is not displayed as an average trace for each subtype. This is because the neurons belonging to a given subtype can have different response traces for each ripple event, largely dependent on the number of spikes fired. The traces do not

bring useful quantitative information, and so instead, we represented each cell by a single point, whereby the heterogeneity within each subtype can be better appreciated. It is also important to remember that the ripples detected contralaterally can have a small but consequent time jitter with the activity seen in the ipsilateral side, which may further degrade the ability to nicely visualize average responses. This analysis can be seen in **Supplementary Figure S4.**

In the second analysis (in **Figure 3**), we reasoned that limitations in calcium sensitivity, baseline levels and ripple amplitude can influence the response activity seen in different subtypes. To circumvent those limitations, we developed a measure of modulation to evaluate whether a cell had an increased activity during a SWR event statistically higher than its baseline fluctuation during immobility. To do so, we computed for each cell a shuffle distribution that consisted of 1000 values. Each value was the average of N randomly chosen $\Delta F/F$ points during immobility (N corresponds to the number of SWRs detected in the session). Then, for each SWR, if the difference in activity in a 400ms window centered around the onset was greater than the 95^{th} percentile of the shuffle distribution, the cell was modulated during this event. The modulation probability reports the percentage of SWRs leading to an increase above baseline.

Bayesian gaussian mixture model: To separate and cluster groups of cells in a given subtype that are modulated during SWR events, we used a Bayesian estimation of a Gaussian model where the number of groups is directly inferred from the data, removing any arbitrary threshold in modulation probability values. The prior for the weight distributions was taken from a finite mixture model, and the weights were initialized using k-means.

Type III ISI transient detection: Activity in Type III ISIs showed calcium transients akin to pyramidal cells. We detected the onset of each transient by finding peaks in the Z-score traces with a threshold of 0.3 sigma, and a minimum value of 15 frames (~2 seconds) for minimal horizontal distance, with smaller transients being discarded first until the condition is fulfilled.

Interneuron dynamics during immobility epochs: To compare the dynamics of VIP+/CCK+ and VIP+/M2R+ interneurons during immobility epochs, immobility intervals were first identified during each imaging session as periods when the velocity remained below 0.2 cm/s for at least 15-20 seconds. Immobility intervals within a given imaging experiment were normalized by upsampling each interval to the length of the longest interval. The baseline-corrected fluorescence ($\Delta F/F$, with static baseline F_0, see above) of each cell was divided into 1,000 bins within each normalized immobility interval and averaged over all immobility intervals within the imaging session to generate an average immobility response. If a given cell was imaged in more than one experiment, its immobility trace was averaged over all experiments in which it was imaged.

Interactions between different interneuron subtypes: To analyze the activity relationships between simultaneously recorded interneurons, the pairwise correlation coefficient (Pearson's R) was calculated between each pair of simultaneously imaged cells.

Machine learning analysis:

To assess whether the six IN subtypes described in Figures 1-6 can be discriminated based on their activity profiles during behavior and/or anatomical features, we employed a machine learning

approach. Specifically, we developed a Deep Neural Network (DNN) and tested its discrimination performance on various tasks:

- a 4-class problem consisting of PV-expressing, perisomatic-targeting INs (PVBCs and AACs), SOM-expressing, dendrite-targeting INs (SomCs and BiCs), CCK-expressing (CCKCs) and NPY-expressing INs (IvCs/NGFCs) (**Supplementary Figure S3**)
- a 6-class problem consisting of all IN subtypes identified in Figures 1-6 (PVBC, AAC, SomC, BiC, CCKC, and IvC/NGFC) (**Supplementary Figure S3**)

Data Preprocessing

We used three types of features to predict the subtype identity of each imaged IN: 1) the cell's Δ*F/F* signal, 2) the velocity of the animal, and 3) the z position of the imaged cell within CA1 (**Figure 1E, Figure 1F**). Each one of these features was added incrementally to the network in order to assess its relative contribution to the decoding performance.

Each cell's Δ*F/F* signal and the velocity signal (which is the same for all cells within the same imaging session) change over time, while the z position is a single variable for each cell. We considered the Δ*F/F* and velocity signals during individual laps, defined by respective run-start and run-stop signals measured at the onset and finish of each lap. To normalize the number of measurements within each lap, we resampled the Δ*F/F* and velocity signals to include 100 measurements for each lap by applying a cubic interpolation to the data. The alignment process is graphically shown in **Supplementary Figure 3A**. The z position of the cell was converted to a 100-element vector by simply repeating the value 100 times.

This process resulted in three types of input features for each cell that were used incrementally as inputs to the DNN (namely Δ*F/F* signal alone, Δ*F/F* signal plus velocity, and

Δ*F/F* signal plus velocity plus z position). Specifically, a Δ*F/F* lap is a single vector of 100 elements that contains the cell's interpolated Δ*F/F* signal between a run-start and run-stop event. Accordingly, a Δ*F/F*-velocity lap consists of two vectors, the Δ*F/F* signal and the velocity signal of a lap. A calcium-velocity-z-position lap includes the Δ*F/F* and velocity vectors plus an additional vector with the z-position of the cell.

DNN architectures

We employed a Convolutional Neural Network architecture previously shown to achieve high accuracy in a cell-type classification task (Troullinou et al., 2019). We first built a 1-Dimensional Convolutional Neural Network (1D-CNN) architecture and used Δ*F/F* signals as the only input feature. The network architecture consisted of a 1-Dimensional Convolutional layer consisting of 256 filters with a kernel of size 3 followed by a ReLu activation function. This layer is followed by a Batch Normalization layer. Then, the model is built up with the following pattern: a 1-Dimensional Convolutional layer- a Batch Normalization layer-1-Dimensional Max-Pooling layer. This pattern is repeated 3 times. In each pattern each convolutional layer consists of 128, 64 and 32 filters respectively, with a kernel of size 3, followed by a ReLU activation function. All max-pooling layers have a kernel of size 3 and stride is defined to 2. All these layers are followed by a dropout layer, where individual nodes of a specific layer are kept with probability $p = 0.5$. At the end of the architecture we used a fully connected layer, which has as many nodes as the number of classes and represents the activation maps of high-level features determining which features most correlate to a particular class. As a final classification step, we used the softmax activation function, which assigns decimal probabilities to each class in a multi-class problem. The optimizer

that is used in order to train our model is the Adam gradient-descent based algorithm with learning rate 0.001, and the loss we used for this multi-class problem is the categorical cross entropy.

Similarly, when using the combined Δ*F/F*-velocity laps as input features for each cell, we built a 2-Dimensional Convolutional Neural Network (2D-CNN) architecture. The general architecture of the 2D-CNN model is the same as that of the 1D-CNN model with some modifications. 1-Dimensional Convolutional and Max-Pooling layers are replaced with 2-Dimensional Convolutional and Max-Pooling layers, respectively. Moreover, the kernel of the first convolutional layer is of size [2,3], so that both of our features (Δ*F/F* and velocity) are convolved with the filter. For the rest of the convolutional layers we used a kernel of size [1,3] and retained the same dimensions for the input and output channels of each layer. This serves implementation purposes, given that each example is now 2-dimensional.

To account for all three input features of our cells, we used the 2D-CNN architecture with the addition of the z position. The kernel of the first convolutional layer is of size [3,3], so that the kernel is also convolved with the z position information. As previously, for the rest of the convolutional layers we used a kernel of size [1,3] and retained the same dimensions for the input and output channels of each layer.

The Deep Learning models that were used in our analysis were implemented with the help of Tensorflow and Keras open-source libraries written in Python. Both TensorFlow and Keras can run calculations on GPU, dramatically decreasing the computational time of the network's training. For these experiments we used Python 3.7.3™, Tensorflow version 2.1, Keras version 2.3.1 and NVIDIAs GPU model, GeForce GTX 1080 Ti, running on a Linux CentOS 7 operating system.

Prediction analysis

The data set consists of representative examples from each cell class. As the number of cell examples is very different for the 6 classes, we have adopted different ways of splitting the data. For each task, we used a fixed number of test examples for all classes to ensure fair comparison. The training set was constrained by the number of examples in the smallest cell class. We thus used a semi-balanced approach, whereby larger categories were augmented by additional samples on a case-by-case basis (reported separately for each figure). In all cases, 10% of the training set is used for validation and based on its performance progress in every epoch, we select the best model to be the one with the highest validation accuracy. We have also applied an early stopping criterion, so that if there is no improvement for 200 consecutive epochs the algorithm stops. In order to evaluate the performance of our models, we apply 10 random train-test splits and report the mean prediction accuracy for different combinations of input features as well as the confusion matrices for better visibility of misclassified samples.

Statistical analyses:

Statistical details of comparisons are specified in either the main text or figure legends. No statistical methods were used to predetermine sample sizes, but our sample sizes are similar to those reported in previous publications. Box plots represent median and interquartile range (IQR) while whiskers extend to cover the distribution without outliers (defined as points above 1.5 IQR below or above the box edges). Bar plots represent mean and s.e.m. Between-subtype comparisons were tested using a one-way ANOVA followed by a Tukey's range test with correction for multiple testing if appropriate. For comparisons between two populations, a paired sample or unpaired t-test was applied if the data points followed a normal distribution (confirmed using the Kolmogorov-Smirnov test). To analyze data that was not normally distributed, the Mann-Whitney

U test was used. *, $p < 0.05$, **, $p < 0.01$, ***, $p < 0.001$. Data analysis and figures were done using custom made software in Python 2.7.15™.

Chapter 3: Organization and Plasticity of Inhibition in Hippocampal Recurrent Circuits[3]

Bert Vancura[1,2,*], Tristan Geiller[1,2,*], and Attila Losonczy[1,2,3]

1) Department of Neuroscience, Columbia University, New York, NY, USA.

2) Mortimer B. Zuckerman Mind Brain Behavior Institute, Columbia University, New York, NY, USA.

3) The Kavli Institute for Brain Science, Columbia University, New York, NY, USA.

** These authors contributed equally to this work.*[4]

*Correspondence should be addressed to T.G.: tcg2117@columbia.edu, or A.L.: al2856@columbia.edu

3.1 Introduction

Episodic memories formed from single experiences can be used to guide behavior throughout the lifetime of an organism (Tulving, 2002). For this to occur, continuous streams of sensory information must be discretized into snapshots which can then be reactivated and consolidated into long-term memory (Buzsáki, 2015, 1989). In the mammalian brain, both the rapid encoding of episodic memories and their subsequent consolidation rely critically on the CA3 recurrent network in the hippocampus (Daumas et al., 2005; Kesner, 2007; Nakashiba et al., 2009; Nakazawa et al., 2003; Wagatsuma et al., 2017). The initial encoding of episodic memories is

[3] This study is currently under review for publication.
[4] I performed all experiments, conducted analysis together with TG, and wrote the manuscript together with TG and AL.

thought to be implemented via excitatory synaptic plasticity at synapses between feedforward mossy fibers on CA3 pyramidal cells, as well as at recurrent synapses between pyramidal cells (Mishra et al., 2016; Nakazawa et al., 2002; Rebola et al., 2017). These nascent representations are subsequently consolidated during sharp-wave ripples (SWRs), a synchronous population event generated within the CA3 recurrent network during which a compressed version of the memory traces is thought to be reactivated and transferred to the neocortex for long-term storage (Buzsáki, 2015; Foster, 2017; Gillespie et al., 2021; Norimoto et al., 2018; Pfeiffer, 2020; Wang and Morris, 2010). Accordingly, the main body of work so far has primarily focused on investigating the temporally structured recruitment of CA3 pyramidal cells during memory formation and consolidation (Buzsáki, 2015; Csicsvari et al., 2000; Guzman et al., 2016; Hunt et al., 2018; Leutgeb et al., 2007; Neunuebel and Knierim, 2014), leaving a major question mark regarding the role played by inhibition in supporting and regulating these memory processes (Buzsáki, 2015; Joo and Frank, 2018; Karlsson and Frank, 2009). Indeed, experimental and computational studies strongly implicate inhibitory motifs in stabilizing recurrent networks and supporting efficient cortical computations (Geiller et al., 2022; Nicola and Clopath, 2019; Sadeh and Clopath, 2021; Vogels et al., 2011). However, as the CA1 output region of hippocampus has traditionally served as a prototype circuit for the study of interneurons (Arriaga and Han, 2019; Booker and Vida, 2018; Buzsáki, 2015; Dudok et al., 2021a; Geiller et al., 2020; Klausberger and Somogyi, 2008; Lovett-Barron et al., 2012; McKenzie, 2018; Pelkey et al., 2017; Rebola et al., 2017; Royer et al., 2012) strikingly little is known about inhibitory microcircuits in the upstream recurrent CA3 network and their role in structuring temporally ordered neuronal firing during behaviorally relevant network states associated with memory encoding and consolidation. Based on investigations in CA1, inhibition is predominantly viewed as an immutable pacemaker of principal

cell firing, without itself being plastic, a concept reflected in the term 'chronocircuit' (Klausberger and Somogyi, 2008). In contrast to this static view of inhibition, *in vivo* structural and molecular studies have revealed robust changes in CA3 inhibitory circuits in response to behavioral manipulations (Donato et al., 2015, 2013; Guo et al., 2018; Ruediger et al., 2011), raising the possibility that CA3 inhibitory dynamics are modifiable in an experience-dependent manner (Rebola et al., 2017; Sharma et al., 2020). Critically, major challenges associated with obtaining population-level recordings of molecularly defined cell types in deep brain regions have impeded addressing these major knowledge gaps concerning operations and plasticity of inhibitory circuits in the CA3 network.

Here, we utilize a two-step method to simultaneously record large numbers of CA3 interneurons with fast, targeted 3-dimensional calcium imaging during behavior and retrospectively identify their molecular profiles with *post hoc* immunohistochemistry. We provide the first comprehensive description of molecularly-identified CA3 interneuron dynamics during both active spatial navigation and awake SWRs associated with memory consolidation. Our results uncover subtype-specific dynamics during behaviorally distinct brain-states, including activity patterns that are both predictive and reflective of SWR properties. Lastly, we provide the first demonstration of subtype-specific, experience-dependent changes in interneuron dynamics around SWRs, suggesting a central role of local inhibition in regulating CA3 microcircuit operations supporting memory consolidation.

3.2 Results

Large-scale imaging of molecularly identified interneurons

To obtain large-scale recordings from CA3 inhibitory circuits, we injected VGAT-Cre mice with a rAAV encoding Cre-dependent GCaMP7f into CA3 and implanted an imaging

window over the alveus of the anterior hippocampus, providing unbiased access to GABAergic interneurons across all CA3 sublayers (Fig 1A). We used acousto-optic deflection (AOD)-based 2p imaging (Geiller et al., 2020; Katona et al., 2012; Szalay et al., 2016) to record from hundreds of interneurons scattered in three dimensions while mice were engaged head-fixed on a treadmill (Geiller et al., 2017) in a spatial foraging task (total of 1,311 interneurons in 14 mice; 93.6 ± 21.6 per mouse, mean ± SD) (Fig 1B, 1C). After the conclusion of imaging experiments, multiplexed *post hoc* immunohistochemistry was performed on fixed brain slices that were registered to *in vivo* structural scans, revealing the molecular identity of imaged cells (Fig 1D, Methods). The precise location of all imaged cells was determined with calbindin (CB) immunohistochemistry, which allows visualization of granule cell mossy fibers (Fig 1E) within the *stratum lucidum* (Dudek et al., 2016). We utilized a combination of five molecular markers (parvalbumin, somatostatin, SATB1, cholecystokinin, and calbindin) to identify five subtypes of CA3 pyramidal cell-targeting interneurons: parvalbumin-positive basket cells (PVBCs), axo-axonic cells (AACs), somatostatin-positive cells (SOMs), cholecystokinin-positive cells (CCKs), and calbindin-positive cells (CBs) (Fig 1F-H, Methods). These five markers were chosen to label some of the most abundant interneuron subtypes in CA3 (Pelkey et al., 2017; TF and G, 1996), including those not readily accessible *via* traditional transgenic driver lines.

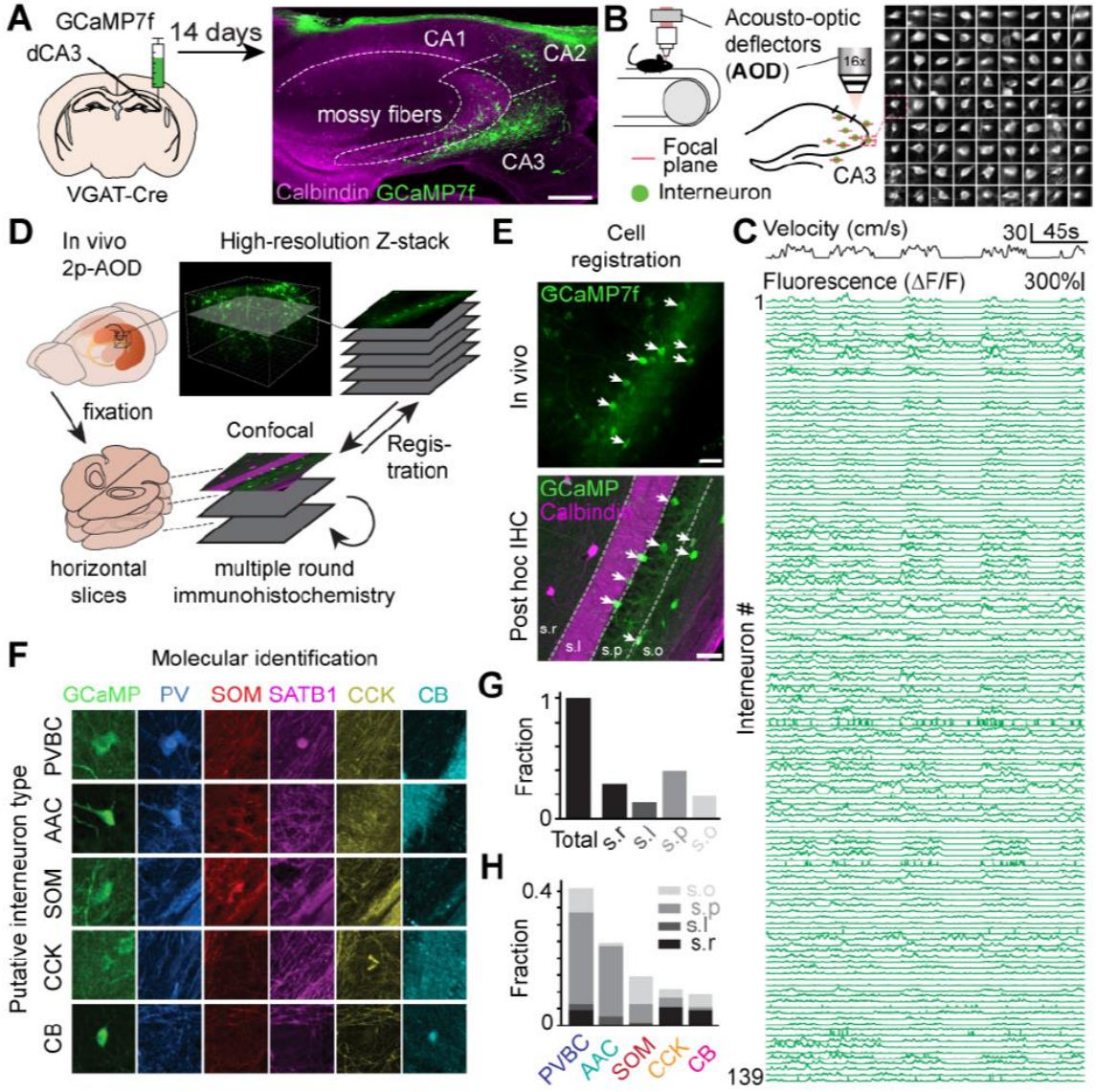

Figure 1 - Large-scale imaging of molecularly-identified GABAergic interneurons in CA3

A. Experimental design: VGAT-Cre mice are injected in CA2/CA3 with a Cre-dependent GCaMP7f virus to record all inhibitory interneurons with 2p imaging. Scale bar on the right confocal image represents 250 µm.

B. Hundreds of interneurons can be recorded simultaneously at 5-10 Hz in three dimensions with the AOD microscope during behavior. Right: time-average examples of 81 interneurons. The images are 50x50µm.

C. Example fluorescence traces from 139 simultaneously recorded interneurons during several minutes of behavior (animal velocity plotted above).

D. Schematic of the experimental pipeline used to determine the molecular identity of imaged cells. Multiple rounds of immunohistochemistry were performed on fixed, horizontal slices that were registered to high-resolution *in vivo* Z-stacks.

E. Example *in vivo* AOD-2p image (top) and condfocal image (bottom) of the registered FOV. White arrows indicate the registered cells. Calbindin immunohistochemistry was used to label the mossy fibers of *stratum lucidum*. Scale bars on the top and bottom images represent 50 and 100 µm, respectively.

F. Example immunohistochemical labeling and combinatorial expression patterns of the 5 markers (PV, SOM, SATB1, CCK, CB) used to separate imaged cells into subtypes. All images are approximately 60 X 60 µm.

G, H. Layer and subtype distributions of all imaged and *post hoc* identified interneurons.

Online inhibitory dynamics during spatial navigation

Locomotory movements are the behavioral correlates of an online and actively engaged brain-state, characterized in the hippocampus by a location-specific rate code in pyramidal cells. Thus, locomotion has been shown to strongly influence the recruitment or disengagement of distinct types of interneurons in CA1 (Arriaga and Han, 2017; Dudok et al., 2021a), but the paucity of data in CA3 to date has hindered efforts in testing whether these dynamics are a global interneuron signature hippocampus-wide. We trained and imaged water-restricted mice during a random foraging task on a 2m-long cue-rich belt (Geiller et al., 2020), during which several water rewards were delivered at random locations on each lap (Fig 2A). We observed a tight correlation between the activity of most cells and the ambulatory state of the animal (locomotion vs.

immobility) (Fig 2B). To systematically characterize this relationship, we calculated Pearson's correlation coefficient between the activity of each cell and the animal's velocity. At the population level, the average correlation was shifted towards positive values (Fig 2C). We then compared the coefficients across subtypes and observed AACs to be overall more tightly correlated with velocity (Fig 2D). In addition, CB cells had overall lower coefficients, and many CB cells were more active during immobility than during locomotion (Fig 2D). Closer inspection of the immobility-active CB cells revealed the vast majority lacked SATB1 expression (CB+/SATB1-), while SATB1-positive CB cells (CB+/SATB1+) displayed high correlations with locomotion (Fig 2E-G). These subtype-specific trends were also reflected in the average run-start and run-stop responses for each subtype (Supp Figure 1). As these functionally unique CB+/SATB1- cells may represent a previously unrecognized interneuron subtype and were negative for the other tested markers (PV, SOM, CCK), we next determined what other molecules they may express and found that the majority of CB cells were also negative for most other hippocampal interneuron markers (VIP, CR, NPY, M2R) and expressed the transcription factor COUP-TFII (Supp Figure 2), although no differences were seen between SATB1+ and SATB1- cells.

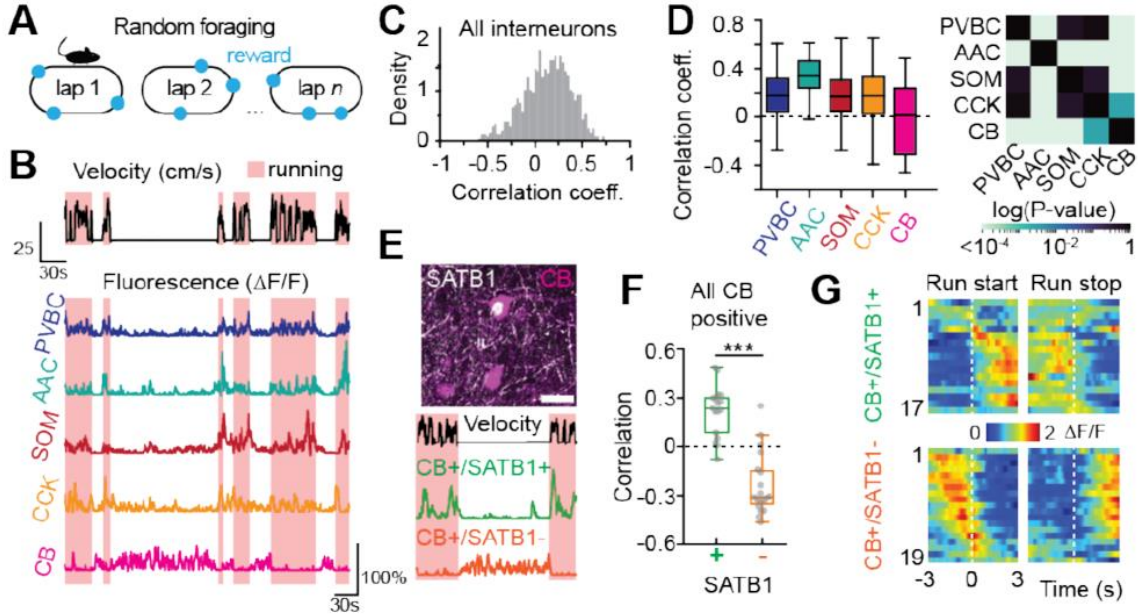

Figure 2 - Online dynamics during spatial navigation

A. Mice are trained to run for randomly delivered water rewards on each lap.

B. Representative fluorescence traces from different interneuron subtypes during running (red shaded area) and immobility (non-shaded) bouts.

C. Distribution of Pearson's correlation coefficients between fluorescence and velocity for all recorded interneurons.

D. Same as C for all identified subtypes. Between-subtype statistical comparisons (t-test) are represented in the heatmap on the right (n = 121 PVBCs, 89 AACs, 86 SOMs, 67 CCKs, and 36 CBs from n = 9 mice).

E. *Top:* Confocal image of a CB+/SATB1+ cell (magenta/white) and a CB+/SATB1- cell (magenta only). Scale bar represents 25 µm. *Bottom:* Example fluorescence traces from these cells during locomotion and immobility.

F. Same as D for CB+/SATB1+ and CB+/SATB1- subtypes (n = 17 CB+/SATB1+ neurons; n = 19 CB+/SATB1- neurons, from n = 9 mice). CB+/SATB1+ cells were significantly more correlated with velocity than CB+/SATB1- cells (Mann-Whitney U Test, $p = 2.17 \times 10^{-6}$).

G. Heatmaps of average activity around run-start (left) and run-stop (right) events for all CB+/SATB1+ (top) and CB+/SATB1- (bottom) interneurons, sorted by the location of their peak activity around run-start events (the same row on the left and right heatmaps represents the same cell).

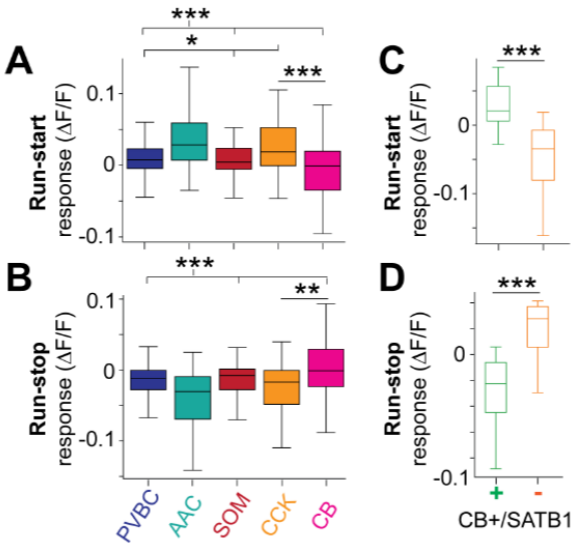

Supplemental Figure 1 - Quantification of locomotory response onsets

A. Quantification of run-start responses for all main subtypes (see Methods). AACs and CCKs had larger responses than many other subtypes (one-way ANOVA with post-hoc Tukey's range test).

B. Same as A, but for run-stop responses (see Methods).

C. Same as A, but now splitting CB interneurons according to their immunoreactivity for SATB1. CB+/SATB1+ neurons had significantly larger run-start responses than CB+/SATB1- neurons (Mann-Whitney U Test).

D. Same as C, but for run-stop responses.

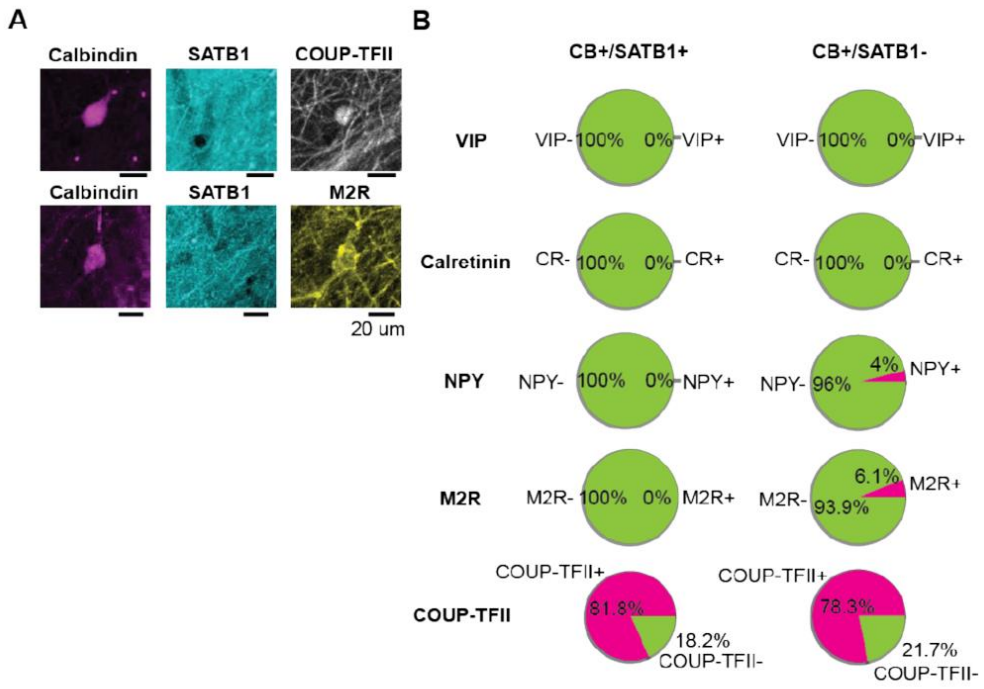

Supplemental Figure 2 - Molecular profiling of calbindin-positive SATB1-negative immobility-active interneurons

A. Confocal micrograph of CB-expressing interneurons, negative for SATB1 but positive for COUP-TFII (top) and M2R (bottom). Scale bars represent 20 µm.

B. Quantification of the overlap of CB-expressing interneurons split by immunoreactivity to SATB1 with other markers.

Akin to pyramidal cells selective for particular regions of an environment (O'Keefe and Dostrovsky, 1971), interneurons have also been reported to display some degree of spatial selectivity in CA1 (Ego-Stengel and Wilson, 2007; Geiller et al., 2020; Grienberger et al., 2017; Hangya et al., 2010; Marshall et al., 2002; Wilent and Nitz, 2007). Thus, we next sought to determine the nature and extent of spatial tuning by quantifying the degree of selectivity among different CA3 interneuron subtypes (Supp Figure 3). While subsets of cells displayed both

significant positive and negative spatial tuning, we did not observe profound differences between subtypes (Supp Figure 3A-D). We then more precisely quantified the relative contributions of various behavioral variables to interneuron activity by constructing a model to predict each cell's fluorescence trace (Supp Figure 3E-I) and found that velocity, followed by position, displayed the highest predictive coefficient.

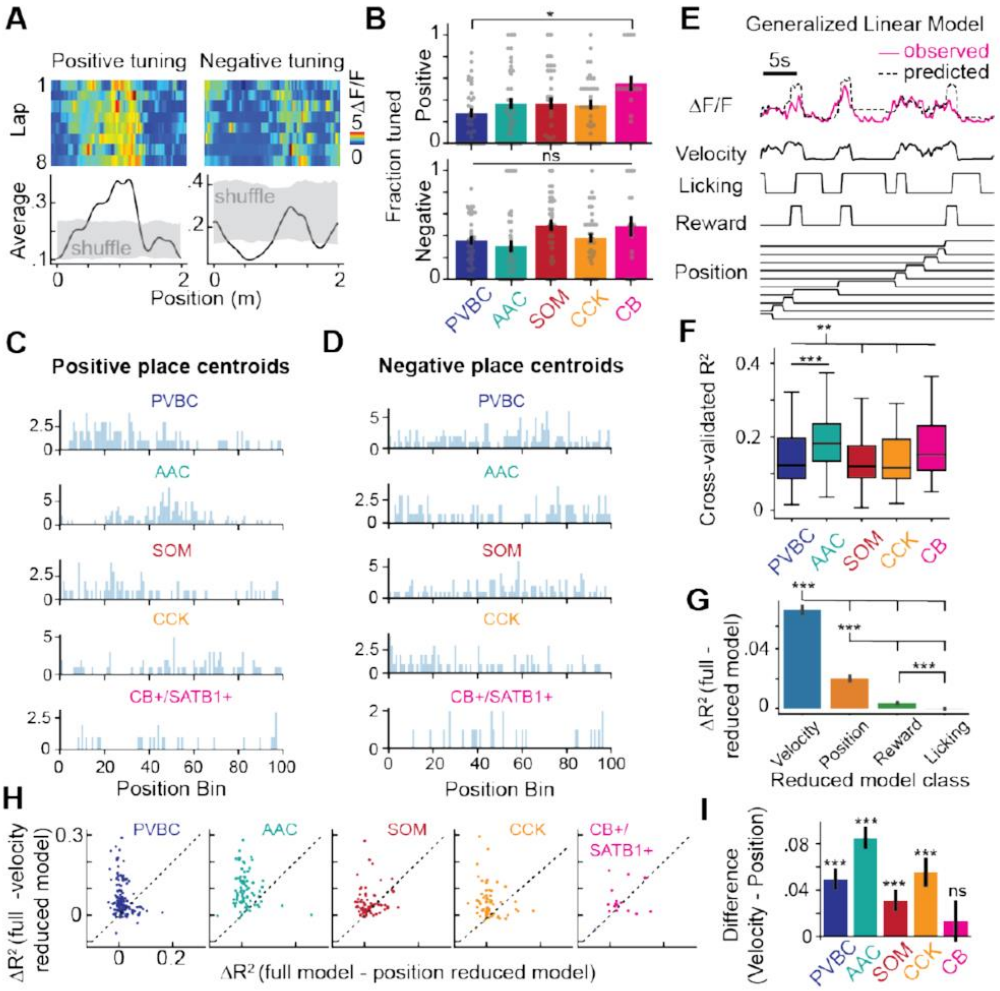

Supplementary Figure 3 - Interneuron spatial selectivity during navigation

A. Representative examples of spatially-selective interneurons with positive (left) and negative tuning (right), defined based on a shuffled distribution (see Methods).

B. Fractions of positively (top) and negatively (bottom) tuned cells by subtype. Each dot represents the fraction of tuned cells for a given subtype during a recording session. CBs had significantly greater fractions of tuned cells than did PVBCs (one-way ANOVA with *post-hoc* Tukey's range test). Note the CB label here represents only CB+/SATB1+ neurons, as CB+/SATB1- cells were shown to be silent during locomotion.

C. Distribution on the belt of all positive place field centroids.

D. Same C, but for negative place field centroids.

E. Schematic of the GLM used to evaluate the contribution of multiple predictors to each interneuron's fluorescence activity.

F. Distribution of goodness of fit (R^2) between the predicted and actual observed activity for each subtype. AACs had significantly greater R^2 values than most other subtypes (one-way ANOVA with *post-hoc* Tukey's range test).

G. Difference in R^2 between the full model (with all predictors from E) and various reduced models, each one lacking one predictor. Each category of reduced model was fit over all cells, regardless of subtype. The velocity predictor contributed most to activity, followed by position, then reward, and finally licking (paired t-tests with *post-hoc* Bonferroni correction).

H. Contribution of position (X-axis) versus velocity (Y-axis) to the activity of each cell, measured as the difference in R^2 in reduced models lacking these predictors. Each dot represents an interneuron. The activity of some cells can be better explained by either one of the two predictors.

I. Difference between the contributions of velocity and position to the activity of each cell shown in H) for each subtype. For most subtypes, the velocity predictor could explain activity better than the position predictor (one-sample t-tests against 0).

Inhibitory dynamics around offline memory consolidation events

The precise circuit mechanisms regulating SWR initiation in CA3 and the role played by distinct inhibitory interneurons in these processes remain unknown, as no data exists from defined interneuron subtypes. To address this major knowledge gap, we used our 2p-AOD method combined with local field potential (LFP) recordings (Fig 3A, Methods) from contralateral CA1 to examine interneuron activity around awake SWRs during periods of immobility. To confirm that we could detect changes in CA3 circuits around contralateral SWR events (Grosmark et al., 2021; Guan et al., 2021; Kohl et al., 2011; Malvache et al., 2016; Terada et al., 2022), we first imaged CA3 pyramidal cell activity using a CA3-specific transgenic mouse line (Supp Figure 5A, B). CA3 pyramidal cell activity was indeed elevated around detected SWRs (Supp Figure 5C), allowing us to next consider the local inhibitory dynamics. At the overall population level and regardless of subtype, we found that the first and second components of a principal component analysis-based decomposition represented activated and inhibited dynamics, respectively, after and around SWR onset (Fig 3B). In stark contrast with the available *in vitro* data where most CA3 interneurons spike during SWRs (Hájos et al., 2013), we in fact found more cells to be inhibited (Fig 3B). We observed highly heterogeneous responses at the subtype level as evidenced by their average peri-SWR traces (Fig 3C, D): PVBCs showed a tight time-locked activation around SWR events, while AACs, CCKs and CB cells showed a net inhibition. CCKs were unique in that the trough of their inhibition preceded the SWR onset (Fig 3C). We then examined how representative

these average responses were for all cells belonging to each subtype. To this end, we calculated a SWR activity index to measure whether a given interneuron is more activated or inhibited during SWRs (Fig 3E). While most PVBCs were strongly activated, the majority of AACs, CCKs, and CBs were inhibited (Fig 3E, F). SOM cells exhibited a bimodal profile, including the most activated cells in the entire dataset but also strongly suppressed ones, explaining the weakly modulated overall peri-SWR trace of the SOM subtype (Fig 3C, E, F and Supp Figure 4); this heterogeneity likely reflects the presence of distinct SOM-expressing subtypes not captured by our molecular identification (Katona et al., 2014; Pelkey et al., 2017). Lastly, we analyzed the timing of individual cells' responses by examining the location of the peaks of activated cells and the troughs of inhibited cells around SWRs, depending on whether a given subtype is composed of a larger fraction of activated or inhibited interneurons ('dominant response') (Fig 3G). While most inhibited cells tended to have their troughs well after the SWR, inhibited CCK cells had their trough before the initiation of SWRs (Fig 3G), ideally positioning them to exert control over the initiation of SWRs bound to the synchronous activity of CA3 pyramidal cells (Fig 3G).

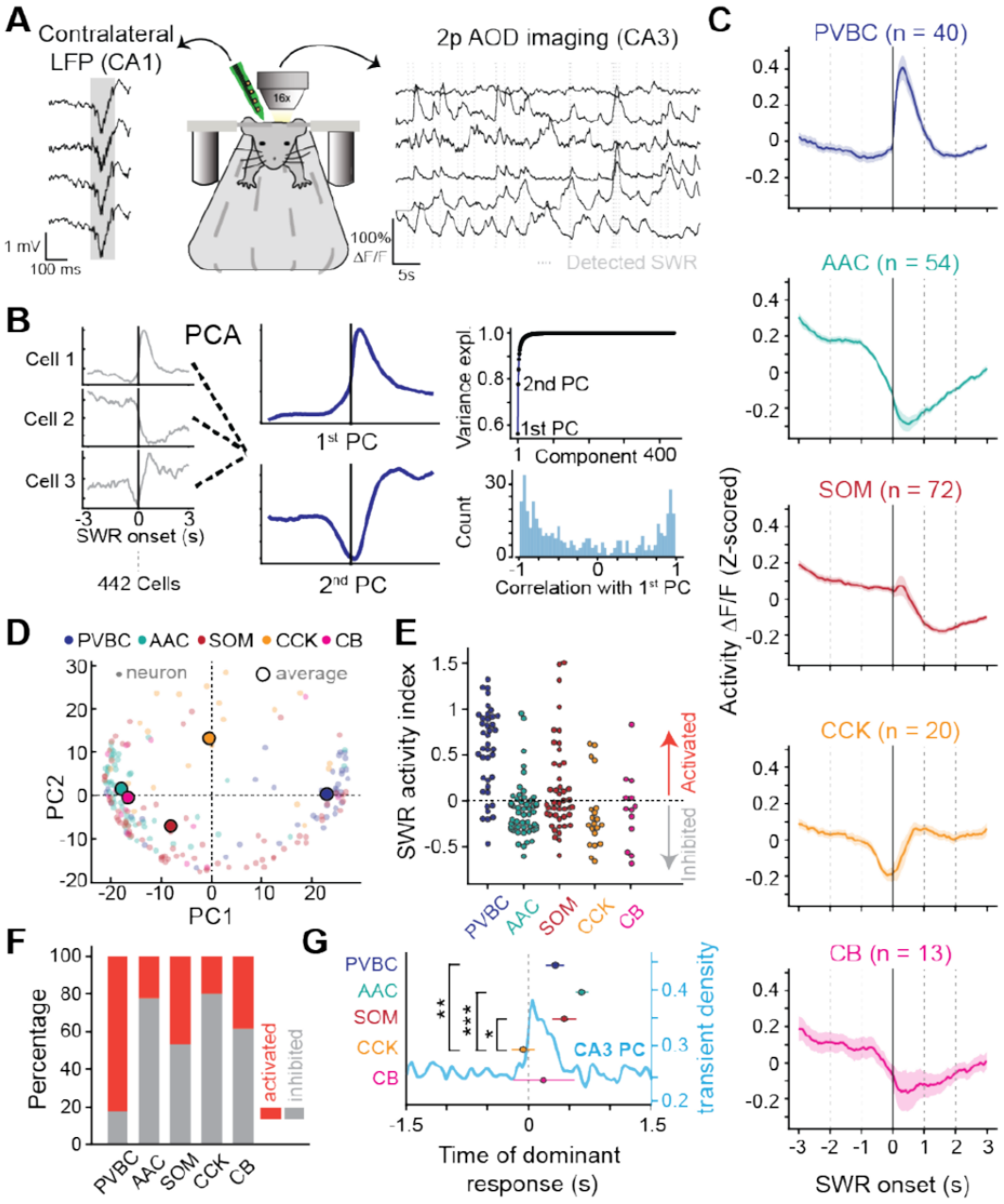

Figure 3 - Subtype-specific offline dynamics during SWR events

A. Experimental setup for simultaneous 2p-AOD imaging and LFP recordings. SWRs were recorded on a 4-channel silicon probe implanted in the contralateral CA1.

B. PCA was performed on the average peri-SWR traces of all cells (left) to produce the first and second principal component time series (center) (n = 442 cells from n = 5 mice). Cumulative explained variance with each additional principal component (top right). Histogram of the correlation coefficient of each cell's average peri-SWR trace with the first principal component (bottom right).

C. Average peri-SWR traces for all subtypes (data from n = 5 mice).

D. Distribution of first and second PC loadings for all cells (small gray dots) and the median values for all identified subtypes (larger colored dots, n = 40 PVBCs, 54 AACs, 72 SOMs, 20 CCKs, and 13 CBs from n = 5 mice).

E. Average SWR activity index for all neurons, grouped by subtype (number of identified cells of each subtype and number of mice is the same as above). As a whole, PVBCs were significantly activated, AACs were significantly inhibited, SOMs were weakly activated, and CCKs and CBs showed no overall net modulation (one-sample t-tests against 0: PVBC: $p = 5.52 \text{ X } 10^{-8}$; AAC: $p = 2.39 \text{ X } 10^{-6}$; SOM: p = 0.028; CCK: p = 0.99; CB: p = 0.57).

F. Fraction of inhibited and activated neurons for each subtype, defined by the SWR activity index.

G. Timing of the dominant response for each subtype as a function of SWR onset. Dominant response was characterized by the highest fraction of neurons within a given subtype (PVBC's dominant response is activated while AAC is inhibited). The corresponding peak or trough location was then calculated for all the neurons falling in the dominant's category (unpaired t-test, p(CCK-SOM)=0.02, $p(\text{CCK-AAC})=2.2 \text{ X } 10^{-5}$, $p(\text{CCK-PVBC})=5.8 \text{ X } 10^{-3}$).

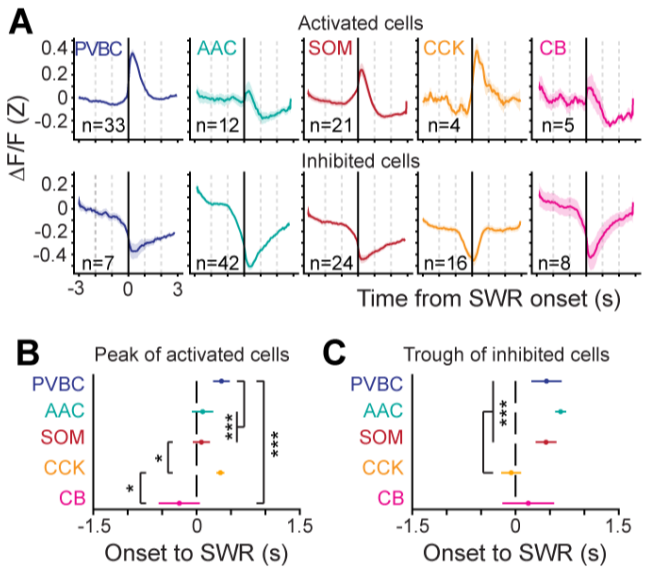

Supplementary Figure 4 - Subtype-specific inhibited and activated response dynamics to SWRs

A. Average peri-SWR time histogram for activated (top) and inhibited (bottom) interneurons, defined by the SWR modulation index (see Methods). The number of activated and inhibited cells for each subtype is reported in *Figure 3*.

B. Timing of the peak location computed for individual activated neurons for each subtype (mean ± sem).

C. Same as B, for the trough location of inhibited neurons (mean ± sem).

Predictive and reflective inhibitory dynamics around SWRs

SWR power recorded *in vivo* exhibits marked event-to-event variability which is thought to reflect differences in the size of recruited pyramidal cell ensembles in the hippocampal network (Buzsáki, 2015; Csicsvari et al., 2000; Grosmark and Buzsáki, 2016). If inhibitory subtypes influence SWR initiation or termination in the CA3 network, we expect that the activity dynamics of those cells would be correlated with the SWR power. To test this, we first sought to confirm

that we could detect differences in local CA3 pyramidal cell network dynamics during high- and low-power SWRs measured on the contralateral side with our imaging approach. As the pyramidal cell transient rate was significantly greater around high-power SWRs than around low-power SWRs (Supp Figure 5D, E), we next sought to determine whether similar correlations could be observed between interneuron dynamics and SWR power. We found that some interneurons indeed displayed responses largely correlated with the amplitude of the SWR they follow (PVBC) or precede (CCK) (Fig 4A). After splitting the dataset between the lowest (0-20th percentile) and the highest (80-100th percentile) SWR power, only PVBC, AAC and CCK subtypes showed a different average response trace (Fig 4B, C). The position in time of the most extreme difference between the average low- and high-SWR responses was, for CCKs, tens of milliseconds before the SWR onset, while AACs and PVBCs had differential responses after SWR onset (Fig 4D). These results suggest that CCK activity before a given SWR should be significantly more predictive of the resulting SWR power than the activity of the other subtypes, while PVBC and AAC activity after a given SWR should be selectively more reflective of the SWR power. To test this more directly, we correlated the average activity of each cell in the 500 ms before and after each SWR with the magnitude of the SWR (Methods, Fig 4E, F). Indeed, we found significant subtype-specific negative and positive relationships: large amplitude SWRs were associated with decreased CCK activity preceding the event, as well as increased PVBC activity and decreased AAC activity following it (Fig 4G). Overall, these results suggest a novel role for CCK interneurons in controlling the size of the population burst that generates the SWR, as well as an important role for PVBCs in regulating peri-SWR network activity.

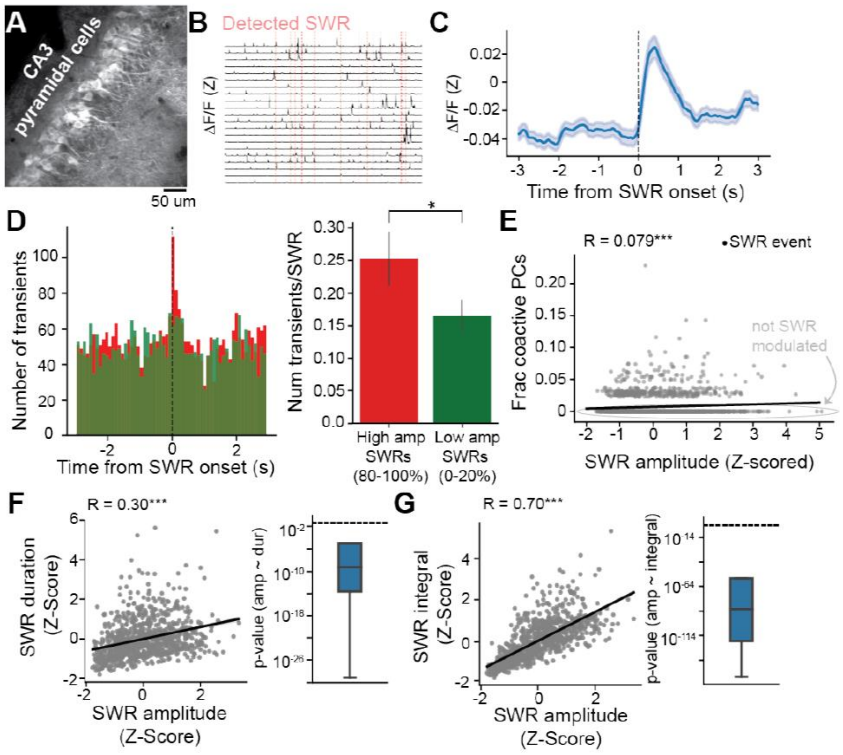

Supplementary Figure 5 - CA3PC data and Correlations between SWR Properties

A. Representative *in vivo* two-photon time-average image of a CA3PC FOV.

B. Example CA3PC ΔF/F traces with detected SWRs depicted as vertical red lines.

C. Peri-SWR fluorescence activity for all CA3PCs, averaged over all SWR events.

D. *Left*: Distribution of peri-SWR CA3PC calcium transients for SWRs with low power (green, taken as SWRs with power falling between 0-20th percentile of all ripples for a given mouse) and high power (red, for SWRs between 80-100th percentile). *Right*: Quantification of the population transient rate for high- and low-power SWRs. CA3PCs emitted significantly more transients during high-power SWRs than during low-power SWRs (Wilcoxon signed-rank test).

E. Correlation between SWR power and the number of co-active pyramidal cells around the SWR. High-power SWRs were associated with greater fractions of co-active CA3PCs around the SWR event.

F. Correlation between amplitude and duration for individual SWRs. *Left:* Example scatter plot and linear regression line depicting the relationship between amplitude and duration for all SWRs recorded during the imaging of one example interneuron. *Right*: Distribution of p-values for the regression between amplitude and duration, calculated over all imaging sessions. The horizontal dashed line corresponds to a p-values of 0.05. A strong relationship between SWR amplitude and duration was present in all imaging sessions.

G. Same as F, but now performed for the relationship between SWR amplitude and SWR integral. Again, these two LFP measures were strongly correlated.

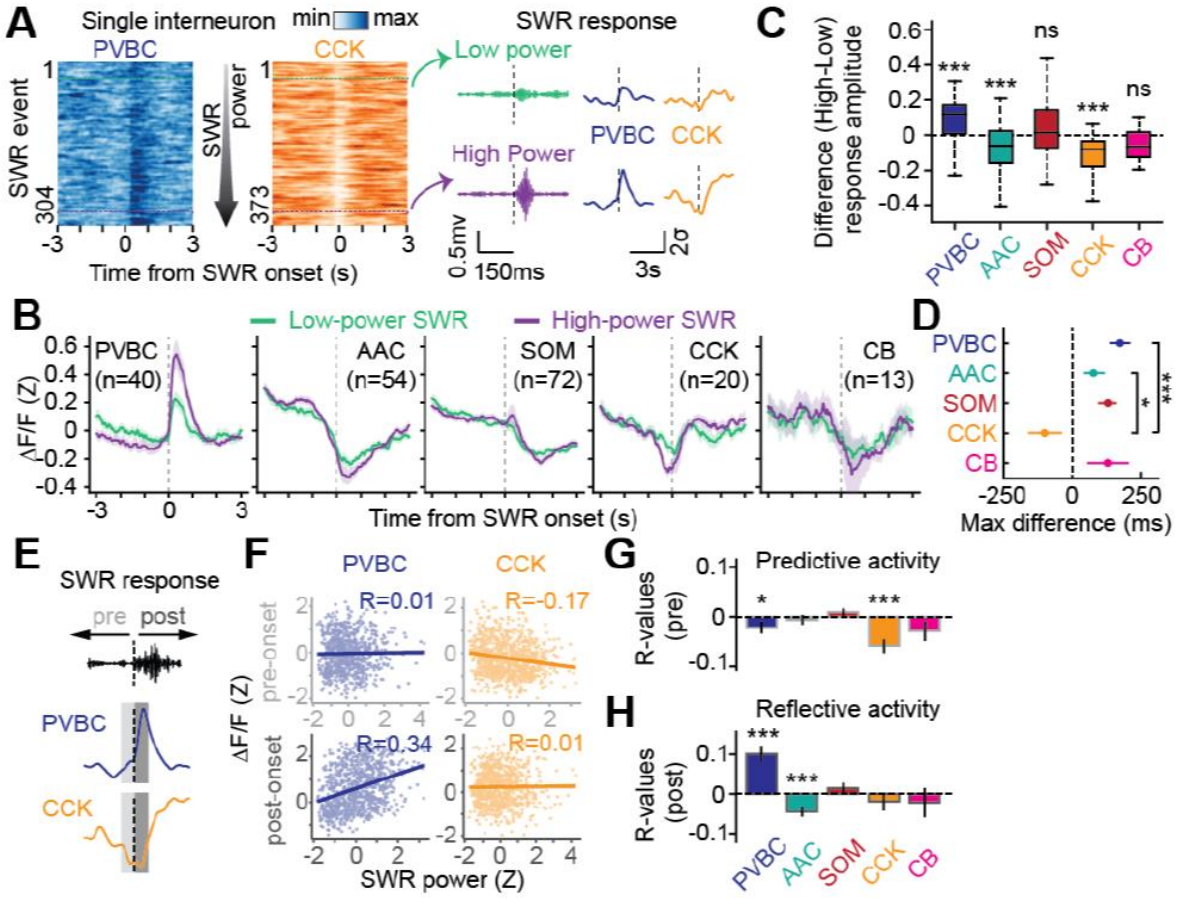

Figure 4 - Peri-SWR dynamics are both predictive and reflective of SWR properties in a subtype-specific manner

A. Example responses of a PVBC and a CCK cell to high- and low-power SWRs. Heatmaps illustrating cell responses around SWR events ordered by their power (left). Both activated and inhibited responses were strongly modulated by SWR power (right).

B. Average Z-scored peri-SWR traces for both low- (0-20th percentile) and high- (80-100th percentile) power SWRs for each subtype (number of cells of each subtype indicated on the figure, n = 5 mice).

C. Average value of the difference in activity between high- and low-power SWRs for each cell, grouped by subtype. PVBCs were significantly more activated around high-power SWRs, while both AACs and CCKs were significantly more inhibited around high-power SWRs (n = 39 PVBCs, 53 AACs, 72 SOMs, 20 CCKs, and 13 CBs from n = 5 mice; one-sample t-tests against 0: PVBC: $p = 2.05 \times 10^{-4}$; AAC: $p = 8.16 \times 10^{-5}$; SOM: $p = 0.11$; CCK: $p = 5.76 \times 10^{-4}$; CB: $p = 0.24$).

D. Location of the maximum difference in activity between high- and low-power SWRs for each cell, grouped by subtype. CCKs were most prominently modulated by high-amplitude SWRs earlier in time compared to AACs and PVBCs, the other two modulated subtypes (same number of cells and mice as in C; Mann-Whitney U Tests, p (CCK-AAC) = 0.015; p (CCK-PVBC) = 5.38×10^{-4}). SOM and CB cells, while not on average differentially modulated by high- vs. low-amplitude SWRs, are shown here for visual comparison.

E. Schematic illustrating the pre- and post-activity around each SWR used for the correlation analysis. A 500 ms window before and after each SWR event was used.

F. Example correlation plots between either average pre- (top) or average post-activity (bottom) and SWR power for individual PVBC (left) and CCK cells (right). Correlations include every SWR event during which the cell was imaged and generate an r-value for each cell.

G. Summary of r-values for all cells for the correlation between each cell's average pre-SWR activity and SWR power, grouped by subtype. CCK activity was most predictive of SWR power (lower CCK activity before high-power SWRs), followed by PVBC activity. The other subtypes were not predictive of SWR power (same number of cells as in C, data from

n = 5 mice; one-sample t-tests against 0: PVBC: p = 0.033; AAC: p = 0.47; SOM: p = 0.10; CCK: p = 1.72 X 10^{-4}; CB: p = 0.16).

H. Same plot as in G, but now for the correlation between each cell's average post-SWR activity and SWR power, grouped by subtype. PVBC and AAC activity were both reflective of SWR power (higher PVBC and lower AAC activity following high-power SWRs). The other subtypes were not reflective of SWR power (same number of cells as in C, data from n = 5 mice; one-sample t-tests against 0: PVBC: p = 1.16 X 10^{-6}; AAC: p = 1.14 X 10^{-4}; SOM: p = 0.22; CCK: p = 0.39; CB: p = 0.56).

Experience-dependent reconfiguration of peri-SWR inhibitory dynamics

Selective recruitment and exclusion of CA3 pyramidal cells during SWRs depending on behavioral relevance of stimuli they encode represent important mechanisms for selective consolidation of salient representations (Terada et al., 2022). While these phenomena suggest a role for inhibitory plasticity, circuit mechanisms enabling the flexible recruitment of individual pyramidal cells to SWRs remain unknown. Instead, interneurons are thought to have stereotyped and immutable activity profiles around SWR events that are subtype-specific (Klausberger and Somogyi, 2008; Somogyi et al., 2014; Varga et al., 2012). Therefore, potential behavior-dependent changes in recruitment of interneurons to SWR events, and the resulting flexible selection of pyramidal cell assemblies to these events, remains an open question. To directly address this, we leveraged a recent finding that CA3 pyramidal cells encoding sensory cues are suppressed from SWRs when the cues have no behavioral relevance (Terada et al., 2022). Thus, we asked whether changes in the activity of CA3 interneurons around SWRs occur immediately after sensory stimulation (Fig 5D). To this end, mice received pseudorandomly delivered water, light, and odor

stimuli while head-fixed on a cue-less burlap belt (Terada et al., 2022), and interneurons were imaged during SWRs before and after the sensory stimulation (Fig 5A). CCK cells were selectively activated in response to the sensory stimuli (Fig 5B). An activation could be seen in the vast majority of CCK cells, the response did not change significantly over trials for any subtype, and the response was generally similar for the three sensory modalities (Fig 5C, Supp Fig 6A, B, C). Next, we constructed average peri-SWR traces for each subtype, both before and after sensory stimulation (Fig 5E, Supp Figure 6D). While most subtypes (PVBC, AAC, and SOM cells) displayed stable peri-SWR activity profiles, CCK cells showed a significantly increased activation around SWR events (Fig 5E) after the sensory stimulation. Additionally, several CB cells displayed a similar increase in peri-SWR activity, although the change was not significant at the subtype level. We quantified this change at the level of individual cells, calculating the peri-SWR modulation for each cell both before and after sensory stimulation (Fig 5F, Methods). This analysis revealed a selective increase in SWR modulation for CCK cells in response to sensory stimulation (Fig 5F). We next asked whether this increase in the overall peri-SWR activity of CCK cells was due to an increased fraction of events recruited to, or to an increased activation in a comparative number of SWR events. We found that individual CCK cells were recruited to an increased number of SWR events post sensory stimulation, while the maximum activation within recruited events remained stable (Fig 5G, 5H). Together, these results provide the first evidence for subtype-specific changes in interneuron recruitment to SWR events in response to experience and suggest a potential role for CCK interneurons in the regulation of the ensemble size and identity of pyramidal cells recruited to SWRs.

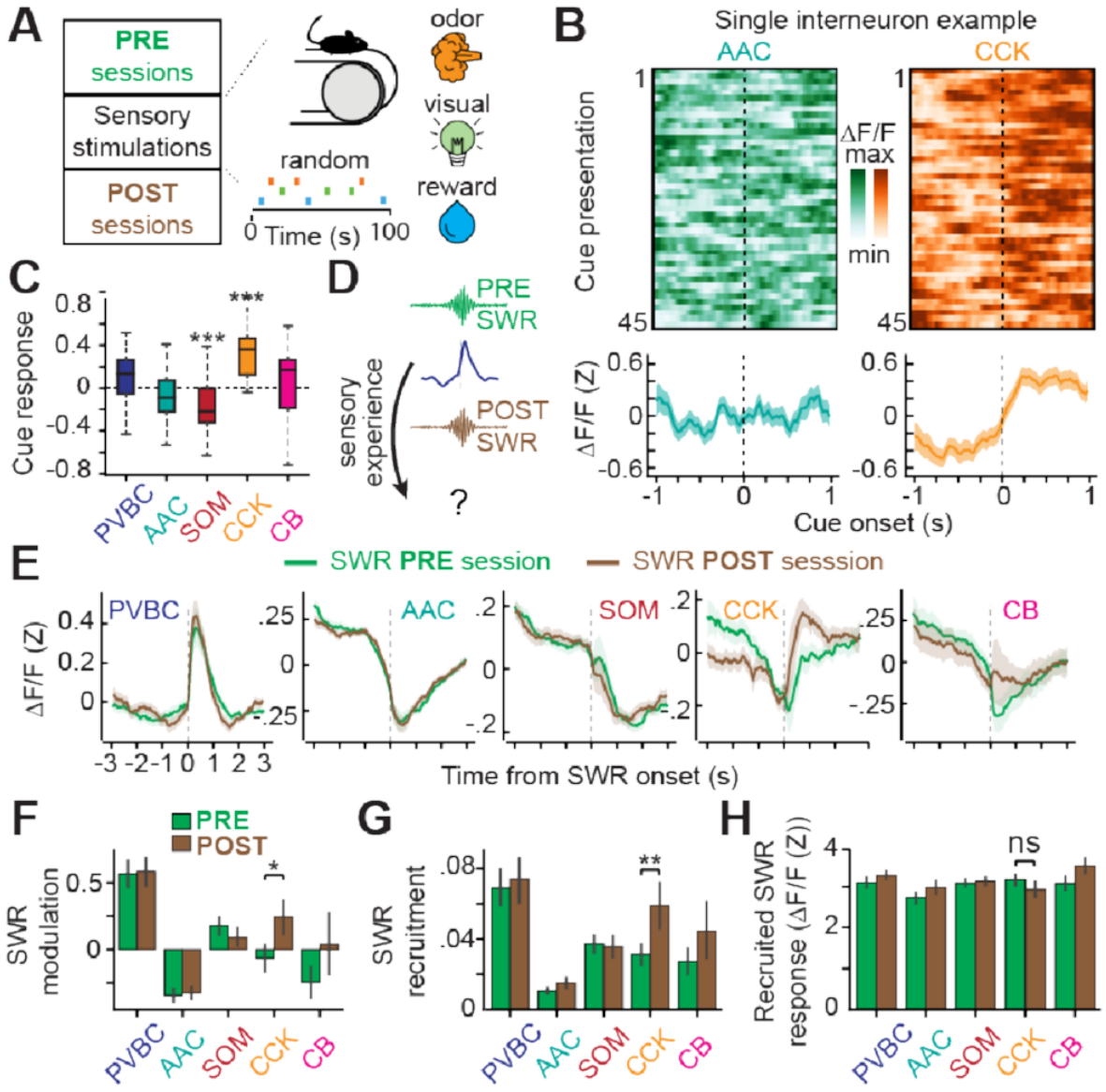

Figure 5 - Peri-SWR dynamics can be modulated by experience

A. Sensory stimulation paradigm. Water, light, and odor stimuli were presented pseudorandomly while the mouse remained head-fixed on a cue-less, burlap belt. Interneurons were imaged during SWRs in both the PRE and POST sessions as well as during stimulus presentations.

B. Representative example of an individual AAC (green) and CCK (orange) interneuron. Heatmaps represent the activity during all sensory stimulus presentations (45 in total) with the corresponding average response (bottom). The CCK neuron is consistently and significantly activated by cue presentations.

C. Average sensory cue response for each cell, grouped by subtype. CCK cells were significantly activated by cue presentation, while SOM cells were significantly inhibited (n = 25 PVBCs, 37 AACs, 42 SOMs, 14 CCKs, and 12 CBs from n = 3 mice; one-sample t-tests against 0: PVBC: $p = 0.076$; AAC: $p = 0.059$; SOM: $p = 1.01 \times 10^{-4}$; CCK: $p = 1.65 \times 10^{-4}$; CB: $p = 0.73$).

D. Sessions PRE and POST cue presentations are split to examine whether sensory cue presentations induced a change in interneuron dynamics around SWRs.

E. Average Z-scored peri-SWR traces for both PRE and POST sessions for all subtypes. Note the different peri-SWR dynamics for CCK cells and the relative stability of the other subtypes.

F. Average SWR modulation for each cell during both the PRE and POST sessions, grouped by subtype. CCK cells had a significantly greater SWR modulation during the POST sessions compared to PRE (n = 29 PVBCs, 35 AACs, 60 SOMs, 16 CCKs, and 9 CBs from n = 5 mice; Wilcoxon signed-rank tests: PVBC: $p = 0.97$; AAC: $p = 0.50$, SOM: $p = 0.10$, CCK: $p = 0.013$; CB: $p = 0.21$).

G. Fraction of SWR events each cell was recruited to for all cells during both the PRE and POST sessions, grouped by subtype. CCK cells were recruited to a significantly greater fraction of SWR events during the POST session compared to PRE (same number of cells

and mice as in F; Wilcoxon signed-rank tests: PVBC: p = 0.75; AAC: p = 0.13; SOM: p = 0.55; CCK: p = 0.0061; CB: p = 0.59).

H. Average response magnitude of each cell within recruited SWR events, grouped by subtype. The response magnitude of CCK cells (or any other subtype) within recruited SWRs did not change between PRE and POST (n = 28 PVBC, 29 AACs, 51 SOMs, 13 CCKs, and 8 CBs from n = 5 mice; Wilcoxon signed-rank tests: PVBC: p = 0.37; AAC: p = 0.48; SOM: p = 0.85; CCK: p = 0.17; CB: p = 0.21).

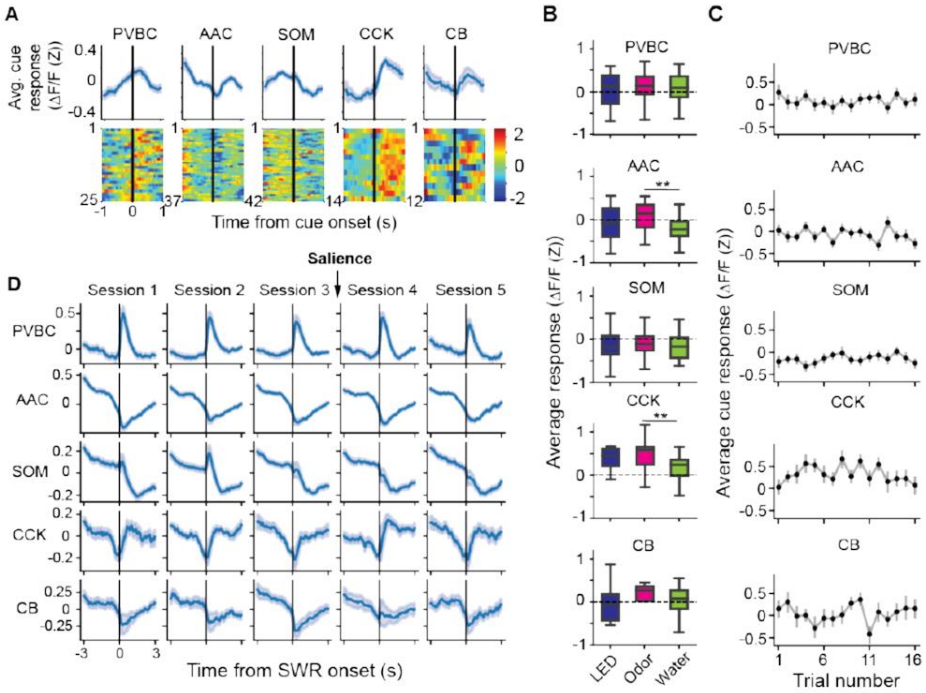

Supplementary Figure 6 - Session-to-session and trial-to-trial cue responses and SWR-associated dynamics in the sensory stimulation task

A. Average cue response traces for each subtype (top) and the response for each individual neuron (bottom; each row represents one cell).

B. Average cue response for each subtype, broken down by the response to each sensory modality (visual stimulation, odor delivery, and water delivery). While most subtypes

responded similarly to the three sensory cues, AACs and CCKs exhibited greater responses to odor than to water stimuli (paired t-tests with *post-hoc* Bonferroni correction; only significant comparisons are shown).

C. Average cue response across trials for each subtype. Each trial represents the average of three sensory stimulations, one of each subtype (one visual, one odor, and one water stimulation).

D. Peri-SWR ΔF/F traces for each session and subtype. Sensory stimulation occurred between Session 3 and Session 4. In Main Figure 5, Sessions 1-3 are considered PRE and Session 4 is considered POST.

3.3 Discussion

The work here represents the first large-scale assessment of CA3 interneuron dynamics during spatial navigation and SWR-associated memory reactivation, providing critical new information on the activity and plasticity of inhibitory circuits at the locus of SWR initiation. The available data regarding CA3 interneurons largely comes from studies detailing their electrophysiological properties *in vitro*, (Botcher et al., 2014; Gulyás et al., 1992; Kohus et al., 2016; Losonczy et al., 2004; Mercer et al., 2007; Papp et al., 2013; Spruston et al., 1997; Vida and Frotscher, 2000), especially as they relate to innervation and plasticity at the mossy fiber – interneuron synapse (Acsády et al., 1998; Lawrence and McBain, 2003; Maccaferri et al., 1998; Mori et al., 2007; Rebola et al., 2017; Szabadics and Soltesz, 2009), and the role of CA3 interneurons in generating SWRs (Bazelot et al., 2016; Dugladze et al., 2012; Ellender et al., 2010; Schlingloff et al., 2014). A complementary line of work has leveraged demanding juxtacellular recordings to record from small numbers of anatomically identified CA3 interneurons under

anesthesia *in vivo* (Lasztóczi et al., 2011; Tukker et al., 2013; Viney et al., 2013). Thus, to date, the sparsity, diversity, and depth of CA3 inhibitory circuits in the intact brain have prevented cell-type specific population recordings during behavior from this critical hippocampal region. Our approach combining large-scale, unbiased sampling of inhibitory network activity during behavior, simultaneous LFP recordings, and *post hoc*, multiplexed molecular characterization allowed us to make novel observations regarding the subtype-specific and brain-state-dependent modulation of inhibition in CA3. We note that many of our findings would not have been achieved with more traditional *in vivo* imaging approaches using transgenic lines, highlighting the power of this experimental strategy.

We find that the *in vivo* dynamics of CA3 inhibitory circuits exhibit similarities to their CA1 counterparts with respect to their overall positive velocity modulation and spatial modulated firing in a subset of interneurons. One notable exception is the CCKs that are almost exclusively immobility active in CA1 (Dudok et al., 2021a; Geiller et al., 2020), but more heterogenous in CA3. Our finding that CA3 CB interneurons comprise two functionally distinct subpopulations with regards to their activity during locomotion, and that these subpopulations strongly correlate with expression of the transcription factor SATB1, represents the first *in vivo* characterization of CB interneuron dynamics in any hippocampal subregion. Although these cells represent a significant inhibitory subpopulation (Bezaire and Soltesz, 2013; TF and G, 1996) they have been understudied, likely because of their preferred location in deep dendritic layers (*radiatum/lacunosum-moleculare*), and because major subpopulations of pyramidal cells in CA1 also express CB, complicating genetic access with transgenic lines (Dong et al., 2009). The immobility-active CB cells we identify are potentially linked to a rare subtype previously identified in single-cell transcriptional data from CA1 (Harris et al., 2018) and recorded from in CA1 under

anesthesia (Fuentealba et al., 2010). As SATB1 acts downstream of other transcription factors that specify an origin from the medial ganglionic eminence (MGE) and is thus enriched in MGE-derived interneurons (Close et al., 2012; Denaxa et al., 2012), our finding suggests that the functional dichotomy we observe in CB-expressing interneurons may represent differences between MGE- and CGE-derived CB interneurons. We hypothesize that differences in the hard-wired input connectivities onto these two cell types might account for their complementary activity profiles during locomotion and immobility, and that these connectivity differences likely apply to MGE- and CGE-derived interneurons more generally. Indeed, to date all hippocampal interneuron subtypes with robust and consistent immobility activation are CGE-derived, including CCK basket cells (Dudok et al., 2021a), VIP/M2R interneurons (Francavilla et al., 2018), and here CB+/SATB1- interneurons. In support of this view, CCK basket cells and CB-expressing cells in CA1 have both been shown to receive large fractions of inhibitory synapses compared to other interneuron subtypes (Gulyás et al., 1999; Matyas et al., 2004), potentially explaining how these cells could be silenced during locomotion, when the majority of interneurons are activated and would provide them with a strong inhibitory input. Complementarily, a common excitatory input to these cell types that is activated during immobility could explain their sustained immobility activation. Although such an input remains to be found, neuromodulatory afferents are attractive candidates (Atherton et al., 2015; Kaufman et al., 2020; Prince et al., 2021), as they have been shown to regulate interneuron dynamics during locomotion/immobility in the neocortex (Fu et al., 2014). Of particular interest, serotonergic afferents from the median raphe have been shown to selectively target CCK and CB cells in CA1 (Freund et al., 1990; Varga et al., 2009), and certain serotonin receptor subtypes are depolarizing and restricted to CGE-derived interneurons (5-HT3AR). It will be critical in future experiments to understand whether CA3's CB+/SATB1- and

CA1's VIP+/CCK+ or VIP+/M2R+ neurons share common inputs, if locomotion/immobility signals are passed from one region to the other, and why this locomotion-state dependent inhibition from specific interneuron subtypes is important in regulating information processing in pyramidal cell networks.

While the robust engagement of most hippocampal interneurons is critical for the control of pyramidal cell dynamics during locomotion, spatial navigation, and online memory encoding, their modulation during the SWRs of subsequent immobility is equally crucial for memory consolidation. Our work provides the first data regarding *in vivo* dynamics of defined interneuron subtypes in CA3 around awake SWRs and thus offers important clues regarding the mechanisms of SWR initiation and termination. Although it is now established that SWRs are brain-wide events indispensable for memory reactivation and consolidation, the mechanisms by which they are generated in the hippocampal recurrent network are still under intense debate. While it was originally proposed that SWRs are generated by the disinhibition of recurrently connected CA3 pyramidal cells (Buzsáki, 1986) and more recent CA3 circuit models have also explored this idea (Evangelista et al., 2020), experimental support for this hypothesis has been limited to the finding that a few AACs in CA3 have been found to be silenced during SWRs under anesthesia (Viney et al., 2013). On the contrary, most experiments with *in vitro* CA3 preparations have observed that the vast majority of local interneurons spike during SWRs (Hájos et al., 2013). We find that the majority of AACs and CCKs are inhibited, starting hundreds of milliseconds before the SWR event (see Figure 3), potentially providing the disinhibition necessary to trigger the synchronous activation of pyramidal cells. However, while the AAC inhibition before the SWR is not correlated with the magnitude of the oscillation, the extent of CCK inhibition preceding the SWR is strongly and specifically predictive of the resulting SWR power (see Figure 4). Thus, while AAC inhibition

and the resulting withdrawal of inhibition from the axon initial segment of pyramidal cells may be a necessary condition for SWRs to occur, our data suggest that AACs are not responsible for regulating the size of the CA3PC burst. Our results instead ascribe this critical function to CCK-expressing interneurons.

Alternative models of SWR initiation in the CA3 microcircuit posit that the strong activation of local PVBCs may strongly hyperpolarize surrounding pyramidal cells, and the rebound activity from this suppression could generate the CA3 pyramidal cell bursts and the resulting SWR (Buzsáki, 2015). Our results do not support this hypothesis, as the peak of PVBC activation occurs several hundred milliseconds after the SWR event (See Figure 3), and after the peak pyramidal cell response. Nevertheless, we do find that the magnitude of the PVBC response around SWRs is correlated with the magnitude of the oscillation (See Figure 4). This finding extends the *in vitro* CA1 observations that the number of spikes emitted by PV+ cells during sharp waves (SWs) is linearly correlated to the SW amplitude, and that PV+ cells receive EPSCs during SWRs that strongly correlate with SW size (Mizunuma et al., 2014). Relatedly, recent experiments with *in vivo* intracellular recordings from CA3 pyramidal cells during awake SWRs have found that larger SWR events are associated with a more pronounced hyperpolarization in most neurons after the SWR; our finding provides a potential cellular source for this increased inhibition (Kajikawa et al., 2021). In the context of this previous work, our findings suggest that CA3 PVBCs provide feedback inhibition to the activated pyramidal network during SWRs, to structure temporal activity of pyramidal cell ensembles and to preclude the recurrent circuitry from sliding into a degenerated state. Together, our results indicate a complementary role of CCKs and PVBCs (Freund, 2003; Klausberger et al., 2005) in organizing pyramidal cell assembly recruitment in a predictive and reflective manner, respectively.

Our finding of a prominent pre-SWR inhibition in both CA3 AACs and CCKs also raises the critical question: What input silences these cell types, and thus may be responsible for SWR initiation? One attractive candidate is GABAergic afferents from the medial septum. Indeed, subsets of medial septal GABAergic cells have been shown to selectively target AACs and CCKs in CA3 (Joshi et al., 2017), and some medial septal GABAergic cells have been shown to be activated during hippocampal SWRs (Viney et al., 2013). However, many subcortical areas have been shown to be modulated before SWRs (Logothetis et al., 2012), some of which have known afferents to the hippocampus (Atherton et al., 2015; Prince et al., 2021). This also includes subsets of raphe cells (Varga et al., 2009) that decrease their firing rate approximately one second before SWRs (Wang et al., 2015). Furthermore, cholinergic inputs from the medial septum have been shown to regulate SWR rates, as optogenetic activation of these inputs suppresses SWRs (Vandecasteele et al., 2014). Future experiments will be necessary to determine how subcortical neuromodulators interact with defined interneuron subtypes and pyramidal cells in the CA3 network to initiate, propagate, and terminate SWRs, as well as to determine the necessity and sufficiency of each of these microcircuit components in these processes.

Our finding that CCK-expressing interneurons significantly alter their peri-SWR dynamics in response to simple sensory stimulation provides, to the best of our knowledge, the first demonstration of inhibitory plasticity around awake SWRs. It is now well appreciated that pyramidal cell recruitment to SWRs can be modulated based on the animal's experience, as pyramidal cells encoding behaviorally-relevant stimuli are robustly replayed during SWRs in time-compressed sequences (Grosmark et al., 2021; Grosmark and Buzsáki, 2016; Terada et al., 2022). This dynamic regulation of pyramidal cell recruitment to SWRs is thought to subserve memory consolidation, as behaviorally relevant representations can be preferentially consolidated into

long-term memory at the expense of less important ones. In this conceptual framework, inhibition is thought to control the precise timing of pyramidal cell firing but is not itself plastic; our findings challenge this view. We propose that the flexible modulation of CCK-expressing interneuron dynamics around SWRs, and perhaps those of other subtypes not identified in this work, can serve to regulate the flexible recruitment of pyramidal cell subsets to SWRs, profoundly influencing which hippocampal representations are preferentially consolidated into long-term memory. These results are also in agreement with a line of work suggesting that CCKs represent a highly plastic and modifiable motif of hippocampal and neocortical circuits (Del Pino et al., 2017; Hartzell et al., 2018; Klausberger et al., 2005; Yap et al., 2021). Our finding of inhibitory plasticity is especially relevant in CA3, where the recurrent circuitry is ideally suited for the rapid generation and flexible selection of pyramidal cell sequences to SWRs (Guzman et al., 2016; Kesner, 2007; Nakazawa et al., 2003; Nicola and Clopath, 2019; Rebola et al., 2017). In contrast to the highly plastic recruitment of CCKs, SWR-related activity of other inhibitory motifs (PVBCs, AACs, SOMs) remains unaltered by sensory experience. The stable recruitment of these subtypes can serve to maintain precise temporal and spatial organization (Klausberger and Somogyi, 2008) and stabilization of recurrent network dynamics (Lovett-Barron et al., 2014; Sadeh and Clopath, 2021). Alternatively, it is possible that these inhibitory motifs also exhibit plasticity during other forms of hippocampal learning. Future studies with combined molecular and physiological readouts in behaving animals are required to fully uncover both stable and plastic elements (Sadeh and Clopath, 2021; Vogels et al., 2011) in hippocampal inhibitory motifs.

3.4 Author Contributions

All authors designed the project and experiments. B.V. and T.G. performed all experiments and analysis. All authors wrote the manuscript. T.G. and A.L. oversaw all aspects of the project.

3.5 Acknowledgements

B.V. is supported by grants (NIH) T32GM007367 and (NIMH) F30MH125628. A.L. is supported by the National Institute of Mental Health (NIMH) 1R01MH124047, 1R01MH124867; National Institute of Neurological Disorders and Stroke (NINDS) 1U19NS104590 and 1U01NS115530, and the Kavli Foundation. The authors thank Zhenrui Liao and other members of the Losonczy lab for their invaluable comments on previous versions of the manuscript.

3.6 Methods

Animals

All experiments were conducted in accordance with NIH guidelines and with the approval of the Columbia University Institutional Animal Care and Use Committee. Experiments were performed with healthy, 3-5 month old, heterozygous adult male and female *VGAT-IRES-Cre* mice (Jackson Laboratory, Stock No: 016962) on a C57BL/6J background. Mice were kept in the vivarium on a reversed 12-hour light/dark cycle and housed 3-5 mice in each cage. Mice with implanted silicon probes were housed individually. Experiments were performed during the dark portion of the cycle.

Viruses

Cre-dependent recombinant adeno-associated virus (rAAV) expressing GCaMP7f under the control of the Synapsin promoter (rAAV1-Syn-FLEX-jGCaMP7f-WPRE-Sv40, Addgene #104492, titer: 1 X 10^{13} vg/mL) was used to express GCaMP7f in interneurons.

Virus injections and hippocampal window/headpost implant for CA3 imaging

For viral injections, 2 to 4-month-old *VGAT-Cre* mice were anesthetized with isoflurane and placed into a stereotaxic apparatus. Meloxicam and bupivacaine were administered subcutaneously to minimize discomfort. After the skin was cut in the midline to expose the skull, the skull was leveled, and a craniotomy was made over the right hippocampus using a drill. A sterile glass capillary loaded with rAAV1-Syn-FLEX-jGCaMP7f-WPRE-Sv40 was attached to a Nanoject syringe (Drummond Scientific) and slowly lowered into the right hippocampus. Dorsal CA3 was targeted with 2 X-Y coordinates, each one consisting of two different injection sites separated in Z: AP -1.35, ML -1.6, DV -2.1, -1.9 and AP -1.6, ML -1.9, DV -2.2, -2.0 relative to Bregma, with 50-64 nL of virus injected at each DV location. After injection, the pipette was left in place for 5-10 minutes and slowly retracted from the brain. The skin was closed with several sutures and the mice were allowed to recover for 4 days before the window/headpost implant.

The surgical procedure for CA3 window/headpost implant is very similar to the one implemented for CA1 imaging (Geiller et al., 2020). Briefly, the injected mice were anesthetized with isoflurane and placed into the stereotaxic apparatus. After subcutaneous administration of meloxicam and bupivacaine, the skull was exposed, leveled, and a 3 mm craniotomy was made over the right anterior hippocampus, centered between the two injection coordinates. The dura overlying the cortex was removed, and the cortex overlying the hippocampus was slowly removed with negative pressure while ice-cold cortex buffer was simultaneously applied. Care was taken to

not damage the lateral ventricle. This process was performed until the white, anterior-posterior fibers overlying the hippocampus became visible and any bleeding subsided. A stainless steel, 3 mm wide X 2 mm long circular cannula fitted with a glass window was inserted into the craniotomy and pushed down to sufficiently flatten the natural curvature of the anterior hippocampus. The cannula was secured in place with Vetbond applied on the skull. Subsequently, dental cement was applied to the entire skull, and a headpost was affixed to the posterior skull with dental cement. The mice received a 1.0 mL subcutaneous injection of saline and recovered in their home cage while heat was applied. The mice were monitored for 3 days post-operatively until behavioral training began.

AOD imaging

Prior to the random foraging experiments, mice first underwent a single imaging session consisting of a high-resolution structural scan. This step was necessary to obtain a reference Z-stack and derive the X-Y-Z positions of GCaMP-expressing neurons. The mice were head-fixed under a custom-modified AOD microscope (Femto3D-ATLAS, Femtonics Ltd) and anesthetized with ketamine/xylazine to reduce motion artifacts during the stack. To provide stable transmission parameters during chronic imaging in the entire 3D scanning volume, the AOD microscope was extended with a high speed and precision beam stabilization unit which was directly attached to the AOD scan head, sensitive to input beam misalignment. The beam stabilization unit consisted of two quadrant detectors (PDQ80A and TPA101, Thorlabs) and two broadband dielectric mirrors (Thorlabs) mounted on motorized mirror mounts (Femtonics). The beam alignment was performed by the LaserControl software (Femtonics). A water-immersion objective (16x Nikon CFI75) was placed above the glass window and lowered until the CA3 pyramidal cell layer was in focus. At this stage, the objective was fixed in position and focus was subsequently adjusted using AO

crystals (Szalay et al., 2016). The laser (Coherent Ultra II) was tuned to λ=920 nm. The reference Z-stack was taken starting from the approximate location of CA2 (~200-300 µm below the glass window) and extending as deep into CA3 as possible (~500-600 µm below the glass window while still being able to visualize individual interneurons). 800x800 pixel images (X-Y resolution of 1.25 µm/pixel) were taken every 4 µm. Laser power and photomultiplier (PMT) detectors (GaAsP, H10770PA-40 Hamamatsu) were compensated appropriately in Z throughout the stack (power at 20-40 mW and detector gain at 80% at the top of the stack, power at 120-150 mW and detector gain at 90% at the bottom). After completion, the mice were returned to their home cage and allowed to recover for 24h until the start of functional imaging.

Prior to simultaneous imaging and LFP experiments, the mice were not anesthetized, and the reference Z stacks were taken on the same day as functional imaging was performed. Small Z stacks of ~ 40um were taken while the mouse was immobile on the belt.

To determine X-Y-Z positions of GCaMP-expressing neurons, the Z-stack was scrolled through, and each visible interneuron was manually selected using the integrated software (MES, Femtonics Ltd) to generate a list of ~100 X-Y-Z coordinates defined as the center of each cell (~20 cells for simultaneous imaging/LFP experiments). These points constituted the centers of regions of interest (ROI) used on subsequent days for functional imaging. Each ROI was defined as a square of 40 to 50 μm^2 (chessboard scan) (Szalay et al., 2016) with a resolution of 1 to 1.5 µm/px. The advantage of the chessboard scanning method is that only neurons and small areas around the pre-selected cells are recorded. Therefore, a high ratio of the total recording time (~20-50%) is spent reading out information from the selected neurons. In contrast, volumetric imaging with the same 2P excitation provides an orders-of-magnitude worse ratio for measurement time utilization as the somata of interneurons occupy a relatively small ratio of the total scanning volume.

On each day of functional imaging, the same field of view was found using the reference Z-stack and X-Y-Z coordinates were loaded into the software to perform 3D imaging. Once all cells were in focus, 10 minute functional imaging sessions were conducted at a frame rate of 5-10 Hz for most experiments (frame rate was dependent on ROI size and resolution). For experiments involving contralateral LFP recordings, imaging was conducted at a higher rate (~40 Hz), which restricted imaging to only 10-20 cells simultaneously. During functional imaging, the laser power and detector gain were compensated based on the reference Z-stack parameters.

Silicon probe implantation, LFP recordings, and sharp-wave ripple identification

For experiments requiring simultaneous two-photon calcium imaging and LFP recordings, mice were implanted with a glass window over the hippocampus as above, and additionally a chronic, 4-channel silicon probe (Qtrode, Neuronexus) was inserted into the contralateral CA1 at a 45 degree angle. The probe was secured in place with dental acrylic and the mouse was allowed to recover for several days, as above. LFP signals were recorded with a multichannel recording system (Intan Technologies) synchronized with the AOD imaging system. The correct position of the silicon probe was confirmed by the presence of sharp-waves ripples in the data. LFP signals were recorded at 20kHz. To identify putative sharp-wave ripple events, the raw LFP signal was band-pass filtered from 150-300 Hz and thresholded at 2.5 standard deviations above the mean value within the passband. All putative sharp-wave ripple events were then manually inspected and false-positives were discarded to obtain the final set of sharp-wave ripple events used for analysis.

Behavioral paradigm

After recovery from surgery, mice were handled for several days and habituated to head-fixation. Mice were subsequently water-restricted to 85-90% of their original weight and trained to run on a single-fabric, cue-free belt. Mice were trained to operantly lick and receive water rewards (water was delivered in response to tongue contact with a capacitive sensor) at random locations along the belt. As performance improved, the number of rewards delivered on each lap decreased. After several days of training on this cue-free belt, the mice were trained for ~1 week on a 2m long, cue-rich belt for randomly delivered water rewards. For random foraging experiments, imaging was started after mice could run approximately 10 laps in 10 minutes (usually after 7-10 days of total training). For combined imaging and LFP experiments, data acquisition was started once GCaMP7f expression was optimal, hippocampal windows were clear, and the mice were habituated to head-fixation; these mice did not undergo additional behavioral training. The sensory stimulation experiments (random cue task) were performed as described previously (Terada et al., 2022) on a burlap belt. Briefly, three sensory cues (odor, light, and a non-operant water reward) were presented randomly at 15 trials per cue independently of the mouse's position on the treadmill and each cue presentation was separated by a random inter-stimulus interval of 10-15s.

Perfusion and tissue processing

After the completion of imaging experiments, mice were transcardially perfused with 40 mL of ice-cold Phosphate-Buffered Saline (PBS, Thermo Fisher), followed by 40 mL of ice-cold 4% paraformaldehyde (PFA, Electron Microscopy Sciences). Brains were stored overnight in 4% PFA at 4°C. The next day, the 4% PFA was removed and the brains were rinsed 3x5 min in PBS. 75 μm horizontal sections of the imaged hippocampus were cut on a vibrating microtome (Leica

VT1200S) and washed 3x15 minutes in PBS. Subsequently, sections were permeabilized for 2x20 minutes in PBS with 0.3% Triton X-100 (Sigma-Aldrich). Blocking was then performed with 10% Normal Donkey Serum (Jackson ImmunoResearch, Catalog #017-000-121) in PBST (PBS with 0.3% Triton X-100) for 45 minutes. The sections were then incubated in a PBS solution containing 3 primary antibodies (see below for antibody information and dilutions) for one hour at room temperature, followed by 2 days at 4°C. After 2 days, the primary antibody solution was removed from the slices and the slices were washed 3x15 minutes in PBS to remove unbound primary antibodies. The slices were subsequently incubated in a PBS solution containing a mixture of appropriate secondary antibodies conjugated to fluorescent labels (see below for antibody information and dilutions) for 2 hours at room temperature. The sections were then washed 5x15 minutes in PBS at room temperature. Finally, sections were mounted on glass slides in Fluoromount-G aqueous mounting medium (ThermoFisher Scientific) and coverslipped. The slides were allowed to dry at 4°C for at least one hour before confocal imaging (see below). After confocal imaging, the slides were submerged in PBS to remove the coverslip, and the sections were removed from the slides with gentle rocking. After washing 3x15 min in PBS and blocking with 10% Normal Donkey Serum in PBST for 45 minutes, the sections were incubated in an additional 2-3 primary antibodies. The sections were subsequently washed, incubated in secondary antibodies, washed again, and mounted and imaged, as in the first round of staining.

Immunohistochemistry (See Resources table for antibody catalog numbers)

<u>Random foraging mice (Figure 2 data):</u>

First round primary antibodies: rabbit anti-proCCK (1:500), rat anti-somatostatin (1:500), and goat anti-calbindin (1:500)

First round secondary antibodies: donkey anti-rabbit DyLight 405 (1:300), donkey anti-rat Rhodamine Red (1:300), and donkey anti-goat Alexa 647 (1:300)

Second round primary antibodies: chicken anti-PV (1:5,000) and rabbit anti-SATB1 (1:1,000)

Second round secondary antibodies: donkey anti-chicken DyLight 405 (1:300) and donkey anti-rabbit Rhodamine Red (1:300)

SWR mice (Figures 3-5 data):

First round primary antibodies: chicken anti-PV (1:5,000), rat anti-somatostatin (1:500), and rabbit anti-SATB1 (1:1,000)

First round secondary antibodies: donkey anti-chicken DyLight 405 (1:300), donkey anti-rat Rhodamine Red (1:300), and donkey anti-rabbit Alexa 647 (1:300)

Second round primary antibodies: rabbit anti-proCCK (1:500) and goat anti-calbindin (1:500)

Second round secondary antibodies: donkey anti-rabbit rhodamine red (1:300) and donkey anti-goat Alexa 647 (1:300)

Confocal imaging

Confocal imaging: A Nikon A1 confocal microscope was used to acquire multi-channel fluorescence images of the immunolabeled tissue sections. 405 nm, 488 nm, 561 nm, and 640 nm laser lines were used for excitation. Each channel was acquired sequentially with a 10x Plan Apo NA 0.45 objective (Nikon) at 1.2-1.3x Zoom. 2048x 2048 pixel images were acquired every ~3 microns through the entire depth of the tissue sections, with the pinhole size set to ~1 Airy unit. Fluorescence was collected with 2 GaAsP PMTs (488 nm and 561 nm channels) and 2 multi-alkali

PMTs (405 nm and 640 nm channels). The resulting 4-channel Z-stacks were viewed in ImageJ (NIH).

Registration of confocal images to *in vivo* Z-stacks and identification of immunopositivity/negativity

The following steps were performed by an experimenter without the use of any automated methods: First, the confocal stacks were rotated and translated until the cells in the green channel (GCaMP-labeled) matched the cells seen in the in vivo Z stack. Second, each imaged cell was found in the confocal stacks, and it was evaluated for immunopositivity or immunonegativity for the tested molecule. For a cell to be considered positive, the fluorescence intensity inside the cell had to be significantly greater than the background intensity level. A cell was considered positive for a given marker only if clear examples of immunonegative cells could be found on the same tissue section. Similarly, a cell was considered negative for a given marker only if clear examples of immunopositive cells could be found on the same tissue section. In the case of ambiguous immunolabeling, cells were discarded and not grouped into a subtype for further analysis. Overall, all efforts were made to use the most stringent criteria for cell classification prior to analysis.

Subtype assignment

Subtypes were assigned based on the immunoreactivity of cells to the five tested markers and the association between these markers and defined interneuron subtypes, based on the previous literature. All imaged cells not within the region innervated by CB-positive mossy fibers were assumed to be within CA1 and were excluded from all analyses.

PVBC: PVBCs were positive for PV and SATB1, and negative for the other three tested markers (SOM, CCK, and CB).

AAC: AACs were positive for PV but negative for SATB1, and negative for the other three tested markers (SOM, CCK, and CB).

SOM: All cells positive for Somatostatin were categorized as SOM cells. While all cells within this category were negative for CCK, some were also positive for PV, SATB1, or CB. Notably, Somatostatin/Calbindin co-expressing cells were included in this category because they represent long-range projecting interneurons located almost exclusively in *stratum oriens* of CA1-CA3 (Jinno, 2009; Jinno et al., 2007). Thus, the SOM subtype here represents putative dendrite-targeting and some long-range projecting interneurons.

CCK: CCKs were necessarily positive for CCK, and all of these cells were always negative for PV and Somatostatin. Cells within this category could express SATB1, although the vast majority of them were SATB1-negative. Although some cells within the dataset co-expressed CCK and Calbindin, the vast majority of CCK- and/or CB- expressing cells expressed only one of the two markers. Thus, CCK and Calbindin double-positive neurons were excluded from further analysis, and this category represents those cells positive for CCK only.

CB: CBs were necessarily positive for CB, and all of these cells were always negative for PV. Although some cells co-expressed Somatostatin and Calbindin, these cells were included in the SOM subtype (see above). Similarly, while some cells co-expressed CCK and CB, only the CB-positive and CCK-negative cells are included in this subtype (see above). CB cells could be either positive or negative for SATB1. Thus, this category represents putative dendrite-targeting, Calbindin-expressing interneurons (Gulyás and Freund, 1996).

Calcium imaging data preprocessing

The raw movies containing each cell were motion corrected independently using a whole-frame cross-correlation algorithm, as implemented in the SIMA software (Kaifosh et al., 2014). The time-average of each imaged cell was manually inspected and a ROI was hand-drawn over each cell. Fluorescence was extracted from each ROI using the FISSA software (Keemink et al., 2018) package to correct for neuropil contamination, using 6 patches of 50% the size of the original ROI. For each resulting raw fluorescence trace, a baseline F was calculated by taking the 1st percentile in a rolling window of 30s and a $\Delta F/F$ trace was calculated. The $\Delta F/F$ trace for each cell was smoothed using an exponential filter and all further analysis was performed on the resulting $\Delta F/F$ traces. All further analyses were implemented in Python 2.7 and are detailed below.

Locomotion and immobility modulation

To calculate the correlation between each cell's activity and the animal's velocity, the Pearson's correlation coefficient was calculated between each cell's $\Delta F/F$ trace and the smoothed velocity trace.

Run-start and run-stop responses

Run-start and run-stop events were identified in the imaging data as frames during which the animal's velocity increased above 0.2 cm/s (run-start event) or decreased below 0.2 cm/s (run-stop event). In addition, each run-start/run-stop event had to be separated from the previous run-start/run-stop event by at least several seconds to be considered as a separate event. For each event, the mean of the pre-event $\Delta F/F$ was subtracted from the mean of the post-event $\Delta F/F$ in a -3s to +3s window to calculate a response magnitude. For each cell, the run-start and run-stop response

magnitudes were averaged over all run-start and run-stop events in the given imaging experiment. If a cell was imaged across more than one imaging experiment, the average run-start and run-stop responses from each experiment were averaged over all experiments.

Spatial tuning curves

To calculate a spatial tuning curve for each imaged cell in a given experiment, the 2m treadmill was divided into 100 2cm-long bins. For each bin, we calculated the average $\Delta F/F$ from frames where the animal was in locomotion (velocity > 5cm/s). To determine whether a cell was spatially tuned during an imaging session, we generated 1,000 shuffled tuning curves by circularly rotating position in relation to $\Delta F/F$ traces (restricted to frames during locomotion). A cell was detected spatially selective if it had 10 consecutive bins (20cm) exceeding the 95^{th} percentile of the shuffle distribution (or lower than the 5^{th} percentile for negative fields). Place field centroids were calculated as the center of mass of the cell's tuning curve.

Generalized linear model

To more explicitly dissociate the effects of the various behavioral variables on each cell's activity during navigation, we developed a multivariate linear regression model to predict each cell's fluorescence activity ($\Delta F/F$) from the following behavioral variables: 1) the animal's velocity, 2) position, 3) reward, and 4) licking. The position variable was itself divided into 10 predictors, corresponding to 10x20cm segments of the treadmill. The model utilized Ridge regression to minimize the effects of potential relationships between the independent variables. The fit values (R^2) for full and reduced (lacking a given predictor) models are cross-validated with a leave-one-out procedure where 1 lap is left out in the time domain.

Peri-SWR time histogram

To construct the average peri-SWR time histogram for a given cell, the cell's ΔF/F trace was Z-scored in a -3s to +3s window around each SWR event, and the resulting peri-SWR traces were averaged together across all SWR events to obtain one trace. All SWR events were considered; none were excluded.

PCA

Decomposition of peri-SWR time histograms, hereafter referred to as PSTHs, was performed using Principal Component Analysis in the scikit-learn library. Each interneuron's average PSTH was projected onto the two first principal components and the median loadings for each subtype were calculated in PC space.

SWR activity index

For each cell, a baseline activity was calculated as the mean fluorescence activity 3s to 2s prior to a given SWR (-3 to -2s from onset) from the cell's average PSTH. Then, both a negative and positive modulation value was computed by respectively subtracting the baseline from the absolute minimum and maximum activity value in the window -1s to +1s from onset. The largest value of the two was kept. If the modulation value was derived from the maximum, the cell was considered activated; otherwise, the cell was considered inhibited.

SWR power

To obtain the amplitude of each SWR event, the broadband LFP trace between the start and end of each detected SWR event was band-pass filtered between 150-300 Hz, and the maximum of the absolute value of the filtered trace was taken as the amplitude. To compare a given cell's activity across SWR events of varying power, all SWRs which occurred during the time that cell was imaged were Z-scored. Thus, while SWR power is highly dependent on the electrode position within CA1, all comparisons were made only between SWR events that occurred on the same day in a given mouse. Additionally, because we consider only Z-scored SWR amplitudes and not absolute figures, we use the terms 'SWR amplitude' and 'SWR power' interchangeably.

To calculate PSTHs for each subtype around low- and high-power SWRs, we first calculated PSTHs around low (0-20th percentile) and high (80th-100 percentile) power SWRs for each cell. The PSTHs for all cells within a subtype were then averaged. To calculate a difference value between high- and low-power SWRs for each cell, the cell's low-power PSTH was subtracted from its high-power PSTH, and the average value of this difference curve in a 500 ms window around the SWR (-500 ms to + 500 ms) was taken as the cell's difference value. The location of the maximum difference between the high- and low-power PSTHs within this window was taken as the maximum difference.

Reflective/predictive activity

To correlate the pre-SWR activity of each cell with SWR power, the cell's ΔF/F trace was first Z-scored in a -3s to +3s window around each SWR event, as above. Then, for each SWR, the cell's average ΔF/F value in the 500ms before the event and the event's power were considered. These two sets of values were fit with a linear regression model, and the R value of the regression

was recorded. To minimize spurious correlations, only cells recorded during at least 100 SWR events were considered; the vast majority of cells were recorded for 500-1,500 SWR events. The same procedure was used to correlate the post-SWR activity of each cell with SWR power, but now the cell's average ΔF/F value in the 500 ms following each SWR event was considered.

Transient detection of CA3 pyramidal cells

Transient intervals were detected from the CA3PC data as intervals where the Z-scored activity for a given cell exceeded 2 and stayed above 0.5 for at least 0.5 seconds. The first frame of this interval was taken as the transient onset and was used for analysis.

Cue responses

The cue response for each interneuron was calculated as the difference between the mean activity from 0 to 1s after cue presentation and the baseline (-1 to 0s before), regardless of cue identity. Cue-specific responses for each subtype are reported in the Supplementary Information.

SWR modulation

To calculate the SWR modulation for a given cell, the average peri-SWR time histogram was first computed, as described above. We defined the SWR modulation as the maximum of this average trace in the 500-ms interval following the SWR event minus the average of the pre-SWR baseline (defined as the -3 to -1 second interval preceding the SWR). To compare the SWR

modulation values for a given cell between the PRE and POST sessions, the cell must have been imaged during at least 100 SWRs in both the PRE and POST sessions.

SWR recruitment

A given cell's SWR recruitment was calculated as the fraction of SWR events during which its response exceeded the 95th percentile of a shuffle distribution. The cell's response to an individual SWR was taken as the maximum of its activity within the 500-ms interval following each SWR, and the shuffle distribution was created by repeating this calculation for 1,000 randomly selected frames that occurred during immobility. To compare the SWR recruitment values for a given cell between the PRE and POST sessions, the cell must have been imaged during at least 100 SWRs in both the PRE and POST sessions.

Statistical analysis

Statistical details of comparisons are specified in either the main text or figure legends. No statistical methods were used to predetermine sample sizes, but our sample sizes are similar to those reported in previous studies. Box plots represent median and interquartile range (IQR) while whiskers extend to cover the distribution without outliers (defined as points above 1.5 IQR below or above the box edges). Bar plots represent mean and s.e.m. Between-subtype comparisons were tested using a one-way ANOVA followed by a Tukey's range test with correction for multiple testing if appropriate. For comparisons between two populations, a paired sample or unpaired t-test was applied if the data points followed a normal distribution. To analyze data that was not normally distributed, the Mann-Whitney U test was used. *, $p < 0.05$, **, $p < 0.01$, ***, $p < 0.001$. Data analysis and figures were done using custom made software in Python 2.7.15^{TM}.

Chapter 4: Discussion

4.1 Technical Strengths and Limitations of AOD-2p Imaging and *Post-hoc* Immunohistochemistry to Study Interneuron Dynamics

Taken together, the methods and approaches described in the previous two chapters of this thesis represent a significant advance in our ability to study the *in vivo* activity patterns of interneurons during behavior. While traditional imaging or electrophysiology approaches typically allow for only a handful of interneurons to be recorded from simultaneously, the AOD-based 2p imaging approach described here allows for hundreds of hippocampal interneurons dispersed in 3D to be recorded from simultaneously during behavior, with high signal-to-noise, speed, and longitudinal tracking. The integration of this large-scale imaging approach with *post-hoc* immunohistochemistry allows for more detailed subtype information to be obtained from the recorded cells compared to traditional imaging approaches in Cre lines. In addition, while imaging or optotagging approaches utilizing Cre lines typically record from one interneuron subtype at a time, the approaches utilized here allow for the imaging of several different interneuron subtypes simultaneously. This advantage is particularly critical for understanding the overall dynamics of inhibitory circuits, as network activity and behavior are orchestrated by many different cell types working together. Finally, the integration of the AOD-based 2p imaging approach described here with simultaneous LFP recordings allows, for the first time, for the population-level activity of defined interneuron subtypes to be related to network oscillatory patterns implicated in cognition and behavior, such as SWRs.

Nevertheless, both calcium imaging of interneurons and *post-hoc* immunohistochemistry suffer from several technical limitations which together impede a more detailed understanding of interneuron dynamics during behavior. First, calcium imaging is not ideal for measuring neural

activity from fast-spiking GABAergic cell types, such as PVBCs, as small changes in constantly high firing rates likely lead to relatively small changes in the collected fluorescence signal, and the collected fluorescence may saturate at high firing rates. At the opposite end of the spectrum, it is not known whether single spikes from low firing-rate GABAergic interneurons, such as Ivy cells, would be visible in calcium fluorescence traces *in vivo*. Thus, some of the differences in interneuron dynamics observed between the different subtypes with calcium imaging may be due to heterogeneities in the spike-to-calcium relationship for the different subtypes. In any case, calcium imaging does not have the temporal resolution to resolve single spikes from interneurons, which may prove important for fine control over hippocampal network activity as a single interneuron may contact hundreds of pyramidal cells. In addition, as with all imaging approaches in scattering tissues, the ability to collect dynamic signals at cellular resolution degrades with the imaging depth. As some interneuron subtypes are preferentially located in certain hippocampal sublayers (such as CCK cells in SR), and these sublayers are located deeper within hippocampal CA1, it is likely more difficult to collect dynamic fluorescence signals from these cells when imaging in CA1. In CA3, on the other hand, this is likely less of a problem, as in our approach all the hippocampal sublayers are located within the same imaging plane, reducing the potential subtype bias related to imaging depth. The ability to record detailed dynamics from interneuron subtypes will likely be improved significantly with advances in voltage imaging techniques in the coming years. Voltage imaging allows for both single spikes and subthreshold voltage dynamics to be recorded from single cells during behavior, facilitating more detailed analysis of interneuron dynamics. However, current instantiations of voltage imaging are typically performed in superficial brain regions (Fan et al., 2020). In addition, because current genetically-encoded voltage indicators bleach quickly, voltage recordings are

typically limited in duration. The development of voltage indicators that are photostable and compatible with deep imaging will allow for unbiased voltage recordings across sublayers with single spike resolution to be conducted over the course of learning tasks that take several days or weeks to perform. While the development of voltage imaging approaches will undoubtedly continue to advance towards these goals, the parallel development of better calcium indicators will also facilitate the study of interneuron dynamics during behavior. For example, the recent development of genetically-encoded calcium sensors with faster rise-times, higher signal-to-noise ratios, and a higher sensitivity to single spikes, such as GCaMP8m, will likely allow for more detailed analysis of interneuron dynamics than conducted with the calcium sensors used in the experiments presented here.

While calcium imaging of interneurons suffers from these technical limitations, *post-hoc* immunohistochemistry also suffers from limitations in cell-type identification. In practice, the antibody-based immunohistochemistry methods employed here are compatible with staining for only a handful of markers simultaneously (~5-6). However, this multiplexing capacity only allows for a subset of hippocampal interneurons to be identified in each mouse, and in many cases only broad classes of interneurons are identifiable (eg. SOM-expressing). Ideally, *post-hoc* methods for molecular identification would preserve the spatial relationships between cells while allowing each cell to be tested for the presence of hundreds or thousands of genes. The further development and improvement of spatial transcriptomics methods, as recently applied in the neocortex, will likely facilitate similar studies in the hippocampus (Bugeon et al., 2021).

Lastly, while the simultaneous imaging and LFP recording approaches described here allow for the population-level dynamics of identified cell types to be related to SWR events, the fact that the LFP is recorded from the contralateral hippocampus is a limitation. Although many

SWR events spread to both hippocampi, some smaller events are likely confined to one hemisphere (Buzsáki, 2015). Thus, although the activity patterns of the different interneuron subtypes can be compared by averaging their activity over many SWR events, it is difficult to analyze responses at the single SWR level. The development of approaches allowing simultaneous imaging and ipsilateral LFP recordings will facilitate these analyses (Liu et al., 2021).

Although these large-scale, unbiased, cell-type specific functional imaging techniques will be foundational for understanding the roles of inhibitory circuits in orchestrating cortical network activity and behavior, these approaches should be complemented with other approaches for this purpose. First, to test the role of specific interneuron subtypes in controlling network activity and behavior, the activation or inhibition of specific subtypes should be performed via expression of pharmacogenetic or optogenetic actuators in Cre-driver lines. These methods should be complemented with network activity or behavioral readouts. For example, the *in vivo* inhibition of SOM+ and PV+ cells in CA1 has been shown to have largely dissociable effects on local pyramidal cell activity: While SOM+ cell silencing significantly increases the burst firing of pyramidal cells, PV+ cell silencing alters the timing of pyramidal cell spikes relative to extracellular theta oscillations (Royer et al., 2012). These experiments demonstrate a role for SOM+ and PV+ cells in regulating pyramidal cell burst firing and spike timing, respectively. Similar approaches can be expanded to other interneuron subtypes and hippocampal (or neocortical) subregions. Although these approaches are limited to cell types for which there exists a Cre-driver line (PV, SOM cells), the development of novel Cre-lines specific for different interneuron subtypes will allow the scope of these experiments to be expanded. For example, in the last few years, the development of Unc5b-Cre and Sncg-FlpO mice will allow

for these experiments to be performed in AACs and CCK basket cells, respectively (Dudok et al., 2021a, 2021b). Second, these functional approaches should be complemented with anatomical experiments to further our understanding of the inputs to specific interneuron subtypes. For this purpose, subtype-specific Cre lines can also be used to perform retrograde, monosynaptic (Rabies) tracing from defined interneurons. These studies will provide important clues regarding the sources of the unique functional dynamics of distinct subtypes observed during imaging experiments; these hypotheses can then in turn be directly tested with pharmacogenetic or optogenetic manipulations.

4.2 Locomotion-State Dependent Activity of Hippocampal Interneuron Subtypes

Taken together, the two studies described in this thesis demonstrate an overall positive correlation between the animal's velocity and the activity of most interneuron subtypes, both in CA1 and CA3. These results suggest that the overall positive velocity modulation observed is a general property of interneurons across the hippocampus, and perhaps across the neocortex as well. Future studies should aim to determine the circuit mechanisms underlying this overall positive velocity modulation.

As subcortical neuromodulators have been shown to generally increase their activity during locomotion and other periods of heightened arousal and project extensively to the hippocampus, they are prime targets for these studies. In neocortical V1, acetylcholine release was shown to modulate the activity of interneurons (Fu et al., 2014), which in turn modulated the response selectivity of excitatory cells. Experiments in the hippocampus could silence different neuromodulatory inputs during locomotion with simultaneous interneuron imaging to determine the role of each input in the influencing the increased interneuron activity during locomotion. For these studies, cholinergic inputs from the medial septum, noradrenergic inputs from the locus

coeruleus, and serotonergic inputs from the dorsal/median raphe could be silenced with optogenetic terminal inhibition.

Perhaps more interestingly, the two studies described in this thesis each described one interneuron subtype that contains a large fraction of preferentially immobility-activated cells: CCK cells in CA1 and CB cells in CA3. Although these observations were made in different hippocampal subregions, what is known about the inputs to CCK cells and CB interneurons in CA1 may hint at the circuit mechanisms responsible for their immobility activation. Both CCKBCs and CB-expressing cells in CA1 have been shown to receive large fractions of inhibitory synapses compared to other interneuron subtypes (Gulyás et al., 1999; Matyas et al., 2004), especially at their soma. This could potentially explain how these cells are silenced during locomotion, when most interneurons are activated and would provide them with a strong inhibitory drive. Although the neuronal sources of these inhibitory synapses onto CCK basket cells and CB-expressing interneurons were not identified in these studies, several possibilities exist. Classical anatomical experiments have shown that subtypes of VIP- and CR-expressing interneurons (Type I and Type II, but not Type III, ISIs) form climbing fiber synapses along the dendritic arbors of CCK- and CB-expressing cells (Acsády et al., 1996b; Gulyás et al., 1996). By contrast, more recent optogenetic experiments have shown that activation of PV+ interneurons in CA1 is sufficient to reduce the activity of CCK basket cells during immobility (Dudok et al., 2021a). In addition, activation of PV+ cells in CA1 was shown to prevent the run-stop activation of CCK basket cells (Dudok et al., 2021a). Thus, while the interneuron subtypes responsible for the strong inhibitory drive onto CCK+ and CB+ cells remain under debate, it is likely that inhibition from other local interneurons can explain their activity suppression during locomotion.

While the data from the two studies described in this thesis demonstrate that CCK cells in CA1 and CB cells in CA3 are suppressed during locomotion, they also show that both of these cell types remain strongly activated over long immobility intervals. Thus, it is likely that these subtypes both receive an excitatory input that is activated during immobility epochs, and a single input that preferentially targets both CCK and CB cells would provide a unifying explanation. Although such an immobility-activated input remains to be found, neuromodulatory afferents are again attractive candidates (Atherton et al., 2015; Kaufman et al., 2020; Prince et al., 2021). Of particular interest, serotonergic afferents from the median raphe have been shown to selectively target CCK and CB cells in CA1 (Freund et al., 1990; Varga et al., 2009), and certain serotonin receptor subtypes, such as the 5-HT3A receptor, are directly depolarizing. Thus, immobility-related signals carried to the hippocampus by these median raphe fibers could be capable of mediating the immobility-related activation of CCK and CB interneurons. This hypothesis could be directly tested with optogenetic or pharmacologic manipulations and simultaneous imaging of interneurons during locomotion and immobility epochs. First, the serotonergic fibers to the hippocampus from the median raphe could be silenced during immobility epochs with simultaneous interneuron imaging to determine whether this manipulation decreases the immobility-activation of CCK and CB interneurons. Conversely, these fibers could be optogenetically activated during locomotion epochs to determine whether their activation is sufficient to active CCK and CB interneurons during locomotion, when their activity would otherwise be suppressed. Furthermore, these ascending serotonergic fibers could be imaged in the hippocampus to determine their endogenous dynamics during locomotion and immobility epochs, although it is likely that heterogenous responses from these fibers would be observed, with some being locomotion-activated and others immobility-activated. Thus, it would be critical

to know which subset of these fibers target CCK and/or CB cells, although this would be challenging to determine experimentally. These heterogeneous responses from serotonergic fibers would be in accordance with the significant molecular and anatomical heterogeneity observed among serotonergic neurons within the raphe nucleus (Huang et al., 2019). A complementary set of experiments could utilize pharmacological approaches to antagonize various neuromodulatory receptors (especially serotonin receptors) in the hippocampus before and after interneuron imaging to determine the role of various receptors in mediating the immobility-activation of CCK and CB cells. As the 5-HT3A receptor has been shown to be expressed by significant subsets of both CCK and CB interneurons (Morales and Bloom, 1997) and it is directly depolarizing (ionotropic), it represents an attractive first target to antagonize with 5-HT3A blockers such as ondansetron. However, similar experiments could be repeated with antagonists for some of the metabotropic serotonin receptors, as well as with antagonists for receptors of other neuromodulatory systems (i.e., acetylcholine, norepinephrine).

Although neuromodulatory systems (especially serotonin) should be thoroughly explored for their role in mediating the immobility-activation of CCK and CB interneurons, other possible circuit mechanisms should also be considered. For example, significant fractions of CA2 pyramidal cells have been shown to be preferentially active during immobility epochs (Kay et al., 2016), and CA2 pyramidal cells have been shown to project both to CA1 and to CA3 (Dudek et al., 2016). Although CA2 pyramidal cells preferentially project to CA1 SO over SR, no evidence exists for target specificity at the level of interneuron subtypes. Recent experiments have tested the hypothesis that glutamatergic afferents to CA1 may carry immobility-related activity by imaging the various glutamatergic inputs to CA1 (CA2, CA3, MEC, and LEC inputs) during locomotion and immobility (Dudok et al., 2021a). These experiments found little, if any,

prominent immobility-related signals in these afferents (Dudok et al., 2021a). Thus, taken together with the lack of evidence supporting the idea that these glutamatergic afferents may target specific interneuron subtypes, these experiments suggest that other inputs should be considered.

The finding that CA3 CB interneurons comprise two functionally distinct subpopulations with regards to their activity during locomotion and immobility, and that these subpopulations strongly correlate with expression of the transcription factor SATB1, provides another important clue regarding the mechanisms underlying the immobility-activation of CCK and CB interneurons. As SATB1 acts downstream of other transcription factors that specify an origin from the MGE and is thus enriched in MGE-derived interneurons (Close et al., 2012; Denaxa et al., 2012), our finding suggests that the functional dichotomy we observe in CB-expressing interneurons may represent differences between MGE- and CGE-derived CB interneurons: MGE-derived CB interneurons may be preferentially activated during locomotion, while CGE-derived CB interneurons may be preferentially activated during immobility. Interestingly, to date, all hippocampal interneuron subtypes that have been shown to have a robust immobility activation are CGE-derived, including CCK basket cells (Dudok et al., 2021a), VIP/M2R interneurons (Francavilla et al., 2018), and here CB+/SATB1- interneurons. In addition, hippocampal interneuron subtypes that have split lineages between the MGE and the CGE, such as SOM+ OLM cells (Chittajallu et al., 2013), have been shown to comprise small, yet significant, subpopulations of immobility-activated neurons (Arriaga and Han, 2017; Turi et al., 2019). On the other hand, subtypes that are exclusively derived from the MGE, such as the PV+ subtypes (PVBCs, AACs, and BiCs), are more uniformly activated during locomotion (Arriaga and Han, 2017; Turi et al., 2019). Together, these findings suggest that CB+/SATB1+ and

CB+/SATB1- interneurons receive very different inputs that can explain their locomotion and immobility activation, respectively. In addition, these differences in synaptic inputs may generalize to MGE- and CGE-derived interneurons as a whole, potentially linking an interneuron's developmental origin, input connectivity in the adult hippocampal circuitry, and functional phenotype during behavior. To further understand these links between development, connectivity, and function, it would be very useful to compare the number and distribution of excitatory and inhibitory synaptic inputs onto MGE- and CGE-derived interneurons, for example between CB+/SATB1+ and CB+/SATB1- cells. The recent development of methods enabling the mapping of excitatory and inhibitory synapses across the whole dendritic arbor of individual neurons should facilitate these studies (Iascone et al., 2020). In addition, it would be useful to perform interneuron imaging experiments, similar to the ones described in this thesis, but with either the MGE- or the CGE-derived cells labeled (for example, with a static red marker). This would allow the functional properties of interneurons, such as locomotion-activation or immobility-activation, to be directly related with their developmental origin. Lastly, the development of more specific Cre-driver lines for various interneuron subtypes will enable circuit mapping experiments to be performed to compare the inputs to MGE- and CGE-derived interneurons.

4.3 Spatial Tuning of Hippocampal Interneurons during Navigation

Although place cells have been traditionally considered to be hippocampal pyramidal cells (O'Keefe and Dostrovsky, 1971), spatial tuning has also been reported for sparse subsets of interneurons, although without subtype identification (Ego-Stengel and Wilson, 2007; Grienberger et al., 2017; Hangya et al., 2010; Marshall et al., 2002; Wilent and Nitz, 2007).

However, as these studies were conducted with few recorded interneurons and without rigorous subtype identification, it has remained an open question whether some interneuron subtypes display significant spatial tuning at the population level. Together, the two studies in this thesis show that considerable subsets of interneurons, both within CA1 and CA3, display both positive and negative spatial tuning during spatial navigation tasks. However, both within CA1 and CA3, the spatially tuned cells did not preferentially belong to one particular subtype but were rather present in similar proportions between the various interneuron subtypes.

The presence of spatially tuned interneurons within each subtype may be explained by strong functional connectivity between interneurons and local spatially tuned pyramidal cells that target the various interneuron subtypes with an approximately equal probability. With this type of connectivity, interneurons could inherit their spatial selectivity from presynaptic pyramidal cells, as pyramidal cells have been shown to be capable of reliably discharging local interneurons (Marshall et al., 2002). Within CA1, interneurons with vertical dendritic morphologies could inherit their spatial tuning from upstream CA3 pyramidal cells in a feedforward manner, while interneurons with horizontal dendritic morphologies could inherit their spatial tuning form local CA1 pyramidal cells in a feedback manner. Because many interneuron subtypes consist of some cells with vertical morphologies and others with horizontal morphologies, a combination of CA3 and CA1 input may be responsible for the spatial tuning observed within each subtype. Similarly, within CA3, local interneurons may inherit their spatial selectivity from presynaptic dentate granule cells in a feedforward manner, or from presynaptic CA3 pyramidal cells in a feedback manner.

Recent experiments within CA1 have utilized *in vivo* single-cell electroporation to initiate retrograde Rabies viral tracing from single CA1 pyramidal cells and perform simultaneous

recordings from single CA1 pyramidal cells and networks of presynaptic interneurons (Geiller et al., 2022). These experiments revealed tight links between the spatial tuning of pyramidal cells and their presynaptic interneurons during navigation. In principle, the same approach could be extended to single interneurons and networks of presynaptic pyramidal cells to probe how single interneurons inherit their spatial tuning from local presynaptic interneurons. Additionally, interneurons of different subtypes can be systematically targeted with Cre-drive lines for single-cell electroporation (PV+ cells, SOM+ cells, VIP+ cells, Unc5b+ cells, Sncg+ cells) and subsequent recording and presynaptic labeling, enabling the relationship between the activity of presynaptic pyramidal cells and postsynaptic interneurons to be probed for the various subtypes.

4.4 Interneuron Activity Supporting Hippocampal Network Dynamics during Context Change and Spatial Learning

Decades of research have examined how CA1 pyramidal cell dynamics are modulated by environmental manipulations, such as by context change or in response to reward. However, much less is know about how interneuron dynamics are modulated at the population level during similar manipulations. The experiments described in Chapter 2 of this thesis demonstrate that most CA1 interneuron subtypes (PVBC, AAC, SOM, and Bistr) decrease their activity upon novel context exposure, and SOM and Bistr subtypes are preferentially recruited in response to learning a rewarded spatial location.

CA1 pyramidal cells exhibit both rate and place remapping in response to context change (Colgin et al., 2008). Notably, during the first several minutes of novel context exploration, the firing rate of most pyramidal cells is significantly increased, with many cells displaying burst firing (Priestley et al., 2021). This observation has been recently extended with virtual reality

experimental setups that enable precise, rapid, and flexible contextual manipulations (Priestley et al., 2021) and is thought to reflect a period of enhanced synaptic plasticity that enables rapid place field formation in novel environments. Critically, the circuit mechanisms supporting the pyramidal cell burst firing in novel environments remain unknown. The decreased activity of both dendrite- and perisomatic-targeting subtypes, observed both in the experiments described in this thesis and in other studies (Arriaga and Han, 2019; Hainmueller and Bartos, 2018; Sheffield et al., 2017), suggests that this decreased activity may be responsible for the burst firing of pyramidal cells. Indeed, it has already been shown that transient optogenetic silencing of SOM-expressing, dendrite-targeting interneurons can induce the burst firing of pyramidal cells, both *in vitro* and *in vivo* (Lovett-Barron et al., 2012; Royer et al., 2012). This decreased dendritic inhibition naturally observed during novel context exposure could function to open windows of increased synaptic plasticity, during which spatially tuned excitatory inputs may have preferential ability to shape selectivity of CA1 pyramidal cells.

These related observations of decreased inhibition and pyramidal cell burst firing in the first few minutes of novel context exposure provide an exciting opportunity to dissect the circuit mechanisms responsible for these circuit dynamics, which are likely to support the ability of the hippocampus to form rapid representations of new experiences. Future studies should leverage virtual reality with imaging and manipulation of the various CA1 microcircuit components during novel context exposure to fully describe the responsible circuit elements. The inhibition of both PV- and SOM-expressing subtypes could be explained by the increased activity of disinhibitory circuit elements, such as VIP-expressing cells, during novel context exposure. As the dynamics of VIP-expressing interneurons during novel context exposure have yet to be

reported, these imaging experiments could be performed either with VIP-Cre transgenic lines or with the post-hoc immunolabeling strategy described in this thesis.

In addition to disinhibitory interneurons, neuromodulatory inputs to the hippocampus could modulate both PV- and SOM-expressing interneurons and pyramidal cells during novel context exposure. Both brainstem and basal forebrain neuromodulators, including noradrenergic neurons in the locus coeruleus, serotonergic neurons in the median and dorsal raphe, and cholinergic neurons in the medial septum send extensive projections to the hippocampus and have shown to be highly sensitive to novelty (Takeuchi et al., 2016; Teles-Grilo Ruivo and Mellor, 2013). These neuromodulatory afferents may be critical for the ability of the hippocampus to create rapid representations of novel experiences via a wide diversity of ionotropic and metabotropic receptors, expressed on both pyramidal cells and interneurons. Future experiments should systematically examine the dynamics of these neuromodulatory afferents during novel context exposure in virtual reality environments with axonal two-photon imaging (Kaufman et al., 2020). A second set of experiments could combine optogenetic manipulation of the various neuromodulatory afferents with simultaneous imaging of pyramidal cells or interneurons to determine their respective roles in regulating circuit dynamics. Together, these studies are likely to develop a more complete description of the neural circuit dynamics supporting the rapid formation of novel episodic memories in the hippocampus.

In addition to context change, CA1 pyramidal cell dynamics have been extensively studied in response to reinforcement or spatial reward learning (Hollup et al., 2001; Kaufman et al., 2020; Zaremba et al., 2017). For example, during the GOL task described in Chapter 2 of this thesis, CA1 place fields are enriched at the rewarded location along the belt, creating a population representation of the environment that is thought to support learning (Kaufman et al.,

2020; Zaremba et al., 2017). The enriched activity of SOM and Bistr cells that develops at the rewarded location over the course of learning in the GOL task, as described in Chapter 2 of this thesis, is thus likely due to the pyramidal cell overrepresention at the reward. Indeed, SOM and Bistr interneurons are anatomically positioned to receive strong inputs from local pyramidal cells, as they are primarily located in SO with horizonal dendrites. This increased activity of SOM and Bistr cells could provide a feedback signal to CA1PC dendrites, regulating the extent of the pyramidal cell overrepresentation (pyramidal cell ensemble size). Optogenetic silencing of these two subtypes at the reward zone location of the GOL task could be performed in SOM-Cre mice with simultaneous pyramidal cell imaging to causally test the role of these cell types in regulating the pyramidal cell representation at the reward. As the SOM and Bistr dynamics follow, rather than lead, the pyramidal cell dynamics during the GOL task, it is unlikely that they play a prominent role in the formation of the pyramidal cell overrepresentation at the reward zone.

In summary, although CA1 pyramidal cell dynamics have been shown to change in relatively similar ways during two common experimental manipulations, namely context change and reward learning (with burst firing and increased place field density, respectively), the interneuron dynamics are very different, suggesting different circuit mechanisms supporting these two processes.

4.5 Role of Local Interneurons in SWR Generation and Termination

Early seminal studies of hippocampal interneuron activity reported subtype-specific firing patterns from single interneurons during SWRs under anesthesia (Klausberger et al., 2003; Klausberger and Somogyi, 2008). Of particular interest, CA3 AACs were found to be inhibited

during SWRs under anesthesia with juxtacellular recordings (Viney et al., 2013). As it was originally proposed that SWRs are generated by the disinhibition of recurrently connected CA3 pyramidal cells (Buzsáki, 1986), it was subsequently hypothesized that the inhibition of AACs, and the resulting disinhibition of the axon initial segment of CA3 pyramidal cells, may be a necessary condition for SWR occurrence (Somogyi et al., 2014). However, as these data consisted of only a few identified AACs recorded under anesthesia and the dynamics of other CA3 interneuron subtypes around *in vivo* SWRs remained unknown, this hypothesis lacked experimental support. The studies described in this thesis provide the first large-scale datasets regarding the *in vivo* dynamics of defined interneuron subtypes in both CA1 and CA3 around awake SWRs. Although similar dynamics were observed for each subtype in CA1 and CA3, the CA3 data is of particular interest, as it offers important clues regarding the mechanisms of SWR initiation and termination. The finding that the majority of CA3 AACs and CCKs are inhibited, starting hundreds of milliseconds before the SWR event, but only the magnitude of the CCK inhibition correlates with the power of the SWR event, is significant as it implicates CCK interneurons in either generating SWRs or in controlling the size of the recruited CA3 pyramidal cell ensemble and the resulting SWR power. On the other hand, AAC inhibition may indeed be a necessary condition for SWR generation in the CA3 recurrent network, but the finding that this inhibition does not scale with the SWR power suggests that it is not causal. Similarly, the finding that the size of CA3 PVBC activation after the SWR event scales with the power of the SWR implicates PVBCs in controlling the recruited CA3 pyramidal cell ensemble size and in terminating SWRs.

To test the role of various subtypes in initiating or terminating SWRs, optogenetic activation or inhibition experiments can now be performed with simultaneous imaging of the

CA3 pyramidal cell network and combined LFP recordings. For example, it would be interesting to test whether inhibition of either CA3 AACs or CCKs is sufficient to depolarize the surrounding CA3 pyramidal cells and trigger SWRs during immobility. These experiments can now be performed, given the recent development of Cre-drive lines targeting AACs and CCKBCs (Dudok et al., 2021b, 2021a). Conversely, one could test whether the inhibition of either one of these subtypes is necessary for SWRs to occur by activating these subtypes in a closed-loop manner upon SWR onset (Girardeau et al., 2009). Additionally, this approach could be extended to causally test the role of PVBCs in SWR termination.

A complementary line of experiments could search for the input mediating the pre-SWR inhibition of AACs and CCKs. This effort could entail both high-throughput connectivity studies with Rabies tracing experiments in AAC- and CCKBC-specific Cre-driver lines, and functional imaging experiments of candidate inputs with simultaneous LFP recordings. Of particular interest are again neuromodulatory inputs to the hippocampus, including cholinergic and GABAergic inputs from the medial septum, and serotonergic and glutamatergic inputs from the raphe (Somogyi et al., 2014; Varga et al., 2009; Viney et al., 2013; Wang et al., 2015). However, the Rabies tracing experiments may identify additional inputs that could be explored as well.

4.6 Role of Local Interneurons in Regulating Pyramidal Cell Recruitment to SWRs

Since the first interneuron recordings during SWRs, it has been thought that an interneuron's activation or inhibition around SWRs depends primarily on its subtype, and that this functional property does not change significantly with the animal's experience. However, this hypothesis has remained largely untested, as most interneuron recordings during SWRs to date have been performed under anesthesia, and thus have not been performed over the course of

behavior. Thus, the finding that CA3 CCK-expressing interneurons significantly alter their peri-SWR dynamics in response to simple sensory stimulation, described in the second study of this thesis, provides the first demonstration of inhibitory plasticity around awake SWRs. It is tempting to speculate that this inhibitory plasticity could in turn regulate which pyramidal cells are recruited to SWRs based on their behavioral relevance.

Future experiments should systematically examine how subtype-specific inhibitory dynamics change around awake SWRs in response to various learning tasks, especially hippocampal-dependent behaviors. Regarding the simple sensory stimulation task described here, it would be interesting to determine, in future experiments, if the cue-driven activity of CCK interneurons during sensory stimulation is required for the peri-SWR plasticity observed. Specifically, these cells could be optogenetically silenced during cue stimulation, and the resulting activity around SWRs could be compared. Additionally, this manipulation could be performed to examine whether the experience-dependent suppression of cue-responsive CA3 pyramidal cells around SWRs requires this inhibitory plasticity (Terada et al., 2022).

References

Acharya, L., Aghajan, Z.M., Vuong, C., Moore, J.J., Mehta, M.R., 2016. Causal Influence of Visual Cues on Hippocampal Directional Selectivity. Cell 164, 197–207. https://doi.org/10.1016/j.cell.2015.12.015

Acsády, L., Arabadzisz, D., Freund, T.F., 1996a. Correlated morphological and neurochemical features identify different subsets of vasoactive intestinal polypeptide-immunoreactive interneurons in rat hippocampus. Neuroscience 73, 299–315. https://doi.org/10.1016/0306-4522(95)00610-9

Acsády, L., Görcs, T.J., Freund, T.F., 1996b. Different populations of vasoactive intestinal polypeptide-immunoreactive interneurons are specialized to control pyramidal cells or interneurons in the hippocampus. Neuroscience 73, 317–334. https://doi.org/10.1016/0306-4522(95)00609-5

Acsády, L., Kamondi, A., Sík, A., Freund, T., Buzsáki, G., 1998. GABAergic cells are the major postsynaptic targets of mossy fibers in the rat hippocampus. J. Neurosci. 18. https://doi.org/10.1523/jneurosci.18-09-03386.1998

Ahmed, O.J., Mehta, M.R., 2009. The hippocampal rate code: anatomy, physiology and theory. Trends Neurosci. https://doi.org/10.1016/j.tins.2009.01.009

Armstrong, C., Krook-Magnuson, E., Soltesz, I., 2012. Neurogliaform and Ivy Cells: A Major Family of nNOS Expressing GABAergic Neurons. Front. Neural Circuits 6, 1–10. https://doi.org/10.3389/fncir.2012.00023

Aronov, D., Nevers, R., Tank, D.W., 2017. Mapping of a non-spatial dimension by the hippocampal-entorhinal circuit. Nature 543. https://doi.org/10.1038/nature21692

Arriaga, M., Han, E.B., 2019. Structured inhibitory activity dynamics in new virtual

environments. Elife 8. https://doi.org/10.7554/eLife.47611

Arriaga, M., Han, E.B., 2017. Dedicated hippocampal inhibitory networks for locomotion and immobility. J. Neurosci. 37, 9222–9238. https://doi.org/10.1523/JNEUROSCI.1076-17.2017

Atherton, L.A., Dupret, D., Mellor, J.R., 2015. Memory trace replay: The shaping of memory consolidation by neuromodulation. Trends Neurosci. https://doi.org/10.1016/j.tins.2015.07.004

Azim, E., Jabaudon, D., Fame, R.M., MacKlis, J.D., 2009. SOX6 controls dorsal progenitor identity and interneuron diversity during neocortical development. Nat. Neurosci. 12. https://doi.org/10.1038/nn.2387

Bartos, M., Vida, I., Jonas, P., 2007. Synaptic mechanisms of synchronized gamma oscillations in inhibitory interneuron networks. Nat. Rev. Neurosci. https://doi.org/10.1038/nrn2044

Basu, J., Siegelbaum, S.A., 2015. The corticohippocampal circuit, synaptic plasticity, and memory. Cold Spring Harb. Perspect. Biol. https://doi.org/10.1101/cshperspect.a021733

Batista-Brito, R., Rossignol, E., Hjerling-Leffler, J., Denaxa, M., Wegner, M., Lefebvre, V., Pachnis, V., Fishell, G., 2009. The Cell-Intrinsic Requirement of Sox6 for Cortical Interneuron Development. Neuron 63. https://doi.org/10.1016/j.neuron.2009.08.005

Bazelot, M., Teleńczuk, M.T., Miles, R., 2016. Single CA3 pyramidal cells trigger sharp waves in vitro by exciting interneurones. J. Physiol. 594. https://doi.org/10.1113/JP271644

Bezaire, M.J., Soltesz, I., 2013. Quantitative assessment of CA1 local circuits: Knowledge base for interneuron-pyramidal cell connectivity. Hippocampus 23, 751–785. https://doi.org/10.1002/hipo.22141

Bland, B.H., Oddie, S.D., Colom, L. V., 1999. Mechanisms of neural synchrony in the

septohippocampal pathways underlying hippocampal theta generation. J. Neurosci. 19. https://doi.org/10.1523/jneurosci.19-08-03223.1999

Bloss, E.B., Cembrowski, M.S., Karsh, B., Colonell, J., Fetter, R.D., Spruston, N., 2016. Structured Dendritic Inhibition Supports Branch-Selective Integration in CA1 Pyramidal Cells. Neuron 89, 1016–1030. https://doi.org/10.1016/j.neuron.2016.01.029

Booker, S.A., Vida, I., 2018. Morphological diversity and connectivity of hippocampal interneurons. Cell Tissue Res. https://doi.org/10.1007/s00441-018-2882-2

Bostock, E., Muller, R.U., Kubie, J.L., 1991. Experience-dependent modifications of hippocampal place cell firing. Hippocampus 1. https://doi.org/10.1002/hipo.450010207

Botcher, N.A., Falck, J.E., Thomson, A.M., Mercer, A., 2014. Distribution of interneurons in the CA2 region of the rat hippocampus. Front. Neuroanat. 8. https://doi.org/10.3389/fnana.2014.00104

Brown, K.N., Chen, S., Han, Z., Lu, C.H., Tan, X., Zhang, X.J., Ding, L., Lopez-Cruz, A., Saur, D., Anderson, S.A., Huang, K., Shi, S.H., 2011. Clonal production and organization of inhibitory interneurons in the neocortex. Science (80-.). 334. https://doi.org/10.1126/science.1208884

Brun, V.H., Leutgeb, S., Wu, H.Q., Schwarcz, R., Witter, M.P., Moser, E.I., Moser, M.B., 2008. Impaired Spatial Representation in CA1 after Lesion of Direct Input from Entorhinal Cortex. Neuron 57. https://doi.org/10.1016/j.neuron.2007.11.034

Bugeon, S., Duffield, J., Dipoppa, M., Prankerd, I., Ritoux, A., Nicoloutsopoulos, D., Orme, D., Shinn, M., Peng, H., Forrest, H., Viduolyte, A., Reddy, C.B., Isogai, Y., Carandini, M., Harris, K.D., 2021. A transcriptomic axis predicts state modulation of cortical interneurons. bioRxiv.

Buhl, E.H., Halasy, K., Somogyi, P., 1994. Diverse sources of hippocampal unitary inhibitory postsynaptic potentials and the number of synaptic release sites. Nature 368, 823–828. https://doi.org/10.1038/368823a0

Buhl, E.H., Szilágyi, T., Halasy, K., Somogyi, P., 1996. Physiological properties of anatomically identified basket and bistratified cells in the CA1 area of the rat hippocampus in vitro. Hippocampus 6, 294–305. https://doi.org/10.1002/(SICI)1098-1063(1996)6:3<294::AID-HIPO7>3.0.CO;2-N

Buzsáki, G., 2015. Hippocampal sharp wave-ripple: A cognitive biomarker for episodic memory and planning. Hippocampus 25, 1073–1188. https://doi.org/10.1002/hipo.22488

Buzsáki, G., 1989. Two-stage model of memory trace formation: A role for "noisy" brain states. Neuroscience 31. https://doi.org/10.1016/0306-4522(89)90423-5

Buzsáki, G., 1986. Hippocampal sharp waves: Their origin and significance. Brain Res. 398. https://doi.org/10.1016/0006-8993(86)91483-6

Capogna, M., 2011. Neurogliaform cells and other interneurons of stratum lacunosum-moleculare gate entorhinal-hippocampal dialogue. J. Physiol. 589, 1875–1883. https://doi.org/10.1113/jphysiol.2010.201004

Caputi, A., Melzer, S., Michael, M., Monyer, H., 2013. The long and short of GABAergic neurons. Curr. Opin. Neurobiol. https://doi.org/10.1016/j.conb.2013.01.021

Cembrowski, M.S., Wang, L., Sugino, K., Shields, B.C., Spruston, N., 2016. Hipposeq: A comprehensive RNA-seq database of gene expression in hippocampal principal neurons. Elife 5. https://doi.org/10.7554/eLife.14997

Chamberland, S., Topolnik, L., 2012. Inhibitory control of hippocampal inhibitory neurons. Front. Neurosci. https://doi.org/10.3389/fnins.2012.00165

Chen, K.H., Boettiger, A.N., Moffitt, J.R., Wang, S., Zhuang, X., 2015. Spatially resolved, highly multiplexed RNA profiling in single cells. Science (80-.). 348, aaa6090–aaa6090. https://doi.org/10.1126/science.aaa6090

Cheng, S., Frank, L.M., 2011. The structure of networks that produce the transformation from grid cells to place cells. Neuroscience 197. https://doi.org/10.1016/j.neuroscience.2011.09.002

Chiovini, B., Turi, G.F., Katona, G., Kaszás, A., Pálfi, D., Maák, P., Szalay, G., Szabó, M.F., Szabó, G., Szadai, Z., Káli, S., Rózsa, B., 2014. Dendritic Spikes Induce Ripples in Parvalbumin Interneurons during Hippocampal Sharp Waves. Neuron 82, 908–924. https://doi.org/10.1016/j.neuron.2014.04.004

Chittajallu, R., Craig, M.T., Mcfarland, A., Yuan, X., Gerfen, S., Tricoire, L., Erkkila, B., Barron, S.C., Lopez, C.M., Liang, B.J., Jeffries, B.W., Pelkey, K.A., McBain, C.J., 2013. Dual origins of functionally distinct O-LM interneurons revealed by differential 5-HT3AR expression. Nat. Neurosci. 16, 1598–1607. https://doi.org/10.1038/nn.3538

Close, J., Xu, H., García, N.D.M., Batista-Brito, R., Rossignol, E., Rudy, B., Fishell, G., 2012. Satb1 is an activity-modulated transcription factor required for the terminal differentiation and connectivity of medial ganglionic eminence-derived cortical interneurons. J. Neurosci. 32. https://doi.org/10.1523/JNEUROSCI.3583-12.2012

Cobb, S.R., Buhl, E.H., Halasy, K., Paulsen, O., Somogyi, P., 1995. Synchronization of neuronal activity in hippocampus by individual GABAergic interneurons. Nature 378, 75–78. https://doi.org/10.1038/378075a0

Colgin, L.L., 2016. Rhythms of the hippocampal network. Nat. Rev. Neurosci. https://doi.org/10.1038/nrn.2016.21

Colgin, L.L., 2013. Mechanisms and functions of theta rhythms. Annu. Rev. Neurosci. https://doi.org/10.1146/annurev-neuro-062012-170330

Colgin, L.L., Moser, E.I., Moser, M.B., 2008. Understanding memory through hippocampal remapping. Trends Neurosci. https://doi.org/10.1016/j.tins.2008.06.008

Cope, D.W., Maccaferri, G., MÁrton, L.F., Roberts, J.D.B., Cobden, P.M., Somogyi, P., 2002. Cholecystokinin-immunopositive basket and Schaffer collateral-associated interneurones target different domains of pyramidal cells in the CA1 area of the rat hippocampus. Neuroscience 109, 63–80. https://doi.org/10.1016/S0306-4522(01)00440-7

Cossart, R., 2014. Operational hub cells: A morpho-physiologically diverse class of GABAergic neurons united by a common function. Curr. Opin. Neurobiol. https://doi.org/10.1016/j.conb.2013.12.002

Csicsvari, J., Hirase, H., Mamiya, A., Buzsáki, G., 2000. Ensemble patterns of hippocampal CA3-CA1 neurons during sharp wave-associated population events. Neuron 28. https://doi.org/10.1016/S0896-6273(00)00135-5

Danielson, N.B., Zaremba, J.D., Kaifosh, P., Bowler, J., Ladow, M., Losonczy, A., 2016. Sublayer-Specific Coding Dynamics during Spatial Navigation and Learning in Hippocampal Area CA1. Neuron 91, 652–665. https://doi.org/10.1016/j.neuron.2016.06.020

Daumas, S., Halley, H., Francés, B., Lassalle, J.M., 2005. Encoding, consolidation, and retrieval of contextual memory: Differential involvement of dorsal CA3 and CA1 hippocampal subregions. Learn. Mem. 12. https://doi.org/10.1101/lm.81905

Daw, M.I., Tricoire, L., Erdelyi, F., Szabo, G., McBain, C.J., 2009. Asynchronous transmitter release from cholecystokinin-containing inhibitory interneurons is widespread and target-cell independent. J. Neurosci. 29, 11112–11122. https://doi.org/10.1523/JNEUROSCI.5760-

08.2009

de Vries, S.E.J., Lecoq, J.A., Buice, M.A., Groblewski, P.A., Ocker, G.K., Oliver, M., Feng, D., Cain, N., Ledochowitsch, P., Millman, D., Roll, K., Garrett, M., Keenan, T., Kuan, L., Mihalas, S., Olsen, S., Thompson, C., Wakeman, W., Waters, J., Williams, D., Barber, C., Berbesque, N., Blanchard, B., Bowles, N., Caldejon, S.D., Casal, L., Cho, A., Cross, S., Dang, C., Dolbeare, T., Edwards, M., Galbraith, J., Gaudreault, N., Gilbert, T.L., Griffin, F., Hargrave, P., Howard, R., Huang, L., Jewell, S., Keller, N., Knoblich, U., Larkin, J.D., Larsen, R., Lau, C., Lee, E., Lee, F., Leon, A., Li, L., Long, F., Luviano, J., Mace, K., Nguyen, T., Perkins, J., Robertson, M., Seid, S., Shea-Brown, E., Shi, J., Sjoquist, N., Slaughterbeck, C., Sullivan, D., Valenza, R., White, C., Williford, A., Witten, D.M., Zhuang, J., Zeng, H., Farrell, C., Ng, L., Bernard, A., Phillips, J.W., Reid, R.C., Koch, C., 2020. A large-scale standardized physiological survey reveals functional organization of the mouse visual cortex. Nat. Neurosci. 23, 138–151. https://doi.org/10.1038/s41593-019-0550-9

DeCoteau, W.E., Thorn, C., Gibson, D.J., Courtemanche, R., Mitra, P., Kubota, Y., Graybiel, A.M., 2007. Learning-related coordination of striatal and hippocampal theta rhythms during acquisition of a procedural maze task. Proc. Natl. Acad. Sci. U. S. A. 104. https://doi.org/10.1073/pnas.0700818104

Del Pino, I., Brotons-Mas, J.R., Marques-Smith, A., Marighetto, A., Frick, A., Marín, O., Rico, B., 2017. Abnormal wiring of CCK+ basket cells disrupts spatial information coding. Nat. Neurosci. 20, 784–792. https://doi.org/10.1038/nn.4544

Denaxa, M., Kalaitzidou, M., Garefalaki, A., Achimastou, A., Lasrado, R., Maes, T., Pachnis, V., 2012. Maturation-Promoting Activity of SATB1 in MGE-Derived Cortical Interneurons.

Cell Rep. 2. https://doi.org/10.1016/j.celrep.2012.10.003

Deshmukh, S.S., Knierim, J.J., 2011. Representation of non-spatial and spatial information in the lateral entorhinal cortex. Front. Behav. Neurosci. https://doi.org/10.3389/fnbeh.2011.00069

Donato, F., Chowdhury, A., Lahr, M., Caroni, P., 2015. Early- and Late-Born Parvalbumin Basket Cell Subpopulations Exhibiting Distinct Regulation and Roles in Learning. Neuron 85. https://doi.org/10.1016/j.neuron.2015.01.011

Donato, F., Rompani, S.B., Caroni, P., 2013. Parvalbumin-expressing basket-cell network plasticity induced by experience regulates adult learning. Nature 504, 272–276. https://doi.org/10.1038/nature12866

Donegan, M.L., Stefanini, F., Meira, T., Gordon, J.A., Fusi, S., Siegelbaum, S.A., 2020. Coding of social novelty in the hippocampal CA2 region and its disruption and rescue in a 22q11.2 microdeletion mouse model. Nat. Neurosci. 23. https://doi.org/10.1038/s41593-020-00720-5

Dong, H.W., Swanson, L.W., Chen, L., Fanselow, M.S., Toga, A.W., 2009. Genomic-anatomic evidence for distinct functional domains in hippocampal field CA1. Proc. Natl. Acad. Sci. U. S. A. 106. https://doi.org/10.1073/pnas.0812608106

Dragoi, G., Buzsáki, G., 2006. Temporal Encoding of Place Sequences by Hippocampal Cell Assemblies. Neuron 50. https://doi.org/10.1016/j.neuron.2006.02.023

Du, T., Xu, Q., Ocbina, P.J., Anderson, S.A., 2008. NKX2.1 specifies cortical interneuron fate by activating Lhx6. Development 135. https://doi.org/10.1242/dev.015123

Dudek, S.M., Alexander, G.M., Farris, S., 2016. Rediscovering area CA2: Unique properties and functions. Nat. Rev. Neurosci. https://doi.org/10.1038/nrn.2015.22

Dudok, B., Klein, P.M., Hwaun, E., Lee, B.R., Yao, Z., Fong, O., Bowler, J.C., Terada, S.,

Sparks, F.T., Szabo, G.G., Farrell, J.S., Berg, J., Daigle, T.L., Tasic, B., Dimidschstein, J., Fishell, G., Losonczy, A., Zeng, H., Soltesz, I., 2021a. Alternating sources of perisomatic inhibition during behavior. Neuron 109. https://doi.org/10.1016/j.neuron.2021.01.003

Dudok, B., Szoboszlay, M., Paul, A., Klein, P.M., Liao, Z., Hwaun, E., Szabo, G.G., Geiller, T., Vancura, B., Wang, B.-S., McKenzie, S., Homidan, J., Klaver, L.M.F., English, D.F., Huang, Z.J., Buzsáki, G., Losonczy, A., Soltesz, I., 2021b. Recruitment and inhibitory action of hippocampal axo-axonic cells during behavior. Neuron. https://doi.org/10.1016/j.neuron.2021.09.033

Dugladze, T., Schmitz, D., Whittington, M.A., Vida, I., Gloveli, T., 2012. Segregation of axonal and somatic activity during fast network oscillations. Science (80-.). 336. https://doi.org/10.1126/science.1222017

Dupret, D., O'Neill, J., Csicsvari, J., 2013. Dynamic Reconfiguration of Hippocampal Interneuron Circuits during Spatial Learning. Neuron 78, 166–180. https://doi.org/10.1016/j.neuron.2013.01.033

Dupret, D., O'Neill, J., Pleydell-Bouverie, B., Csicsvari, J., 2010. The reorganization and reactivation of hippocampal maps predict spatial memory performance. Nat. Neurosci. 13, 995–1002. https://doi.org/10.1038/nn.2599

Ego-Stengel, V., Wilson, M.A., 2007. Spatial selectivity and theta phase precession in CA1 interneurons. Hippocampus 17, 161–174. https://doi.org/10.1002/hipo.20253

Eichenbaum, H., 2017. The role of the hippocampus in navigation is memory. J. Neurophysiol. https://doi.org/10.1152/jn.00005.2017

Eichenbaum, H., Cohen, N.J., 2014. Can We Reconcile the Declarative Memory and Spatial Navigation Views on Hippocampal Function? Neuron.

https://doi.org/10.1016/j.neuron.2014.07.032

Ekstrom, A.D., Kahana, M.J., Caplan, J.B., Fields, T.A., Isham, E.A., Newman, E.L., Fried, I., 2003. Cellular networks underlying human spatial navigation. Nature 425. https://doi.org/10.1038/nature01964

Ellender, T.J., Nissen, W., Colgin, L.L., Mann, E.O., Paulsen, O., 2010. Priming of hippocampal population bursts by individual perisomatic- targeting interneurons. J. Neurosci. 30. https://doi.org/10.1523/JNEUROSCI.3962-09.2010

English, D.F., McKenzie, S., Evans, T., Kim, K., Yoon, E., Buzsáki, G., 2017. Pyramidal Cell-Interneuron Circuit Architecture and Dynamics in Hippocampal Networks. Neuron 96, 505-520.e7. https://doi.org/10.1016/j.neuron.2017.09.033

Evangelista, R., Cano, G., Cooper, C., Schmitz, D., Maier, N., Kempter, R., 2020. Generation of sharp wave-ripple events by disinhibition. J. Neurosci. 40. https://doi.org/10.1523/JNEUROSCI.2174-19.2020

Fan, L.Z., Kheifets, S., Böhm, U.L., Wu, H., Piatkevich, K.D., Xie, M.E., Parot, V., Ha, Y., Evans, K.E., Boyden, E.S., Takesian, A.E., Cohen, A.E., 2020. All-Optical Electrophysiology Reveals the Role of Lateral Inhibition in Sensory Processing in Cortical Layer 1. Cell 180. https://doi.org/10.1016/j.cell.2020.01.001

Fernández-Ruiz, A., Oliva, A., Soula, M., Rocha-Almeida, F., Nagy, G.A., Martin-Vazquez, G., Buzsáki, G., 2021. Gamma rhythm communication between entorhinal cortex and dentate gyrus neuronal assemblies. Science (80-.). 372. https://doi.org/10.1126/science.abf3119

Fishell, G., Kepecs, A., 2020. Interneuron Types as Attractors and Controllers. Annu. Rev. Neurosci. 43. https://doi.org/10.1146/annurev-neuro-070918-050421

Flames, N., Pla, R., Gelman, D.M., Rubenstein, J.L.R., Puelles, L., Marín, O., 2007. Delineation

of multiple subpallial progenitor domains by the combinatorial expression of transcriptional codes. J. Neurosci. 27. https://doi.org/10.1523/JNEUROSCI.2750-07.2007

Fogarty, M., Grist, M., Gelman, D., Marín, O., Pachnis, V., Kessaris, N., 2007. Spatial genetic patterning of the embryonic neuroepithelium generates GABAergic interneuron diversity in the adult cortex. J. Neurosci. 27. https://doi.org/10.1523/JNEUROSCI.1629-07.2007

Forro, T., Valenti, O., Lasztoczi, B., Klausberger, T., 2015. Temporal organization of GABAergic interneurons in the intermediate CA1 hippocampus during network oscillations. Cereb. Cortex 25, 1228–1240. https://doi.org/10.1093/cercor/bht316

Foster, D.J., 2017. Replay Comes of Age. Annu. Rev. Neurosci. 40. https://doi.org/10.1146/annurev-neuro-072116-031538

Francavilla, R., Villette, V., Luo, X., Chamberland, S., Muñoz-Pino, E., Camiré, O., Wagner, K., Kis, V., Somogyi, P., Topolnik, L., 2018. Connectivity and network state-dependent recruitment of long-range VIP-GABAergic neurons in the mouse hippocampus. Nat. Commun. 9, 1–17. https://doi.org/10.1038/s41467-018-07162-5

Frank, L.M., Stanley, G.B., Brown, E.N., 2004. Hippocampal plasticity across multiple days of exposure to novel environments. J. Neurosci. 24, 7681–7689. https://doi.org/10.1523/JNEUROSCI.1958-04.2004

Freund, T.F., 2003. Interneuron Diversity series: Rhythm and mood in perisomatic inhibition. Trends Neurosci. https://doi.org/10.1016/S0166-2236(03)00227-3

Freund, T.F., Gulyas, A.I., Acsady, L., Gorcs, T., Toth, K., 1990. Serotonergic control of the hippocampus via local inhibitory interneurons. Proc. Natl. Acad. Sci. U. S. A. 87. https://doi.org/10.1073/pnas.87.21.8501

Freund, T.F., Katona, I., 2007. Perisomatic Inhibition. Neuron.

https://doi.org/10.1016/j.neuron.2007.09.012

Fu, Y., Tucciarone, J.M., Espinosa, J.S., Sheng, N., Darcy, D.P., Nicoll, R.A., Huang, Z.J., Stryker, M.P., 2014. A cortical circuit for gain control by behavioral state. Cell 156, 1139–1152. https://doi.org/10.1016/j.cell.2014.01.050

Fuentealba, P., Begum, R., Capogna, M., Jinno, S., Márton, L.F., Csicsvari, J., Thomson, A., Somogyi, P., Klausberger, T., 2008. Ivy Cells: A Population of Nitric-Oxide-Producing, Slow-Spiking GABAergic Neurons and Their Involvement in Hippocampal Network Activity. Neuron 57, 917–929. https://doi.org/10.1016/j.neuron.2008.01.034

Fuentealba, P., Klausberger, T., Karayannis, T., Suen, W.Y., Huck, J., Tomioka, R., Rockland, K., Capogna, M., Studer, M., Morales, M., Somogyi, P., 2010. Expression of COUP-TFII nuclear receptor in restricted gabaergic neuronal populations in the adult rat hippocampus. J. Neurosci. 30. https://doi.org/10.1523/JNEUROSCI.4199-09.2010

Fuhrmann, F., Justus, D., Sosulina, L., Kaneko, H., Beutel, T., Friedrichs, D., Schoch, S., Schwarz, M.K., Fuhrmann, M., Remy, S., 2015. Locomotion, Theta Oscillations, and the Speed-Correlated Firing of Hippocampal Neurons Are Controlled by a Medial Septal Glutamatergic Circuit. Neuron 86, 1253–1264. https://doi.org/10.1016/j.neuron.2015.05.001

Fyhn, M., Hafting, T., Treves, A., Moser, M.B., Moser, E.I., 2007. Hippocampal remapping and grid realignment in entorhinal cortex. Nature 446. https://doi.org/10.1038/nature05601

Ganter, P., Szücs, P., Paulsen, O., Somogyi, P., 2004. Properties of horizontal axo-axonic cells in stratum oriens of the hippocampal CA1 area of rats in vitro. Hippocampus 14, 232–243. https://doi.org/10.1002/hipo.10170

Geiller, T., Fattahi, M., Choi, J.S., Royer, S., 2017. Place cells are more strongly tied to landmarks in deep than in superficial CA1. Nat. Commun. 8, 1–11.

https://doi.org/10.1038/ncomms14531

Geiller, T., Sadeh, S., Rolotti, S. V., Blockus, H., Vancura, B., Negrean, A., Murray, A.J., Rózsa, B., Polleux, F., Clopath, C., Losonczy, A., 2022. Local circuit amplification of spatial selectivity in the hippocampus. Nature 601. https://doi.org/10.1038/s41586-021-04169-9

Geiller, T., Vancura, B., Terada, S., Troullinou, E., Chavlis, S., Tsagkatakis, G., Tsakalides, P., Ócsai, K., Poirazi, P., Rózsa, B.J., Losonczy, A., 2020. Large-Scale 3D Two-Photon Imaging of Molecularly Identified CA1 Interneuron Dynamics in Behaving Mice. Neuron 108. https://doi.org/10.1016/j.neuron.2020.09.013

Gillespie, A.K., Astudillo Maya, D.A., Denovellis, E.L., Liu, D.F., Kastner, D.B., Coulter, M.E., Roumis, D.K., Eden, U.T., Frank, L.M., 2021. Hippocampal replay reflects specific past experiences rather than a plan for subsequent choice. Neuron 109. https://doi.org/10.1016/j.neuron.2021.07.029

Giocomo, L.M., Hussaini, S.A., Zheng, F., Kandel, E.R., Moser, M.B., Moser, E.I., 2011. Grid cells use HCN1 channels for spatial scaling. Cell 147. https://doi.org/10.1016/j.cell.2011.08.051

Girardeau, G., Benchenane, K., Wiener, S.I., Buzsáki, G., Zugaro, M.B., 2009. Selective suppression of hippocampal ripples impairs spatial memory. Nat. Neurosci. 12. https://doi.org/10.1038/nn.2384

Goutagny, R., Jackson, J., Williams, S., 2009. Self-generated theta oscillations in the hippocampus. Nat. Neurosci. 12. https://doi.org/10.1038/nn.2440

Grienberger, C., Milstein, A.D., Bittner, K.C., Romani, S., Magee, J.C., 2017. Inhibitory suppression of heterogeneously tuned excitation enhances spatial coding in CA1 place cells. Nat. Neurosci. 20, 417–426. https://doi.org/10.1038/nn.4486

Grosmark, A.D., Buzsáki, G., 2016. Diversity in neural firing dynamics supports both rigid and learned hippocampal sequences. Science (80-.). 351. https://doi.org/10.1126/science.aad1935

Grosmark, A.D., Sparks, F.T., Davis, M.J., Losonczy, A., 2021. Reactivation predicts the consolidation of unbiased long-term cognitive maps. Nat. Neurosci. 24. https://doi.org/10.1038/s41593-021-00920-7

Guan, H., Middleton, S.J., Inoue, T., McHugh, T.J., 2021. Lateralization of CA1 assemblies in the absence of CA3 input. Nat. Commun. 12. https://doi.org/10.1038/s41467-021-26389-3

Gulyás, A.I., Freund, T.F., 1996. Pyramidal cell dendrites are the primary targets of calbindin D28k-immunoreactive interneurons in the hippocampus. Hippocampus 6. https://doi.org/10.1002/(SICI)1098-1063(1996)6:5<525::AID-HIPO5>3.0.CO;2-H

Gulyás, A.I., Hájos, N., Freund, T.F., 1996. Interneurons containing calretinin are specialized to control other interneurons in the rat hippocampus. J. Neurosci. 16, 3397–3411. https://doi.org/10.1523/jneurosci.16-10-03397.1996

Gulyás, A.I., Megías, M., Emri, Z., Freund, T.F., 1999. Total number and ratio of excitatory and inhibitory synapses converging onto single interneurons of different types in the CA1 area of the rat hippocampus. J. Neurosci. 19, 10082–10097. https://doi.org/10.1523/jneurosci.19-22-10082.1999

Gulyás, A.I., Miettinen, R., Jacobowitz, D.M., Freund, T.F., 1992. Calretinin is present in non-pyramidal cells of the rat hippocampus-I. A new type of neuron specifically associated with the mossy fibre system. Neuroscience 48. https://doi.org/10.1016/0306-4522(92)90334-X

Guo, N., Soden, M.E., Herber, C., Kim, M.T.W., Besnard, A., Lin, P., Ma, X., Cepko, C.L., Zweifel, L.S., Sahay, A., 2018. Dentate granule cell recruitment of feedforward inhibition

governs engram maintenance and remote memory generalization. Nat. Med. 24. https://doi.org/10.1038/nm.4491

Guzman, S.J., Schlögl, A., Frotscher, M., Jonas, P., 2016. Synaptic mechanisms of pattern completion in the hippocampal CA3 network. Science (80-.). 353. https://doi.org/10.1126/science.aaf1836

Hafting, T., Fyhn, M., Molden, S., Moser, M.B., Moser, E.I., 2005. Microstructure of a spatial map in the entorhinal cortex. Nature 436. https://doi.org/10.1038/nature03721

Hainmueller, T., Bartos, M., 2020. Dentate gyrus circuits for encoding, retrieval and discrimination of episodic memories. Nat. Rev. Neurosci. https://doi.org/10.1038/s41583-019-0260-z

Hainmueller, T., Bartos, M., 2018. Parallel emergence of stable and dynamic memory engrams in the hippocampus. Nature 558, 292–296. https://doi.org/10.1038/s41586-018-0191-2

Hájos, N., Karlócai, M.R., Németh, B., Ulbert, I., Monyer, H., Szabó, G., Erdélyi, F., Freund, T.F., Gulyás, A.I., 2013. Input-output features of anatomically identified CA3 neurons during hippocampal sharp wave/ripple oscillation in vitro. J. Neurosci. 33. https://doi.org/10.1523/JNEUROSCI.5729-12.2013

Hangya, B., Borhegyi, Z., Szilágyi, N., Freund, T.F., Varga, V., 2009. GABAergic neurons of the medial septum lead the hippocampal network during theta activity. J. Neurosci. 29. https://doi.org/10.1523/JNEUROSCI.5665-08.2009

Hangya, B., Li, Y., Muller, R.U., Czurkó, A., 2010. Complementary spatial firing in place cell-interneuron pairs. J. Physiol. 588, 4165–4175. https://doi.org/10.1113/jphysiol.2010.194274

Harris, K.D., Hochgerner, H., Skene, N.G., Magno, L., Katona, L., Bengtsson Gonzales, C., Somogyi, P., Kessaris, N., Linnarsson, S., Hjerling-Leffler, J., 2018. Classes and continua

of hippocampal CA1 inhibitory neurons revealed by single-cell transcriptomics. PLoS Biol. 16. https://doi.org/10.1371/journal.pbio.2006387

Hartzell, A.L., Martyniuk, K.M., Brigidi, G.S., Heinz, D.A., Djaja, N.A., Payne, A., Bloodgood, B.L., 2018. NPAS4 recruits CCK basket cell synapses and enhances cannabinoid-sensitive inhibition in the mouse hippocampus. Elife 7. https://doi.org/10.7554/elife.35927

Harwell, C.C., Fuentealba, L.C., Gonzalez-Cerrillo, A., Parker, P.R.L., Gertz, C.C., Mazzola, E., Garcia, M.T., Alvarez-Buylla, A., Cepko, C.L., Kriegstein, A.R., 2015. Wide Dispersion and Diversity of Clonally Related Inhibitory Interneurons. Neuron 87. https://doi.org/10.1016/j.neuron.2015.07.030

Hefft, S., Jonas, P., 2005. Asynchronous GABA release generates long-lasting inhibition at a hippocampal interneuron-principal neuron synapse. Nat. Neurosci. 8, 1319–1328. https://doi.org/10.1038/nn1542

Hitti, F.L., Siegelbaum, S.A., 2014. The hippocampal CA2 region is essential for social memory. Nature 508. https://doi.org/10.1038/nature13028

Hollup, S.A., Molden, S., Donnett, J.G., Moser, M.B., Moser, E.I., 2001. Accumulation of hippocampal place fields at the goal location in an annular watermaze task. J. Neurosci. 21, 1635–1644. https://doi.org/10.1523/jneurosci.21-05-01635.2001

Hu, H., Gan, J., Jonas, P., 2014. Fast-spiking, parvalbumin+ GABAergic interneurons: From cellular design to microcircuit function. Science (80-.). 345, 1255263–1255263. https://doi.org/10.1126/science.1255263

Huang, K.W., Ochandarena, N.E., Philson, A.C., Hyun, M., Birnbaum, J.E., Cicconet, M., Sabatini, B.L., 2019. Molecular and anatomical organization of the dorsal raphe nucleus. Elife 8. https://doi.org/10.7554/eLife.46464

Hunt, D.L., Linaro, D., Si, B., Romani, S., Spruston, N., 2018. A novel pyramidal cell type promotes sharp-wave synchronization in the hippocampus. Nat. Neurosci. 21. https://doi.org/10.1038/s41593-018-0172-7

Iascone, D.M., Li, Y., Sümbül, U., Doron, M., Chen, H., Andreu, V., Goudy, F., Blockus, H., Abbott, L.F., Segev, I., Peng, H., Polleux, F., 2020. Whole-Neuron Synaptic Mapping Reveals Spatially Precise Excitatory/Inhibitory Balance Limiting Dendritic and Somatic Spiking. Neuron 106. https://doi.org/10.1016/j.neuron.2020.02.015

Inan, M., Welagen, J., Anderson, S.A., 2012. Spatial and temporal bias in the mitotic origins of somatostatin- and parvalbumin-expressing interneuron subgroups and the chandelier subtype in the medial ganglionic eminence. Cereb. Cortex 22. https://doi.org/10.1093/cercor/bhr148

Isaacson, J.S., Scanziani, M., 2011. How inhibition shapes cortical activity. Neuron. https://doi.org/10.1016/j.neuron.2011.09.027

Jacobs, J., 2014. Hippocampal theta oscillations are slower in humans than in rodents: Implications for models of spatial navigation and memory. Philos. Trans. R. Soc. B Biol. Sci. https://doi.org/10.1098/rstb.2013.0304

Jezek, K., Henriksen, E.J., Treves, A., Moser, E.I., Moser, M.B., 2011. Theta-paced flickering between place-cell maps in the hippocampus. Nature 478. https://doi.org/10.1038/nature10439

Jinno, S., 2009. Structural organization of long-range GABAergic projection system of the hippocampus. Front. Neuroanat. https://doi.org/10.3389/neuro.05.013.2009

Jinno, S., Klausberger, T., Marton, L.F., Dalezios, Y., Roberts, J.D.B., Fuentealba, P., Bushong, E.A., Henze, D., Buzsaki, G., Somogyi, P., 2007. Neuronal diversity in GABAergic long-

range projections from the hippocampus. J. Neurosci. 27, 8790–8804. https://doi.org/10.1523/JNEUROSCI.1847-07.2007

Jones, M.W., Wilson, M.A., 2005. Theta rhythms coordinate hippocampal-prefrontal interactions in a spatial memory task. PLoS Biol. 3. https://doi.org/10.1371/journal.pbio.0030402

Joo, H.R., Frank, L.M., 2018. The hippocampal sharp wave–ripple in memory retrieval for immediate use and consolidation. Nat. Rev. Neurosci. https://doi.org/10.1038/s41583-018-0077-1

Joshi, A., Salib, M., Viney, T.J., Dupret, D., Somogyi, P., 2017. Behavior-Dependent Activity and Synaptic Organization of Septo-hippocampal GABAergic Neurons Selectively Targeting the Hippocampal CA3 Area. Neuron 96. https://doi.org/10.1016/j.neuron.2017.10.033

Jung, M.W., Wiener, S.I., McNaughton, B.L., 1994. Comparison of spatial firing characteristics of units in dorsal and ventral hippocampus of the rat. J. Neurosci. 14. https://doi.org/10.1523/jneurosci.14-12-07347.1994

Kaifosh, P., Zaremba, J.D., Danielson, N.B., Losonczy, A., 2014. SIMA: Python software for analysis of dynamic fluorescence imaging data. Front. Neuroinform. 8, 80. https://doi.org/10.3389/fninf.2014.00080

Kajikawa, K., Hulse, B.K., Siapas, A.G., Lubenov, E. V., 2021. Inhibition is the hallmark of CA3 intracellular dynamics around awake ripples. bioRxiv.

Kanatani, S., Yozu, M., Tabata, H., Nakajima, K., 2008. COUP-TFII is preferentially expressed in the caudal ganglionic eminence and is involved in the caudal migratory stream. J. Neurosci. 28. https://doi.org/10.1523/JNEUROSCI.2132-08.2008

Kanter, B.R., Lykken, C.M., Avesar, D., Weible, A., Dickinson, J., Dunn, B., Borgesius, N.Z.,

Roudi, Y., Kentros, C.G., 2017. A Novel Mechanism for the Grid-to-Place Cell Transformation Revealed by Transgenic Depolarization of Medial Entorhinal Cortex Layer II. Neuron 93. https://doi.org/10.1016/j.neuron.2017.03.001

Karlsson, M.P., Frank, L.M., 2009. Awake replay of remote experiences in the hippocampus. Nat. Neurosci. 12. https://doi.org/10.1038/nn.2344

Katona, G., Szalay, G., Maák, P., Kaszás, A., Veress, M., Hillier, D., Chiovini, B., Vizi, E.S., Roska, B., Rózsa, B., 2012. Fast two-photon in vivo imaging with three-dimensional random-access scanning in large tissue volumes. Nat. Methods 9, 201–208. https://doi.org/10.1038/nmeth.1851

Katona, I., Freund, T.F., 2012. Multiple Functions of Endocannabinoid Signaling in the Brain. Annu. Rev. Neurosci. 35, 529–558. https://doi.org/10.1146/annurev-neuro-062111-150420

Katona, L., Lapray, D., Viney, T.J., Oulhaj, A., Borhegyi, Z., Micklem, B.R., Klausberger, T., Somogyi, P., 2014. Sleep and Movement Differentiates Actions of Two Types of Somatostatin-Expressing GABAergic Interneuron in Rat Hippocampus. Neuron 82, 872–886. https://doi.org/10.1016/j.neuron.2014.04.007

Katona, L., Micklem, B., Borhegyi, Z., Swiejkowski, D.A., Valenti, O., Viney, T.J., Kotzadimitriou, D., Klausberger, T., Somogyi, P., 2017. Behavior-dependent activity patterns of GABAergic long-range projecting neurons in the rat hippocampus. Hippocampus 27, 359–377. https://doi.org/10.1002/hipo.22696

Kaufman, A.M., Geiller, T., Losonczy, A., 2020. A Role for the Locus Coeruleus in Hippocampal CA1 Place Cell Reorganization during Spatial Reward Learning. Neuron 105, 1018-1026.e4. https://doi.org/10.1016/j.neuron.2019.12.029

Kay, K., Sosa, M., Chung, J.E., Karlsson, M.P., Larkin, M.C., Frank, L.M., 2016. A

hippocampal network for spatial coding during immobility and sleep. Nature 531, 185–190. https://doi.org/10.1038/nature17144

Keemink, S.W., Lowe, S.C., Pakan, J.M.P., Dylda, E., Van Rossum, M.C.W., Rochefort, N.L., 2018. FISSA: A neuropil decontamination toolbox for calcium imaging signals. Sci. Rep. 8, 1–12. https://doi.org/10.1038/s41598-018-21640-2

Keller, A.J., Martin, K.A.C., 2015. Local circuits for contrast normalization and adaptation investigated with two-photon imaging in cat primary visual cortex. J. Neurosci. 35, 10078–10087. https://doi.org/10.1523/JNEUROSCI.0906-15.2015

Kepecs, A., Uchida, N., Mainen, Z.F., 2006. The sniff as a unit of olfactory processing. Chem. Senses. https://doi.org/10.1093/chemse/bjj016

Kerlin, A.M., Andermann, M.L., Berezovskii, V.K., Reid, R.C., 2010. Broadly Tuned Response Properties of Diverse Inhibitory Neuron Subtypes in Mouse Visual Cortex. Neuron 67, 858–871. https://doi.org/10.1016/j.neuron.2010.08.002

Kesner, R.P., 2007. Behavioral functions of the CA3 subregion of the hippocampus. Learn. Mem. https://doi.org/10.1101/lm.688207

Khalaf-Nazzal, R., Francis, F., 2013. Hippocampal development - Old and new findings. Neuroscience. https://doi.org/10.1016/j.neuroscience.2013.05.061

Khan, A.G., Poort, J., Chadwick, A., Blot, A., Sahani, M., Mrsic-Flogel, T.D., Hofer, S.B., 2018. Distinct learning-induced changes in stimulus selectivity and interactions of GABAergic interneuron classes in visual cortex. Nat. Neurosci. 21, 851–859. https://doi.org/10.1038/s41593-018-0143-z

Klausberger, T., 2009. GABAergic interneurons targeting dendrites of pyramidal cells in the CA1 area of the hippocampus. Eur. J. Neurosci. 30, 947–957.

https://doi.org/10.1111/j.1460-9568.2009.06913.x

Klausberger, T., Magill, P.J., Márton, L.F., Roberts, J.D.B., Cobden, P.M., Buzsáki, G., Somogyi, P., 2003. Brain-state- and cell-type-specific firing of hippocampal interneurons in vivo. Nature 421, 844–848. https://doi.org/10.1038/nature01374

Klausberger, T., Márton, L.F., Baude, A., Roberts, J.D.B., Magill, P.J., Somogyi, P., 2004. Spike timing of dendrite-targeting bistratified cells during hippocampal network oscillations in vivo. Nat. Neurosci. 7, 41–47. https://doi.org/10.1038/nn1159

Klausberger, T., Marton, L.F., O'Neill, J., Huck, J.H.J., Dalezios, Y., Fuentealba, P., Suen, W.Y., Papp, E., Kaneko, T., Watanabe, M., Csicsvari, J., Somogyi, P., 2005. Complementary roles of cholecystokinin- and parvalbumin-expressing GABAergic neurons in hippocampal network oscillations. J. Neurosci. 25, 9782–9793. https://doi.org/10.1523/JNEUROSCI.3269-05.2005

Klausberger, T., Somogyi, P., 2008. Neuronal diversity and temporal dynamics: The unity of hippocampal circuit operations. Science (80-.). https://doi.org/10.1126/science.1149381

Klinzing, J.G., Niethard, N., Born, J., 2019. Mechanisms of systems memory consolidation during sleep. Nat. Neurosci. https://doi.org/10.1038/s41593-019-0467-3

Kohl, M.M., Shipton, O.A., Deacon, R.M., Rawlins, J.N.P., Deisseroth, K., Paulsen, O., 2011. Hemisphere-specific optogenetic stimulation reveals left-right asymmetry of hippocampal plasticity. Nat. Neurosci. 14. https://doi.org/10.1038/nn.2915

Kohus, Z., Káli, S., Rovira-Esteban, L., Schlingloff, D., Papp, O., Freund, T.F., Hájos, N., Gulyás, A.I., 2016. Properties and dynamics of inhibitory synaptic communication within the CA3 microcircuits of pyramidal cells and interneurons expressing parvalbumin or cholecystokinin. J. Physiol. 594. https://doi.org/10.1113/JP272231

Kramis, R., Vanderwolf, C.H., Bland, B.H., 1975. Two types of hippocampal rhythmical slow activity in both the rabbit and the rat: Relations to behavior and effects of atropine, diethyl ether, urethane, and pentobarbital. Exp. Neurol. 49. https://doi.org/10.1016/0014-4886(75)90195-8

Krook-Magnuson, E., Luu, L., Lee, S.H., Varga, C., Soltesz, I., 2011. Ivy and neurogliaform interneurons are a major target of μ-Opioid receptor modulation. J. Neurosci. 31. https://doi.org/10.1523/JNEUROSCI.2269-11.2011

Kubie, J.L., Levy, E.R.J., Fenton, A.A., 2019. Is hippocampal remapping the physiological basis for context? Hippocampus hipo.23160. https://doi.org/10.1002/hipo.23160

Langer, D., Helmchen, F., n.d. Post hoc immunostaining of GABAergic neuronal subtypes following in vivo two-photon calcium imaging in mouse neocortex. https://doi.org/10.1007/s00424-011-1048-9

Lapray, D., Lasztoczi, B., Lagler, M., Viney, T.J., Katona, L., Valenti, O., Hartwich, K., Borhegyi, Z., Somogyi, P., Klausberger, T., 2012. Behavior-dependent specialization of identified hippocampal interneurons. Nat. Neurosci. 15, 1265–1271. https://doi.org/10.1038/nn.3176

Lasztóczi, B., Tukker, J.J., Somogyi, P., Klausberger, T., 2011. Terminal field and firing selectivity of cholecystokinin-expressing interneurons in the Hippocampal CA3 Area. J. Neurosci. 31, 18073–18093. https://doi.org/10.1523/JNEUROSCI.3573-11.2011

Lawrence, J.J., McBain, C.J., 2003. Interneuron Diversity series: Containing the detonation - Feedforward inhibition in the CA3 hippocampus. Trends Neurosci. https://doi.org/10.1016/j.tins.2003.09.007

Leão, R.N., Mikulovic, S., Leão, K.E., Munguba, H., Gezelius, H., Enjin, A., Patra, K., Eriksson,

A., Loew, L.M., Tort, A.B.L., Kullander, K., 2012. OLM interneurons differentially modulate CA3 and entorhinal inputs to hippocampal CA1 neurons. Nat. Neurosci. 15. https://doi.org/10.1038/nn.3235

Lee, S., Geiller, T., Jung, A., Nakajima, R., Song, Y.K., Baker, B.J., 2017. Improving a genetically encoded voltage indicator by modifying the cytoplasmic charge composition. Sci. Rep. https://doi.org/10.1038/s41598-017-08731-2

Lee, S., Kruglikov, I., Huang, Z.J., Fishell, G., Rudy, B., 2013. A disinhibitory circuit mediates motor integration in the somatosensory cortex. Nat. Neurosci. 16, 1662–1670. https://doi.org/10.1038/nn.3544

Lee, S.H., Földy, C., Soltesz, I., 2010. Distinct endocannabinoid control of GABA release at perisomatic and dendritic synapses in the hippocampus. J. Neurosci. 30, 7993–8000. https://doi.org/10.1523/JNEUROSCI.6238-09.2010

Lee, S.H., Marchionni, I., Bezaire, M., Varga, C., Danielson, N., Lovett-Barron, M., Losonczy, A., Soltesz, I., 2014. Parvalbumin-positive basket cells differentiate among hippocampal pyramidal cells. Neuron 82, 1129–1144. https://doi.org/10.1016/j.neuron.2014.03.034

Lee, S.M.K., Tole, S., Grove, E., McMahon, A.P., 2000. A local Wnt-3a signal is required for development of the mammalian hippocampus. Development 127. https://doi.org/10.1242/dev.127.3.457

Leitner, F.C., Melzer, S., Lütcke, H., Pinna, R., Seeburg, P.H., Helmchen, F., Monyer, H., 2016. Spatially segregated feedforward and feedback neurons support differential odor processing in the lateral entorhinal cortex. Nat. Neurosci. 19. https://doi.org/10.1038/nn.4303

Leutgeb, J.K., Leutgeb, S., Moser, M.B., Moser, E.I., 2007. Pattern separation in the dentate gyrus and CA3 of the hippocampus. Science (80-.). 315.

https://doi.org/10.1126/science.1135801

Leutgeb, S., Leutgeb, J.K., Barnes, C.A., Moser, E.I., McNaughton, B.L., Moser, M.B., 2005. Neuroscience: Independent codes for spatial and episodic memory in hippocampal neuronal ensembles. Science (80-.). 309, 619–623. https://doi.org/10.1126/science.1114037

Lim, L., Mi, D., Llorca, A., Marín, O., 2018. Development and Functional Diversification of Cortical Interneurons. Neuron. https://doi.org/10.1016/j.neuron.2018.10.009

Lin, M.Z., Schnitzer, M.J., 2016. Genetically encoded indicators of neuronal activity. Nat. Neurosci. https://doi.org/10.1038/nn.4359

Liu, X., Terada, S., Kim, J.-H., Lu, Y., Ramezani, M., Grosmark, A., Losonczy, A., Kuzum, D., 2021. E-Cannula reveals anatomical diversity in sharp-wave ripples as a driver for the recruitment of distinct hippocampal assemblies. bioRxiv.

Liu, Y., Dolan, R.J., Kurth-Nelson, Z., Behrens, T.E.J., 2019. Human Replay Spontaneously Reorganizes Experience. Cell 178. https://doi.org/10.1016/j.cell.2019.06.012

Lodato, S., Rouaux, C., Quast, K.B., Jantrachotechatchawan, C., Studer, M., Hensch, T.K., Arlotta, P., 2011. Excitatory Projection Neuron Subtypes Control the Distribution of Local Inhibitory Interneurons in the Cerebral Cortex. Neuron 69. https://doi.org/10.1016/j.neuron.2011.01.015

Logothetis, N.K., Eschenko, O., Murayama, Y., Augath, M., Steudel, T., Evrard, H.C., Besserve, M., Oeltermann, A., 2012. Hippocampal-cortical interaction during periods of subcortical silence. Nature 491. https://doi.org/10.1038/nature11618

Losonczy, A., Biró, Á.A., Nusser, Z., 2004. Persistently active cannabinoid receptors mute a subpopulation of hippocampal interneurons. Proc. Natl. Acad. Sci. U. S. A. 101. https://doi.org/10.1073/pnas.0304752101

Losonczy, A., Zemelman, B. V., Vaziri, A., Magee, J.C., 2010. Network mechanisms of theta related neuronal activity in hippocampal CA1 pyramidal neurons. Nat. Neurosci. 13. https://doi.org/10.1038/nn.2597

Losonczy, A., Zhang, L., Shigemoto, R., Somogyi, P., Nusser, Z., 2002. Cell type dependence and variability in the short-term plasticity of EPSCs in identified mouse hippocampal interneurones. J. Physiol. 542, 193–210. https://doi.org/10.1113/jphysiol.2002.020024

Lovett-Barron, M., Kaifosh, P., Kheirbek, M.A., Danielson, N., Zaremba, J.D., Reardon, T.R., Turi, G.F., Hen, R., Zemelman, B. V., Losonczy, A., 2014. Dendritic inhibition in the hippocampus supports fear learning. Science (80-.). 343, 857–863. https://doi.org/10.1126/science.1247485

Lovett-Barron, M., Turi, G.F., Kaifosh, P., Lee, P.H., Bolze, F., Sun, X.H., Nicoud, J.F., Zemelman, B. V., Sternson, S.M., Losonczy, A., 2012. Regulation of neuronal input transformations by tunable dendritic inhibition. Nat. Neurosci. 15, 423–430. https://doi.org/10.1038/nn.3024

Luo, X., Guet-McCreight, A., Villette, V., Francavilla, R., Marino, B., Chamberland, S., Skinner, F.K., Topolnik, L., 2020. Synaptic Mechanisms Underlying the Network State-Dependent Recruitment of VIP-Expressing Interneurons in the CA1 Hippocampus. Cereb. Cortex. https://doi.org/10.1093/cercor/bhz334

Maccaferri, G., 2011. Microcircuit-specific processing in the hippocampus. J. Physiol. 589, 1873–1874. https://doi.org/10.1113/jphysiol.2011.205112

Maccaferri, G., David, J., Roberts, B., Szucs, P., Cottingham, C.A., Somogyi, P., 2000. Cell surface domain specific postsynaptic currents evoked by identified GABAergic neurones in rat hippocampus in vitro. J. Physiol. https://doi.org/10.1111/j.1469-7793.2000.t01-3-

00091.x

Maccaferri, G., McBain, C.J., 1996. Long-term potentiation in distinct subtypes of hippocampal nonpyramidal neurons. J. Neurosci. 16, 5334–5343. https://doi.org/10.1523/jneurosci.16-17-05334.1996

Maccaferri, G., Tóth, K., McBain, C.J., 1998. Target-specific expression of presynaptic mossy fiber plasticity. Science (80-.). 279. https://doi.org/10.1126/science.279.5355.1368

Maingret, N., Girardeau, G., Todorova, R., Goutierre, M., Zugaro, M., 2016. Hippocampo-cortical coupling mediates memory consolidation during sleep. Nat. Neurosci. 19. https://doi.org/10.1038/nn.4304

Mallory, C.S., Giocomo, L.M., 2018. Heterogeneity in hippocampal place coding. Curr. Opin. Neurobiol. https://doi.org/10.1016/j.conb.2018.02.014

Malvache, A., Reichinnek, S., Villette, V., Haimerl, C., Cossart, R., 2016. Awake hippocampal reactivations project onto orthogonal neuronal assemblies. Science (80-.). 353, 1280–1283. https://doi.org/10.1126/science.aaf3319

Marín, O., Yaron, A., Bagri, A., Tessier-Lavigne, M., Rubenstein, J.L.R., 2001. Sorting of striatal and cortical interneurons regulated by semaphorin-neuropilin interactions. Science (80-.). 293. https://doi.org/10.1126/science.1061891

Markus, E.J., Qin, Y.L., Leonard, B., Skaggs, W.E., McNaughton, B.L., Barnes, C.A., 1995. Interactions between location and task affect the spatial and directional firing of hippocampal neurons. J. Neurosci. 15. https://doi.org/10.1523/jneurosci.15-11-07079.1995

Marshall, L., Henze, D.A., Hirase, H., Leinekugel, X., Dragoi, G., Buzsáki, G., 2002. Hippocampal pyramidal cell-interneuron spike transmission is frequency dependent and responsible for place modulation of interneuron discharge. J. Neurosci. 22, RC197–RC197.

https://doi.org/10.1523/JNEUROSCI.22-02-j0001.2002

Martina, M., Vida, I., Jonas, P., 2000. Distal initiation and active propagation of action potentials in interneuron dendrites. Science (80-.). 287, 295–300. https://doi.org/10.1126/science.287.5451.295

Masurkar, A. V., Srinivas, K. V., Brann, D.H., Warren, R., Lowes, D.C., Siegelbaum, S.A., 2017. Medial and Lateral Entorhinal Cortex Differentially Excite Deep versus Superficial CA1 Pyramidal Neurons. Cell Rep. 18. https://doi.org/10.1016/j.celrep.2016.12.012

Matyas, F., Freund, T.F., Gulyas, A.I., 2004. Convergence of excitatory and inhibitory inputs onto CCK-containing basket cells in the CA1 area of the rat hippocampus. Eur. J. Neurosci. 19, 1243–1256. https://doi.org/10.1111/j.1460-9568.2004.03225.x

McBain, C.J., DiChiara, T.J., Kauer, J.A., 1994. Activation of metabotropic glutamate receptors differentially affects two classes of hippocampal interneurons and potentiates excitatory synaptic transmission. J. Neurosci. 14, 4433–4445. https://doi.org/10.1523/jneurosci.14-07-04433.1994

McKenzie, S., 2018. Inhibition shapes the organization of hippocampal representations. Hippocampus 28, 659–671. https://doi.org/10.1002/hipo.22803

Mercer, A., Trigg, H.L., Thomson, A.M., 2007. Characterization of neurons in the CA2 subfield of the adult rat hippocampus. J. Neurosci. 27. https://doi.org/10.1523/JNEUROSCI.1829-07.2007

Milivojevic, B., Doeller, C.F., 2013. Mnemonic networks in the hippocampal formation: From spatial maps to temporal and conceptual codes. J. Exp. Psychol. Gen. 142. https://doi.org/10.1037/a0033746

Miller, J.F., Neufang, M., Solway, A., Brandt, A., Trippel, M., Mader, I., Hefft, S., Merkow, M.,

Polyn, S.M., Jacobs, J., Kahana, M.J., Schulze-Bonhage, A., 2013. Neural activity in human hippocampal formation reveals the spatial context of retrieved memories. Science (80-.). 342. https://doi.org/10.1126/science.1244056

Milstein, A.D., Bloss, E.B., Apostolides, P.F., Vaidya, S.P., Dilly, G.A., Zemelman, B. V., Magee, J.C., 2015. Inhibitory Gating of Input Comparison in the CA1 Microcircuit. Neuron 87, 1274–1289. https://doi.org/10.1016/j.neuron.2015.08.025

Mishra, R.K., Kim, S., Guzman, S.J., Jonas, P., 2016. Symmetric spike timing-dependent plasticity at CA3-CA3 synapses optimizes storage and recall in autoassociative networks. Nat. Commun. 7. https://doi.org/10.1038/ncomms11552

Mitchell, S.J., Rawlins, J.N.P., Steward, O., Olton, D.S., 1982. Medial septal area lesions disrupt θ rhythm and cholinergic staining in medial entorhinal cortex and produce impaired radial arm maze behavior in rats. J. Neurosci. 2. https://doi.org/10.1523/jneurosci.02-03-00292.1982

Miyoshi, G., Fishell, G., 2011. GABAergic interneuron lineages selectively sort into specific cortical layers during early postnatal development. Cereb. Cortex 21. https://doi.org/10.1093/cercor/bhq155

Mizumori, S.J.Y., Perez, G.M., Alvarado, M.C., Barnes, C.A., McNaughton, B.L., 1990. Reversible inactivation of the medial septum differentially affects two forms of learning in rats. Brain Res. 528. https://doi.org/10.1016/0006-8993(90)90188-H

Mizunuma, M., Norimoto, H., Tao, K., Egawa, T., Hanaoka, K., Sakaguchi, T., Hioki, H., Kaneko, T., Yamaguchi, S., Nagano, T., Matsuki, N., Ikegaya, Y., 2014. Unbalanced excitability underlies offline reactivation of behaviorally activated neurons. Nat. Neurosci. 17. https://doi.org/10.1038/nn.3674

Monaco, J.D., Abbott, L.F., 2011. Modular realignment of entorhinal grid cell activity as a basis for hippocampal remapping. J. Neurosci. 31. https://doi.org/10.1523/JNEUROSCI.1433-11.2011

Morales, M., Bloom, F.E., 1997. The 5-HT3 receptor is present in different subpopulations of GABAergic neurons in the rat telencephalon. J. Neurosci. 17. https://doi.org/10.1523/jneurosci.17-09-03157.1997

Mori, M., Gähwiler, B.H., Gerber, U., 2007. Recruitment of an inhibitory hippocampal network after bursting in a single granule cell. Proc. Natl. Acad. Sci. U. S. A. 104. https://doi.org/10.1073/pnas.0702164104

Morris, R.G.M., Garrud, P., Rawlins, J.N.P., O'Keefe, J., 1982. Place navigation impaired in rats with hippocampal lesions. Nature 297. https://doi.org/10.1038/297681a0

Moser, E.I., Kropff, E., Moser, M.B., 2008. Place cells, grid cells, and the brain's spatial representation system. Annu. Rev. Neurosci. https://doi.org/10.1146/annurev.neuro.31.061307.090723

Muller, R.U., Kubie, J.L., 1987. The effects of changes in the environment on the spatial firing of hippocampal complex-spike cells. J. Neurosci. 7. https://doi.org/10.1523/jneurosci.07-07-01951.1987

Nakashiba, T., Buhl, D.L., McHugh, T.J., Tonegawa, S., 2009. Hippocampal CA3 Output Is Crucial for Ripple-Associated Reactivation and Consolidation of Memory. Neuron 62. https://doi.org/10.1016/j.neuron.2009.05.013

Nakazawa, K., Quirk, M.C., Chitwood, R.A., Watanabe, M., Yeckel, M.F., Sun, L.D., Kato, A., Carr, C.A., Johnston, D., Wilson, M.A., Tonegawa, S., 2002. Requirement for hippocampal CA3 NMDA receptors in associative memory recall. Science (80-.). 297.

https://doi.org/10.1126/science.1071795

Nakazawa, K., Sun, L.D., Quirk, M.C., Rondi-Reig, L., Wilson, M.A., Tonegawa, S., 2003. Hippocampal CA3 NMDA receptors are crucial for memory acquisition of one-time experience. Neuron 38. https://doi.org/10.1016/S0896-6273(03)00165-X

Neunuebel, J.P., Knierim, J.J., 2014. CA3 retrieves coherent representations from degraded input: Direct evidence for CA3 pattern completion and dentate gyrus pattern separation. Neuron 81. https://doi.org/10.1016/j.neuron.2013.11.017

Nicola, W., Clopath, C., 2019. A diversity of interneurons and Hebbian plasticity facilitate rapid compressible learning in the hippocampus. Nat. Neurosci. 22. https://doi.org/10.1038/s41593-019-0415-2

Nóbrega-Pereira, S., Kessaris, N., Du, T., Kimura, S., Anderson, S.A., Marín, O., 2008. Postmitotic Nkx2-1 Controls the Migration of Telencephalic Interneurons by Direct Repression of Guidance Receptors. Neuron 59. https://doi.org/10.1016/j.neuron.2008.07.024

Nolan, M.F., Malleret, G., Dudman, J.T., Buhl, D.L., Santoro, B., Gibbs, E., Vronskaya, S., Buzsáki, G., Siegelbaum, S.A., Kandel, E.R., Morozov, A., 2004. A behavioral role for dendritic integration: HCN1 channels constrain spatial memory and plasticity at inputs to distal dendrites of CA1 pyramidal neurons. Cell 119. https://doi.org/10.1016/j.cell.2004.11.020

Norimoto, H., Makino, K., Gao, M., Shikano, Y., Okamoto, K., Ishikawa, T., Sasaki, T., Hioki, H., Fujisawa, S., Ikegaya, Y., 2018. Hippocampal ripples down-regulate synapses. Science (80-.). 359. https://doi.org/10.1126/science.aao0702

O'Keefe, J., Dostrovsky, J., 1971. The hippocampus as a spatial map. Preliminary evidence from

unit activity in the freely-moving rat. Brain Res. 34, 171–175. https://doi.org/10.1016/0006-8993(71)90358-1

O'Keefe, J., Recce, M.L., 1993. Phase relationship between hippocampal place units and the EEG theta rhythm. Hippocampus 3. https://doi.org/10.1002/hipo.450030307

Overstreet-Wadiche, L., McBain, C.J., 2015. Neurogliaform cells in cortical circuits. Nat. Rev. Neurosci. https://doi.org/10.1038/nrn3969

Palacios-Filardo, J., Mellor, J.R., 2019. Neuromodulation of hippocampal long-term synaptic plasticity. Curr. Opin. Neurobiol. https://doi.org/10.1016/j.conb.2018.08.009

Papp, O.I., Karlócai, M.R., Tóth, I.E., Freund, T.F., Hájos, N., 2013. Different input and output properties characterize parvalbumin-positive basket and Axo-axonic cells in the hippocampal CA3 subfield. Hippocampus 23. https://doi.org/10.1002/hipo.22147

Pawelzik, H., Hughes, D.I., Thomson, A.M., 2002. Physiological and morphological diversity of immunocytochemically defined parvalbumin- and cholecystokinin-positive interneurones in CA1 of the adult rat hippocampus. J. Comp. Neurol. 443, 346–367. https://doi.org/10.1002/cne.10118

Payne, H.L., Lynch, G.F., Aronov, D., 2021. Neural representations of space in the hippocampus of a food-caching bird. Science (80-.). 373. https://doi.org/10.1126/science.abg2009

Pelkey, K.A., Chittajallu, R., Craig, M.T., Tricoire, L., Wester, J.C., McBain, C.J., 2017. Hippocampal gabaergic inhibitory interneurons. Physiol. Rev. 97, 1619–1747. https://doi.org/10.1152/physrev.00007.2017

Petsche, H., Stumpf, C., Gogolak, G., 1962. The significance of the rabbit's septum as a relay station between the midbrain and the hippocampus I. The control of hippocampus arousal activity by the septum cells. Electroencephalogr. Clin. Neurophysiol. 14.

https://doi.org/10.1016/0013-4694(62)90030-5

Pfeffer, C.K., Xue, M., He, M., Huang, Z.J., Scanziani, M., 2013. Inhibition of inhibition in visual cortex: The logic of connections between molecularly distinct interneurons. Nat. Neurosci. 16, 1068–1076. https://doi.org/10.1038/nn.3446

Pfeiffer, B.E., 2020. The content of hippocampal "replay." Hippocampus. https://doi.org/10.1002/hipo.22824

Pi, H.J., Hangya, B., Kvitsiani, D., Sanders, J.I., Huang, Z.J., Kepecs, A., 2013. Cortical interneurons that specialize in disinhibitory control. Nature 503, 521–524. https://doi.org/10.1038/nature12676

Pouille, F., Marin-Burgin, A., Adesnik, H., Atallah, B. V., Scanziani, M., 2009. Input normalization by global feedforward inhibition expands cortical dynamic range. Nat. Neurosci. 12, 1577–1585. https://doi.org/10.1038/nn.2441

Pouille, F., Scanziani, M., 2004. Routing of spike series by dynamic circuits in the hippocampus. Nature 429, 717–723. https://doi.org/10.1038/nature02615

Pouille, F., Scanziani, M., 2001. Enforcement of temporal fidelity in pyramidal cells by somatic feed-forward inhibition. Science (80-.). 293, 1159–1163. https://doi.org/10.1126/science.1060342

Price, C.J., Cauli, B., Kovacs, E.R., Kulik, A., Lambolez, B., Shigemoto, R., Capogna, M., 2005. Neurogliaform neurons form a novel inhibitory network in the hippocampal CA1 area. J. Neurosci. 25, 6775–6786. https://doi.org/10.1523/JNEUROSCI.1135-05.2005

Price, C.J., Scott, R., Rusakov, D.A., Capogna, M., 2008. GABAB receptor modulation of feedforward inhibition through hippocampal neurogliaform cells. J. Neurosci. 28, 6974–6982. https://doi.org/10.1523/JNEUROSCI.4673-07.2008

Priestley, J.B., Bowler, J.C., Rolotti, S. V., Fusi, S., Losonczy, A., 2021. Signatures of Rapid Synaptic Learning in the Hippocampus During Novel Experiences. SSRN Electron. J. https://doi.org/10.2139/ssrn.3900714

Prince, L.Y., Bacon, T., Humphries, R., Tsaneva-Atanasova, K., Clopath, C., Mellor, J.R., 2021. Separable actions of acetylcholine and noradrenaline on neuronal ensemble formation in hippocampal CA3 circuits. PLoS Comput. Biol. 17. https://doi.org/10.1371/journal.pcbi.1009435

Qian, X., Harris, K.D., Hauling, T., Nicoloutsopoulos, D., Muñoz-Manchado, A.B., Skene, N., Hjerling-Leffler, J., Nilsson, M., 2020. Probabilistic cell typing enables fine mapping of closely related cell types in situ. Nat. Methods 17, 101–106. https://doi.org/10.1038/s41592-019-0631-4

Quirk, G.J., Muller, R.U., Kubie, J.L., 1990. The firing of hippocampal place cells in the dark depends on the rat's recent experience. J. Neurosci. 10. https://doi.org/10.1523/jneurosci.10-06-02008.1990

Ramos, R.L., Bai, J., LoTurco, J.J., 2006. Heterotopia formation in rat but not mouse neocortex after RNA interference knockdown of DCX. Cereb. Cortex 16. https://doi.org/10.1093/cercor/bhj074

Rebola, N., Carta, M., Mulle, C., 2017. Operation and plasticity of hippocampal CA3 circuits: Implications for memory encoding. Nat. Rev. Neurosci. https://doi.org/10.1038/nrn.2017.10

Rivera, C., Voipio, J., Payne, J.A., Ruusuvuori, E., Lahtinen, H., Lamsa, K., Pirvola, U., Saarma, M., Kaila, K., 1999. The K+/Cl- co-transporter KCC2 renders GABA hyperpolarizing during neuronal maturation. Nature 397. https://doi.org/10.1038/16697

Robinson, N.T.M., Descamps, L.A.L., Russell, L.E., Buchholz, M.O., Bicknell, B.A., Antonov,

G.K., Lau, J.Y.N., Nutbrown, R., Schmidt-Hieber, C., Häusser, M., 2020. Targeted Activation of Hippocampal Place Cells Drives Memory-Guided Spatial Behavior. Cell 183. https://doi.org/10.1016/j.cell.2020.09.061

Rolotti, S. V., Ahmed, M., Szoboszlay, M., Geiller, T., Negran, A., Blockus, H., Gonzalez, K.C., Sparks, F., Solis Canales, A.S., Tuttman, A., Peterka, D., Zemelman, B., Polleux, F., Losonczy, A., 2021. Local Feedback Inhibition Tightly Controls Rapid Formation of Hippocampal Place Fields. SSRN Electron. J. https://doi.org/10.2139/ssrn.3863581

Royer, S., Zemelman, B. V., Losonczy, A., Kim, J., Chance, F., Magee, J.C., Buzsáki, G., 2012. Control of timing, rate and bursts of hippocampal place cells by dendritic and somatic inhibition. Nat. Neurosci. 15, 769–775. https://doi.org/10.1038/nn.3077

Rueckemann, J.W., Dimauro, A.J., Rangel, L.M., Han, X., Boyden, E.S., Eichenbaum, H., 2016. Transient optogenetic inactivation of the medial entorhinal cortex biases the active population of hippocampal neurons. Hippocampus 26. https://doi.org/10.1002/hipo.22519

Ruediger, S., Vittori, C., Bednarek, E., Genoud, C., Strata, P., Sacchetti, B., Caroni, P., 2011. Learning-related feedforward inhibitory connectivity growth required for memory precision. Nature 473. https://doi.org/10.1038/nature09946

Sadeh, S., Clopath, C., 2021. Inhibitory stabilization and cortical computation. Nat. Rev. Neurosci. https://doi.org/10.1038/s41583-020-00390-z

Scharfman, H.E., 2016. The enigmatic mossy cell of the dentate gyrus. Nat. Rev. Neurosci. https://doi.org/10.1038/nrn.2016.87

Schlingloff, D., Káli, S., Freund, T.F., Hájos, N., Gulyás, A.I., 2014. Mechanisms of sharp wave initiation and ripple generation. J. Neurosci. 34. https://doi.org/10.1523/JNEUROSCI.0867-14.2014

SCOVILLE, W.B., MILNER, B., 1957. Loss of recent memory after bilateral hippocampal lesions. J. Neurol. Neurosurg. Psychiatry 20. https://doi.org/10.1136/jnnp.20.1.11

Sharma, V., Sood, R., Khlaifia, A., Eslamizade, M.J., Hung, T.Y., Lou, D., Asgarihafshejani, A., Lalzar, M., Kiniry, S.J., Stokes, M.P., Cohen, N., Nelson, A.J., Abell, K., Possemato, A.P., Gal-Ben-Ari, S., Truong, V.T., Wang, P., Yiannakas, A., Saffarzadeh, F., Cuello, A.C., Nader, K., Kaufman, R.J., Costa-Mattioli, M., Baranov, P. V., Quintana, A., Sanz, E., Khoutorsky, A., Lacaille, J.C., Rosenblum, K., Sonenberg, N., 2020. eIF2α controls memory consolidation via excitatory and somatostatin neurons. Nature 586. https://doi.org/10.1038/s41586-020-2805-8

Sheffield, M.E.J., Adoff, M.D., Dombeck, D.A., 2017. Increased Prevalence of Calcium Transients across the Dendritic Arbor during Place Field Formation. Neuron 96, 490-504.e5. https://doi.org/10.1016/j.neuron.2017.09.029

Shuman, T., Aharoni, D., Cai, D.J., Lee, C.R., Chavlis, S., Page-Harley, L., Vetere, L.M., Feng, Y., Yang, C.Y., Mollinedo-Gajate, I., Chen, L., Pennington, Z.T., Taxidis, J., Flores, S.E., Cheng, K., Javaherian, M., Kaba, C.C., Rao, N., La-Vu, M., Pandi, I., Shtrahman, M., Bakhurin, K.I., Masmanidis, S.C., Khakh, B.S., Poirazi, P., Silva, A.J., Golshani, P., 2020. Breakdown of spatial coding and interneuron synchronization in epileptic mice. Nat. Neurosci. 23, 229–238. https://doi.org/10.1038/s41593-019-0559-0

Siapas, A.G., Wilson, M.A., 1998. Coordinated interactions between hippocampal ripples and cortical spindles during slow-wave sleep. Neuron 21. https://doi.org/10.1016/S0896-6273(00)80629-7

Sik, A., Penttonen, M., Ylinen, A., Buzsaki, G., 1995. Hippocampal CA1 interneurons: An in vivo intracellular labeling study. J. Neurosci. 15, 6651–6665.

https://doi.org/10.1523/jneurosci.15-10-06651.1995

Skaggs, W.E., McNaughton, B.L., Wilson, M.A., Barnes, C.A., 1996. Theta phase precession in hippocampal neuronal populations and the compression of temporal sequences. Hippocampus 6. https://doi.org/10.1002/(SICI)1098-1063(1996)6:2<149::AID-HIPO6>3.0.CO;2-K

Slomianka, L., Amrein, I., Knuesel, I., Sørensen, J.C., Wolfer, D.P., 2011. Hippocampal pyramidal cells: The reemergence of cortical lamination. Brain Struct. Funct. https://doi.org/10.1007/s00429-011-0322-0

Solstad, T., Moser, E.I., Einevoll, G.T., 2006. From grid cells to place cells: A mathematical model. Hippocampus 16. https://doi.org/10.1002/hipo.20244

Soltesz, I., Losonczy, A., 2018. CA1 pyramidal cell diversity enabling parallel information processing in the hippocampus. Nat. Neurosci. https://doi.org/10.1038/s41593-018-0118-0

Somogyi, J., Baude, A., Omori, Y., Shimizu, H., Mestikawy, S. El, Fukaya, M., Shigemoto, R., Watanabe, M., Somogyi, P., 2004. GABAergic basket cells expressing cholecystokinin contain vesicular glutamate transporter type 3 (VGLUT3) in their synaptic terminals in hippocampus and isocortex of the rat. Eur. J. Neurosci. 19, 552–569. https://doi.org/10.1111/j.0953-816X.2003.03091.x

Somogyi, P., Katona, L., Klausberger, T., Lasztóczi, B., Viney, T.J., 2014. Temporal redistribution of inhibition over neuronal subcellular domains underlies state-dependent rhythmic change of excitability in the hippocampus. Philos. Trans. R. Soc. B Biol. Sci. https://doi.org/10.1098/rstb.2012.0518

Sosa, M., Giocomo, L.M., 2021. Navigating for reward. Nat. Rev. Neurosci. https://doi.org/10.1038/s41583-021-00479-z

Spruston, N., Lübke, J., Frotscher, M., 1997. Interneurons in the stratum lucidum of the rat hippocampus: An anatomical and electrophysiological characterization. J. Comp. Neurol. 385. https://doi.org/10.1002/(SICI)1096-9861(19970901)385:3<427::AID-CNE7>3.0.CO;2-5

Squire, L.R., 2009. The Legacy of Patient H.M. for Neuroscience. Neuron. https://doi.org/10.1016/j.neuron.2008.12.023

Squire LR., 1986. Mechanisms of memory. Science 232(4758):1612-9. doi: 10.1126/science.3086978. PMID: 3086978.

Squire, L.R., 1992. Memory and the Hippocampuss: A Synthesis From Findings With Rats, Monkeys, and Humans. Psychol. Rev. https://doi.org/10.1037/0033-295X.99.2.195

Suzanne Corkin, 2002. Whats new with the amnesic patient H.M? Nat. Rev. Neurosci. 3.

Szabadics, J., Soltesz, I., 2009. Functional specificity of mossy fiber innervation of GAB aergic cells in the hippocampus. J. Neurosci. 29. https://doi.org/10.1523/JNEUROSCI.5390-08.2009

Szabo, G.G., Du, X., Oijala, M., Varga, C., Parent, J.M., Soltesz, I., 2017. Extended Interneuronal Network of the Dentate Gyrus. Cell Rep. 20. https://doi.org/10.1016/j.celrep.2017.07.042

Szalay, G., Judák, L., Katona, G., Ócsai, K., Juhász, G., Veress, M., Szadai, Z., Fehér, A., Tompa, T., Chiovini, B., Maák, P., Rózsa, B., 2016. Fast 3D Imaging of Spine, Dendritic, and Neuronal Assemblies in Behaving Animals. Neuron 92, 723–738. https://doi.org/10.1016/j.neuron.2016.10.002

Takeuchi, T., Duszkiewicz, A.J., Sonneborn, A., Spooner, P.A., Yamasaki, M., Watanabe, M., Smith, C.C., Fernández, G., Deisseroth, K., Greene, R.W., Morris, R.G.M., 2016. Locus

coeruleus and dopaminergic consolidation of everyday memory. Nature 537. https://doi.org/10.1038/nature19325

Taniguchi, H., Lu, J., Huang, Z.J., 2013. The spatial and temporal origin of chandelier cells in mouse neocortex. Science (80-.). 339, 70–74. https://doi.org/10.1126/science.1227622

Teles-Grilo Ruivo, L.M., Mellor, J.R., 2013. Cholinergic modulation of hippocampal network function. Front. Synaptic Neurosci. https://doi.org/10.3389/fnsyn.2013.00002

Terada, S., Geiller, T., Liao, Z., O'Hare, J., Vancura, B., Losonczy, A., 2022. Adaptive stimulus selection for consolidation in the hippocampus. Nature 601. https://doi.org/10.1038/s41586-021-04118-6

TF, F., G, B., 1996. Interneurons of the Hippocampus. Hippocampus 6. https://doi.org/10.1002/(SICI)1098-1063(1996)6:4<347::AID-HIPO1>3.0.CO;2-I

Tolman, E.C., 1948. Cognitive maps in rats and men. Psychol. Rev. 55. https://doi.org/10.1037/h0061626

Tremblay, R., Lee, S., Rudy, B., 2016. GABAergic Interneurons in the Neocortex: From Cellular Properties to Circuits. Neuron. https://doi.org/10.1016/j.neuron.2016.06.033

Tricoire, L., Pelkey, K.A., Daw, M.I., Sousa, V.H., Miyoshi, G., Jeffries, B., Cauli, B., Fishell, G., McBain, C.J., 2010. Common origins of hippocampal ivy and nitric oxide synthase expressing neurogliaform cells. J. Neurosci. 30, 2165–2176. https://doi.org/10.1523/JNEUROSCI.5123-09.2010

Tricoire, L., Pelkey, K.A., Erkkila, B.E., Jeffries, B.W., Yuan, X., McBain, C.J., 2011. A blueprint for the spatiotemporal origins of mouse hippocampal interneuron diversity. J. Neurosci. 31, 10948–10970. https://doi.org/10.1523/JNEUROSCI.0323-11.2011

Troullinou, E., Tsagkatakis, G., Chavlis, S., Turi, G., Li, W.-K., Losonczy, A., Tsakalides, P.,

Poirazi, P., 2019. Artificial neural networks in action for an automated cell-type classification of biological neural networks 14, 1–10.

Tsao, A., Moser, M.B., Moser, E.I., 2013. Traces of experience in the lateral entorhinal cortex. Curr. Biol. 23. https://doi.org/10.1016/j.cub.2013.01.036

Tsao, A., Sugar, J., Lu, L., Wang, C., Knierim, J.J., Moser, M.B., Moser, E.I., 2018. Integrating time from experience in the lateral entorhinal cortex. Nature 561. https://doi.org/10.1038/s41586-018-0459-6

Tukker, J.J., Lasztóczi, B., Katona, L., Roberts, J.D.B., Pissadaki, E.K., Dalezios, Y., Márton, L., Zhang, L., Klausberger, T., Somogyi, P., 2013. Distinct dendritic arborization and in vivo firing patterns of parvalbumin-expressing basket cells in the hippocampal area CA3. J. Neurosci. 33. https://doi.org/10.1523/JNEUROSCI.5052-12.2013

Tulving, E., 2002. Episodic memory: From mind to brain. Annu. Rev. Psychol. 53. https://doi.org/10.1146/annurev.psych.53.100901.135114

Turi, G.F., Li, W.K., Chavlis, S., Pandi, I., O'Hare, J., Priestley, J.B., Grosmark, A.D., Liao, Z., Ladow, M., Zhang, J.F., Zemelman, B.V., Poirazi, P., Losonczy, A., 2019. Vasoactive Intestinal Polypeptide-Expressing Interneurons in the Hippocampus Support Goal-Oriented Spatial Learning. Neuron 101, 1150-1165.e8. https://doi.org/10.1016/j.neuron.2019.01.009

Tyan, L., Chamberland, S., Magnin, E., Camiré, O., Francavilla, R., Suzanne David, L., Deisseroth, K., Topolnik, L., 2014. Dendritic inhibition provided by interneuron-specific cells controls the firing rate and timing of the hippocampal feedback inhibitory circuitry. J. Neurosci. 34, 4534–4547. https://doi.org/10.1523/JNEUROSCI.3813-13.2014

Van Cauter, T., Poucet, B., Save, E., 2008. Unstable CA1 place cell representation in rats with entorhinal cortex lesions. Eur. J. Neurosci. 27. https://doi.org/10.1111/j.1460-

9568.2008.06158.x

van de Ven, G.M., Trouche, S., McNamara, C.G., Allen, K., Dupret, D., 2016. Hippocampal Offline Reactivation Consolidates Recently Formed Cell Assembly Patterns during Sharp Wave-Ripples. Neuron 92. https://doi.org/10.1016/j.neuron.2016.10.020

Vandecasteele, M., Varga, V., Berényi, A., Papp, E., Barthó, P., Venance, L., Freund, T.F., Buzsáki, G., 2014. Optogenetic activation of septal cholinergic neurons suppresses sharp wave ripples and enhances theta oscillations in the hippocampus. Proc. Natl. Acad. Sci. U. S. A. 111. https://doi.org/10.1073/pnas.1411233111

Varga, C., Golshani, P., Soltesz, I., 2012. Frequency-invariant temporal ordering of interneuronal discharges during hippocampal oscillations in awake mice. Proc. Natl. Acad. Sci. U. S. A. 109, E2726–E2734. https://doi.org/10.1073/pnas.1210929109

Varga, C., Oijala, M., Lish, J., Szabo, G.G., Bezaire, M., Marchionni, I., Golshani, P., Soltesz, I., 2014. Functional fission of parvalbumin interneuron classes during fast network events. Elife 3, 1–23. https://doi.org/10.7554/eLife.04006

Varga, V., Hangya, B., Kránitz, K., Ludányi, A., Zemankovics, R., Katona, I., Shigemoto, R., Freund, T.F., Borhegyi, Z., 2008. The presence of pacemaker HCN channels identifies theta rhythmic GABAergic neurons in the medial septum. J. Physiol. 586. https://doi.org/10.1113/jphysiol.2008.155242

Varga, V., Losonczy, A., Zemelman, B. V., Borhegyi, Z., Nyiri, G., Domonkos, A., Hangya, B., Holderith, N., Magee, J.C., Freund, T.F., 2009. Fast synaptic subcortical control of hippocampal circuits. Science (80-.). 326, 449–453. https://doi.org/10.1126/science.1178307

Vida, I., Frotscher, M., 2000. A hippocampal interneuron associated with the mossy fiber

system. Proc. Natl. Acad. Sci. U. S. A. 97. https://doi.org/10.1073/pnas.97.3.1275

Vida, I., Halasy, K., Szinyei, C., Somogyi, P., Buhl, E.H., 1998. Unitary IPSPs evoked by interneurons at the stratum radiatum-stratum lacunosum-moleculare border in the CA1 area of the rat hippocampus *in vitro*. J. Physiol. 506, 755–773. https://doi.org/10.1111/j.1469-7793.1998.755bv.x

Viney, T.J., Lasztoczi, B., Katona, L., Crump, M.G., Tukker, J.J., Klausberger, T., Somogyi, P., 2013. Network state-dependent inhibition of identified hippocampal CA3 axo-axonic cells in vivo. Nat. Neurosci. 16, 1802–1811. https://doi.org/10.1038/nn.3550

Vogels, T.P., Sprekeler, H., Zenke, F., Clopath, C., Gerstner, W., 2011. Inhibitory plasticity balances excitation and inhibition in sensory pathways and memory networks. Science (80-.). 334. https://doi.org/10.1126/science.1211095

Wagatsuma, A., Okuyama, T., Sun, C., Smith, L.M., Abe, K., Tonegawa, S., 2017. Locus coeruleus input to hippocampal CA3 drives single-trial learning of a novel context. Proc. Natl. Acad. Sci. U. S. A. 115. https://doi.org/10.1073/pnas.1714082115

Wang, S.H., Morris, R.G.M., 2010. Hippocampal-neocortical interactions in memory formation, consolidation, and reconsolidation. Annu. Rev. Psychol. 61. https://doi.org/10.1146/annurev.psych.093008.100523

Wang, D. V., Yau, H.J., Broker, C.J., Tsou, J.H., Bonci, A., Ikemoto, S., 2015. Mesopontine median raphe regulates hippocampal ripple oscillation and memory consolidation. Nat. Neurosci. 18. https://doi.org/10.1038/nn.3998

Wang, X., Allen, W.E., Wright, M.A., Sylwestrak, E.L., Samusik, N., Vesuna, S., Evans, K., Liu, C., Ramakrishnan, C., Liu, J., Nolan, G.P., Bava, F.A., Deisseroth, K., 2018. Three-dimensional intact-tissue sequencing of single-cell transcriptional states. Science (80-.).

361. https://doi.org/10.1126/science.aat5691

Wester, J.C., McBain, C.J., 2014. Behavioral state-dependent modulation of distinct interneuron subtypes and consequences for circuit function. Curr. Opin. Neurobiol. https://doi.org/10.1016/j.conb.2014.07.007

Wick, Z.C., Tetzlaff, M.R., Krook-Magnuson, E., 2019. Novel long-range inhibitory nNOS-expressing hippocampal cells. Elife 8. https://doi.org/10.7554/eLife.46816

Wilent, W.B., Nitz, D.A., 2007. Discrete Place Fields of Hippocampal Formation Interneurons. J. Neurophysiol. 97, 4152–4161. https://doi.org/10.1152/jn.01200.2006

Wilson, M.A., McNaughton, B.L., 1993. Dynamics of the hippocampal ensemble code for space. Science (80-.). 261, 1055–1058. https://doi.org/10.1126/science.8351520

Winterer, J., Lukacsovich, D., Que, L., Sartori, A.M., Luo, W., Földy, C., 2019. Single-cell RNA-Seq characterization of anatomically identified OLM interneurons in different transgenic mouse lines. Eur. J. Neurosci. 50, 3750–3771. https://doi.org/10.1111/ejn.14549

Xu, W., Wilson, D.A., 2012. Odor-evoked activity in the mouse lateral entorhinal cortex. Neuroscience 223. https://doi.org/10.1016/j.neuroscience.2012.07.067

Yao, Z., Nguyen, T.N., van Velthoven, C.T.J., Goldy, J., Sedeno-Cortes, A.E., Baftizadeh, F., Bertagnolli, D., Casper, T., Crichton, K., Ding, S.-L., Fong, O., Garren, E., Glandon, A., Gray, J., Graybuck, L.T., Hirschstein, D., Kroll, M., Lathia, K., Levi, B., McMillen, D., Mok, S., Pham, T., Ren, Q., Rimorin, C., Shapovalova, N., Sulc, J., Sunkin, S.M., Tieu, M., Torkelson, A., Tung, H., Ward, K., Dee, N., Smith, K.A., Tasic, B., Zeng, H., 2020. A taxonomy of transcriptomic cell types across the isocortex and hippocampal formation. bioRxiv 2020.03.30.015214. https://doi.org/10.1101/2020.03.30.015214

Yap, E.L., Pettit, N.L., Davis, C.P., Nagy, M.A., Harmin, D.A., Golden, E., Dagliyan, O., Lin,

C., Rudolph, S., Sharma, N., Griffith, E.C., Harvey, C.D., Greenberg, M.E., 2021. Bidirectional perisomatic inhibitory plasticity of a Fos neuronal network. Nature 590. https://doi.org/10.1038/s41586-020-3031-0

Yozu, M., Tabata, H., Nakajima, K., 2005. The Caudal migratory stream: A novel migratory stream of interneurons derived from the caudal ganglionic eminence in the developing mouse forebrain. J. Neurosci. 25. https://doi.org/10.1523/JNEUROSCI.2072-05.2005

Zaremba, J.D., Diamantopoulou, A., Danielson, N.B., Grosmark, A.D., Kaifosh, P.W., Bowler, J.C., Liao, Z., Sparks, F.T., Gogos, J.A., Losonczy, A., 2017. Impaired hippocampal place cell dynamics in a mouse model of the 22q11.2 deletion. Nat. Neurosci. 20, 1612–1623. https://doi.org/10.1038/nn.4634

Zhao, C., Deng, W., Gage, F.H., 2008. Mechanisms and Functional Implications of Adult Neurogenesis. Cell. https://doi.org/10.1016/j.cell.2008.01.033

Ziv, Y., Burns, L.D., Cocker, E.D., Hamel, E.O., Ghosh, K.K., Kitch, L.J., Gamal, A. El, Schnitzer, M.J., 2013. Long-term dynamics of CA1 hippocampal place codes. Nat. Neurosci. 16. https://doi.org/10.1038/nn.3329

Zsiros, V., Maccaferri, G., 2005. Electrical coupling between interneurons with different excitable properties in the stratum lacunosum-moleculare of the juvenile CA1 rat hippocampus. J. Neurosci. 25, 8686–8695. https://doi.org/10.1523/JNEUROSCI.2810-05.2005